Frictional behaviour of volcanic debris avalanches following catastrophic flank collapses

Thesis submitted in accordance with the requirements of the University of Liverpool for the degree of Doctor in Philosophy

by Amy Claudette Hughes

March 2021

“Fault lines tremble underneath our glass house,

But I put it out of my mind

Long enough to call it courage.”

-Earth, Sleeping At Last

Declaration of Authorship

I, Amy Claudette Hughes, declare that this thesis entitled "Frictional behaviour of volcanic debris avalanches following catastrophic flank collapses" and the work presented in it are my own. I confirm that:

- This thesis was completed as part of a research degree at the University of Liverpool;
- The material contained in this thesis has not been presented, nor is currently being presented, either wholly or in parts, for any other degree or qualifications;
- Where I have consulted published studies, this has always been clearly referenced;
- Where the work was part of a collaborative effort, I have made clear what others have done and what I have contributed myself;
- Parts of this thesis have been submitted for publication or have been published as:
    - **Hughes, A.**, Kendrick, J. E., Salas, G., Wallace, P. A., Legros, F., Di Toro, G., Lavallée, Y. (published in *Journal of Structural Geology*). **Shear localisation, strain partitioning and frictional melting in a debris avalanche generated by volcanic flank collapse.**
    - **Hughes, A.**, Kendrick, J., Lamur, A., Salas, G., Lavallée, Y. (in preparation for *Tectonophysics*). **The juxtaposition of lithologies and the role of strength heterogeneities during frictional sliding.**
    - **Hughes, A.**, Kendrick, J. E., Lamur, A., Wadsworth, F. B., Wallace, P. A., Di Toro, G., Lavallée, Y. (published in *Frontiers in Earth Science*). **Frictional behaviour, wear and comminution of synthetic porous geomaterials.**

Signed: 

Amy Claudette Hughes

22rd March 2020

Abstract

Volcanic edifices are inherently unstable structures formed by the superimposition of highly variable volcanic products during dynamic and frequently rapid formation. Collapses of these structures occur at a range of scales, with larger mass movements posing significant hazards to surrounding populations. Volcanic debris avalanches formed from large collapses have been observed to have anomalously long runout distances, making it difficult to predict their potential extent. This observation suggests the presence of a lubricating mechanism that reduces shear resistance at the base of these mass movements. This thesis combines field observations, microstructural and geochemical analysis, rheological modelling, and frictional experiments conducted on both natural volcanic rocks and synthetic analogues to investigate the frictional response and resistance to shear pertaining to large mass movements in volcanic complexes.

The Arequipa volcanic landslide deposit in Peru, resulted from the collapse and propagation of material from the andesitic volcanic complex of Pichu Pichu for ~27 km over the rhyolitic ignimbrite substratum. Field observations revealed varying degrees of strain localisation in basal and secondary shear zones. In an extreme case strain was localised to a > 75 m long, planar 1-2 cm thick pseudotachylyte-bearing layer, the relic of syn-emplacement frictional melting. The adjacent cataclasite contained fragments of an earlier pseudotachylyte. Rheological modelling of both pseudotachylytes indicated that the early frictional melt underwent fragmentation at a velocity exceeding 31 m s^{-1}, whereas the intact melt layer likely formed at lower velocities. Across the spectrum of velocities at which melt could be sustained, the melt would not have resulted in a lubricating effect. In several localities, the presence of secondary shear zones within the lower deposit were identified, acting to partition the strain away from the primary contact, which could result from the viscous brake effect (high shear resistance) of the basal melt.

Samples of both the andesitic lava that comprises the majority of the debris avalanche (11 % porosity) and the rhyolitic ignimbrite substratum (49 % porosity), were collected from the Arequipa volcanic landslide deposit. These rocks were used to conduct experiments using a rotary shear apparatus to elucidate the frictional and tribological behaviour of both the individual lithologies and mixed lithology pairings during slip. All lithology combinations underwent velocity weakening at slip rates > 1 m s^{-1}. Single lithology experiments exhibited friction coefficients of between 0.6 and 0.8, but the mixed lithology tests showed lower

coefficients of between 0.45 and 0.6 at slip rates of 0.01 to 2.4 m s^{-1}. Juxtaposition of strong avalanche materials with weak and/or porous substrata may therefore lower basal friction in volcanic debris avalanches and encourage long run out distances, especially at high slip rates. It was also observed that strength heterogeneities within the lithologies and incorporation of rigid clasts into the slip zone intensified wear processes by ploughing, leading to highly unstable slip.

To further examine the effect of porosity on frictional behaviour of geomaterials, a series of glass analogue samples with porosities of 8, 19 and 30 % were produced by sintering glass beads, for rotary shear experiments. Porosity was found to provide an inherent roughness that cannot be smoothed by wear or abrasion of the material. At slip rates from 0.1 to 1 m s^{-1} the increase in porosity resulted in an increase in friction coefficients from < 0.4 for 8 % porosity to between 0.6 and 0.8 for 30 % porosity. Wear rates were also greater for more porous materials, as also observed in experiments on the natural rhyolitic ignimbrite, facilitating the rapid formation of comminuted fault products that lubricate slip. The increased wear rates at high porosity observed in both natural and analogue samples is shown to compete against the process of frictional heating due the surface energy creation associated with fracturing and the ejection of comminuted gouge. Therefore, materials that suffer high wear may delay, or even prevent, the onset of thermally activated weakening mechanisms during natural slip events.

The integration of field observations, laboratory experiments and rheological modelling presented in this study has identified new processes behind the reduction in basal friction in large volcanic mass movements and the mechanical behaviour that controls them. The localisation of strain in variable and juxtaposed volcanic materials gives rise to a range of tribological features, including the generation of frictional melt layers which may, or may not, aid basal lubrication. This study pioneers new lines of enquiry on mechanical wear, strength heterogeneity, and the rheologic potential of frictional melts, and sets a benchmark for the interrogation of the factors contributing to the anomalously long runout distances of volcanic landslides.

Contents

List of Figures

Chapter 1

Chapter 2

Chapter 3

Chapter 4

List of Tables

Acknowledgements

During my long (so very long) time in producing the following work, I have had help from so many people, and I would like take time to thank the vast group of people who made all of this possible.

To Yan and Jackie, my ever-patient supervisors. Yan, chatting science with you, either in the lab or over a beer, has kept my love of science glowing even in the darkest of times. Your breadth of knowledge on so many topics is humbling, and I have loved doing some crazy science with you over the past 4+ years and hope we do more in the future. Jackie, you made being stuck in a freezing cold basement lab torturing rocks not just tolerable, but insanely fun. I cannot thank you enough for the time and effort you have dedicated to helping me grow both as a person and as a scientist. I leave this PhD with a much greater amount of confidence and determination due to your mentorship. Thank you both for pushing me to go for things I never thought I could do and encouraging me every step of the way.

Anthony, thank you for stopping me from rage quitting a few times over the years and for lending your magic coding skills to fix some really pesky issues. You have always known exactly when I need a beer (often) or a coffee (always). To the next generation crew: Jenny, thanks for being unapologetically you, and for reminding me that in a world of flamingos, it is much better to be a pigeon (unless it's Bryce the crackhead pigeon, in which case, probably anything else is preferable); Josh, thanks for the memes, bud. I may someday forgive you for stealing my computer and putting it in the ceiling, but it is not this day.

To all the other members of the experimental volcanology lab group, co-authors and colleagues that I have worked with over the years; thank you for accepting a little baby volcanologist into your midst and making me feel so welcome despite the complete lack of previous volcanology experience. We definitely had some laughs, including some great adventures scrambling over some incredibly sharp rocks and countless conference shenanigans.

Thanks also to everyone who shared this PhD path with me along the way as fellow PhD students in both Liverpool and Manchester, of which there are way too many to name here, including all the people who have had the (mis)fortune of sharing an office with me over the years. Special thanks to Simon, Caroline and Suraya for supplying sanity and doggos; Mila, for never letting me leave without copious amounts of food; and Izzy, for the cake.

To the members of the "Amy's home for wayward PhD students" club, thank you for reminding me that housemates are fun and occasionally useful entities. Paul, thanks for the 1am geochemistry chats and the kitchen frolicking. Shaun; a great housemate for helping me opening jars, less so for reaching things on the top shelf. Thanks to you I now own more onesies than it is acceptable for a grown woman to have, a box of stupid inflatables I don't even want, and the ability to (badly) juggle. To Louise, my social bubble in virus times; thank you for the hugs, making sure I actually got out of bed each day, and the adventures to find some really strange beers.

A late, but essential, addition to the list of people who helped me along the way; thank you to all the regular crew in the PhDForum online workspace, for their (mostly) silent, but

unwavering support in the final isolated months before submission. Keep eating the frogs and don't kill the trees.

Finally, to my parents, without whom I would never have got this far and who have always been by greatest cheerleaders. Thank you for always supporting me and for believing in me even when I lost faith in myself. To Mum, thanks for the proofreading, and yes, I do want to put a comma there. To Dad, thanks for coming to rescue me when COVID hit so I wasn't stuck alone in my flat for a year. During my time at Liverpool, every time something went wrong, or I got a little lost, I had a little voice in the back of my head sounding suspiciously like you saying… "It's an adventure...".

“There was an earthquake,

There was an avalanche of change.”

-Earth, Sleeping At Last

Chapter 1: Introduction

1.1. Volcanic instability and sector collapses

Volcanic structures, active and extinct, display a range of morphologies and internal structures. Polygenetic volcanoes, forming from multiple eruptive phases, are constructed from the successive deposition of weak pyroclastic layers, lava flows and magma intrusion (McGuire, 1996, 2003; van Wyk de Vries and Davies, 2015). The incremental and rapid (on geological timescale) growth of volcanoes makes them variably coherent which differs from other mountainous structures that form by slow tectonic uplift (van Wyk de Vries and Davies, 2015). Polygenetic volcanoes are inherently unstable due to the overlapping and superimposition of mechanically differing materials within their complex formation, from coherent lava flow units to unconsolidated fall deposit layers. They are therefore more likely to undergo a spectrum of collapse or gravitational sliding events. Smaller monogenetic cones tend to only produce smaller rockfalls, sliding and slumping events as their simpler structure and lesser size does not promote major structural instabilities. Instability, in relation to volcanoes, can be defined by "*the condition within which a volcanic edifice has been destabilised to a degree sufficient to increase the likelihood of the structural failure of all or part of the edifice*" (McGuire, 1996; Voight and Elsworth, 1997; van Wyk de Vries and Davies, 2015).

Small scale collapses and rock falls have a high frequency of occurrence in a given system (weeks, days, hours); whereas more hazardous, large scale events involving several million cubic metres of material (with the largest events involving several cubic kilometres of material) occur at a much lower frequency, with repeat times of several hundreds or thousands of years (McGuire, 1996, 2003). Evidence of these larger events are found in collapse scarps and deposits around volcanoes worldwide, suggesting that the majority of large volcanoes have had a history of collapse (Siebert, 1984; McGuire, 1996; van Wyk de Vries and Davies, 2015) and large scale collapses occur globally several times per century (Siebert, 1992; van Wyk de Vries and Davies, 2015). Many modern population centres exist in close proximity to volcanoes, and they are therefore at risk from the hazards posed by volcanic collapses (Loughlin et al., 2015). There are multiple examples of large debris avalanche deposits in close proximity to cities (e.g. collapse from Popocatépetl in Mexico City) and it is estimated that 20,000 people have been killed historically by volcanic collapses (Siebert et al., 1987). However, the low frequency of these events means that large scale

collapses are not generally considered a primary volcanic hazard by the general population, as such events fade from collective memory or have not occurred in the history of the settlement. Post collapse, the slow re-addition of material to the edifice (through intrusion and eruption of volcanic products) must occur for the generation of the new structure to form, which is again capable of large-scale instability and collapse (van Wyk de Vries and Davies, 2015). This addition of material is dependent on the intensity and style of activity at each specific volcano. As the instability of volcanic edifices is caused by their internal structure, all volcanic edifices have the potential to partially collapse, whether active or dormant, within their lifetime which can often last up to hundreds of thousands of years. Collapses may occur even beyond the end of active volcanism at a volcano, especially if further weakening of the material occurs by progressive weathering/alteration over time. Regional earthquakes have been inferred/ observed to be a likely trigger at volcanoes, irrespective of its level of activity. In active structures, collapses may be associated with magma intrusion, or with the onset of an eruptive phase, with the failure of the edifice leading to an eruption (van Wyk de Vries and Davies, 2015; Maccaferri et al., 2017).

A sector collapse changes the subvolcanic stress distribution, which may cause magma vesiculation and fragmentation, leading to an explosive eruption, such as witnessed during the 1980 eruption at Mount St. Helens (Lipman and Mullineaux, 1981). At Mt St Helens the eruption caused a multitude of volcanic hazards in addition to the initial collapse and debris avalanche. The event was the first occurrence of a large-scale edifice collapse monitored continuously (Lipman and Mullineaux, 1981) and highlighted the importance of these events as a serious, though rare, volcanic hazard. This event prompted several decades of research into the large-scale instability of volcanic structures (Lagmay et al., 2000; McGuire, 1996; Shea and van Wyk de Vries, 2010; Sherrod et al., 2008; Voight, 2000; Vries and Borgia, 1996).

Studies on sector collapse and associated debris avalanches have utilised and integrated field investigations, numerical modelling, mechanical testing and analogue experiments to determine the mechanics of instability and collapse, and to improve our hazard assessment and risk mitigation strategies.

1.1.1. Causes of volcanic structure instability

Instability can be driven by several factors over a range of timescales, from near instantaneous destabilisation and failure to instability formed over several thousands of years by mechanical loading (McGuire, 1996). Long term destabilising factors can prime the structure for failure, which is then triggered by a shorter term event or fluctuation in

conditions (Fig. 1.1; McGuire, 1996; van Wyk de Vries and Davies, 2015). These factors can be the increased overloading of flanks by eruptive materials (e.g. McGuire, 1996; van Wyk de Vries and Davies, 2015); the incremental displacement from repeated dyke intrusion (e.g. McGuire et al., 1990; Giampiccolo et al., 2020); the oversteepening of slopes by magma emplacement (e.g. Lipman and Mullineaux, 1981; Siebert et al., 1987); edifice spreading (e.g. Borgia et al., 2000); basement uplift or subsidence from long term gravitational deformation of volcanic structures (e.g. van Wyk de Vries and Francis, 1997; Murray et al., 2018); and the ongoing alteration and weakening of edifice building materials (e.g. Reid et al., 2001, 2010).

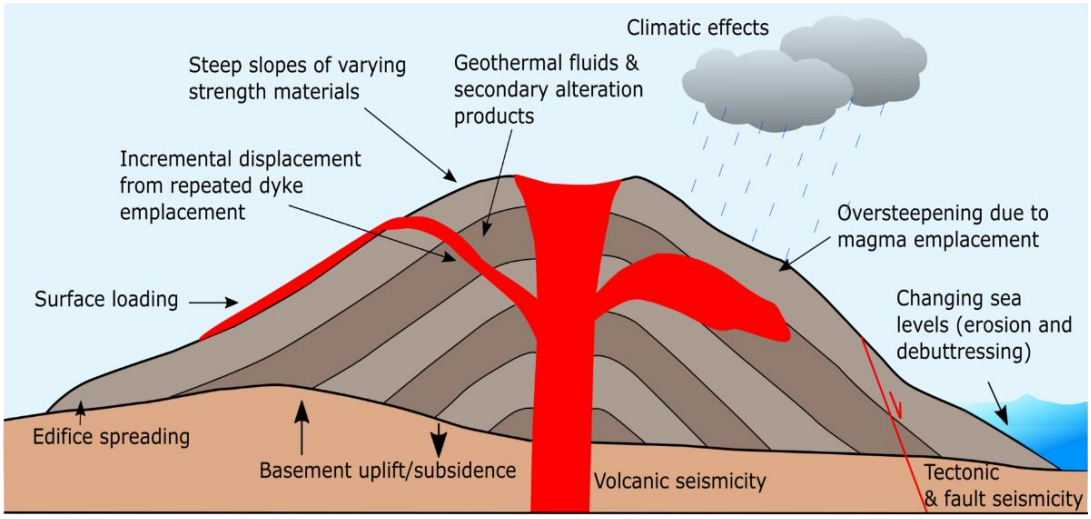

Figure 1.1. Diagram of common destabilising collapse primers (long term) and triggers (short term) (adapted from McGuire 1996).

Once primed for collapse, a failure may then be triggered by shorter term phenomenon such as fluctuating pore pressure from hydrothermal systems (e.g. Day, 1996; Voight and Elsworth, 1997; Reid, 2004); increased rainfall (e.g. Yamasato et al., 1998; Matthews and Barclay, 2004); regional earthquakes (e.g. Hall et al., 1999; Ventura et al., 1999); or volcanic seismicity (e.g. Ando, 1979; Acocella and Neri, 2003).

Collapses may be preceded or succeeded by increased volcanic and/or hydrothermal activity which may act as the trigger for a collapse (Siebert et al., 1987) or as a result of the collapse which causes a subsequent eruption. The depressurisation due to unroofing of pressurised systems of magma (e.g. Mt St Helens; Lipman and Mullineaux, 1981) or hydrothermal fluids (e.g. Bandai-San; Siebert et al., 1987) during collapses, may result in the onset of explosive activity (Lipman and Mullineaux, 1981; Alvarado and Soto, 2002; Acocella and Neri, 2003; Hunt et al., 2018). The instability of volcanic structures continues in periods of dormancy or once activity has ceased altogether and can be triggered by non-volcanic triggers. Therefore,

volcanic structures can still pose significant hazards in the form large scale collapses even in the absence of volcanic activity (Shea and van Wyk de Vries, 2010).

1.1.2. Structural controls on sector collapse events

The collapse of a volcanic edifice initiates when a failure occurs, either by brittle failure or shearing within weaker or unconsolidated layers, leading to a loss of cohesion at the base of the detached edifice section. This commonly occurs within weak layers which initially added to the instability of the structure. These weaknesses can be layers of unconsolidated pyroclastic materials, soils, volcanic breccia or fractured lavas within the piecemeal structure of the volcano (van Wyk de Vries and Davies, 2015). Alternatively hydrothermal activity can create pervasive weak clay-rich materials from initially strong volcanic rocks which may promote failure (e.g. Reid et al., 2001, 2010; van Wyk de Vries and Davies, 2015). Due to the active and complex structural history of some edifices, with some having undergone several phases of collapse and regrowth, old collapse scars infilled with new eruptive products through time represent a plane of weakness at the interface of old pre collapse structure and the newer deposits (Walter et al., 2019; Barrett et al., 2020). Deep-seated failures promoted by these weak layers or zones can result in the detachment of large masses of material along a basal decollement. Upon movement, the mass accelerates due to a rapid loss of shear resistance against the detachment, causing fast-moving debris avalanches (van Wyk de Vries and Davies, 2015). Therefore, of all volcanic constructs, polygenetic volcanoes have amongst the greatest potential to form large (> 10 km^3) mass movements (Pudasaini and Miller, 2013; van Wyk de Vries and Davies, 2015).

1.1.3. Mobility of large mass movements

Both volcanic and non-volcanic debris avalanches have the capability to exhibit high mobility, where mobility is calculated considering both the velocity and runout distance (Iverson et al., 2015). Large mass movements can reach approximately 100 m s^{-1} (Siebert et al., 1987; Shea and van Wyk de Vries, 2008) although this can vary greatly (McGuire, 1996). Runout distance is often evaluated by the fall height/length of runout ratio (often abbreviated to H/L or the Heim ratio) which represents the scale free coefficient of Coulomb sliding friction. The inverse of this ratio is the mobility of the mass movement (Dade and Huppert, 1998; Pudasaini and Miller, 2013). The total fall height is the change in elevation of the mass from source to final position and the length of runout is the extent of deposit after the event (Erismann and Abele, 2001; Legros, 2002). The volume of landslide material was constrained to influence the runout distance (Fig. 1.2). Small events, with correspondingly small volumes have H/L ratios of approximately 0.6. An increase in volume is linked to a decrease in H/L

and an increase in mobility, however events with volumes > 0.01 km^3 exhibit disproportionately (anomalously) long runouts (Scheidegger, 1973). The largest events, with volumes > 0.1 km^3, can have H/L values as low as ~0.1. This is presumed to be an effect of a drop in friction coefficient experienced at the base of the mass movements (Legros, 2002; van Wyk de Vries and Davies, 2015).

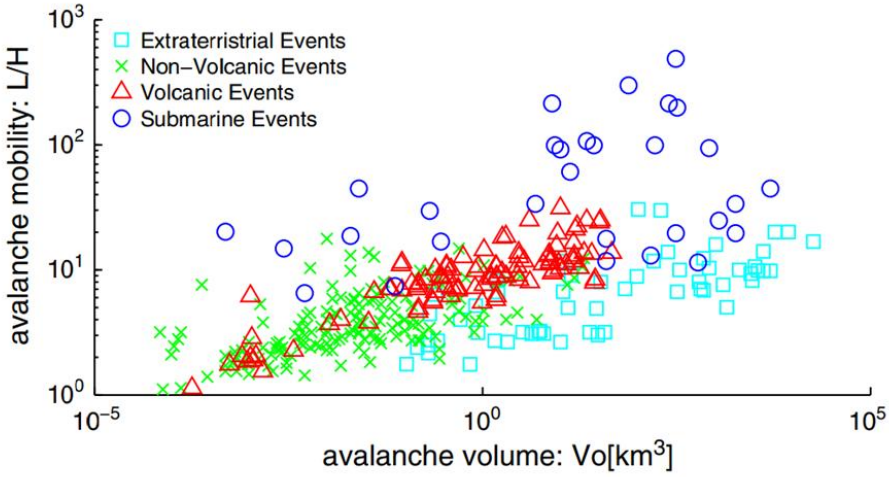

Figure 1.2. Relationship of avalanche mobility (inverse Hiem ratio) with avalanche volume. Note that volcanically-sourced avalanches from flank and sector collapses produce some of the greatest volume and hence greatest mobility of the terrestrial avalanches (from Pudasaini and Miller, 2013).

In order to recreate the H/L ratios seen in natural collapse events, modellers invoke a reduced friction on the basal planes, and analogue models use low friction basal materials (Shea and van Wyk de Vries, 2008; Paguican et al., 2014). Although this correlation of models and field evidence may indeed result from a reduced basal shear resistance, the exact mechanism (or mechanisms) is currently elusive. Multiple mechanisms have been suggested to enable this apparent decrease in basal friction. These include; lubricating basal layers of groundwater or ice (e.g Lucchitta, 1987; Legros, 2002; De Blasio, 2011), trapped air (e.g. Shreve, 1968), salt (e.g. De Blasio, 2011), acoustic fluidisation (e.g. Melosh, 1979, 1986; Johnson et al., 2016), mechanical fluidisation (e.g. Davies, 1982; Campbell et al., 1995), mechanical and thermal fluid pressurisation (e.g. Ferri et al., 2011; Mitchell et al., 2015), velocity weakening (e.g. Wang et al., 2017) and lubrication by frictional melting (e.g. Legros et al., 2000; De Blasio and Elverhøi, 2008; Wang et al., 2017).

Mass movements formed from slope instability, such as volcanic sector and flank collapse, were designated by Spray (1997) as “superfaults”. Superfaults are defined as faults that

experience a single slip event with very large displacement (> 100 m) at seismogenic slip rates (> 0.1 m s^{-1}) associated with extremely high strain rates. Aside from landslides, Spray (1997) also categorised collapses of impact craters following hypervelocity impacts (e.g. meteorite impacts) and the faulting associated with roof collapse leading to caldera formation (Spray, 1997; Legros et al., 2000) as other instances of superfaulting. In the case of landslides, the disaggregation of a coherent rock mass to a mixed block and granular flow changes the shearing behaviour at the basal contact, from coherent rock contacts to variably localised shear zones. This deviates from the initial description of a superfault to a more complex, yet still extremely rapid, sliding event. Understanding the frictional behaviours at very high strain rates is therefore key to understanding the mechanics of these high velocity, single slip events, including large scale volcanic collapses.

1.1.4. Sector collapse deposit morphology

The deposits from these mass movements tend to have a characteristic hummocky geomorphology and the structure is determined by the initial landslide configuration (Glicken, 1990, 1991; van Wyk de Vries and Francis, 1997; Belousov et al., 1999). The hummocks are formed from the spreading of the landslide mass, decreasing in size and frequency with increasing distance from the source (Glicken, 1990; van Wyk de Vries and Davies, 2015). Deposits can be broadly separated into facies, determined by the degree of disaggregation and fragmentation of the sliding mass (van Wyk de Vries and Davies, 2015). Block facies are formed from intact to highly fractured material with features still in their original positions. Matrix facies are formed from primarily small grain size material with only isolated small clasts. Mixed facies show an increase in clasts suspended in matrix material. Debris avalanche blocks of coherent material up to a hundred metres in size, which were transported relatively intact from their original position, and associated block facies, are usually concentrated in the area proximal to the source and in the interior of the deposit. Matrix facies are found in the distal areas (Glicken, 1990, 1991; Dufresne et al., 2016). In many deposits, there is also another basal facies identified, with material finer than in matrix facies and with no blocks found in the lower few metres of the deposit at the basal plane. This is due to the concentration of shear and increased fragmentation in a basal shear zone (Belousov et al., 1999; Davies et al., 2010; van Wyk de Vries and Davies, 2015).

1.2 The Friction of Rocks

The friction, wear and lubrication of natural slip events depends on a multitude of factors dictated by the environment and loading conditions, (temperature, applied normal stress,

slip velocity and pore fluids), the material properties (strength parameters and composition) and the contact conditions (roughness and the presence of lubricating layers) as highlighted in Figure 1.3 (Boneh and Reches, 2018).

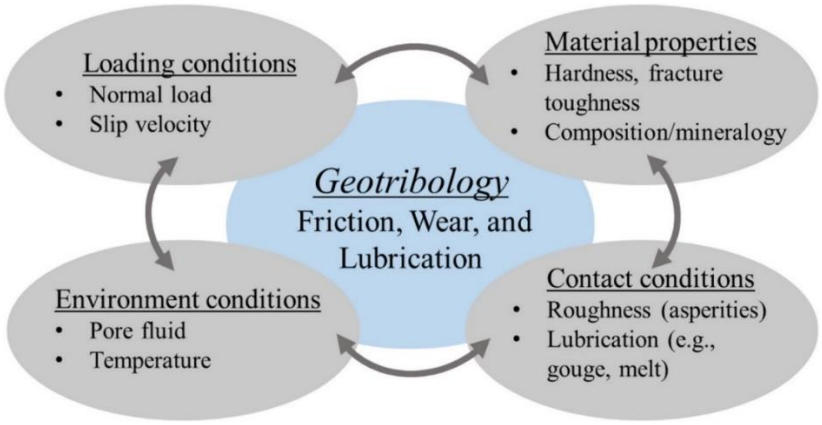

Figure 1.3. The interaction of different tribological processes with material properties and environmental conditions (Boneh and Reches, 2018).

As well as controlling the overall frictional behaviour, each of these factors may influence one another and evolve dynamically; for example, the presence of minerals with a propensity to undergo frictional melting would encourage the formation of melt along the fault (Spray, 2010) or variations in pore fluid pressure would modulate the effective normal load (Byerlee, 1978). Consideration of all the factors described here, as well as their interrelations are therefore paramount to understand the frictional behaviour and properties of geomaterials occurring during fault activity in a range of natural environments.

1.2.1. Byerlee Friction and Early experiments

A range of apparatuses and methods have been developed to study the frictional properties of rocks. Early on direct shear (Wang et al., 1975), double shear (Hoskins et al., 1968), biaxial (Scholz and Engelder, 1976) and triaxial (Byerlee, 1967) apparatuses were developed and used to great outcome. The results obtained from this diversity of approaches were collated in Byerlee (1978) and found to coarsely follow a seemingly simple relationship between the applied normal stress and resultant shear stress (Fig. 1.4). Much of our current understanding of the frictional behaviours is guided by this initial body of work.

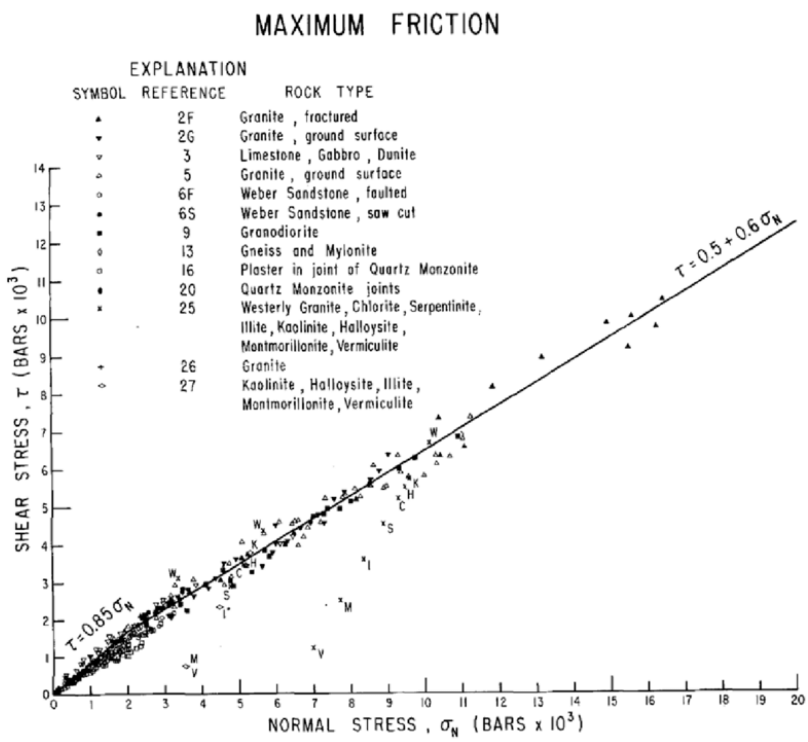

Figure. 1.4. Early and formative work of Byerlee (1978) with collated experimental frictional data from which the friction laws generated by this work were established.

Using compiled data from the rock physics community, Byerlee (1978) produced a universal friction law for rocks based on the Mohr-Coulomb failure criterion (Mohr, 1914), defining the frictional coefficient (μ) that relates the shear stress (τ) to the applied normal stress (σ_n), such that:

$$\mu = \frac{\tau}{\sigma_n} \tag{1.1}$$

At low normal stresses (< 200 MPa) μ = 0.85, and at higher normal stresses (> 200 MPa) μ = 0.6 with an additional cohesion of 50 MPa (0.5 bars x10^3, Fig. 1.4). This appears to frame the frictional properties of the majority of rock types with the exception of phyllosilicate-rich rocks which exhibit lower friction coefficients (Byerlee, 1978; Ikari et al., 2009; Moore and Lockner, 2011; Collettini et al., 2019).

The pressure of fluids in the porous structure of rocks (P_p) counteracts the normal stress applied against the rock interface, thus decreasing the net applied stress so that:

$$\mu = \frac{\tau}{\sigma_n - P_p} \tag{1.2}$$

1.2.2. High velocity frictional experiments: melting in the laboratory

The development of experimental set-ups capable of applying high slip rates and infinite slip distances promoted a surge of transformative studies in the late 1980s and 1990s. In 1990, the first purpose-built high-velocity rotary shear friction apparatus capable of measuring the shear stress of rock whilst controlling the slip rate and the applied stress was created (Shimamoto and Tsutsumi, 1994). Use of this apparatus resulted in seminal early rotary friction experiment studies on the development of frictional melts during extreme shear such as Shimamoto and Lin (1994) and Lin and Shimamoto (1998). The success of the apparatus informed the successive development of new generations of rotary shear apparatuses, capable of a very wide range of slip rates and (near) infinite displacements (Ma et al., 2014 and references therein). Using these apparatuses, the investigation of the frictional properties of rocks at a wide range of conditions could be conducted and the effects of faulting conditions on the mechanics of slip analysed.

1.2.3. Evolution of friction during slip

The frictional resistance evolution that occurs during slip follows a general trend that is similar for most rocks (e.g. Hirose and Shimamoto, 2005a). Upon the initiation of slip, an instantaneous increase in shear stress and hence friction coefficient is observed. This is due to the initial rupture of locked asperities and of areas that may have been coherent and or variably healed between sliding events (Dieterich, 1979; Ruina, 1983). Shear stress then decreases with displacement to a lower value, thus reaching a steady state resistance to shear. The distance over which the shear stress (and friction coefficient) reduces to this new steady value is the weakening distance described in the rate and state laws (Dieterich, 1979; Ruina, 1983).

In some experiments (if the slipe rate or applied normal stress is high), a second peak in shear stress may develop in association with melting along the rock interface due to the accumulation of frictional heat (e.g. Hirose and Shimamoto, 2005a). The melting of rocks due to extreme and often rapid heating is a disequilibrium, selective process in which minerals individually melt when the ambient temperature exceeds their melting temperature; as such, the early melt forms discrete patches (Hirose and Shimamoto, 2005a), with contrasting, unhomogenised chemistry and high fractions of suspended solid particles (restites) (Wallace et al., 2019a). Spreading of the melt patches promotes an increase in shear stress and further frictional heating (via viscous energy dissipation), further enhancing melting and coalescence of melt patches to form a continuous layer with reduced suspended solid fraction. Once the fault zone reaches a critical melt fraction, temperature tends to

stabilise and the viscosity of the melt layer dictates the shear response to slip (Chen et al., 2017; Fialko and Khazan, 2005; Kendrick et al., 2014; Wallace et al., 2019a).

1.2.4. Rate and state friction

The frictional resistance to fault slip is often described by the rate and state constitutive law (Dieterich, 1979, 1992; Ruina, 1983) where the effects of both slip rate and time-dependent physical state of the slipping interface describe frictional evolution. The empirical equations for the state parameter (θ) (Ruina, 1983) linked to deformation of asperities (Dieterich and Kilgore, 1994), and the rate parameter (Dieterich, 1979) can be written as:

$$\mu(V,\theta) = \mu^* + a\ln\left(\frac{V}{V^*}\right) + b\ln\left(\frac{V\theta}{D_c}\right) \tag{1.3}$$

where V is slip rate, θ is the state parameter, μ_{ss} is the steady state friction coefficient, μ^* is the friction coefficient at slip rate V^*, D_c is the displacement over which the evolution of friction occurs. From this, the expression (a - b) describes the velocity dependence of μ_{ss} (Fig. 1.5). This can either be velocity strengthening (where $a > b$ and resistance to sliding increases with velocity; Fig. 1.5a) or velocity weakening (where $a < b$ and resistance to sliding decreases with velocity; Fig. 1.5b). In a velocity weakening situation, instabilities and potential for earthquakes and larger movements on slip planes are possible. This weakening behaviour is observed in a wide range of rock types (Di Toro et al., 2011).

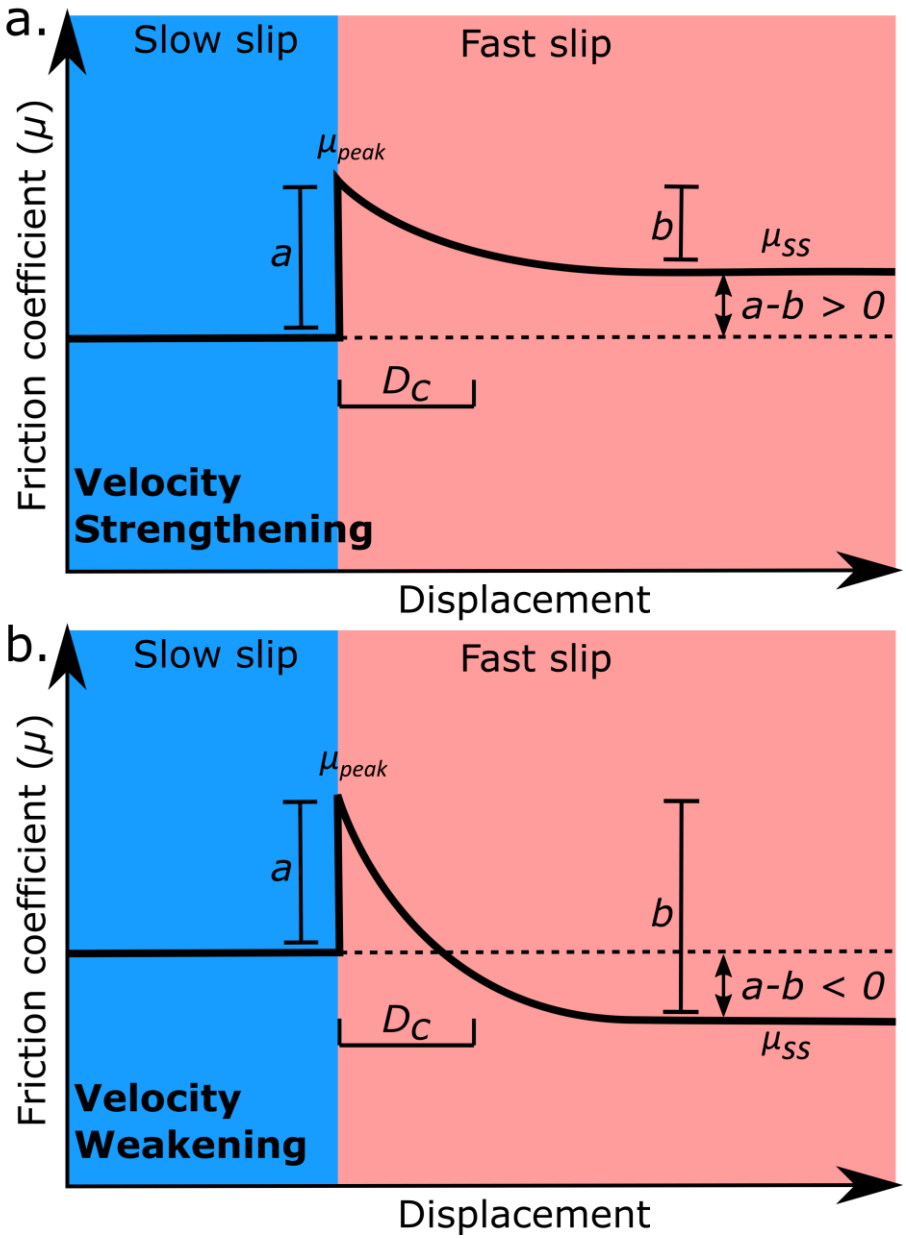

Figure 1.5. The evolution of friction from peak friction (μ_{peak}) to new steady state friction (μ_{ss}) over weakening distance (D_c) after a velocity increase in a a) velocity strengthening regime where a > b and b) velocity weakening regime where a < b (adapted from An et al., 2018).

1.2.5. Rate weakening behaviour

The rate weakening behaviour experimentally identified at slip rates approaching 1 m s^{-1} (equivalent to co-seismic slip rates) for a variety of rock types, suggests the contribution of one or multiple mechanisms depending on rock types, variably impacted by the chemical and mechanical attributes of each rock type. Investigation into the behaviour of rock at high slip rates has alluded to a variety of primarily thermally activated weakening mechanisms, which may promote a reduction in friction coefficient to values ≤ 0.1 in some instances (Fig. 1.6; Di Toro et al., 2011).

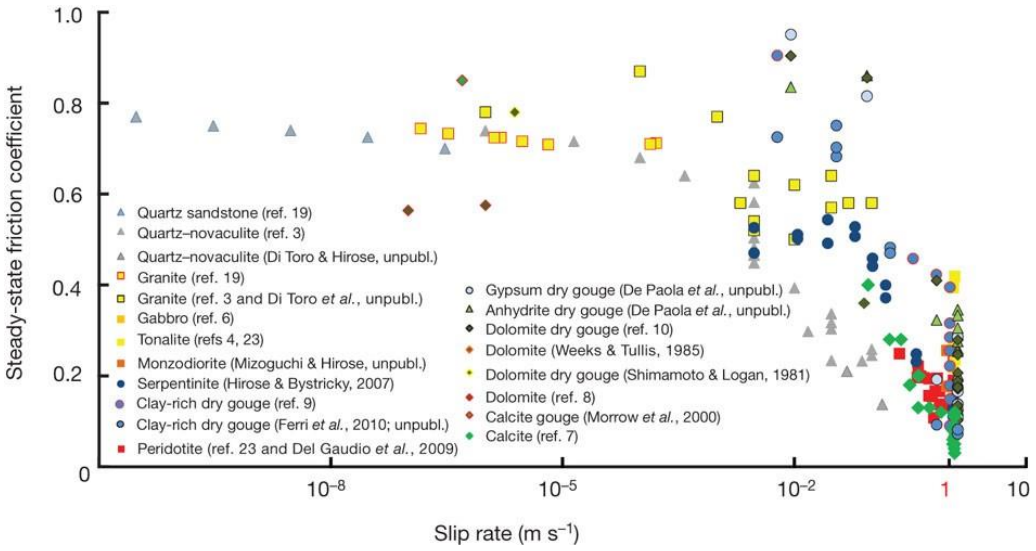

Figure. 1.6. Steady state friction coefficients in experiments run on varying rock types (data compiled by Di Toro et al. (2011) and references within). Note the decrease in friction coefficient at slip rates approaching 1 m s^{-1} due to rate weakening behaviour.

The mechanisms for dynamic slip weakening include the pressurisation of pore fluids trapped in the slip zone either by mechanical pressurisation (e.g. Faulkner et al., 2018) or heating (e.g. Sibson, 1973; Andrews, 2002; Rice, 2006); flash heating at asperity contacts leading to thermal weakening (e.g. Rice, 2006); the chemical decomposition of the wall rock at high temperature (e.g. Han et al., 2007, 2010) which can also lead to the development of nanograins leading to powder lubrication (e.g. Han et al., 2010; De Paola et al., 2011); devolatilisation reactions in of certain rock-forming minerals (carbonates, zeolite, clays) during heating, resulting in the release of volatiles (H_2O, CO2); the production of gouge by material wear, abrasion and comminution (e.g. Matsu'ura et al., 1992; Han et al., 2010; Reches and Lockner, 2010); the formation of silica-gel layers from the amorphisation of quartz upon interaction with water in quartz rich rocks (e.g. Goldsby and Tullis, 2002; Di Toro et al., 2004); and, the production and presence of frictional melt in fault zones at extreme shear conditions (e.g. Hirose and Shimamoto, 2005a; Di Toro et al., 2006). Some of these mechanisms are shared with the theoretical mechanisms for reducing the basal friction of large mass movements and avalanches, leading to their enhanced runout capabilities described in Section 1.1.3.

1.3. Wear and comminution during sliding

Frictional sliding produces wear and damage to the wall rocks and rock interfaces. Wear is dependent on the tribological factors of contact conditions and material properties listed in Figure 1.3, as the physical properties of the contact surfaces determine the generation of wear product layers in the slip zone.

The "true" contact area of sliding surfaces is generally smaller than the total surface area of the fault due to surface roughness and asperities. This concentrates the shear stress to asperity contacts, which, in turn, localises the accumulation of frictional heat (Rice, 2006; as discussed in Section 1.2.5) and mechanical wear (Engelder and Scholz, 1976; Scholz and Engelder, 1976; Bhushan, 1998). The interaction of the edges of pores and fractures with the contact surfaces further increases roughness and decreases the true contact area; and with greater normal stresses applied across the interface, the true contact area increases due to asperity deformation (Bhushan, 1998; Bowden and Tabor, 2001).

In the absence of gouge or fault product layers separating the two contact surfaces, the roughness of those surfaces is therefore a primary factor controlling the frictional resistance and the tribological response during sliding. Natural slip surfaces are observed to have a fractal roughness, self-similar across scales (Power et al., 1988; Sagy et al., 2007) and these tend to smooth with increasing slip (Scholz, 1987; Power et al., 1988; Sagy et al., 2007; Candela et al., 2012; Brodsky et al., 2016). This smoothing is achieved by wear and the failure of asperity contacts (Archard, 1953; Rabinowicz, 1965; Bowden and Tabor, 2001). The interacting mechanism acting to cause this damage and material removal are: adhesive, at asperity contacts (Archard, 1953); abrasive due to asperity ploughing (Moore and King, 1980); delamination, damaging material away from the sliding surface (Fleming and Suh, 1977); fatigue from repeating events (Rozeanu, 1963); and corrosive due to chemical weakening (Watson et al., 1995). These processes are reliant on the hardness and fracture toughness of the materials involved (Spray, 1992, 2010; Boneh and Reches, 2018) and local conditions (pressure, stress, temperature, fluid and rock chemistry) as shown in Figure 1.3.

Early work conducted by Archard (1953) to quantify the accumulation of wear (G) along faults coined the following expression:

$$G = KD\left(\frac{\sigma_n}{H}\right) \tag{1.4}$$

where K is the wear coefficient (in units m^2), D is the slip distance, σ_n is the applied normal stress and H is the hardness of the material. In the case of slip along two contrasting

materials, *H* is the hardness of the softer material as the softer material generally undergoes the most wear (Boneh et al., 2013). This relationship assumes that wear is constant. However, observation of wear evolution revealed an initial "running in" phase of high wear rates before reducing to a lower wear rate (Queener et al., 1965). This running-in phase is linked with initial asperity removal and is reliant on the original roughness of the surfaces (Power et al., 1988; Wang and Scholz, 1994).

Scholz (1987) suggested that the rate of wear (i.e., wear per meters of slip) is linearly proportional to the applied normal stresses based on the work of Archard (1953) and low velocity experimental data (Yoshioka, 1986). Later, Morohashi et al. (1973) used experimental investigation and suggested that wear followed a power law with normal stress. High velocity experimental data shows an additional control of slip rate on wear, with multiple materials exhibiting lower wear rates in high velocity experiments (Fig. 1.7; Hirose et al., 2012; Boneh et al., 2013; Boneh and Reches, 2018).

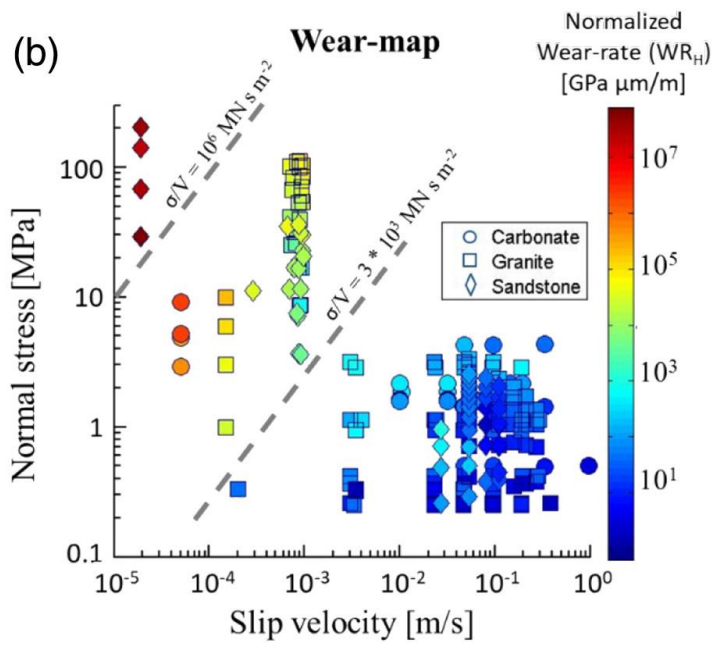

Figure 1.7. Wear map of wear rates plotted against applied normal stress and slip velocity showing lithology independent trends (from Boneh and Reches, 2018).

Material removed during slip is included into the slip zone, creating a cataclastic gouge layer with comminution reducing grain size with further slip (Engelder, 1974; Chester and Logan, 1986; Mair and Abe, 2011; Phillips and Williams, 2021). This creates a three-body system consisting of two wall rocks and a granular layer, as opposed to the initial two-body system where the two wall rocks interact directly, with asperity strength controlling the resistance to slip (Fig. 1.8; Sagy et al., 2007; Reches and Lockner, 2010; Boneh et al., 2013). In three-

body systems where large clasts exist within the slip zone, they can still interact with the wall rocks, generating localised stress and wear despite the presence of a gouge layer (Reches and Lockner, 2010).

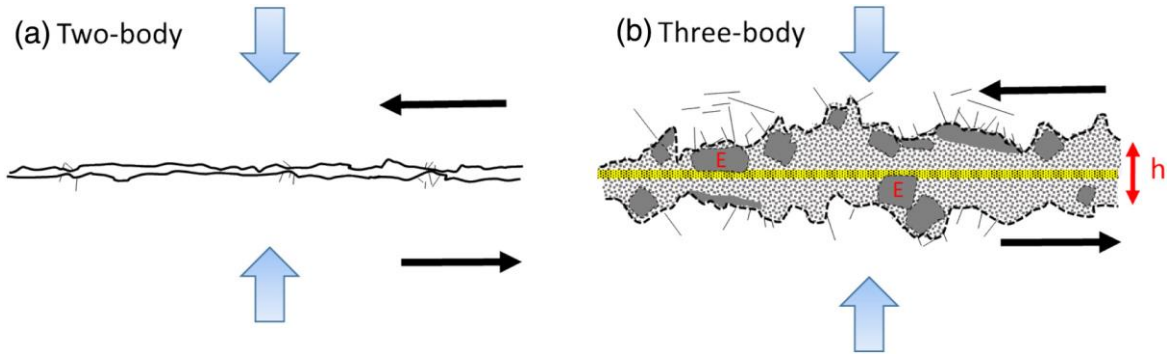

Figure 1.8. Sketch diagram of a) a two-body system with asperity contacts and localised damage. b) a three-body system with gouge layer and large clasts (E) controlling the localisation of wear (Boneh and Reches, 2018).

Gouge zone thickness tends to increase for faults that have experienced greater slip distances (Scholz, 1987). The zones or layers of cataclasite or gouge have different frictional behaviours to that of the wall rocks (Sibson, 1994; Niemeijer et al., 2010; Lavallée et al., 2014), and field observations find that the presence of cataclasites indicate a lower frictional coefficients than that of faults with solid rock interfaces (Sibson, 1994; Townend, 2006). This is supported by a range of experimental studies conducted on gouge samples (Ikari et al., 2009; Niemeijer et al., 2010; Lavallée et al., 2014; Faulkner et al., 2018) and demonstrates that the generation of gouge layers has a lubricant during faulting and other friction-controlled mass transport events (Boneh and Reches, 2018).

1.4. Frictional melting and melt rheology

1.4.1. Pseudotachylytes

Evidence for frictional melting in faults is preserved in the geological record as pseudotachylytes. The term pseudotachylyte comes from Shand (1916) and was initially used to describe the networks of dark glassy veins from the Parys region of South Africa, part of a large meteorite impact structure. Therefore, the term was adopted to describe the material that has a dark aphanitic rock with glassy appearance, similar to tachylyte but with different formation mechanisms. Historically, multiple other terms have been used to label these structures such as “trap-shotten gneiss” (Holland, 1900), “flinty crush rocks” (Clough et al., 1909), “injection mylonite” (Philpotts, 1964), “hyalomylonite” (Scott and Drever, 1954;

Masch et al., 1985) and “frictionite” (Maddock, 1986; Legros et al., 2000). These terms have now been widely abandoned in favour of the term pseudotachylyte (alternative spelling pseudotachylite).

There is some discourse on the formation mechanisms of the pseudotachylytes observed in nature, which challenges the use of a simple definition (Lin, 2007). A gradation exists between melt-origin pseudotachylyte and pseudotachylyte-like textures stemming from extreme cataclasis with little or no associated frictional melting (Philpotts, 1964; Magloughlin and Spray, 1992; Wenk et al., 2000; Rowe et al., 2005; Spray, 2010). For this thesis, the definition of Spray, (2010) is adopted: “*pseudotachylyte originates by frictional melting on a slip plane as a polyphase suspension comprising a once liquid matrix containing unmelted mineral and/or lithic clasts”* and is therefore narrowed to only melt-origin type, with at least partial frictional melting.

Impact craters on Earth and even on the moon exhibit pseudotachylytes, often in large quantities (Christie et al., 1973; Reimold, 1995; Spray, 1998; Melosh, 2005). By contrast pseudotachylytes caused by faulting tend to be more limited in volume and extent, and the presence of pseudotachylyte is often taken as evidence of seismogenic slip rates (e.g. Philpotts, 1964; Sibson, 1975; Cowan, 1999; Di Toro et al., 2005) and they are found in a wide range of localities. Pseudotachylytes are observed in exhumed lower crustal rocks from earthquake nucleation during deep intracontinental earthquakes (Campbell et al., 2020), through the seismogenic zone within the crust (e.g. Sibson, 1975; Magloughlin and Spray, 1992; Di Toro et al., 2011) and even in the upper crust (Sibson and Toy, 2006).

Upper crustal pseudotachylytes are not necessarily associated with faults causing regionally significant seismicity, although they always represent highly dynamic events. Volcanic environments in particular offer a range of deformation scenarios, which can result in frictional melting. For example, pseudotachylytes are found in extrusive lava (Kendrick et al., 2012; Kendrick et al., 2014; Wallace et al., 2019b); explosive pyroclastic products (Lavallée et al., 2015a); caldera collapse superfaults (Clough et al., 1909; Kokelaar, 2007; Han et al., 2019); and on the surface of tumbling blocks in pyroclastic density currents (Grunewald et al., 2000; Schwarzkopf et al., 2001). Pseudotachylytes have also been found beneath landslide deposits in a range of rock types (not restricted to igneous) such as the Markagunt and Sevier gravity slides in Utah, USA (Hacker et al., 2014; Biek et al), Langtang in Nepal (Masch et al., 1985), Köfels in Austria (Erismann, 1979; Masch et al., 1985), Arequipa volcanic landslide in Peru (Legros et al., 2000), Chiufener-Shan landslide in Taiwan (Lin et al., 2001;

2019) and French Massif Central in France (Bernard and van Wyk de Vries, 2017). Despite the common occurrence of large landslides worldwide, examples of preserved and identified landslide-generated pseudotachylytes are rare. Some may remain unexposed beneath uneroded deposits, whilst there may also be a preservation bias that obscures the frequency of frictional melting associated with landslides, as the alteration or destruction of near-surface pseudotachylytes over time removes them from the geological record (Kirkpatrick and Rowe, 2013). This rarity may conversely indicate that, though possible, the generation of frictional melting at the base of large landslides is not common due to generally unfavourable conditions and low normal stresses.

In shallow settings such as landslides, where the overburden imposes low normal stresses on the basal shear zone, the slip rate is the key control on frictional heating and subsequent likelihood of melting (Lin, 2007). For example, the Chiufener-Shan landslide created a deposit with a thickness of < 40 metres (which would have only applied a normal stress of < 1.5 MPa) that is underlain by a pseudotachylyte resulting from frictional melting (Lin et al., 2001). The precise conditions required to produce frictional melting at the base of landslides are still unclear and requires further investigation including the use of frictional experiments using appropriate materials and conditions (Erismann and Abele, 2001; Wang et al., 2017).

1.4.2. Frictional heating and disequilibrium melting

As many of the aforementioned weakening mechanisms identified for both mass movements (Section 1.1.3) and rock friction (Section 1.2.5) are triggered by temperature, an understanding of frictional heating experienced along slip surfaces and within shear zones is therefore essential to resolve the slip behaviour. During frictional slip the kinetic energy is in large part converted into heat along (and then conducted away from) the fault surface (Carslaw and Jaeger, 1959; Kennedy, 2000). Using the equation of Carslaw and Jaeger (1959), the temperature rise (ΔT) at a slip surface may be calculated, assuming conduction of heat diffuses perpendicular to the slip surface, such that:

$$\Delta T = \frac{\mu \sigma_n V \sqrt{t}}{\rho C_p \sqrt{\pi k}} \tag{1.5}$$

where μ is friction coefficient, σ_n is normal stress, V is the slip velocity, t is the duration of the slip event, ρ is the bulk rock density, C_p is the heat capacity and k is the diffusivity.

The concentration of heating to asperity contacts on the slip surface leads to flash heating in localised areas. This allows for the temperature windows of operating mechanical

weakening, processes (e.g. thermal decomposition and frictional melting) to be reached extremely quickly, and often inhomogeneously on the slip plane (Rice, 2006). The rapid rates of heating occurring during frictional sliding means that any resultant melting is a disequilibrium process involving the selective melting of minerals (Scott and Drever, 1954; Sibson, 1975; Spray, 1992; Lin and Shimamoto, 1998; Wallace et al., 2019a). Certain minerals are more prone to melting during frictional sliding (Spray, 2010), as illustrated by Figure 1.9 where minerals with lower melting temperatures are therefore more likely to melt first. Additionally, lower fracture toughness and strength of minerals can lead to preferential comminution which increases surface area to promote melting in the slip zone (Spray, 2010). For igneous rocks undergoing frictional melting, early generations of melt can be more mafic than the bulk rock composition due to the preferential melting of mafic phases (Hornby et al., 2015; Wallace et al., 2019a; Sarkar and Chattopadhyay, 2020) before continued melting and homogenisation leads to continuing evolution of the melt chemistry (Spray, 1992; Hirose and Shimamoto, 2005a; Jiang et al., 2015; Wallace et al., 2019a).

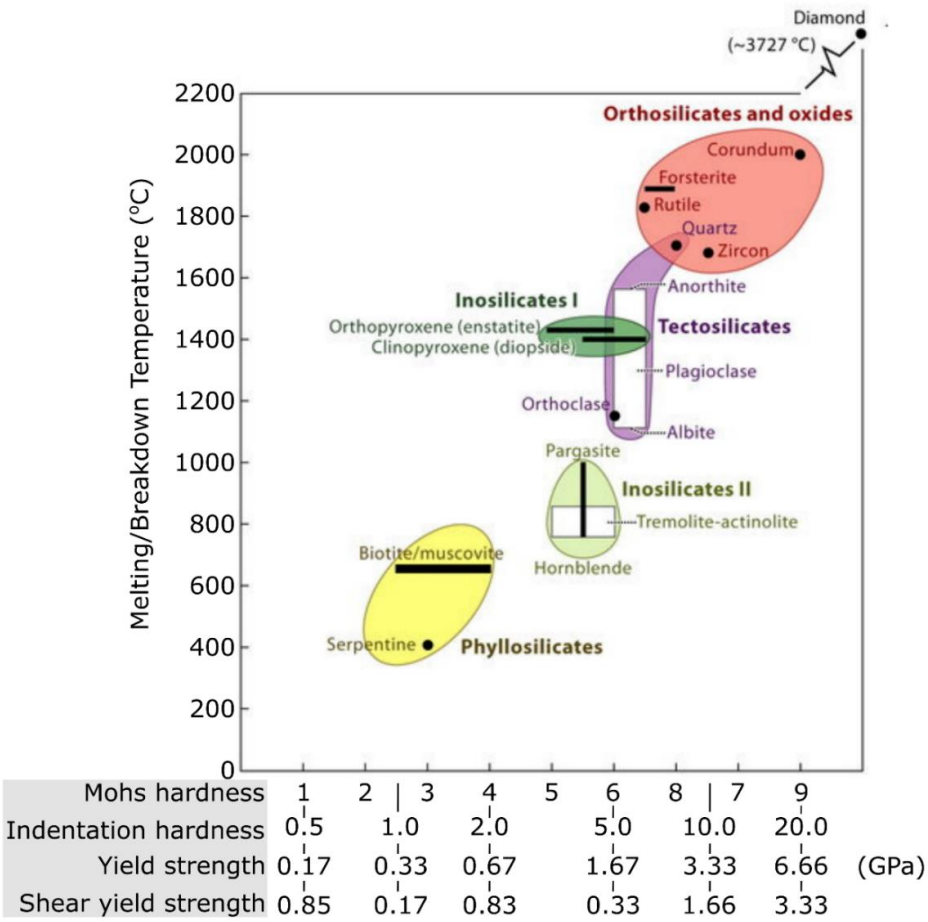

Figure. 1.9. The melting/breakdown temperature of common rock-forming minerals against a range of strength indicators: Mohs hardness, indentation hardness, yield strength and shear yield strength determining mineral fracturing (Spray, 2010).

1.4.3. Frictional melt rheology

Early high-velocity friction experiments by Spray (1987, 1988) successfully created the first experimentally-developed pseudotachylytes using welding apparatuses. However, these early experiments could not record the shear stress experienced on the simulated fault plane. The advent of the high velocity rotary shear apparatus (Section 1.2.2) has allowed a large number of studies to improve our understanding of the process of frictional melting and the implications for fault slip dynamics (Di Toro et al., 2011, 2006; Hirose and Shimamoto, 2005b; Hornby et al., 2015; Kendrick et al., 2014; Lavallée et al., 2015b; Lin and Shimamoto, 1998; Nielsen et al., 2008; Niemeijer et al., 2011; Shimamoto and Lin, 1994; Shimamoto and Tsutsumi, 1994; Spray, 1993, 1987). Findings have shown that the rheological behaviour of the melt (primarily viscosity) determines the shear resistance of melt-bearing faults. The rheology of the melt (i.e., the flow properties of material: e.g. viscous flow or rupture), is determined by a series of factors controlled by the physico-chemical properties of the materials involved and the ambient shearing conditions: normal stress, temperature, chemistry of system, and importantly, slip rate which controls the strain rate experienced by the melt. Spray (1993b) noted and postulated in early experimental observations that as the viscosity of frictional melt is highly dependent on its temperature (e.g. Giordano et al., 2008; Hess and Dingwell, 1996), frictional melts could act as lubricating layers under certain conditions. The viscosity of silicate melts is controlled by its chemical composition, which is in turn controlled by the process of disequilibrium melting and homogenisation (Spray, 2010; Wallace et al., 2019a). The chemical composition of melts, critically silica and volatile content (especially H_2O at shallow crustal depths) is crucial to their rheological behaviour, with decreasing silica content and increasing water content leading to lower viscosities and viscous deformation (Fig. 1.10; Dingwell, 1996; Giordano et al., 2008).

Early on, it was inferred that frictional melts can be modelled as Newtonian bodies with an Arrhenian relationship with temperature (i.e., viscosity is simply inversely proportional to temperature) to constrain the rheological controls of the melt on the resultant slip dynamics (Spray, 1993; Di Toro et al., 2011). However, such simplifications may not be adequate, as frictional silicate melts are viscoelastic bodies, sharing a non-Arrhenian relationship with temperature, which may exhibit non-Newtonian behaviour, especially when crystal restites

and fluid bubbles are present (Lavallée et al., 2012, 2015b; Hornby et al., 2015). As do all viscoelastic bodies, frictional melts exhibit a glass transition (T_g), which divides the liquid state (whereby melts can viscously relax an applied stress via diffusion) from the glassy state (whereby a melt cannot relax an applied stress. This thermo-kinetic divide is cast in terms of temperature and observation timescale or reciprocally, rate (Dingwell and Webb, 1989; Lavallée et al., 2015)). So, when sheared at high strain rates or when cooled, a silicate melt behaves elastically as a solid. If, in this regime the stress is sufficient, the melt may undergo brittle failure.

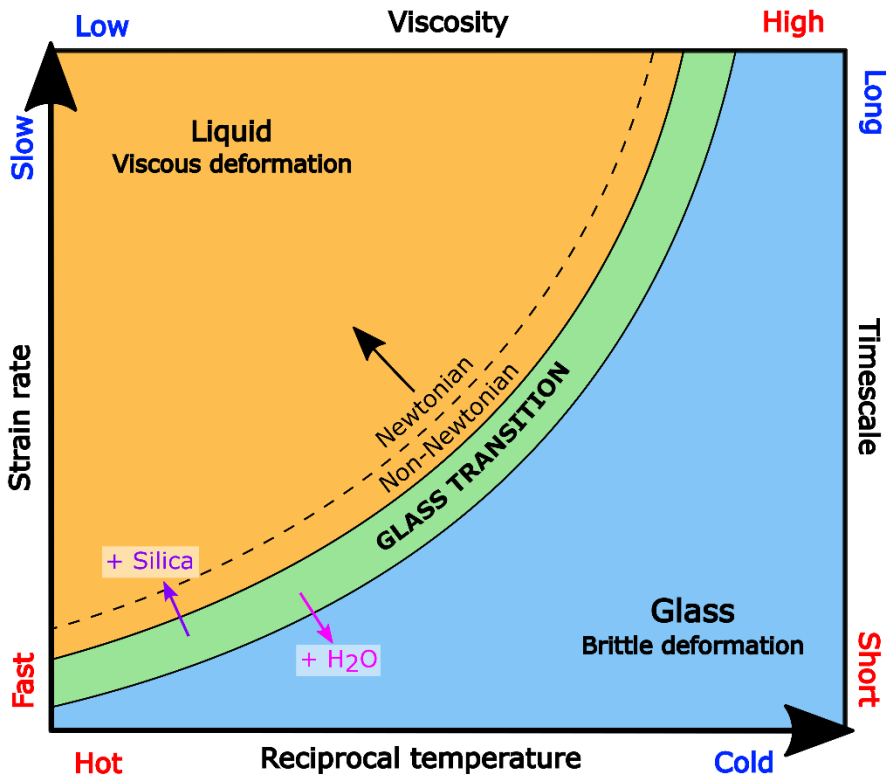

Figure. 1.10. The glass transition of silicate melts expressed in strain rate and reciprocal temperature (with respect to both viscosity and timescale) where increasing strain rate/reducing temperature induces brittle deformation and inversely decreasing strain rate/increasing temperature favours the relaxation of the applied stress without fracture. Silica content and water content modulates the position of T_g (adapted from Dingwell, 1996).

Frictional melts frequently contain suspended particles, unmelted fragments of wall rock or crystals within the melt layer. These are known as survivor clasts (or restites) and can result in highly variable rheological responses of the frictional melt layers. Most work on suspension rheology for multiphase silicate melts has explored the effects of crystal load on suspension viscosity. The fraction of solid clasts or crystals act as rigid framework within the melt, increasing the effective viscosity nonlinearly with crystallinity, whilst adding a rate

dependence as the suspension acquires a shear-thinning non-Newtonian behaviour (Fig. 1.11; e.g. Lejeune and Richet, 1995; Caricchi et al., 2007; Lavallée et al., 2007; Costa et al., 2009; Cordonnier et al., 2012; Truby et al., 2015). This manifests as a reduction in viscosity as strain rate increases for a given crystallinity.

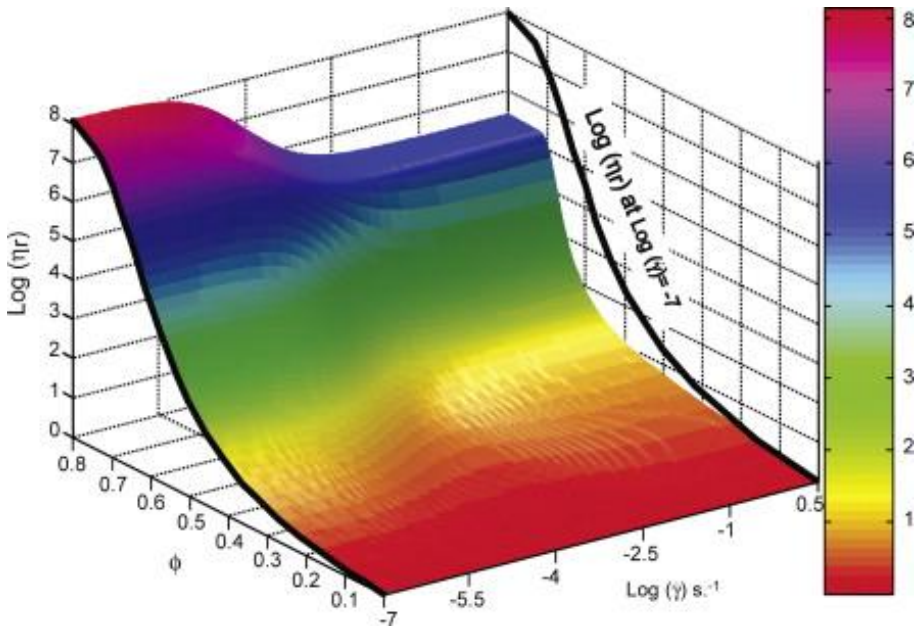

Figure. 1.11. Changes to the relative viscosity (ηr) of silicate melts at different strain rates (γ) and crystal fraction (φ). The model shows increasing relative viscosity with crystal fraction, whereas greater strain rates result in a decrease in the relative viscosity (from Caricchi et al., 2007).

In instances of high solid fraction load, the maximum packing fraction represents a boundary beyond which the particles cannot effectively move past one another (Einstein, 1906; Roscoe, 1952), and strain localises between phases (Lavallée et al., 2007; Caricchi et al., 2008; Kohlstedt and Holtzman, 2009; Kohlstedt et al., 2010). The maximum packing fraction is determined by the variation in grain size known as polydispersivity (Cimarelli et al., 2011) and the variable aspect ratio of the solid fraction (Mueller et al., 2010, 2011). The gradual nature of frictional melt formation, from crushing to selective melting and homogenisation can result in highly variable survivor clasts content within preserved pseudotachylytes layers (Lin, 1999, 2007; Kendrick et al., 2012; Sarkar et al., 2019).

Other aspects affecting rheology are the presence of bubbles, linked with the melting of hydrous phases and incorporation of fluids (e.g. water and other hydrothermal fluids) in the shear zone during melting. The ability of bubbles to deform depends on the capillary number determined by the stress field and viscosity of the suspension in which they are hosted (Rust

and Manga, 2002). If they are unable to deform, bubbles can act as rigid bodies, as crystals or survivor clasts do, and thus increase the effective viscosity (e.g. Truby et al., 2015; Coats et al., 2018). Where they are able to deform, the presence of bubbles can decrease the apparent viscosity of a suspension. In highly porous suspensions, the combination of low melt viscosity and deformable vesicles may result in a very low apparent viscosity. In extreme deformation, bubbles may become elongated and act as free slip surfaces, greatly reducing viscosity (Rust and Manga, 2002), until they outgas and the bubble walls fully collapse and start to heal.

1.4.4. Frictional melts: Lubricate, brake or fracture?

The rheological properties of a frictional melt layer controls the shear resistance and slip response of faulting events (Hirose and Shimamoto, 2005a; Di Toro et al., 2006; Nielsen et al., 2008; Niemeijer et al., 2011; Kendrick et al., 2014a; Kendrick et al., 2014b; Hornby et al., 2015; Lavallée et al., 2015b; Wallace et al., 2019a). The apparent viscosity of a frictional melt suspension (versus the frictional resistance of rock-rock slip without melt) controls whether it acts as potential lubricant or viscous brake. The development of frictional melt layers in low silica rocks (e.g. basalts) produce melts with lubricating properties (Violay et al., 2014); however, the frictional melts from intermediate to felsic rocks (e.g. andesite, dacites) have higher viscosities (see Fig. 1.10 for influence of silica content on melt viscosity) and the layer can conversely act as a viscous brake (Kendrick et al., 2014), whereby the shear resistance caused by the melt is greater than the Mohr-Coulomb friction (Fialko and Khazan, 2005) this process results in the reduction and eventual halting of slip. The resistance of frictional melt to shear strain may be higher than Byerlee's frictional values associated with non-melt bearing slip surfaces (e.g. Lavallée et al., 2012; Kendrick et al., 2014; Hornby et al., 2015; Wallace et al., 2019).

The early generation of melt that leads to isolated, low temperature melt patches can also act as a viscous brake on sliding (Tsutsumi and Shimamoto, 1997; Fialko and Khazan, 2005; Hirose and Shimamoto, 2005a), acting to arrest motion before a continuous melt layer is formed. The viscous brake can also occur in areas with low normal stress or if the rate of slip slows, leading to lower frictional heating, reducing the melt temperature and increasing viscosity (Fialko and Khazan, 2005; Lavallée et al., 2012). Viscous braking results in a feedback loop where decreasing slip rates result in overall cooling and melt viscosity increase, further increasing shear resistance, cooling, and so on. This process can lead to the complete arrest of movement on the slip plane, or to brittle fragmentation of the melt if continued displacement is enforced (Kendrick et al., 2014; Lavallée et al., 2015b). As alluded to by the

viscoelastic nature of silicate melts, frictional melts may undergo brittle failure if unable to structurally relax applied stresses; either by fast shearing rates and/or slow relaxation timescales at high viscosities (Fig. 1.10). Frictional melt layers in shear zones may therefore undergo catastrophic failure and be subsequently reworked into shear zones with continued slip (Lavallée et al., 2015b). This has implications for the mechanics of slip (which might regularly transition as melt forms and is destroyed) and may also explain the apparent low preservation rate of pseudotachylytes in nature (Kirkpatrick and Rowe, 2013).

In the case of volcanic collapse events, the properties of the rock in the mass movements and the underlying basal strata will determine the system's potential for the production of frictional melting during the ultra-fast slip event. The mineralogy of rocks undergoing friction (Spray, 2010) controls both the generation (and ultimately, rheological behaviour) of frictional melts. Their textural properties (such as porosity, crystallinity, and glass content) determines the mechanical properties controlling frictional wear and the evolution of the shear zones, eventually leading to frictional melting. These controls are particularly important in landslides where the basal contact evolves spatially over extensive transport distances.

1.5. Characteristics of volcanic materials

1.5.1. Physical properties

Volcanic materials, in which large sector and flank collapse superfaults form, have highly variable properties that influence both their mechanical and tribological behaviours. The strength of the material, as discussed in Section 1.1.2, determines the stability of the volcanic structure (Voight and Elsworth, 1997; Voight, 2000). Due to the varied petrogenetic evolution of rocks following a range of magmatic, volcanic, tectonic and hydrothermal processes, volcanic materials have highly differing textures, which varies the mechanical heterogeneity of the material (Le Bas and Streckeisen, 1991; Heap et al., 2016; Lavallée and Kendrick, 2021). Igneous rocks display wide ranges of mineralogical assemblage due to their varying chemical compositions and conditions of formation; i.e., due to different and complex pressure, temperature and strain histories of the magma during storage, transport and/or eruption (Lesher and Spera, 2015). Upon cooling, extrusive volcanic rocks preserve different mineralogy and crystallinity, often containing interstitial, amorphous glass phase, which formed by vitrification of melts. The common presence of an interstitial glass phase adds an additional rheological complexity to our description of volcanic materials behaviour in high temperature environments. Frictional heating and/or latent heat of crystallisation

(possible in the case where faulting intersects an active volcanic/hydrothermal areas) can cause viscous remobilisation of the interstitial glass phase by crossing at the glass transition (T_g); T_g can be met at temperatures lower than the melting point of any of mineral constituents, which can be of particular importance during faulting in volcanic rocks (Hornby et al., 2015; Lavallée et al., 2015b; Wallace et al., 2019b). Such low-temperature viscous remobilisation may promote localised deformation in the interstitial melt phase, causing dynamic rheological changes (such as associated with pore collapse).

In addition to a crystalline and glass phase, volcanic rocks commonly host vesicles, relics of bubbles within the magma. The vesicular volume varies greatly in volcanic rocks from 0 to 97% (Lavallée and Kendrick, 2021) and these vesicles vary in size, shape and connectivity depending on the process of their formation and any shearing or variation in conditions the magma underwent and during cooling to a rock. Other void space in the porous network takes the form of microfractures imparted by local stresses formed during shear and cooling (Kendrick et al., 2013; Heap et al., 2014a; Browning et al., 2016; Lamur et al., 2018) and any subsequent deformation in the brittle field. The presence of a porous network within the rock changes the mechanical behaviour including strength and can localise strain depending on local conditions and the dominant deformation mode (Heap et al., 2015).

1.5.2. Strength of volcanic rock

The strength of rock has been experimentally defined to decrease with porosity (see Paterson and Wong, 2005, for a review of rock properties in the brittle field); this is the case for both, the compressive (Schaefer et al., 2015; Coats et al., 2018; Harnett et al., 2019; Lavallée and Kendrick, 2021) and tensile (Harnett et al., 2019; Hornby et al., 2019; Lavallée and Kendrick, 2021) strength (Fig. 1.12). Denser materials have a primarily elastic response at a wide range of stresses with only a minor a strain hardening response associated with inelastic deformation. For more porous materials, this strain hardening response is greater, associated with brittle rupture and grain sliding (at low temperatures), and is observed at low applied stresses (Heap et al., 2020; Lavallée and Kendrick, 2021). Hence, porous rocks undergo high strain and lower applied stresses at failure than denser rocks (Lavallée and Kendrick, 2021).

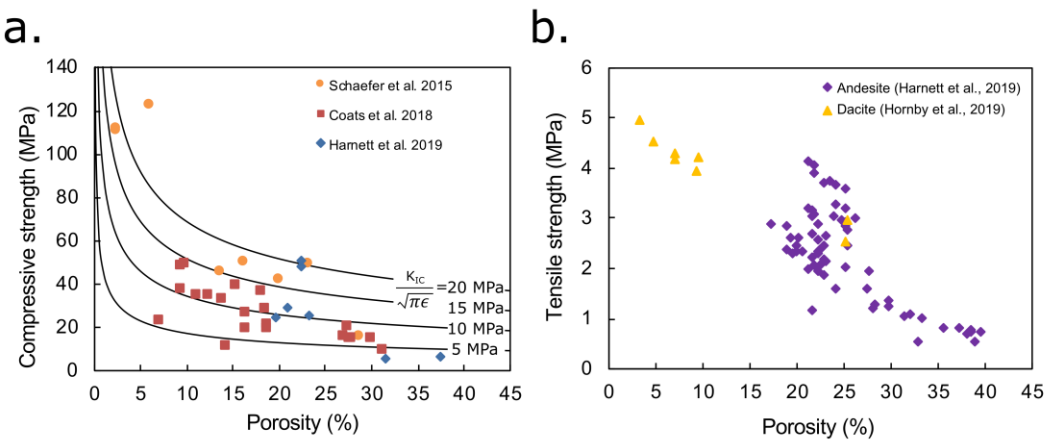

Figure. 1.12. Unconfined (a) compressive and (b) tensile strengths of volcanic materials determined experimentally (from Lavallée and Kendrick, 2021). a) compressive strength of dacite, andesite and basalt at strain rate of 10^{-5} s^{-1}. The data is accompanied by modelled strength from the pore-emanated crack model (data from Schaefer et al., 2015; Coats et al., 2018; Harnett et al., 2019). b) tensile strengths of andesite and dacite obtained via Brazil disc testing (Harnett et al., 2019; Hornby et al., 2019).

Other textural characteristics such as fabrics, crystallinity and variable mineralogy influence the behaviour of porous rocks (Bubeck et al., 2017; Coats et al., 2018; Schaefer et al., 2015). The use of micromechanical modelling of material failure, using the pore-emanated crack model (Sammis and Ashby, 1986), where tensile cracks propagate from existing pores in the direction of the applied stress, linking to promote system-size failure, can elucidate the role of different variables on material strength and failure. Heap et al. (2016) expanded the pore-emanated crack model by adding consideration of the effects of textural heterogeneity (crystallinity and vesicularity) to evaluate their contribution to volcanic rocks mechanical behaviour. Porosity was found to impact material strength more than crystallinity (Heap et al., 2016). An alternative model, commonly used to define the strength of dense rock, is the sliding wing-crack model, which models the concentration of tensile stresses on the tips of pre-existing fractures (oblique to the applied stress) in the material (Ashby and Sammis, 1990) but does not consider the effect of pores. When looking at the performance of both, the pore-emanated and wing-crack models, studies have found that neither model can resolve the porosity dependence of volcanic rock strength exactly (see Fig. 1.12a), as it is likely that a combination of the two models is in action during deformation due to the complex microfracture networks and pore interactions in natural rocks (Heap et al., 2014a; Schaefer et al., 2015; Coats et al., 2018). In aphyric porous glass the pore-emanated model was used to constrain the strength of the rock analogue reasonably well (Vasseur et al., 2013;

Heap et al., 2014b) due to less complication imparted by the crystalline phase. Both models are reliant on the fracture toughness of the material which describes the resistance of a material to tensile failure (Balme et al., 2004) and is also important during abrasion and damage at the slip surface during frictional sliding (Spray, 2010; Boneh and Reches, 2018). Therefore, both the overall strength of coherent material (before rupture) and their propensity to wear and abrade during collapse and sliding in mass movements is reliant on its fracture toughness.

In this thesis, I aim to investigate the effects of the varying physical properties of volcanic materials (such as porosity, glass content and strength heterogeneity) on their frictional response pertaining to large mass movements, such as debris avalanches associated with sector collapse of volcanic edifice. This was done by using integrating results of field observations and modelling in order to target specific variables for experimental investigation using both natural and analogue samples. Field observations of a natural debris avalanche deposit from the collapse of Pichu Pichu volcano, Peru (Chapter 2) was selected to guide my experimental research. I designed a suite of rotary shear experiments, using natural samples collected during the field expedition, to investigate the role of volcanic rock properties and slip parameters on the frictional response (Chapter 3) and then synthesised variably porous glasses, as rock analogues, to investigate the behaviour of porous materials subjected to wear using rotary shear experiments (Chapter 4).

1.6. Structure of the thesis

Following the introduction (Chapter 1), which provides a background to topics involved in this thesis, Chapters 2-4 then presents, in a logical order, the findings of the original research I undertook to investigate the frictional behaviour of volcanic debris avalanches following catastrophic flank collapses. Each chapter has been written as a manuscript for publication but is formatted for presentation in this document with appropriate modifications to the numbering of figures, tables and equations. All references are collated at the end of the thesis in the bibliography. Details of authorship and publication status for each of these chapters can be found in Section 1.7.

In Chapter 2, I detail the findings of the field expedition to the Arequipa volcanic landslide deposit in southern Peru. The results of this study were used to guide the targeted experiments presented in the following chapters. In Chapter 3, I used natural samples collected from the field area described in Chapter 2 to examine the behaviour of the natural materials in conditions of extreme sliding, and the juxtaposition of collapse material over

different substrata material. In Chapter 4, I used glass analogue materials to investigate the role of porosity and glass content on frictional behaviour of homogenous samples.

Chapter 5 summarises the key results presented in each piece of work and discusses the implications of the findings related to the entire body of work presented this thesis and, on a broader scale, to the area of research involving rock friction, tribology and the occurrence of volcanic debris avalanches stemming from edifice failure. I then explore possible avenues for further research to answer the questions arising from the output of this thesis.

Appendices (I-III) are included at the end of the thesis, containing the supplementary information and figures that accompany each chapter (figure numbering here has also been altered from the published versions for presentation in this thesis).

1.7. Status of Papers and Co-Author Contributions

CHAPTER 2

Manuscript Title: Shear localisation, strain partitioning and frictional melting in a debris avalanche generated by volcanic flank collapse

Authors: Amy Hughes[a], Jackie E. Kendrick[a], Guido Salas[b], Paul A. Wallace[a], François Legros[c], Giulio Di Toro[d], Yan Lavallee[a]

Affiliations:

[a]Department of Earth, Ocean and Ecological Sciences, University of Liverpool, Liverpool, L69 3GP, United Kingdom
[b]Department of Geology and Geophysical Sciences, National University of San Agustin, Arequipa, Peru
[c]Freelance researcher, Arequipa, Peru
[d]Department of Geoscience, University of Padova, Via Gradenigo, 6, 35131, Padova, Italy

Journal: Journal of Structural Geology

Review process: Peer reviewed

Status: Published

DOI: https://doi.org/10.1016/j.jsg.2020.104132

Date of Submission: 24th December 2019

Date of Publication: Accepted 30th June 2020, published 3rd July 2020

Author Contributions:

AH, JK, GS, FL and YL conducted the field work and sample collection; AH conducted microstructural analysis; AH and PW performed the geochemical analysis; AH conducted the

rheological modelling with aid from PW, JK and YL; Manuscript preparation lead by AH with input and discussion from all authors.

CHAPTER 3

Manuscript Title: The juxtaposition of lithologies and the role of strength heterogeneities during frictional sliding

Authors: Amy Hughes[a], Jackie Kendrick[a,b], Anthony Lamur[a], Guido Salas[c], Yan Lavallée[a]

Affiliations:

[a] Department of Earth, Ocean and Ecological Sciences, University of Liverpool, Liverpool, L69 3GP, United Kingdom.
[b] School of Geosciences, University of Edinburgh, James Hutton Road, Edinburgh, EH9 3FE, United Kingdom.
[c] Department of Geology and Geophysical Sciences, National University of San Augustin, Arequipa, Peru

Journal: Tectonophysics

Status: In Preparation

Author Contributions: AH, JK, GS and YL conducted the field work and sample collection; AH, JK and YL designed the concept and experiment plan; AH prepared the samples; AH and JK collected the mechanical and thermal data; AL modelled the thermal profiles during wear; AH took lead in data processing and manuscript preparation with input from all authors.

CHAPTER 4

Manuscript Title: Frictional Behaviour, Wear and Comminution of Synthetic Porous Geomaterials

Authors: Amy Hughes[a], Jackie E. Kendrick[a,b], Anthony Lamur[a], Fabian B. Wadsworth[c], Paul A. Wallace[a,d], Giulio Di Toro[e] and Yan Lavallée[a]

Affiliations:

[a]Department of Earth, Ocean and Ecological Sciences, University of Liverpool, Liverpool, United Kingdom
[b]School of Geosciences, University of Edinburgh, Edinburgh, United Kingdom
[c]Department of Earth Sciences, University of Durham,Durham, United Kingdom [d]Department of Geosciences, Environment and Society, Université Libre de Bruxelles, Brussels, Belgium
[e]Department of Geoscience, University of Padova, Padova, Italy

Journal: Frontiers in Earth Science

Review process: Peer reviewed

Status: Published

DOI: 10.3389/feart.2020.562548

Date of Submission: 15th May 2020

Date of Publication: Accepted 29th September 2020, published 24th November 2020.

Author Contributions:

AH, JK and YL designed the concept and experiment plan; AH and FW prepared the samples; AH and JK collected the mechanical and thermal data; PW collected the thermal expansion data; AL modelled the thermal expansion during wear; AH led data processing and manuscript preparation with input from all authors.

Chapter 2: Shear localisation, strain partitioning and frictional melting in a debris avalanche generated by volcanic flank collapse

Abstract

The Arequipa volcanic landslide deposit to the east of Arequipa (Peru) originated from the Pichu Pichu volcanic complex, covering an area > 100 km^2. The debris avalanche deposit exhibits internal flow structures and basal pseudotachylytes. We present field, microstructural and chemical observations from slip surfaces below and within the deposit which show varying degrees of strain localisation. At one locality the basal shear zone is localised to a 1-2 cm thick, extremely sheared layer of mixed ultracataclasite and pseudotachylyte containing fragments of earlier frictional melts. Rheological modelling indicates brittle fragmentation of the melt may have occurred due to high strain rates, at velocities of > 31 m s^{-1} and that frictional melting is unlikely to provide a mechanism for basal lubrication. Elsewhere, we observe a < 40 cm thick basal shear zone, overprinted by sub-parallel faults that truncate topological asperities to localise strain. We also observe shear zones within the avalanche deposit, suggesting that strain was partitioned. In conclusion, we find that deformation mechanisms fluctuated between cataclasis and frictional melting during emplacement of the volcanic debris avalanche; exhibiting strain partitioning and variable shear localisation, which, along with underlying topography, changed the resistance to flow and impacted runout distance.

2.1. Introduction

Volcanic edifices are inherently unstable structures formed by the superimposition of layers of varying volcanic materials on relatively rapid geological timescales (Voight, 2000; Acocella and Puglisi, 2010). Structural instability of volcanoes and other orogenic landforms can be prompted by a range of factors such as: magma intrusion e.g. Mount St. Helens (Lipman and Mullineaux, 1981); overloading of flanks (Swanson et al., 1976), tectonic stresses (Lagmay et al., 2000), ground motion during earthquakes (Voight and Elsworth, 1997), hydrothermal activity (Day, 1996; Voight and Elsworth, 1997), alteration (Reid, 2004), precipitation (McGuire, 1996), freeze-thaw (Kawamura and Miura, 2013), and erosion (McGuire, 1996). This is combined with a natural variability in coherency, porosity, crystallinity and glass content of materials, which affects the strength and primary deformation mode (e.g. brittle vs ductile) of the edifice-forming rocks (e.g. Heap et al., 2010; Benson et al., 2012). Collapses of unstable volcanic structures occur at a wide range of scales, the smallest examples form from shallow slope instability events (Cecchi et al., 2004) and rockfalls (Calder et al., 2002), whereas larger scale instabilities can produce deep-seated slip events that may subject magmatic systems to decompression that trigger unrest and even eruptions (e.g. Hunt et al., 2018).

Large-scale collapse landslides pose significant hazards to life and property within the spatial range of the event (e.g. Siebert, 1992). Quantifying the potential distance these collapses may travel, the rate at which onset occurs and the speed of the avalanche itself as it propagates from the source area is therefore paramount in hazard risk assessments. Large landslide volumes can exceed 10^9 m^3 (Siebert, 1984) and travel at speeds up to 100 m s^{-1} (Siebert et al., 1987; Shea and van Wyk de Vries, 2008) and those with volumes in excess of 10^6 m^3 often exhibit anomalously high mobility (Scheidegger, 1973). Mobility considers a combination of velocity and runout distance from source (Iverson et al., 2015), which can often be greater than ten times the height of fall (the elevation change from source to final position of the mass of material) in these instances (Legros, 2002). Analysis of the ratio of height of fall to runout distance against volume of landslides highlights that landslides with larger volumes travel longer distances, suggesting the importance of a mechanism that acts to lower frictional coefficients, allowing them to be more mobile than predicted by simple frictional sliding models (Shea and van Wyk de Vries, 2008). Such behaviour has been identified in events developing in all rock types (Legros, 2002 and references therein), suggesting a commonality of the process. Several mechanisms to reduce frictional coefficients during frictional sliding of landslides have been put forth, including: mechanical

fluidisation (Davies, 1982; Campbell et al., 1995), the lubricating effects of basal groundwater or ice (Lucchitta, 1987; Legros, 2002; De Blasio, 2011), trapped air (Shreve, 1968), salt (De Blasio, 2011), acoustic fluidisation (Melosh, 1979, 1986; Johnson et al., 2016), mechanical and thermal fluid pressurisation (e.g. Ferri et al., 2011) elastohydrodynamic lubrication (Brodsky and Kanamori, 2001), frictional velocity weakening (e.g. Wang et al., 2017) and the formation of a lubricating frictional melt layer (Legros et al., 2000; De Blasio and Elverhøi, 2008; Wang et al., 2017).

The production of frictional melts is the result of frictional heating due to strain localisation onto a discrete, thin slipping layer (Sibson, 1975). These frictional melts are then preserved in the geological record as pseudotachylytes, and are usually ascribed to seismogenic fault activity (Sibson, 1975, 1977; Spray, 1992; Shimamoto and Lin, 1994; Di Toro et al., 2006; Nielsen et al., 2008), volcanic conduit shear zones (e.g. Kendrick et al., 2012), and at the base of some mass movements (Erismann, 1979; Masch et al., 1985; Legros et al., 2000; Lin et al., 2001; Hacker et al., 2014; Bernard and van Wyk de Vries, 2017). The presence of frictional melts along fault slip zones has often been suggested to act as a lubricant (Di Toro et al., 2006); yet, they may conversely act as a viscous brake (Fialko and Khazan, 2005), especially in intermediate and felsic volcanic rocks sheared at low (< 10 MPa) normal stresses or low lithostatic loads (Lavallée et al., 2012; Kendrick et al., 2014). Importantly, the transient physico-chemical evolution of frictional melt during slip impacts rheological evolution (Lin and Shimamoto, 1998; Wallace et al., 2019), which controls slip velocity, shear resistance and any thermo-mechanical feedback due to viscous energy dissipation (Nielsen et al., 2010) that, in the case of mass movements, may ultimately regulate the runout distance.

Careful examination of the internal structures of mass movement deposits, such as large landslides (including debris avalanches), suggests a spectrum of behaviour; from those which disaggregate during transport to those transported over long distances whilst maintaining their coherence, exhibited by undisturbed structures such as discrete lithological units and intrusions (Glicken, 1998; Erismann and Abele, 2001; Hacker et al., 2014). Some evidence suggests that larger events have preserved their internal structures (Erismann and Abele, 2001; De Blasio and Elverhøi, 2008). In order to preserve these features, shear must have been localised to a relatively narrow layer to prevent wholescale deformation. Shear localisation is an integral part of flow segregation and means that the basal mechanisms of debris avalanches and volcanic collapses largely control emplacement. On this layer, shear rates (and thus frictional heating) may be extremely high as a result of the high velocity of the mass movement (De Blasio and Elverhøi, 2008). Pseudotachylytes have only been

identified at the base of a few landslides, including: Kofels, Austria (Erismann, 1979); Langtang, Nepal (Masch et al., 1985); Tsaoling, Taiwan (Lin et al., 2001); Markagunt slide, Utah (Hacker et al., 2014), Sevier slide, Utah (Biek et al., 2019), French Massif Central (Bernard and van Wyk de Vries, 2017) and Arequipa, Peru (Legros et al., 2000). The Arequipa volcanic landslide deposit displays a rare example of preserved pseudotachylyte at the base of a landslide originating from a volcanic source, namely Pichu Pichu volcano. The internal structure of the deposit is exposed owing to multiple incisions by rivers since emplacement > 1 Ma ago (Legros et al., 2000). Here we present new observations from an extensive geological survey of the Arequipa volcanic landslide deposit, including re-examination of the original outcrops investigated in Legros et al. (2000) as well as newly identified shear exposures.

2.2. Geological background

Pichu Pichu is part of the modern Central Andean Volcanic Zone and is located along the NE margin of the Arequipa basin, 30 km to the east of the city of Arequipa (Fig. 2.1). The volcanic arc trends approximately NW-SE, associated with major regional sinistral strike-slip faults trending NW-SE (de Silva and Francis, 1990; Lavallée et al., 2009). The Arequipa basin is filled with four distinct, high-K calc-alkaline ignimbrites commonly referred to as the “Sillar” (Lebti et al., 2006). These range in age from the 13.19 ± 0.09 Ma Rio Chili Ignimbrite to the 1.03 ± 0.09 Ma Yura Tuff (Lebti et al., 2006). The source of these ignimbrites has been inferred to evidence a relict volcanic caldera now buried by the construction of Chachani volcanic complex during the quaternary (in the last 1 Ma to 642 ka; Aguilar et al., 2016). Similarly, the ignimbrites underlie the younger Arequipa volcanic landslide deposit (Legros et al., 2000; Lebti et al., 2006) estimated to have occurred at ~1 Ma (Lebti et al., 2006).

Pichu Pichu itself is an extinct volcanic complex with andesitic lava flows dated to 6.71 ± 0.57 Ma using K-Ar dating (Kaneoka and Guevara, 1984) with no evidence of younger activity. The collapse of a significant portion of the volcanic flank resulted in the formation of an open arcuate ridge morphology, facing the large volcanic debris avalanche deposit found to the east of Arequipa (Fig. 2.1). Initially the deposit was mapped to extend to the NE of Arequipa, however further investigation of those deposits found that the chemistry of entrained lava blocks and flow package characteristics more closely correlate to lava flows from an earlier cone of El Misti that underwent collapse before the formation of the modern day cone (Thouret et al., 2001). These more recent flows partially overlie and obscure the older collapse deposits now interpreted to originate from Pichu Pichu. More recently the northern

boundary of the debris flow deposit was re-mapped in the area of Chiguata to follow the break in slope between the flank of El Misti and the irregular topography identified as the Pichu Pichu collapse formation (Thouret et al., 2001). The debris avalanche deposit has been stated to evidence both mixed and block facies using nomenclature of Glicken (1991), and has a basal pseudotachylyte (Legros et al., 2000), but has not been mapped in detail (Thouret et al., 2001).

2.3. Methods

The debris avalanche deposit was surveyed in 2017. Topographic maps were used to identify valleys and gullies that would be potential sites for basal exposures using the relative altitudes from the previously identified basal contact (Legros et al., 2000) at 2600 m above sea level. Where basal contacts were located, we also examined the debris avalanche deposit above for internal flow features.

Samples were collected from several localities; for basal contacts samples were generally taken from above, below and within the shear zone. For all samples, flow direction was noted (determined from the position from source, clast imbrication and striations if present) in the field and ascribed to each specimen to enable structural analysis. Orientated, polished thin sections were used for both microtextural and geochemical analyses. Backscattered electron images (BSE) used for microtextural analysis were taken on a Phillips XL30 scanning electron microscope (SEM) at the University of Liverpool with 20 kV accelerating voltage and 10 µm working distance.

Bulk chemistry was determined by X-ray fluorescence (XRF) at the University of Leicester using a PANalytical Axios Advanced XRF Spectrometer. Major element analyses were determined from glass beads fused from ignited powders and trace elements on pressed powder pellets. Relative precision and accuracy were better than 1.5 % for major elements and 5 % for trace elements based on a series of repeat analyses on reference materials (Bardon Hill granodiorite and Whin Sill dolerite; see Supplementary Tables A.I.6).

The geochemical compositions of phases in the underlying ignimbrite, pseudotachylytes, cataclasites and lithic clasts from within the debris avalanche were measured using a Cameca SX100 electron probe micro-analyser (EPMA) at the University of Manchester, using wavelength dispersive spectroscopy (WDS). Calibration of the detectors were conducted on a range of standards (albite for Si and Na, wollastonite for Ca, fayalite for Fe, corundum for Al, ilmenite for Ti, periclase for Mg, tephrite for Mn and potassium feldspar for K). These

standards were revisited at the start of each working day, although the albite standard and the VG568 rhyolite glass standard (Yellowstone National Park, Wyoming) were revisited regularly during analyses and before and after each sample to ensure there was no drift. Measurements on crystals were conducted with a focused ~1 µm beam with 20 nA current and 15 kV accelerating voltage. Analyses conducted on pseudotachylyte and interstitial glass in lithic clasts were conducted using a defocused 10 µm beam with 5 nA current and 15 kV accelerating voltage. Additionally, a defocused beam was also used to sample the bulk chemistry of areas of ultracataclasite. All tests with both focused and defocused beam had peak count times of 20 seconds and background (off peak) of 10 seconds.

In an attempt to obtain accurate and precise glass chemistries and minimise potential contamination from common restites (surviving crystals) in the pseudotachylyte glass, a 5 µm beam was also used for 6 analyses; they were found to return similar totals and chemistries to analyses done with the 10 µm beam.

In order to perform a rheological analysis of the frictional melt, the chemical composition obtained by EPMA was used as input in the GRD viscosity calculator (Giordano et al., 2008). ImageJ (Schneider et al., 2012) was employed to analyse phases in BSE images and estimate the crystal fraction as well as a maximum packing fraction, calculated following Mueller et al. (2010) and Klein et al. (2017). This data was input into the empirical relative viscosity calculator of Costa et al. (2009) to compute the rheology of the frictional melt suspensions.

2.4. Results

2.4.1. Field Observations

During our field campaign, we surveyed the Arequipa volcanic landslide deposit and closely examined key structures. The deposit is characterised by a heavily eroded area of high topography extending 26 km west from Pichu Pichu in a broad, fan-like shape (Fig. 2.1). The upper surface of the deposit is draped by fall deposits of more recent volcanic activity in the area. Legros et al. (2000) originally estimated the volume of the deposit to be > 10 km^3, however, with the deposit covering over 200 km^2 and thicknesses observed at > 100 m even at distances > 20 km from the source, the volume could exceed even 20 km^3. Outcrops of the basal contact suggest a gentle 5° average slope of the original underlying topography. Current topography indicates that the central section of the deposit exceeds 300 m in thickness. An accurate estimation of the volume in this case is impossible due to the

unknown basal topography, erosion of the deposit, poor mapping of the distal extent and a number of overlying fall deposits.

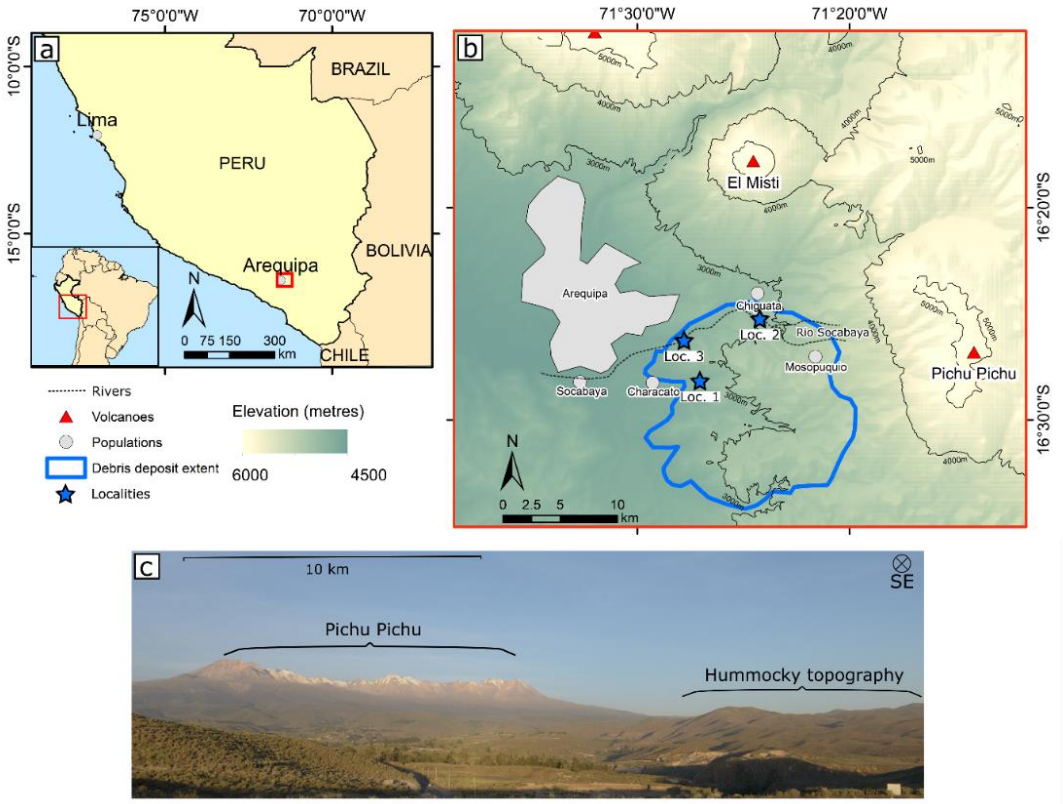

Figure 2.1. Locality map and field photos to illustrate debris avalanche deposit and source location. a) Map of southern Peru (red box marks area in b) with inset of South America (red box shows the map area). b) Topographic map of the Arequipa basin, Pichu Pichu, the debris avalanche deposit (blue outline) and field localities for this study (Loc. 1-3). c) Photo of dissected Pichu Pichu arcuate ridge and the debris avalanche deposit showing raised humocky topography, view is SE from Chiguata.

The deposit is cut by multiple rivers and their tributaries, including the Rio Socabaya in which localities 2 and 3 are found (Fig. 2.1). Locality 1 is situated in a different river-cutting near the Characato District. These incisions expose some of the internal flow structures developed during the debris avalanche. Here, we describe observations of key structures from three localities with extensive exposure. These include basal contacts, defining the paleotopography, as well as mid-body shear zones and clastic dykes.

2.4.1.1. Locality 1 – Basal pseudotachylyte

Originally, the base of the debris avalanche deposit was observed in a river-cutting near Characato District to the SE of Arequipa (Legros et al., 2000), approximately 24 km from Pichu Pichu (Loc.1 see Fig. 2.1). Here, the exposure presented by the river-cut is approximately 75 m long and 10 m high approximately parallel to the expected transport

direction (Fig. 2.2a-b). Although the deposit extends further in all directions, vegetation covers most of the rocks on shallow topography. In this locality, the debris avalanche deposit is rather massive, made of a white-grey, granular medium consisting primarily of ash- and lapilli-size clasts of andesite lithics and individual crystals (Fig. 2.2a-b). The andesite blocks are porphyritic, containing 20 % plagioclase (up to 2.2 mm) and 15.3 % amphibole phenocrysts (up to 2 mm) with microlite-rich groundmass. The andesite blocks occasionally reach 30 cm in size within the deposit and often display jigsaw brecciation fracture patterns.

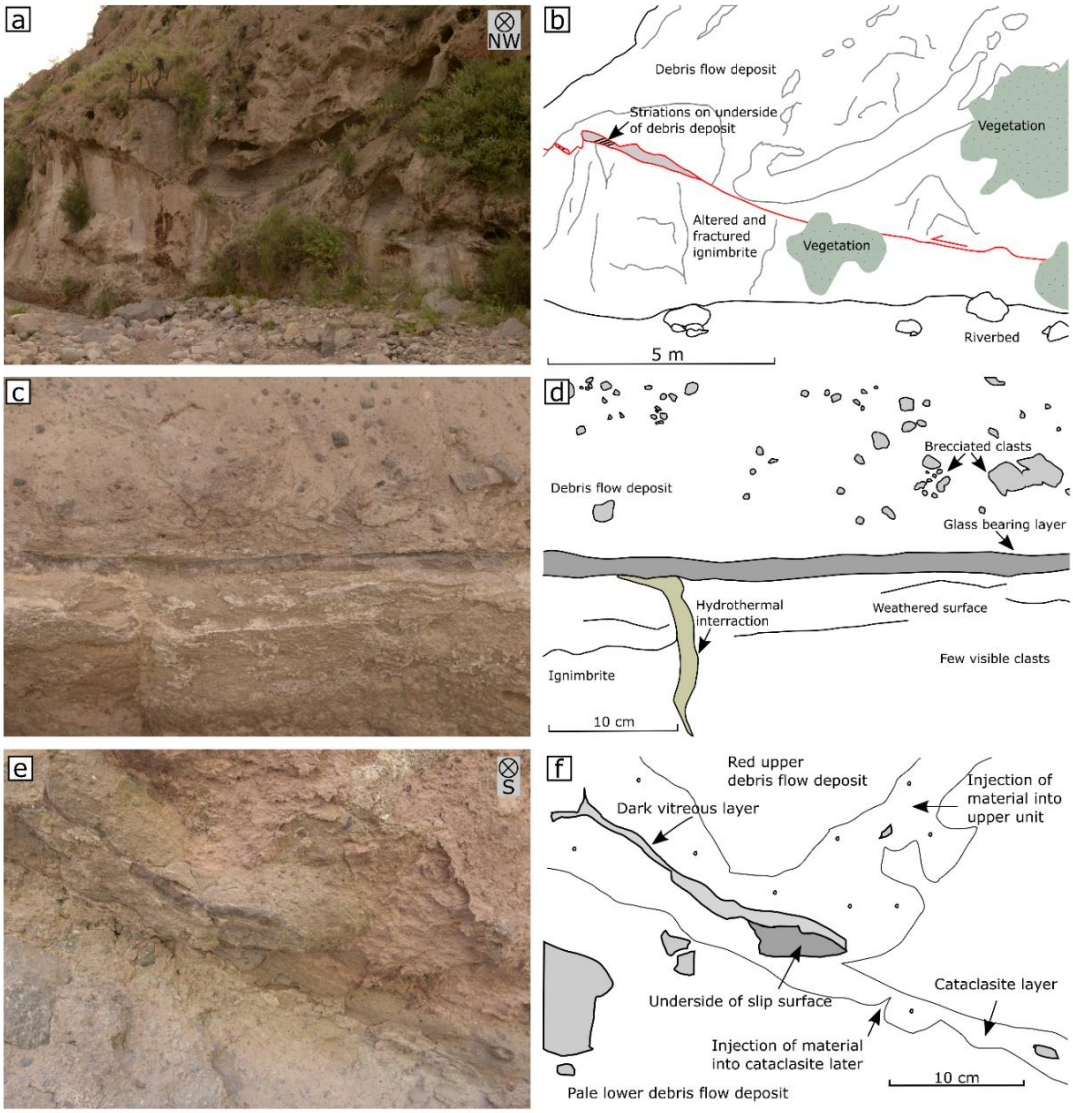

Figure 2.2. Field photos and sketches of features at Locality 1. a-b) Basal contact of the debris flow with basal topology leading to extreme shear localisation. c-d) Close view of the basal surface with localised dark, vitreous, glass-bearing layer. e-f) Secondary shear zone 20 m above the outcrop in panels a-d showing juxtaposition of units separated by cataclasite plus a dark, vitreous seam.

The underlying ignimbrite is exposed as a poorly consolidated and highly weathered rock of pale grey colour consisting of ash-sized grains without large lapilli. Crystals of both biotite and plagioclase are identifiable alongside dark lithic fragments but all are rarely larger than 1 mm in size. The rock is highly fractured and contains non-continuous veins of silicic hydrothermal material up to 1 cm thick (Fig. 2.2c-d). These veins all follow a similar orientation, striking in a 014-020 direction with high dip angles of 80-90° to the east, following the orientation of regional tectonic features (Lebti et al., 2006).

The contact between the debris deposit and the underlying basal ignimbrite is sharp, consisting of a thin, dark grey, vitreous layer approximately 1-1.5 cm thick (Fig 2.2c-d). The contact is observed at an elevation of 2610-2620 m in the northern face of the river-cutting and is dipping away from the outcrop face towards the north (strike 090 and 091) at variable angles, but generally around 35° (Fig. 2.2a-b). The contact visibly extends over a length of ca. 60 m and is curvilinear, increasing in elevation by approximately 4-5 m over a distance of approximately 10 m away from Pichu Pichu at this locality. Over-hanging areas of the upper slip surface at the base of the deposit exhibit striations trending 286 degrees which deviates approximately 25 degrees north from the expected flow direction. The material either side of the contact is highly brecciated, containing no fragments larger than 4 cm within 50 cm of the contact.

2.4.1.2. Locality 1 – Intra-body shear zone

Strain localisation was not restricted to the basal contact at Loc. 1. An additional shear zone was identified within the deposit, some 20 m above the basal contact at 2636 m elevation and 30 m due NE from the basal contact previously described. Here, a change in colour is noted above and below the shear zone. The lower unit is a pale grey colour, fine-grained breccia, similar to that described directly above the basal contact but with rare larger (> 20 cm) andesitic blocks. Above is a breccia with red-coloured matrix, rich in andesitic blocks (Fig. 2.2e-f). The clasts in this upper lithology are larger, up to 50 cm, with less jigsaw brecciation and more angular shapes. These two units are separated by a layer of light brown material with no large clasts that varies from 2- 10 cm thick and which is seen to inject into the lithology above. Within this, there is a thin layer of dark, microcrystalline material, approximately 3-4 mm thick (Fig. 2.2e-f). The shear zone is observed to extend laterally for approximately 45 m and runs sub-parallel to the basal contact below at a strike of 108 degrees dipping to the north by ~20°.

2.4.1.3. Locality 2 – Cataclastic basal contact

A new exposure of the deposit base was found to the northeast of the original locality in a different river valley, approximately 17.5 km from Pichu Pichu (Loc. 2 see Fig. 2.1). Here, the materials forming the debris avalanche deposit and the underlying ignimbrite remain the same as in Loc. 1, yet the upper surface of the ignimbrite is, in some laterally discontinuous sections, draped by a 1-2 m thick layer of more clay rich, lahar deposit material with some imbrication of small clasts. The nature of the contact is however different and varies laterally within the outcrop, which totals approximately 300 m along a river-cutting (Fig. 2.3). The contact, observed at an elevation of 2854 to 2858 m, is seen in the north face of the river-cutting, near-parallel to the flow direction and is generally linear and almost horizontal (Fig. 2.3a-b). It is largely visible as a sharp boundary between the two units (with either the thin lahar layer or ignimbrite as the lower unit). A large clast is preserved near the base of the debris avalanche, cut by multiple well-defined fractures parallel to the primary contact (Fig. 2.3c-d). In this locality, no vitreous layer is present, but the shear zone contains extremely fragmented, fine, angular material and displays red iron oxide stains and 303° trending striations on the lower contact surface with the lahar (Fig. 2.3c-d). This is a more northerly direction of flow, due to the fanning of the deposit across the land surface.

140 m to the west, separated from the previously described outcrop by an area of vegetation, an undulating contact is visible between the debris flow and the ignimbrite material where troughs were present in the paleotopography (i.e., the upper surface of the ignimbrite; Fig. 2.3e-f). The deposit filled the depression and exhibits diffusely distributed alignment of material (akin to inclined sub-parallel laminations) up to a sharp slip surface that crosscuts the debris avalanche deposit (Fig. 2.3e-f). Here, the base of a > 2 m large andesitic clast is flat and parallel to the primary slip surface, showing signs of a throughgoing, bisecting rupture. No vitreous layer is present in the shear zone at this locality.

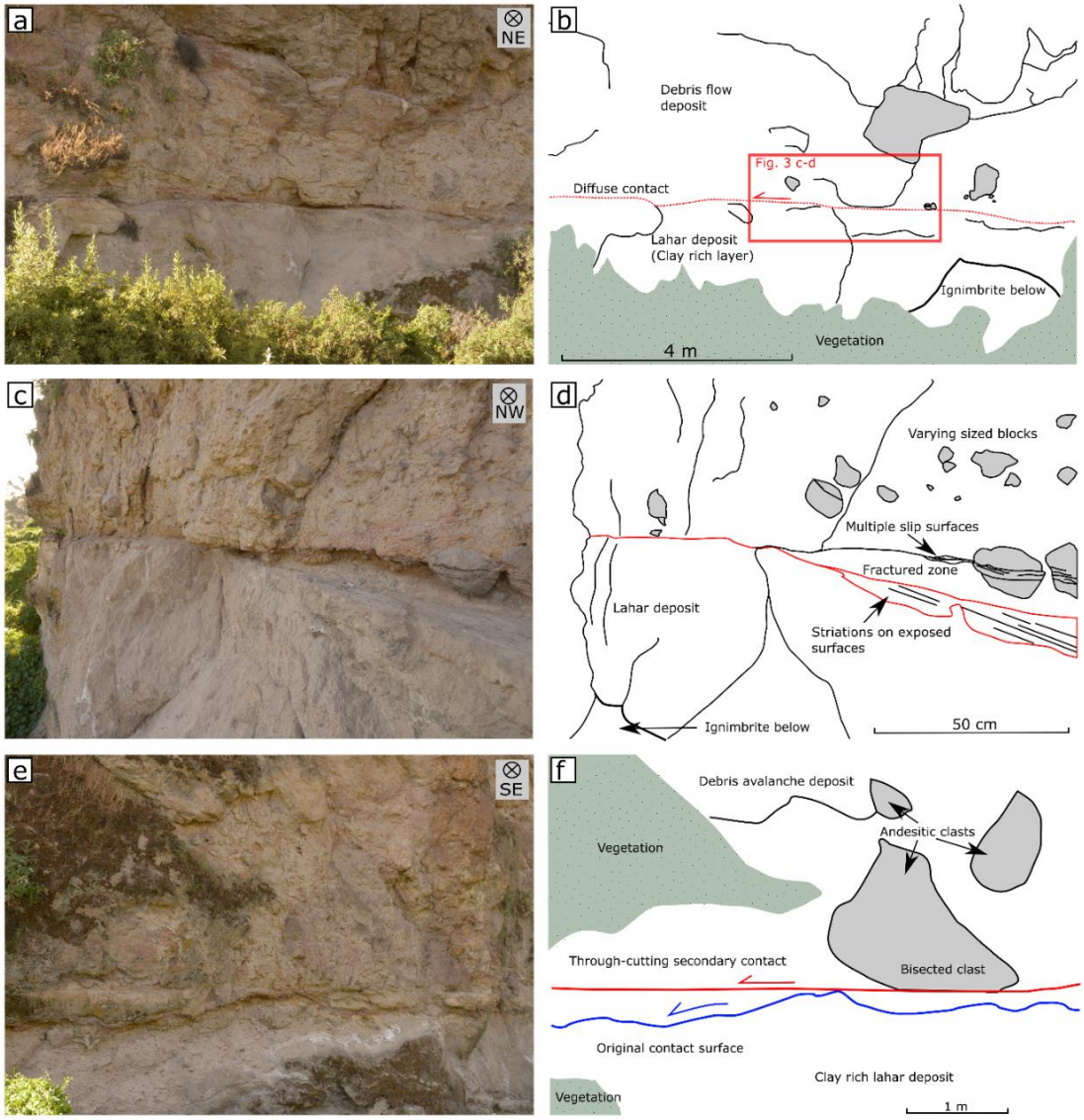

Figure 2.3. Field photos and sketches from Locality 2. a-b) Debris avalanche deposit with large clasts and 40 cm thick diffuse basal contact. c-d) Closer view showing intense fracturing and cataclasis along the slip zone, multiple fractures cutting andesitic blocks in the fractured zone marked and striations on the lower slip surface. e-f) Basal contact 140 m west (downstream) showing how rough topology of the original contact (blue) is superseded by a secondary through-cutting contact (red) that also bisects a clast.

2.4.1.4. Locality 3 – Intra-body shear zone and clastic dykes

In the Rio Socabaya gorge (Loc. 2.3 see Fig. 2.1), river incision exposes a > 800 m long, up to 100 m high section of the debris avalanche deposit on both sides of the river valley. Here, the deposit is made of a massive, white-grey, granular medium consisting primarily of ash- and lapilli-size clasts of andesite lithics and crystals. However, in this locality, rare larger blocks of andesite were observed in the deposit up to 3-4 m in size. There is no visible basal contact between the facies identified, though the ignimbrite is exposed approximately 200

m to the west. Instead, the main rock mass exhibits multiple clastic dykes as well as intra-body shear zones some 5-10 m above the river bottom. The structurally-lowest shear zone, identified at the western end of the southern bank, developed within the main body of rock and does not separate disparate units within the debris avalanche deposit (Fig. 2.4). The shear zone appears as a linear feature marked by a thin, microcrystalline layer some 0.5 cm thick and extending over a length of approximately 5 m. The layer is not straight, but rather undulose. There is no discernible variation in clast shape or size in relation to the shear zone, though it is often obscured by vegetation. A few metres to the west of the end of the visible shear zone there is a clastic dyke, 2 m thick and > 10 m high intruding sub-vertically into the deposit.

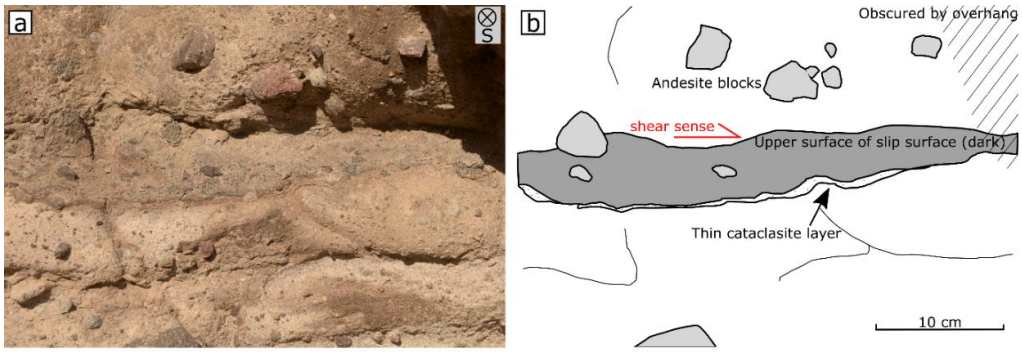

Figure 2.4. Field photo and sketch of a secondary shear surface within the debris avalanche at Locality 3 bounded by a thin layer of very fine cataclasite. The outcrop is oblique to vertical, revealing the top surface of the cataclastic vein. Moderately large clasts and blocks are present either side of the boundary, with shear indicators largely absent.

Multiple clastic dykes have been injected into the debris deposit from below, though the source of the material is not observed in the field. These structures range in size from 10 cm to 2-3 m in thickness and reach up to several tens of metres in length (Fig. 2.5a-b). The thickness of the larger clastic dykes changes along their length, generally tapering towards their tips. Most of the dykes are sub-vertical, but there are several occurrences of sections of dykes, locally projecting horizontally around large, metre-scale clasts. The edges are sharp with the deposit, and material entrained in the clastic dykes varies in size and prevalence. The majority of the dykes contain predominantly fine-grained clastic material with small lithic clasts (mostly andesitic) and crystal fragments. In one case, a dyke contained over 50 % mass of clasts (in a fine-grained groundmass), varying in composition and 1-30 cm in size. The margins of this dyke are devoid of large clasts, are fine-grained and show evidence of laminar shear banding (Fig. 2.5c-d). In other cases, the dykes do not show evidence of internal strain localisation or gradational deposition. The dykes are intact and do not exhibit

any offset, anticipated from post-emplacement shear within the bulk of the avalanche, indicative of their late stage occurrence.

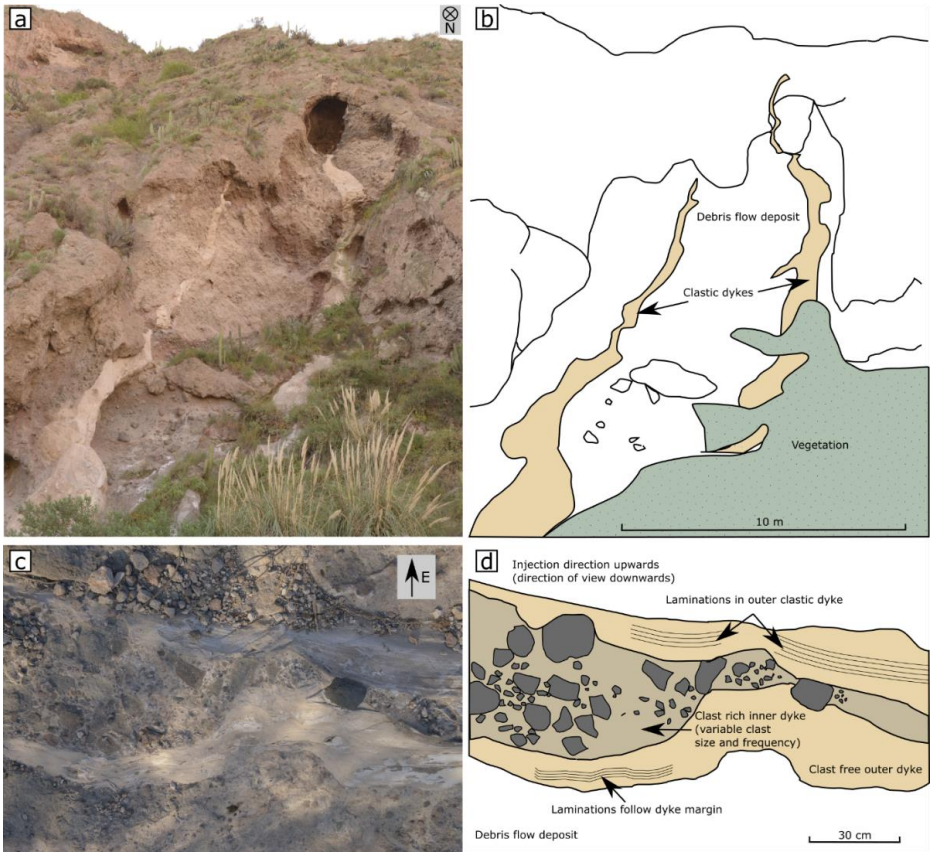

Figure 2.5. Field photos and sketches of Locality 3. a-b) Clastic dykes with variable thickness (0.05-1.5 m) injected up to 20 m sub-vertically into the debris avalanche deposit with sharp, undulating boundaries. c-d) Clast rich (primarily andesitic) clastic dyke located 80 m east of that shown in a-b, with larger clasts in the centre and a fine grained boundary. The direction of injection is upwards.

A second site observed in the same river valley is a shear zone consisting of a near-planar feature through the deposit exposed on the inside bend of the southern bank. This shear zone is approximately 25 m in length, with no discernible variation in lithology on either side. There is an observed reduction of the number of clasts above 3 cm in a layer 20 cm in thickness above the planar feature (Fig. 2.6), though intermittent large clasts up to 50 cm in size are present. At this shear zone the planar feature is additionally highlighted by its interaction with the clastic dykes. A dyke propagating from below terminates at the shear zone, increasing in width from 1 m to 3 m at the intersection, visible in the outcrop and extending several metres along the shear plane, gradually pinching out. 3 m to the west of the large clastic dyke, another dyke, 30 cm in width cuts across the planar shear zone into the unit above (Fig. 2.6).

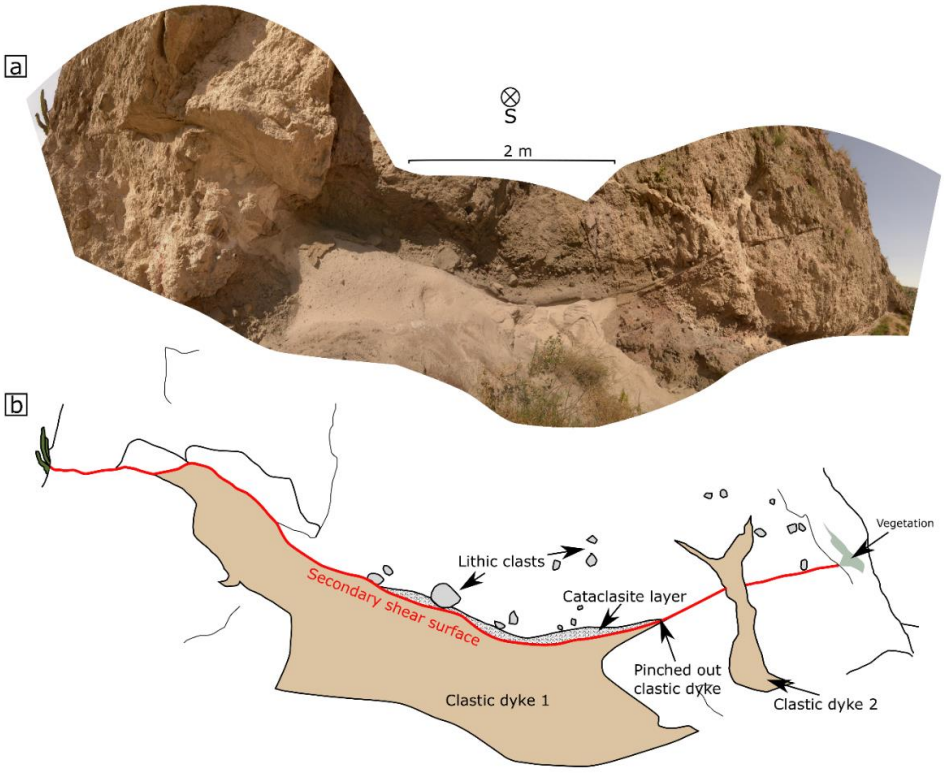

Figure 2.6. Stitched panoramic field photo and sketch of secondary shear surface interaction with clastic dyking at Locality 3. A large clastic dyke initiated from the primary basal slip surface below (not shown) terminating at the linear secondary shear surface feature in the outcrop. A second clastic dyke to the right of the image cross-cuts this linear feature with no displacement.

2.4.2. Microstructural analysis

Thin sections of sheared samples were made perpendicular to shear and parallel to the slip vector. Micro-textural analysis was performed using optical microscopy and BSE imagery.

2.4.2.1. Locality 1 – Pseudotachylyte basal contact

Microtextural analysis of the basal contact at Loc. 1 reveals that the dark layer observed at outcrop scale comprises a 12 mm thick vitreous layer with ~3 mm thick undulose, and diffuse boundaries at the top and bottom to cataclasites, which contain lithic clasts of bounding lithologies up to 2 mm in size (Fig. 2.7).

Visual observation of the central dark vitreous layer shows that it is made of a mix of tortuous (fluidal) black isotropic filaments (in plane-polarised light), up to 0.7 mm thick and 5 mm long, and a large fraction (around 40 %) of a dark brown material consisting of identifiable small rock fragments and crystals (Fig. 2.7). SEM image analysis reveals the black isotropic filaments to be bubble-bearing material with no identifiable crystal structure (Fig. 2.8). Later EPMA analysis produced consistent chemistry, ruling out the presence of small

crystals. Therefore, as identified in Legros et al. (2000), the isotropic black material is interpreted to be glass, with interspersed ultracataclastic, crystal-rich dark brown material. The glass filaments contain varying fractions of vesicles (Fig. 2.8a-b) which are up to 8 µm in size and occasionally elongated in the direction of en-echelon alignment of the melt filaments. Where preserved around large clasts, elongate vesicles form trails following the direction of shearing. Within the filaments, small, rounded patches of silica (5 µm) are observed.

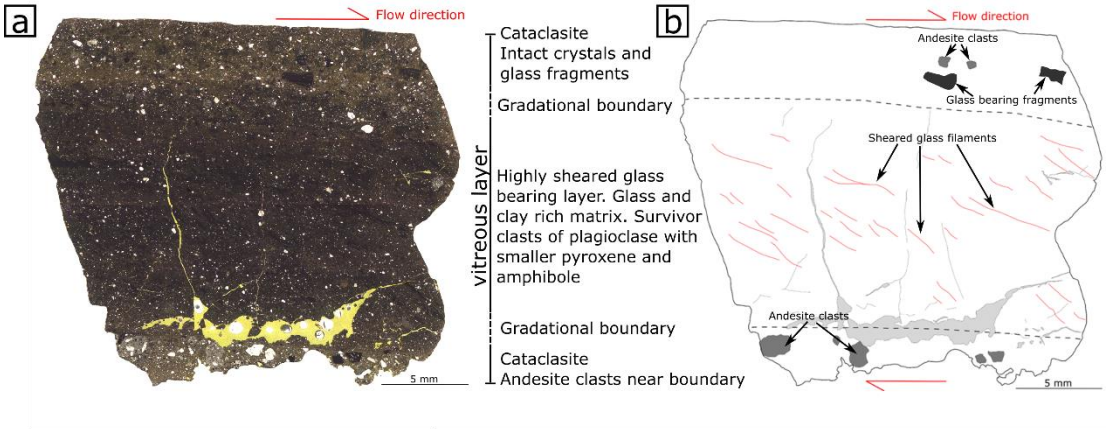

Figure 2.7. Thin section photomicrograph (in plane polarised light) showing the full thickness of the glass-bearing basal layer from Loc. 1. The layer is bounded by cataclasite and separates andesitic debris avalanche deposit above and the ignimbrite below (not shown here). A dark, glass bearing central layer contains sheared glass filaments (black areas, annotated with red lines in sketch), ultracataclasite (brown areas) and survivor clasts. The bounding cataclasite contains coarser crystal, lithic and relict melt fragments (thin section PPA1_1.1).

In the brown material the crystals are predominantly plagioclase feldspar up to 0.6 mm in size with a modal size < 0.4 mm. They show as equant fragments with multiple fractures. Additionally, smaller pyroxene crystals and occasional hornblende (< 0.1 mm) are observed but are concentrated on the outer edges of the dark, vitreous layer. SEM image analysis reveals that the larger clasts have extensive cracking (Fig. 2.8d) but remain together forming a brecciated texture. The fractured and sheared plagioclase crystals (Fig. 2.8a & c) form elongate layers of plagioclase-dominated fragments.

The layering between pseudotachylyte glass and ultracataclasite follows Riedel shear bands concordant with the shear in the flow direction (Fig. 2.7). The darker, glass-rich filaments are more predominant in the centre of the layer and are absent from the bounding cataclasite. In these marginal cataclastic zones (separating glass layer from the andesite above and ignimbrite below), we observed large clasts consisting of fragments of mixed vesicular

pseudotachylyte-ultracataclasite banded materials (pst in Fig. 2.8e-f), similar in texture to the intact vitreous layer. The fragments are further fractured (showing trivial offset) and the margins are sub-angular.

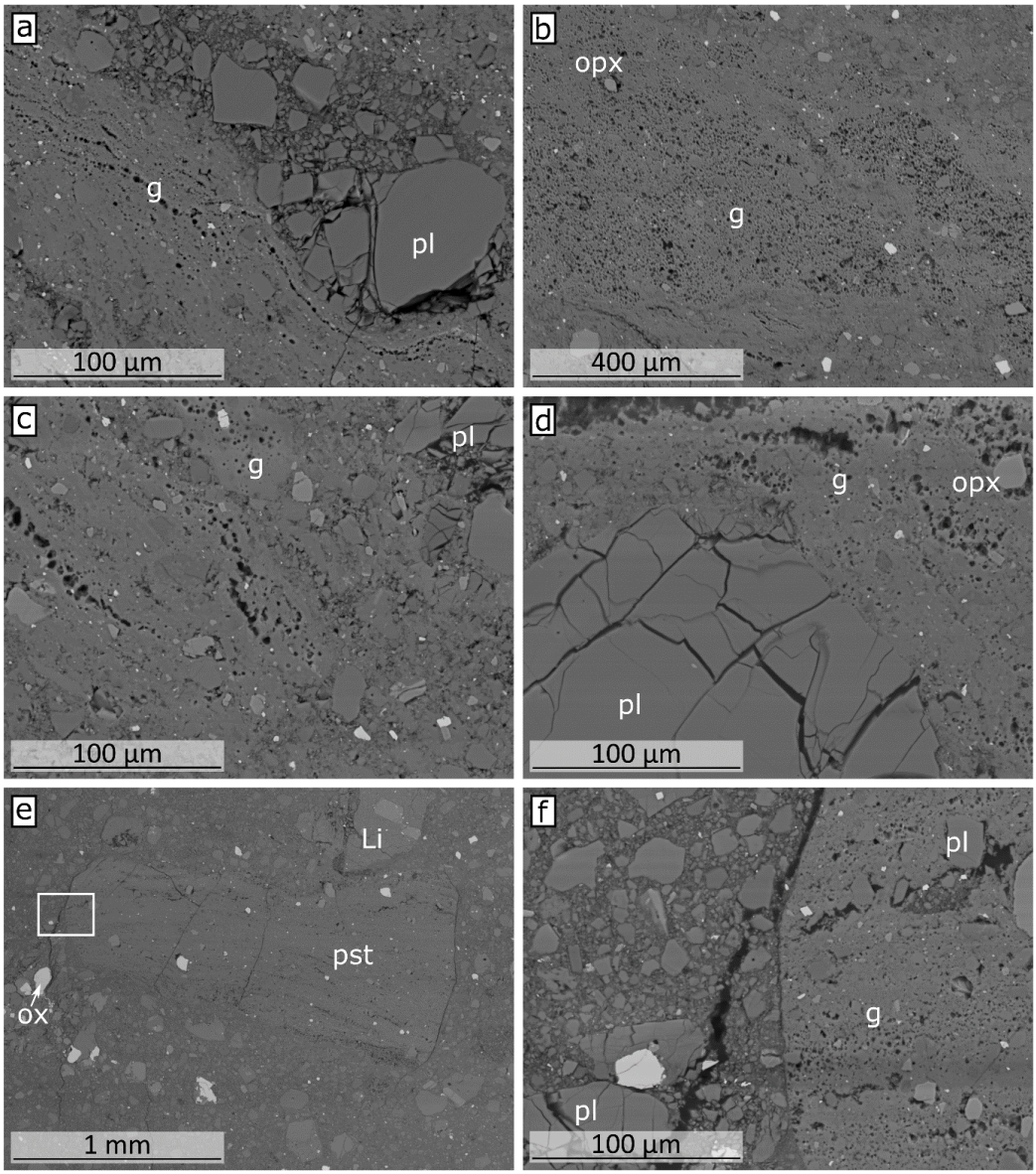

Figure 2.8. BSE images of the vitreous basal layer from Loc. 1 (also shown in Fig. 2.7). a) A sheared and fractured plagioclase clast within the glass-bearing layer. b) Vesicular glass in the primary slip surface with stretched bubbles along the lower boundary indicating shear. c) Sheared and vesicular glass and ultracataclasite, following Riedel shear directions. d) Fractured plagioclase survivor clast within the preserved glass bearing layer. e) Glass-bearing pseudotachylyte fragment within the cataclasite (box shows position of f). f) The rounded margin of the pseudotachylyte fragment with intermixed layers of ultracataclasite and glass, within the granular cataclasite. pl=plagioclase, g=glass, ox=oxides, opx=orthopyroxene, Li=lithic clast, pst=pseudotachylyte clast (thin section PPA1_1.1).

2.4.2.2. Locality 1 – Intra-body shear surface

The intra-body shear plane approximately 20 m above the basal contact at Loc. 1 is dominated by the presence of clasts and microcrystalline material. The visibly pale layer in the outcrop is a poorly sorted clast rich cataclasite, the dark vitreous layer is denser ultracataclasite welded with small amounts of amorphous material between grain contacts (Fig. 2.9a). The largest clasts observed here are andesitic, 5-6 mm in size and semi-rounded, which are larger than the clasts near to the basal contact hosting frictional melt (section 4.2.1). Smaller crystal fragments, primarily of plagioclase are also present (Fig. 2.9b). In addition, the contact between the cataclasite and the thin, denser ultracataclasite layer is sharp (Fig. 2.9b-c).

2.4.2.3. Locality 1 – Basal ignimbrite

Analysis of the ignimbrite below the contact at Loc. 1 found that the formation is rich in similar sized anhedral plagioclase and sanidine crystals, commonly 1-2 mm in size and up to 3 mm with occasional smaller quartz and biotite crystals up to a maximum of 1 mm in size (Fig. 2.10a). The plagioclase and sanidine crystals occasionally form glomerocrysts containing a combination of the two most abundant phenocryst types. These crystals are hosted in a matrix of small needle-shaped glass shards, (< 0.5 mm). In the sample collected there is no evident welding of the material, which has high porosity. The crystal assemblage matches that described for the La Joya Ignimbrite formation mapped within the Arequipa basin infill, which is thought to extend across the whole area below the debris avalanche deposit (Lebti et al., 2006).

2.4.2.4. Locality 2 – Cataclastic basal contact

From the basal contact at Locality 2, there is no evidence of the localisation of shear onto a single zone. Instead, the material across a band of approximately 40 cm thickness is formed of highly fractured lithic and crystalline fragments and clasts hosted in a matrix of clay (Fig. 2.10c) with no evidence of glass. Larger lithic fragments, ranging in size from < 1 mm up to 7-10 mm in size, are identifiable as andesitic in composition with similar crystal content as clasts from Loc. 1, with abundant sub-euhedral plagioclase (< 1 mm) and subhedral amphibole phenocrysts (< 0.8 mm). Plagioclase forms the largest of the crystalline fragments in the shear zone, though small, subangular, amphibole and biotite crystals around 1 mm in size are also observed in the cataclasite. Several large pumiceous clasts up to ~4 cm in size are also preserved within the shear zone with only minor fracturing. These pumiceous clasts contain plagioclase, sanidine and biotite. Small fragments are often monocrystalline, commonly plagioclase up to 2 mm in size. The orientation of these fragments shows no

evidence of Riedel shearing and there are no pervasive shear fabrics observed within the cataclasite.

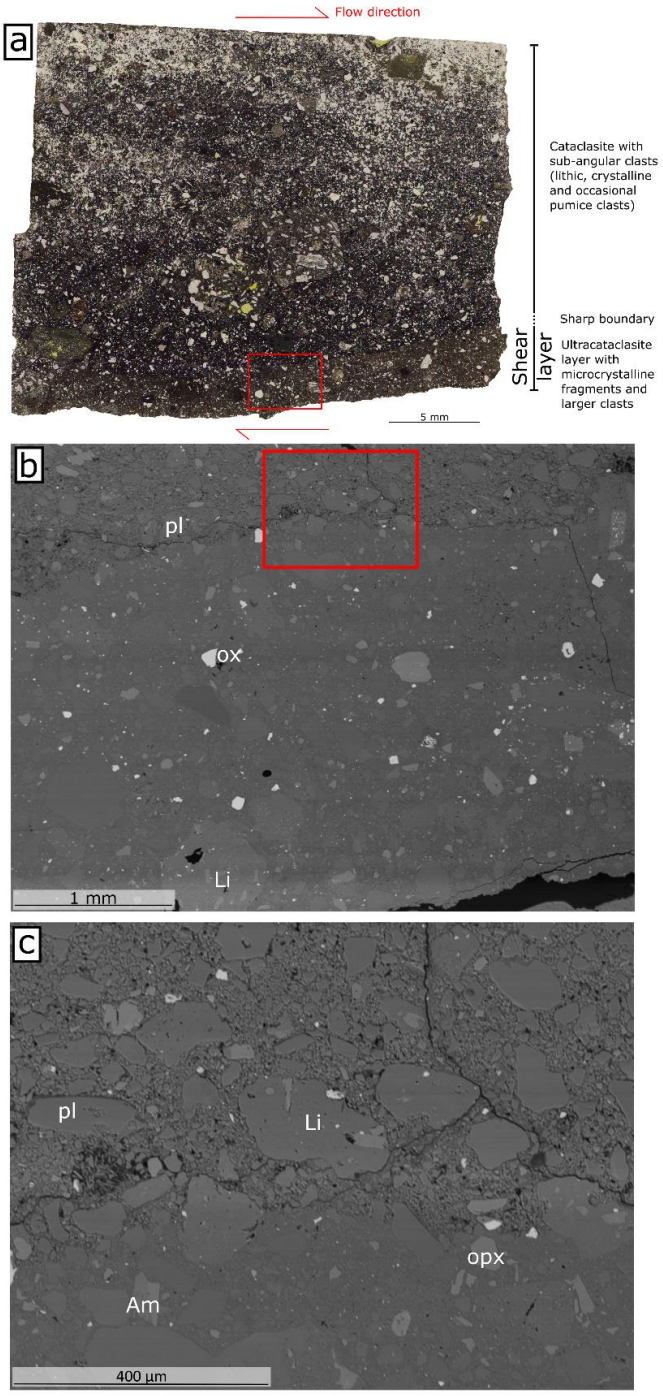

Figure 2.9. Thin section from secondary slip surface at Loc. 1. a) A PPL photomicrograph showing cataclastic textures (clasts > 0.5 mm) with darker brown ultracataclasite making up the primary shear layer at the base (red box shows area in b). b) BSE image of the granular cataclasite above the denser ultracataclasite (red box shows area in c). c) The cataclasite and ultracataclasite show similar components (crystal and lithic clasts) but are distinguished by an abrupt porosity contrast (thin section PPA1_5.3).

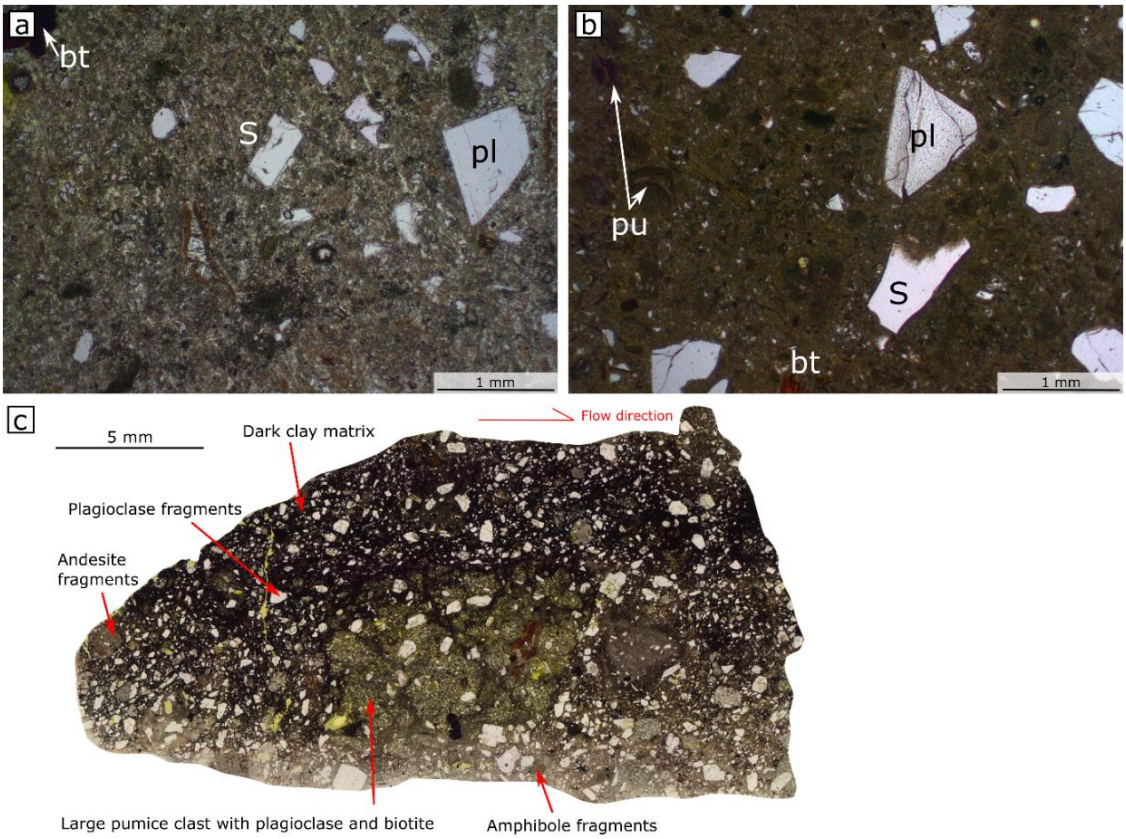

Figure 2.10. PPL photomicrographs illustrating mineralogy of a) Porous ignimbrite from Loc. 1 with sanidine (S), plagioclase (pl) and biotite (bt) crystals in a glass shard matrix (thin section PPA1_1.1). b) Clastic dyke from Loc. 3 with sanidine, plagioclase, biotite and pumice (pu) shards with high clay content in the matrix (thin section PPA2_2.1). c) The cataclastic basal shear zone at Loc. 2 hosts a range of clasts of different size and composition (thin section PPA3_2.1).

2.4.2.5. Locality 3 - Clastic dyke

A sample of a large clastic dyke in the northern face exposure at Loc. 3 is observed to contain considerable fractured glassy pumice fragments, andesite clasts (up to 7 mm in thin section though field observations indicate larger clasts are present), individual crystals of plagioclase and a high clay content (Fig. 2.10b). Additionally, some biotite (tabular, up to 1 mm) is present, which is not observed in the lithologies of the debris avalanche but is observed in the ignimbrite and cataclastic basal shear zone.

2.4.3. Geochemical analysis

Geochemical analysis was performed to reconcile physico-chemical processes associated with the evolution of shear and frictional melting. XRF analysis was used to constrain the chemical composition of the host rocks, confirming the andesitic nature of the avalanche deposit and the rhyolitic chemistry of the ignimbrite (Fig. 2.11, see Appendix I, Table A.I.2).

EPMA was conducted on several mineral phases from host rocks and crystal fragments and amorphous areas from the basal layer at Loc. 1 to constrain the development of frictional melting (with respect to the host lithologies). The plagioclase crystals in the vitreous layer as well as in andesite lithics within the ultracataclasite and ignimbrite host wall rock are compositionally grouped (Fig. 2.11), with CaO ranging from 6 to 9 wt.% and NaO from 6 to 8 wt.% (see Appendix I, Table A.I.1). Amphibole crystals in lithic fragments as well as rare individual crystals in the ultracataclasite at Loc. 1 were found to be compositionally similar and were absent in the vitreous layer (Fig. 2.11, see Appendix I, Table A.I.1). The two types of pyroxene present in the andesite, cataclasite and vitreous layer, were identified as augite (clinopyroxene; Ca-rich) and enstatite (orthopyroxene; Mg-Fe rich).

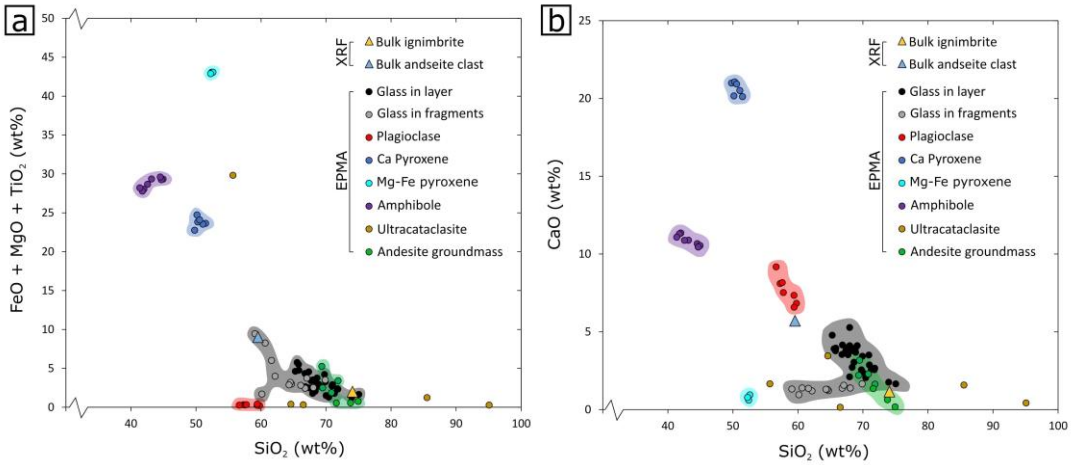

Figure 2.11. Chemical analyses by XRF (triangles) of an andesite clast from the debris avalanche and ignimbrite from Loc. 1, and chemical analyses by EPMA of the glass within the pseudotachylyte layer from Loc. 1, as well as plagioclase, amphibole, pyroxene and the groundmass from 3 andesite clasts and plagioclase and biotite from the ignimbrite, plotted as: a) Mafic (FeO + MgO + TiO_2) wt.% against silicon dioxide (SiO_2) wt.% showing relation of frictional melt (glass) to bulk chemistry and individual minerals; and b) Calcium oxide (CaO) wt% against SiO_2 wt%, with low CaO wt% suggesting involvement of andesitic enstatite (Mg-Fe pyroxene) in generation of the fragmented glass.

Glasses in both the preserved vitreous layer and in a fragment of glass-bearing material found in the cataclasite were analysed (Fig. 2.8). The EPMA chemical composition of glass from the basal pseudotachylyte plots between the XRF bulk chemistry of the underlying ignimbrite and the andesitic blocks from the debris avalanche deposit (Fig. 2.11). The glass however tends to be enriched in SiO_2, plotting closer to the composition of the ignimbrite than that of the andesite. In contrast, the glass fragments preserved in the marginal cataclasite of the basal shear zone spans a wider range in chemistry that is notably more mafic in composition. The glass in these pseudotachylyte fragments has less CaO wt.% and

SiO_2 wt.% than either the andesite or the ignimbrite (Fig. 2.11b). Analyses on the ultracataclasite within the layer returned poor totals with highly varying chemistries, suggesting mixed lithology fragments.

2.5. Interpretation

The field, microstructural and geochemical data can be used to make several interpretations about the mechanics of shearing within the debris avalanche.

2.5.1. Intergranular forces and fragmentation

The contrasting nature of the different basal shear zone exposures provide clues as to the emplacement mechanisms. At the basal contact at Loc. 1, we do not observe large andesitic clasts within 5 m of the contact and there is evidence of intense brecciation (Fig. 2.2). In comparison, at Loc. 2 we observe a number of large andesitic clasts, up to metre scale in close proximity to the basal shear localisation zone (Fig. 2.3). This suggests greater intergranular forces may have occurred near the base of the flow at Loc. 1 compared to Loc. 2 that exceed the elastic limit of the clasts (Davies and McSaveney, 2009), resulting in intense fracturing and reduction in clast and particle sizes (Arabnia and Sklar, 2016). This qualitative observation can also be made at a smaller scale within the shear localisation zone itself, where centimetre-scale clasts at Loc. 2 have survived (in comparison to the smaller fragments in the glass-bearing layer at Loc. 1). Some of these fragments are pumiceous (Fig. 2.10c) material that, due to their highly vesicular nature, would be mechanically weaker than other crystalline and lithic fragments. Their survival means that there was less cataclastic damage associated with this shear zone. The inferred greater intergranular forces at Loc. 1 also enhances the ability for frictional heating (Carslaw and Jaeger, 1959) that can lead to melting. In support of this, biotite and amphibole fragments present in the cataclasite (Fig. 2.9 & 2.10c) are absent in the vitreous pseudotachylyte (Fig. 2.7 & 2.8), suggestive of selective melting of the mineral assemblage due to the lower fracture toughness and melting temperature of these phases (Spray, 2010).

2.5.2. Transient nature of slip zones and slip zone morphology

Despite the deposit only preserving the cumulative history and final state of the debris avalanche, there is evidence to suggest the temporal evolution of the basal shear zones during the flow of the debris avalanche. At Loc. 1, the presence of glassy fragments in the cataclasite bounding the glass-bearing pseudotachylyte layer (Fig. 2.7 & 2.8e-f) suggests that there were at least two melting events. The “glass in layer” and “glass in fragments” have different textures and chemistry (Figs. 2.8 & 2.11) so either formed from different mixtures

of material in the basal shear zone or under different temperatures, timescales and slip conditions. The original layer became fractured and subsequently a new layer comprising ultracataclasite and pseudotachylyte was formed. This process may have occurred multiple times throughout deposition. The development of a secondary slip layer at this locality was likely a late stage development, potentially induced by the slowing of the lower portion of the flow by loss of momentum and interaction with topography.

Similarly, at Loc. 2, the initially rough topography of the basal contact is cut through by a secondary linear contact (Fig. 2.3e-f) suggesting gradational shifts in slip rate or overburden to localise slip to different surfaces at different times. Additionally, multiple fractures splay from these surfaces and cross-cut within the shear zone (Fig. 2.3c-d) suggesting distinct ruptures.

Within the body of the avalanche deposit at Loc. 3, clastic dykes interact with a linear localised shear plane (Fig. 2.6). The dyke is wider and contains evidence of shear at the contact with the shear plane, indicating it may have terminated at the shear zone during active slip on that contact. In contrast a second clastic dyke at this locality injects through the preserved linear shear plane and is not subjected to any displacement along the shear plane. Therefore, this dyke must have occurred after shearing on this secondary shear plane ceased. This interaction of dykes and shear surfaces is additional evidence supporting the transient nature of active shear surfaces both at the base and within the flow.

2.5.3. Melt chemistry and source rocks

The chemical analyses for the frictional melt glass at Loc. 1 plot between the two bulk rock chemistries of the lower ignimbrite and andesitic upper plate material (Fig. 2.11). This suggests that a combination of both materials, initially incorporated and sheared in the basal zone, melted to form the glass preserved in the intact basal shear zone.

The more mafic composition of the analysed frictional melt glass fragments within the cataclasite (Fig. 2.11a), interpreted as remnants of a previous melt-producing shear zone, is likely due to early melting of amphibole and biotite (present in the host rocks and cataclasites). This is also supported by the highly vesicular nature of these fragments, as melting of hydrous phases releases water (e.g. Magloughlin, 2011). Primitive or partial frictional melts are frequently more mafic than more mature melts (Wallace et al., 2019a and references therein) and leave suspended survivor clasts of minerals with higher fracture toughness and/or melting temperature (Spray, 2010). Further melting of the more resistant minerals brings the melt chemistry back towards the bulk chemistry, as seen here with the

chemistry of the intact basal pseudotachylyte composition which plots between the andesite and ignimbrite.

2.5.4. Frictional melt rheology evolution

Understanding the development and impact of frictional melting on the debris avalanche requires consideration of its rheology. Here the observations that slip caused frictional melting as well as fragmentation of frictional melt are used to constrain conditions in the debris avalanche during runout. We used the geochemical compositions of the glass (from the preserved layer and the fragment of glass-bearing earlier melt identified within the bounding cataclasite, both from the basal contact at Loc. 1) as input parameters in the GRD viscosity calculator of Giordano et al. (2008) to constrain the temperature (T in Kelvin) dependence of the viscosity (η in Pa s) of the early frictional melt present in fragments (η_e) and late frictional melt forming the main basal pseudotachylyte (η_l):

$$log\eta_e = A + \frac{B}{T(K) - C} \tag{2.1}$$

Table 2.1 provides the values of A, B and C (where B and C are adjustable parameters controlled by composition and A is a constant independent of composition related to the viscosity at infinite temperature, see Giordano et al. (2008)) to model both melts (Fig 2.12a). The chemical compositions vary significantly locally due to the presence of small unhomogenised melt filaments (schlieren), which would have contrasting rheologies. However, the chemical compositions input do not include the water concentrations which would have likely been transiently present in the frictional melts owing to the presence of amphibole in the host rock (e.g. Wallace et al., 2019a). Here, we assume the melt phase contained a nominal 0.1 wt.% water concentration in this low-pressure environment.

Table 2.1. Values for variables A, B and C used to determine melt viscosity with Eq. 1 and 2. Min and max represent compositional ranges from low to high (respectively) SiO_2 concentration of the glass-bearing layer and fragment. The values of A, B and C are used to constrain the viscosity of each frictional melt (η) and apparent viscosity of each suspension (at a strain rate of 10^3 s^{-1}) at a nominal temperature of 1250 ˚C.

Sample	A		B		C		$log\eta$ at 1250 ˚C		$log\eta_{app}$	
	Min	Max	Min	Max	Min	Max	Min	Max	Min	Max
Layer	-4.55	-4.55	9126.4	11264.3	406.7	304.8	3.62	4.69	4.34	5.42
Fragment	-4.55	-4.55	8681.8	10666.0	421.2	332.4	3.33	4.41	3.67	4.75

The frictional melts described here contain variable fractions of suspended crystals and bubbles, known to impact the rheology and contribute to a non-Newtonian behaviour (Caricchi et al., 2007; Lavallée et al., 2007; Truby et al., 2015b; Coats et al., 2018). Here we consider the influence of crystals (i.e., fraction, shape and maximum packing) using the two-phase rheology calculator from Costa et al. (2009). We first constrained the solid fraction present in the pseudotachylyte (i.e., surviving crystals and lithics) via SEM image analysis using the ImageJ online toolbox (Schneider et al., 2012). We estimated the solid fraction in the early pseudotachylyte at 0.25 and late pseudotachylyte at 0.43 and the aspect ratio of the particles as 1.761 in the early and 1.684 in the late pseudotachylyte. Then, following guidelines from Mueller et al. (2010), we used the aspect ratio of the solid fraction to define a critical maximum packing of a monodisperse distribution $\varphi_{m,m}$ for both suspensions at 0.57. However, due to the polydispersivity (δ) of the solid fraction, the true maximum packing is higher. We used Phan et al. (1998) to define the polydispersivity where $\delta = \frac{r_{sd}}{\langle r \rangle}$ where r_{sd} is the standard deviation of the fragment radii (3.00 and 2.71 for the fragment and layer respectively) and $\langle r \rangle$ is the mean of the fragment radii (3.66 and 3.67 for the fragment and layer respectively). This is based on measurements from 205 particles from the glass bearing fragment and 417 particles in the preserved layer over an analysis area of 200 and 100 μm^2 respectively (see Appendix I, Supplementary Table A.I.7 & A.I.8). Subsequently, the polydispersivity of the fragment (δ_e) and later preserved layer (δ_l) pseudotachylytes were input into the fitting equation from Klein et al. (2017) substituting the monodisperse maximum packing of spheres $(\varphi_{m,0})$ for our previously defined monodisperse packing of the solid fraction's aspect ratio $(\varphi_{m,m} = 0.57)$. This defines the true maximum packing of the solid fraction of the early fragment $(\varphi_{m,e})$ and late preserved layer $(\varphi_{m,l})$ such that:

$$\varphi_{m,e} = (1 - \varphi_{m,m})e^{(-\delta_e * \varphi_{m,m})} \tag{2.2}$$

These geometrical parameters were then used in the Costa et al. (2009) model to define the apparent viscosity of the frictional melt suspensions; here, considering the mass movements' runout speeds of > 10 ms^{-1} (Legros, 2002 and references therein) and the preserved frictional melt thickness of 12 mm, we estimated the maximum frictional melt strain rate at 10^3 s^{-1} for use in our calculations (Fig. 2.12b; Table 2.1). [Whilst we posit that melt generation and thus melt thickness varied temporally and spatially, we used the preserved frictional melt layer thickness to define strain rate here to illustrate the impact of particles on suspension viscosity.] We observe that the presence of solid particles in the frictional melt significantly increase the range of probable viscosities which impact slip

during the debris avalanche. Yet, further constraints of suspension viscosity are difficult without knowledge of temperature conditions in the melt.

Frictional melting has commonly been described to be a disequilibrium process occurring via selective melting of mineral phases (Spray, 1992, 2010; Shimamoto and Lin, 1994; Lin and Shimamoto, 1998; Wallace et al., 2019a). This provides a framework to evaluate frictional melt temperature based on mineral breakdown temperature. Considering that the frictional melting likely involved both wall rocks and that the pyroxenes, some plagioclase and few amphiboles survived implies that most of the amphiboles, any biotite inherited from the ignimbrite, the andesitic interstitial glass and some of the plagioclase likely underwent melting. This analysis suggests that the frictional melt may have reached temperatures of approximately 1200-1300°C. At such temperatures, the viscosity of the frictional melt preserved in the basal layer would have been $10^{5.1}$ -$10^{4.3}$ Pa s (for the highest silica melt chemistry) and the apparent viscosity of the suspensions at a strain rate of 10^3 s^{-1} (η_{app}) approximately $10^{5.8}$ – $10^{5.1}$ Pa s (assuming a nominal 0.1 wt.% water dissolved in the melt).

The theory of heat conduction detailed by Carslaw and Jaeger (1959) can be used to estimate slip conditions required to generate temperature change (ΔT) :

$$\Delta T = \frac{\mu \sigma_n V \sqrt{t}}{\rho C_p \sqrt{\pi k}} \tag{2.3}$$

Considering a friction coefficient (μ) of 0.85 (at static conditions) (Byerlee, 1978), a normal stress (σ_n) of 2.6 MPa [based on an overburden of 100 m and a bulk rock density (ρ) of 2656.6 kg m^{-3} (as determined by He-pycnometry)], a specific heat capacity (C_p) of 900 J kg^{-1} K^{-1}, and a thermal diffusivity (k) of 10^{-6} m^2 s^{-1}, we can bracket slip velocity (V) and duration (t) along the basal contact. Given that distance (d) is proportional to the products of slip rate and duration, $d= Vt$, the above analysis suggests that frictional melting (reaching a nominal temperature of 1250°C), would have occurred in < 2 m if the slip velocity was greater than 5 m s^{-1}. Figure 2.12c shows that for more rapid slip rates, the distance of slip required would have needed to be shorter. This does not agree with the observation that only a thin pseudotachylyte was observed at much greater runout distances of 24 km. Yet, considering that the basal contact did not generate (or preserve) a pseudotachylyte at a slip distance of 17.5 km, it suggests that the slip conditions must have locally evolved rapidly during the avalanche, highlighting the transient nature of slip during debris avalanches, including the potential reduction of μ during dynamic slip. Thus, we must turn to other proxies to define local slip rate conditions that led to frictional melting.

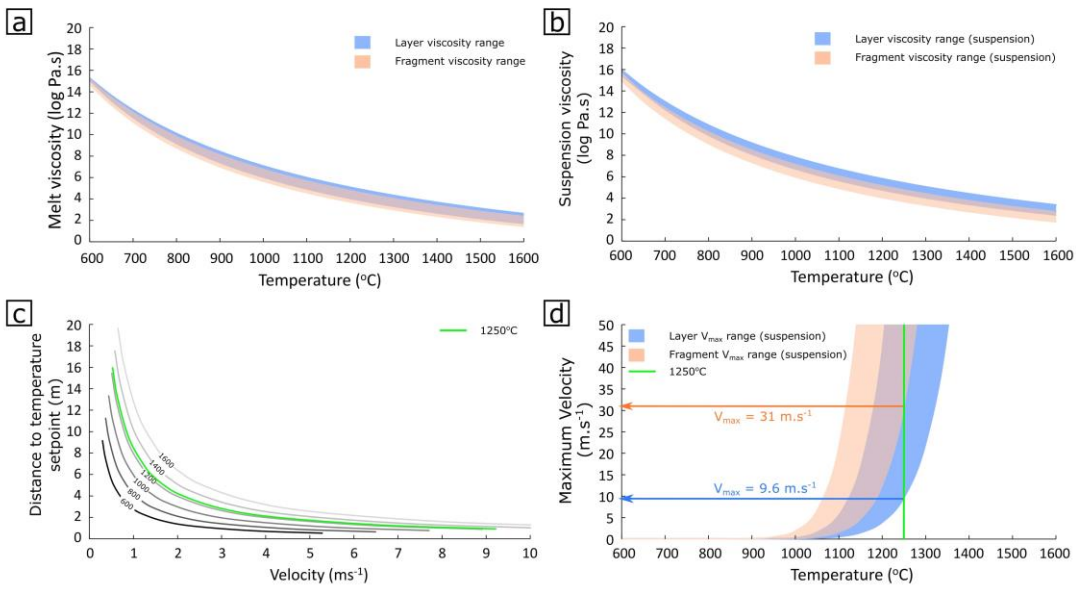

Figure 2.12. Modelling the generation and rheology of the frictional melts. a) Temperature-viscosity relationships of the glass in the preserved layer (blue) and fragment (orange), using Eqs. 1-2. b) Temperature-viscosity relationships of the preserved layer and fragment considering the suspended solid fraction and bubbles, using Eq. 9. c) Slip distance required to produce heating of a given magnitude (contours) for different slip velocities, using Eq.3, showing the estimated maximum temperature, 1250 °C (green). d) Maximum possible velocity experienced by the modelled suspensions avoiding brittle failure. Presence of fragments suggests velocity exceeded 31 ms^{-1} at 1250 °C and melting persisted to form the preserved layer.

The early occurrence of frictional melt fragmentation, as witnessed by the presence of pseudotachylyte fragments (with different chemistry to the main pseudotachylyte) in the marginal cataclastic region of the shear zone, demands further appraisal. Silicate melts are viscoelastic bodies which abide by Maxwell's structural relaxation concept (Dingwell and Webb, 1989), where the timescale of relaxation (τ) is proportional to the ratio between the melt's shear viscosity (η) and the elastic modulus at infinite frequency (G_∞, approximated at 10^{10} Pa for silicate melts at relevant conditions; Webb and Dingwell, 1990):

$$\tau = \frac{\eta}{G_\infty} \tag{2.4}$$

In rheological analysis, if the timescale of observation (t_{obs}) approaches the relaxation timescale, the material exhibits increasingly elastic behaviour and may rupture if the accumulated stress is sufficient. This can be accessed via the dimensionless Deborah number (De_0), whereby $De_0 = \frac{\tau}{t_{obs}}$. It has been found that silicate melts tend to rupture at strain rates two orders of magnitude lower than that predicted by viscoelasticity theory; that is, at

a critical Deborah limit, $De_{c,0} = 10^{-2}$ (Webb and Dingwell, 1990). Thus, the critical timescale for rupture has commonly been simplified to $\tau_c = \frac{\eta}{De_{c,0}G_\infty}$ (Lavallée et al., 2015b). Given that the inverse of the relaxation timescale corresponds to the structural relaxation timescale, $\dot{\varepsilon} = 1/\tau$, Lavallée et al. (2015) coined the following expression to define the strain rate at which a frictional melt would undergo rupture ($\dot{\varepsilon}_{max}$):

$$\dot{\varepsilon}_{max} = \frac{De_{c,0}G_\infty}{\eta} \tag{2.5}$$

Assuming that shear is distributed across the entire thickness of the frictional melt layer ($z \cong 12\ \mathrm{mm}$), they suggest that we can estimate the maximum slip rate (V_{max}) using

$$V_{max} = \frac{De_{c,0}G_\infty z}{\eta} \tag{2.6}$$

Considering an early frictional melt viscosity (η_e) estimate of $10^{4.4}$ Pa s, Eq. 5 would suggest that the melt phase underwent a strain rate greater than $10^{3.6}$ s^{-1} and Eq. 6 would constrain the local slip velocity at 46.9 m s^{-1}. However, the presence of the solid fragments and bubbles in the melt layer would have also modified the rheological conditions leading to rupture (e.g. Coats et al., 2018); thus any modelling of frictional melt rheology should account for the complexity borne by suspended particles. Here we detail how to implement this analysis. Cordonnier et al. (2012) suggested that the fraction of crystals in suspension (φ_x) would lower the critical Deborah number $De_{c,x}$ following:

$$De_{c,x} = De_{c,0}\left(1 - \frac{\varphi_x}{\varphi_{m,e}}\right) \tag{2.7}$$

where $\varphi_{m,e}$ is the maximum packing value estimated for the frictional melt at 0.73 for the early fragmented pseudotachylyte and 0.71 for the later preserved layer. The fraction of bubbles φ_b in the suspension would have similarly lowered the critical Deborah limit of the suspension ($De_{c,s}$), which according to Coats et al. (2019) would follow:

$$De_{c,s} = 1.7 \times 10^{-4}\varphi_b + De_{c,x} \tag{2.8}$$

which can be rewritten as

$$De_{c,s} = 1.7 \times 10^{-4}\varphi_b + De_{c,0}\left(1 - \frac{\varphi_x}{\varphi_{m,e}}\right) \tag{2.9}$$

So, considering this failure criterion in our previous analysis of maximum strain rate and slip velocity experienced by the frictional melt, we can rewrite Eq. 5 and 6, by considering $De_{c,s}$ instead of $De_{c,0}$, obtaining:

$$\dot{\varepsilon}_{max} = \left(1.7 \times 10^{-4}\varphi_b + 10^{-2}\left(1 - \frac{\varphi_x}{\varphi_{m,e}}\right)\right)\frac{G_\infty}{\eta} \tag{2.10}$$

And

$$V_{max} = \left(1.7 \times 10^{-4}\varphi_b + 10^{-2}\left(1 - \frac{\varphi_x}{\varphi_{m,e}}\right)\right)\frac{G_\infty z}{\eta} \tag{2.11}$$

respectively. As the fragmented pseudotachylyte has interstitial melt with a viscosity of $10^{4.4}$ Pa s and contains $\varphi_x = 0.25$ and $\varphi_b = 0.14$, we estimate rupture occurred when the strain rate exceeded ~$10^{3.4}$ s^{-1} which would have occurred when the slip velocity exceeded at least 31 m s^{-1} during debris avalanche (Fig. 2.12d); this critical slip velocity (for fragmentation) may have been higher for less evolved schlieren present in this early frictional melt. The same calculation for the later formed preserved layer using interstitial melt viscosity (η_l) of $10^{4.7}$ Pa s, $\varphi_x = 0.43$, $\varphi_b = 0.15$ and $\varphi_{m,l} = 0.71$ gives a lower maximum velocity of 9.6 m s^{-1} for the most evolved schlieren within the late frictional melt (but higher values for the less evolved melt filaments). So, these rheological constraints provide a view that the slip velocity varied during the debris avalanche.

Finally, in order to assess the rheological impact of frictional melt on debris avalanches, we compare the shear resistance (σ_s) of the modelled melt layers to the shear resistance that would occur in a purely frictional, rock-rock slip environment (i.e., without melt). To do this, we use the viscosity equation:

$$\sigma_s = \eta_{app}\dot{\varepsilon} \tag{2.12}$$

where the strain rate for the layer modelled is calculated by:

$$\dot{\varepsilon} = \frac{V}{z} \tag{2.13}$$

Frictional melt suspension viscosity (η_{app}) previously calculated (see Table 2.1) following Costa et al. (2009) constrain the range of shear resistance imposed by the frictional melt onto slip at 4.7-56.1 MPa, evolving to 22.1-260.4 MPa with further slip (under the same conditions). In contrast, the frictional resistance of rock-rock slip at the base of the deposit

may be estimated using Byerlee's frictional law of $\sigma_s = \mu\sigma_n$ (Byerlee, 1978); assuming a friction coefficient of 0.85 and a normal stress, $\sigma_n = \rho g D = 2.6$ MPa, we estimate the shear resistance during rock-rock sliding at 2.2 MPa. Comparing the shear resistances offered by rock-rock friction versus frictional melt, we find that the shear resistance calculated for the melt layer at 10^3 s^{-1} strain rate exceeds that predicted by Byerlee's frictional law. Yet, we surmise that the rate weakening tendency of rock-rock friction (Fialko and Khazan, 2005) would likely promote even lower shear resistances at the slip rates of meters/seconds described in this section. However, local variations in chemistry, solid fraction and temperature would have promoted strain localisation which may have drastically impacted the resultant shear resistance during slip. It must be noted here, that the modelled apparent viscosities of the frictional melts may have been overestimated as they are constrained at a strain rate (10^3 s^{-1}) exceeding the empirically validated strain rate limit (10^{-1} s^{-1}) of the Costa et al. (2009) model. Beyond that limit, the model assumes (hence predicts) that the apparent viscosity no longer decreases as a function of strain rate (i.e., that slip with frictional melt no longer undergoes rate weakening at such extreme rates); thus the shear resistance (calculated for a given viscosity) increases with strain rate, though this remains untested. Further rheological experiments at such extreme rates are required to improve our ability to model the rapid shear regime extant in sector collapse events.

2.6. Discussion

2.6.1. Emplacement style

The palaeotopography of the original land surface included ridges and gullies as evidenced by the preserved palaeotopography and lahar deposits which are restricted to narrow channels in the ignimbrite. Clastic dyking may have resulted from the avalanche crossing fluid rich areas of palaeotopography such as riverbeds, or simply saturated regions of the porous ignimbrite. Local flow directions at Loc. 1 (Fig. 2.2) indicate that the debris avalanche was at least partially directed by local topography, which may be especially relevant near the thinned margins.

In each locality investigated there appears to be very little range in lithic composition. Although little literature exists on the composition of eruptive and intrusive products from Pichu Pichu, the observations made here suggest that the volcanic edifice-forming rocks are consistent with intermediate volcanic products typical of a compound volcano present in the Andes. The homogeneity of the surviving clasts within the flow in the areas studied therefore suggests there was limited internal shear that would have enhanced mixing of different

lithologies during the debris avalanche. This is supported by the sharp contact between compositionally different flow packages at Loc. 1 (see Fig. 2.2e-f). Such separation of flow packages suggests that overall, the flow mostly moved as discrete bodies, though without knowledge of the volcanic units incorporated this interpretation is speculative. Higher up in the flow at Loc. 3 away from high shear at the basal contact, large clasts have been transported intact. In this survey, as all the studied shear structures were all in distal localities, it is difficult to convey any constraint about coherence within the core of the flow. Several field mapping studies of collapse deposits have previously noted that mixed-matrix supported facies were rare in the deposit core, but were more common in marginal regions (Glicken, 1998; Belousov et al., 1999). These studies have highlighted that the centre of deposits and proximal areas consist of larger blocks in block-supported facies.

2.6.2. Evolving degree of strain localisation

The basal sliding surface or shear zone of a mass movement is subjected to extreme shear conditions (Erismann and Abele, 2001). As noted at Loc. 1 there is evidence for intense shearing in the lower 2-3 m of the flow, causing the destruction of large clasts, forming a matrix-dominated, well-sorted granular layer. The presence of a matrix-supported basal layer has previously been observed at other avalanche deposits worldwide, such as at Parinacota (Chile) where structureless sedimentary layers occur at the base of each deposit and are interpreted to originate from the localisation of shear during emplacement (Clavero et al., 2002). Similarly, the small grain sizes in the lower 1 m at the base of multiple debris avalanche deposits from Shiveluch (Kamchatka peninsula, Russia), has also been interpreted as the result of shear localisation at the base of a debris flow (Belousov et al., 1999). Although none are associated with a basal pseudotachylyte, it is an indicator for the common occurrence of basal shear localisation and comminution in volcanic debris avalanches. The extreme localisation to produce frictional melting, as seen at Loc. 1 in this study, is still rarely reported. However, earlier studies on this phenomenon at field sites such as Langtang (Nepal: Masch et al., 1985) and Kofels (Austria; Erismann, 1979) have been joined by more recent studies on Markagunt gravity slide in Utah (Hacker et al., 2014), Heart Mountain in Wyoming (Goren et al., 2010), Mont Dore volcanic massif (France; Bernard and van Wyk de Vries, 2017) and a rockslide near Kanchenjunga (Nepal; Weidinger and Korup, 2009) where further landslide generated pseudotachylytes have been identified.

Observations made in Loc. 2 suggest that basal granular zones may be subjected to a high degree of strain localisation, as observed by an area of pervasive cataclastic shear crosscut by a fault surface, showing slip transfer upon enhanced localisation. Such cross-cutting

behaviour, indicative of an increased degree of strain localisation, was further observed in the intra-body shear zones, suggesting that these switches in the degree of strain localisation may not necessarily be restricted to the basal shear zone, but may affect the development of the avalanche as a whole. This may be likely if shear occurs in an unfavourable region as in cases where a contact is uneven with asperities (see Loc. 2) or if local topography slopes against the deposit flow direction or during acceleration or deceleration phases. Rough surface topology across all scales would locally induce higher normal stresses which would respectively promote higher shear stresses (and intergranular forces) in this region of the flow, as illustrated by a sketch diagram in Figure 2.13. This concentration of stress at the asperities may have promoted the rupture in the granular medium of a new, smoother surface and facilitate flow with lower frictional resistance. This would either act to shift shear to above the asperity (Fig. 2.13c) and/or remove some or all of the basal asperity (Fig. 2.13d), incorporating the fragmented materials in the flow, and promoting shear on a smooth surface as seen at Loc. 2 (Fig. 2.3e-f). Evidence for both mechanisms are seen, first by the generation of secondary slip surfaces and second by incorporation of ignimbrite material into the flow deposit. The Koefels landslide in Austria underwent a similar process but at a larger scale, forming new internal slip surfaces upon encountering a topographic barrier (in this case a valley wall) (Erismann, 1979). This is somewhat similar to the decoupling process in pyroclastic density currents and block-and-ash flows, where the dilute upper portion of the flow can detach from the lower flow and override a topographic barrier and even travel in a different direction to the lower flow (Fisher, 1995; Douillet et al., 2013). Here, the outcrops at Loc. 1 show 2 distinct zones of shear localisation at different levels within the flow body, similar to the suggestion of De Blasio and Elverhøi (2008).

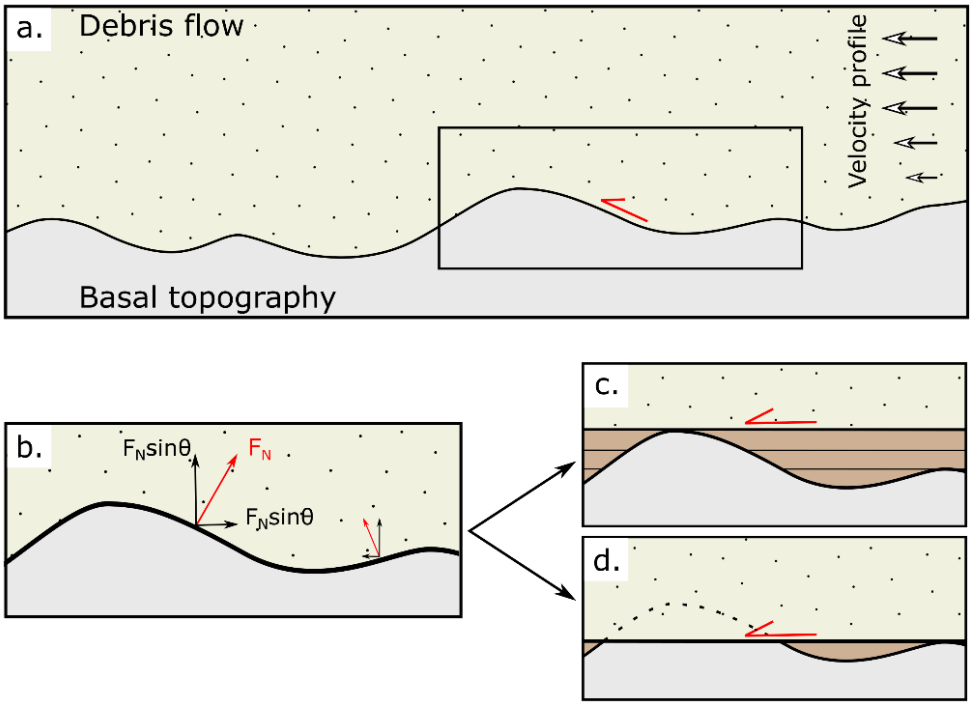

Figure 2.13. Sketch diagrams illustrating successive shear localisation by rupture or asperity ploughing (may occur at a range of scales). a) A rough surface with velocity profile (indicated by arrow size). b) A rough surface influencing normal, compressive force (F_N) induced by topography. c) Scenario 1, faster moving upper flow propagates along a newly formed shear surface. d) Scenario 2, an asperity is removed by fracturing and is incorporated into the flow.

2.6.3. Frictional melting

As pseudotachylytes were not ubiquitous along the basal contact, we advance that the generation of frictional melt at the base of debris avalanches may be considered to be both spatially and temporally discontinuous. The occurrence of a fluidised basal layer with enhanced injection and mixing, seen at Loc. 3 and in other landslides (Anders et al., 2010; Craddock et al., 2012) can prevent the strain localisation necessary for frictional melting. Melt formation in volcanic collapses is highly dependent on the conditions (including normal stress from overburden and pore pressure) (Legros, 2002; Nielsen et al., 2008; Violay et al., 2014), extent and rate of shear localisation (De Blasio and Elverhøi, 2008; Magloughlin and Spray, 1992), heat generation versus diffusion away from slip surface (Carslaw and Jaeger, 1959), any residual heat from volcanism, surface topography and roughness (Nielsen et al., 2010), and the melting points and shear strength of the materials (Spray, 1992), many of which would vary and evolve during transport. This may in part explain the common absence of pseudotachylyte at the basal contacts of debris avalanche deposits worldwide, which may also be a result of alteration or destruction (Kirkpatrick and Rowe, 2013). As modelled in section 5.4, debris avalanches flowing at high rates (along one or several thin shear zones)

may promote shear rates likely to exceed the structural relaxation of frictional melts to induce brittle failure, preventing preservation.

The maximum strain rates that may be accommodated by the thickness of the inhomogeneous melt layer observed indicates that the flow exceeded ~31 m s^{-1} to fragment it. However, the higher modelled viscosity of the preserved layer suggests that it would have fragmented at slip velocities exceeding 9.6 m s^{-1} (at the estimated temperatures). As the layer has remained intact, this suggests that the flow slowed between the fragmentation of the early melt-bearing layer and the formation of the preserved melt-bearing layer. This may also imply that the shear was localised elsewhere, a hypothesis supported by the occurrence of a secondary slip surface above the basal contact at this locality, or the layer preserved in the outcrop was a late stage feature formed as the flow slowed. Thus, slip velocity may dynamically vary during transport, as a function of distance, palaeotopography and strain partitioning onto different fault surfaces; such contrasting slip conditions may promote compressional and extensional regimes in the flow, which could induce secondary shear zones and intrusion of clastic dykes.

Although frictional melts are commonly regarded as potential lubricating layers promoting increased runout distances (Erismann, 1979; De Blasio and Elverhøi, 2008), the rheological comparison of the apparent viscosity to Byerlee (1978) friction indicates that frictional melting is unlikely to have lessened the basal shear resistance at the high shear rates expected; even though the early frictional melt (prior to fragmentation) exhibited a relatively low apparent viscosity. Additionally, variation in melt layer thickness, temperature, and the incorporation of both exsolved and dissolved water from the breakdown of amphiboles could have rheologically impacted the development of frictional melts and promoted lubrication through time. If the formation of pseudotachylyte is a cyclic process in which melting may be followed by fragmentation (if strain rate is too high) and slip re-localisation onto a new fault plane, then the lubricating or viscous braking effects of frictional melts may equally be cyclic. It must be noted that variability in chemistry and, importantly, crystallinity during selective melting and melt homogenisation controls the rheological evolution of frictional melt (Spray, 2010; Wallace et al., 2019a) and whether lubrication or viscous brake locally develops with slip.

2.7. Concluding remarks

The Arequipa volcanic landslide deposit originated from the sector collapse of Pichu Pichu volcano and forms an area of elevated hummocky topography approximately 300 m thick at its maxima, which extends 26 km west from the dissected volcanic complex in a broad, fan-like shape that covers > 100 km^2. The andesitic debris avalanche, which likely exceeded 20 km^3 in volume, ramped up over a palaeotopography of ignimbrite during runout.

The subsequent deposition of eruption products of other proximal volcanoes and the incision of rivers into the deposit obscures the original topography. However, river valleys reveal the basal contact and structures within the lower portion of the flow. Field examination, chemical analyses and microstructural observations highlight the complex nature of shear during the debris avalanche. We observed evidence of a variety of shear deformation mechanisms (cataclasis and frictional melting), degrees of strain localisation, and strain partitioning across the body of the flow (summarised in Fig. 2.14).

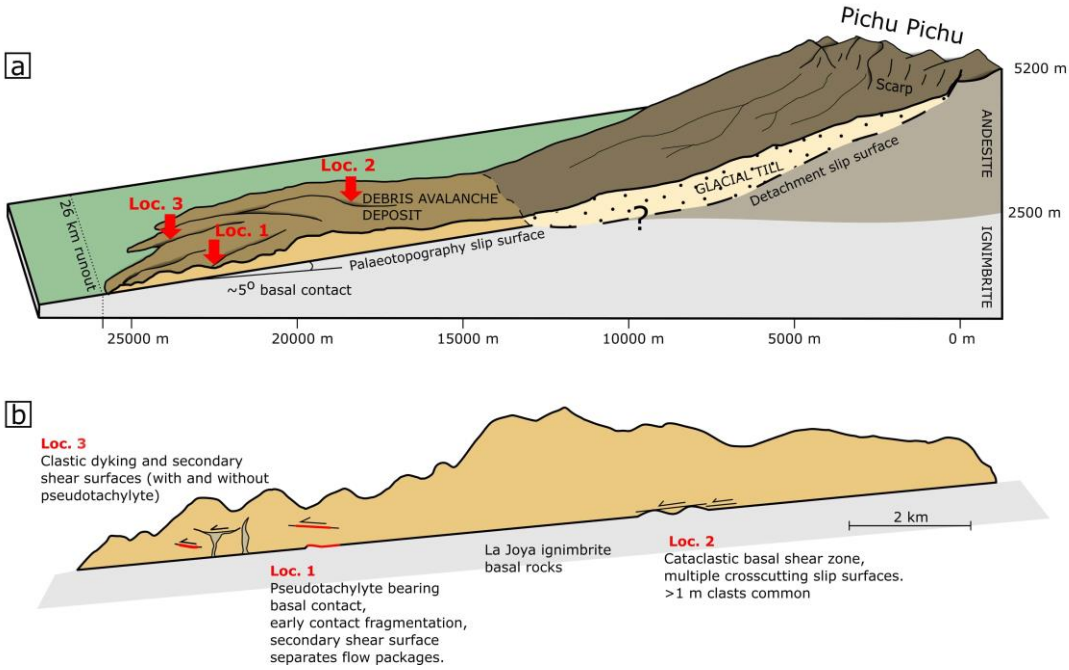

Figure 2.14. Sketches outlining preserved processes in the Pichu Pichu debris avalanche deposit. a) Scaled sketch illustrating deposit, source and studied outcrops in this study. b) Flattened idealised cross section of features of the flow interior (topography scale increased by factor of 2 and features not to scale) summarising the observations of the field study and variation in basal shear zone morphology.

The basal contacts show varying degrees of shear localisation. The first example evidences a high level of shear with near total fragmentation of clasts near the basal contact and extreme localisation of shear to form a thin layer of pseudotachylyte. Fragments of pseudotachylyte

within the cataclasite at the base suggests multiple generations of melt. Geochemical results combined with rheology modelling are used to suggest that the fragmentation of melt layers could be attributed to high strain rates that forced the melt into brittle rupture, thus limiting the chance of a persisting melt layer. Contrastingly, the second locality studied has a more diffuse basal shear zone, less fragmentation of clasts, multiple fracture sets and crosscutting slip surfaces that show slip zone evolution and indicate more distributed shear.

Within the lower portion of the debris avalanche body, at several localities, secondary shear zones are observed in the deposit. This highlights the propensity to delocalise shear from the basal plane to be accommodated on other discrete planes. Additionally, we note the presence of clastic dyking which likely originates from the basal plane and suggests the presence of a pressurised, fluidised layer in some areas that may have been enhanced by crossing of river beds or water saturation of the underlying porous ignimbrite. The interaction of clastic dykes, shear planes and the juxtaposition of distinct flow units suggests that active shearing planes acted as barrier layers limiting material mixing and causing segregation of the flow.

We conclude that shear localisation can occur at both the basal contact and on discrete planes within the flow and that frictional melting at the debris flow base may be possible at areas of extreme localisation of shear. However, it is unlikely that frictional melt aided lubrication at the base or that it persisted throughout the debris avalanche deposition, instead local deformation mechanisms at the flow base likely switched rapidly. The localisation of shear can therefore change both through time and spatially across the flow due to topographic, lithological and environmental changes of the land surface.

Chapter 3: The juxtaposition of lithologies and the role of strength heterogeneities during frictional sliding

Abstract

Faulting in a variety of geological environments causes the juxtaposition of contrasting geomaterials, which would impact frictional sliding. Yet, laboratory experiments traditionally investigate the frictional properties of materials considering single, often homogenous, lithologies. Here we explore the mechanical consequence of slip on single lithology pairs as well as on juxtaposed contrasting lithologies, using dense, crystalline, andesitic lava (11 % porosity) and porous, glassy, rhyolitic ignimbrite (49 % porosity) from the Arequipa volcanic landslide deposit in Southern Peru, to resolve its long (~27 km) runout distance. We experimentally constrain the frictional and broader tribological behaviours of each rock type individually and in mixed lithology pairings, using a rotary shear apparatus, to constrain how their combination may have influenced the basal slip associated with the landslide.

The experiments on single lithology pairs of rhyolitic ignimbrite and andesitic lava returned friction coefficients approximating 0.6-0.8. In the presence of mixed lithologies we observed lower friction coefficients of ~0.45-0.6. This suggests that the juxtaposition of weak and strong lithologies may promote lower frictional coefficients than anticipated from individual lithologies at a range of slip rates in shallow crustal conditions. At fast slip rates (> 1 m s^{-1}), all lithology combinations underwent velocity weakening, and high wear rates from the involvement of weak rock types may limit frictional heating, as the two processes compete. The presence of a weak ignimbrite wall rock enhanced wear and the formation of a thick cataclastic gouge layer. The interaction of strong clasts hosted in the rhyolitic ignimbrite with the slip zone increases shear stress and reverses the rate weakening mechanisms at high slip rates by strengthening the slip surface. Conversely, due to reduced wear rates, localised frictional heating caused by clasts may trigger thermally activated processes. The juxtaposition of rock types and the resultant changes in friction, wear and lubrication mechanisms is therefore vital in understanding the dynamics of fault slip events along contrasting lithologies, including regional faults, volcanic flank collapses and large mass movements. Preferential wear of the weaker ignimbrite, increased by clast ploughing, may have reduced basal friction coefficients and aided the long runout distance of the Arequipa volcanic landslide.

3.1. Introduction

The movement of rock masses along faults is controlled by stress conditions and the frictional properties of the rocks involved (Scholz, 2019). Our understanding of frictional properties has long been based on laboratory experiments exploring the shear resistance and development of shear structures in a wide range of rock types; yet in most, if not all, cases, the experiments are conducted on individual rock types. The juxtaposition of contrasting rock types along faults is common in nature with displacement causing the contact of different lithologies (e.g. Chester and Chester, 1998). During mass movements such as landslide events, volcanic sector collapse and associated debris avalanches (the topic of this study), or caldera collapse, displacements may reach great distances (e.g. Legros et al., 2000; Biek et al., 2019) and the majority of slip may then be accommodated along faults between juxtaposed contrasting rock types (Hughes et al., 2020b).

Volcanic settings are particularly dynamic environments, comprising numerous faults and highly variable materials, that may be particularly prone to the occurrence of faulting along mixed lithologies. Volcanic provinces are formed, in part, from the deposition of eruptive products (coherent lava and variably coherent volcaniclastic rocks) and the intrusion of magma (Elsworth et al., 2007; van Wyk de Vries and Davies, 2015); as such, they are commonly heterogeneous, consisting of different rock types, each of which may display extensive chemical, physical, mineralogical and textural variabilities even within a given unit. The physical and chemical diversity of volcanic rocks would affect the respective mechanical response of each rock involved in faults (Lavallée and Kendrick, 2021 and references therein). In the case of volcanic sector collapse, the resulting debris avalanche may travel over multiple basal units (not necessarily volcanic in origin) if runout is extensive (McGuire, 1996; Legros, 2002; Hacker et al., 2014; van Wyk de Vries and Davies, 2015; Hughes et al., 2020b). In fact, volcanic collapse events may exhibit anomalously long runout distances, suggesting that frictional resistance can be minimal in some instances (Shea and van Wyk de Vries, 2008). In such scenarios, the faults and/or basal decollement may exhibit varying mechanical and frictional properties and behaviours. The differing mechanical properties of the juxtaposed lithologies may critically impact the frictional behaviour and properties of the slip event (e.g. Bullock et al., 2014; Floyd et al., 2016).

3.1.1. The frictional properties of rocks

Tribology, as defined by Boneh and Reches (2018), describes the processes of friction, wear and lubrication of materials, controlled by a number of factors: loading and environmental conditions (normal stress, slip rate, pore fluid and temperature), contact properties

(roughness and the presence of lubricating layers such as gouge or melt) and material properties of the wall rocks (hardness, fracture toughness, composition, mineralogy). All of these factors may interact to influence the overall frictional behaviour of materials.

The frictional properties of geomaterials has been studied extensively using laboratory experiments (e.g. Byerlee, 1978; Marone, 1998; Scholz, 1998), field observation (e.g. Sibson, 1994; Di Toro et al., 2005) and modelling (e.g. Nielsen et al., 2008; Weng and Yang, 2018). Byerlee (1978) compiled experimental laboratory data and found that the shear stress of geomaterials (τ) is linearly proportional to the normal stress (σ_n), such that:

$$\tau = \mu\sigma_n \tag{3.1}$$

where μ is the friction coefficient. The compiled dataset indicated that at low normal stresses (shallow crustal conditions < 200 MPa) the frictional coefficient of most rocks is generally ~0.85, although the data shows large variations (e.g. $0.3 < \mu < 3$ at $\sigma_n = 5$ MPa) and a dependence on surface roughness (Byerlee, 1978; Bowden and Tabor, 2001; Hughes et al., 2020a). This variability reduces at higher normal stresses (deep crustal settings > 200 MPa) as μ values diminishes to ~0.6. Although these relationships hold true for the majority of geomaterials, rocks with high concentrations of clay minerals exhibit lower shear resistance (Collettini et al., 2009, 2019; Ikari et al., 2009). Additionally, time-dependent physico-chemical processes can drastically modify the frictional properties of rocks (Di Toro et al., 2011), both of which point to the potential influence of dissimilar rock types on frictional properties.

In nature, slip conditions are dynamic as the fault properties evolve, which is not explicitly considered in Byerlee's friction relationship. Hence, a rate and state friction constitutive law, which includes consideration of time (for fault healing), slip rate (shown to impact the shear resistance) and displacement (in order to account for the evolution of behaviour with increasing slip distances), are commonly invoked to constrain the evolving frictional properties of materials during slip events (Dieterich, 1979; Ruina, 1983). An increase in slip rate generally results in a reduced shear resistance for most rock types, promoting dynamic friction coefficients, which may be as low as 0.1 (Di Toro et al., 2011). Such low shear resistances have been attributed to a range of processes, including: flash heating (e.g. Rice, 2006); thermal pressurisation of fluids (e.g. Sibson, 1973; Rice, 2006); frictional melting (e.g. Hirose and Shimamoto, 2005; Di Toro et al., 2006); chemical decomposition (e.g. Han et al., 2007); formation of silica gel (caused by water-quartz interaction e.g. Di Toro et al., 2004) and the production of a gouge layer via material abrasion, wear and comminution (e.g.

Matsu'ura et al., 1992; Reches and Lockner, 2010). These processes are by-products of friction, as energy is converted into the development of frictional heat and into the creation of new surfaces via rupture, which are material specific. Typically, experimental studies on the frictional behaviour of rocks are conducted on pairs of samples from a given lithology and on homogeneous material. Despite allowing for reproducible results for the determination of the frictional properties of primary rock type, this does not enable the analysis of, and any inference about, the effects of lithology juxtaposition and the role of heterogeneities on frictional properties, including wear and heat, which has been suggested to impose spatial variations in frictional properties along faults (e.g. Floyd et al., 2016).

3.1.2. Wear

During slip, friction may induce wear and abrasion of materials at different scales - a process controlled by the strength and harness of materials (Spray, 1992, 2010). This is strongly affected by the degree of heterogeneity of the material along a slip surface. At large scale, fault roughness and the presence of asperities controls the distribution and concentration of stress (shear vs normal stresses) and influence the development of wear (Bowden and Tabor, 2001; Brodsky et al., 2016). This also applies to clasts within conglomeratic rocks, or other rock types with clast inclusions such as ignimbrites. In the case of frictional resistance, the rock strength and mineral hardness of asperities will change the imposed resistance to slip, with the occurrence of weak vs strong surface asperities leading to the preferential wear of one lithology over the other. Greater normal stresses increase geometric interaction along rough surfaces across scales by deforming asperities and localising stress which may promote rupture (Bhushan, 1998; Bowden and Tabor, 2001). The coherence (including fracture density as well as the degree of cementation, welding or induration) of materials controls their overall strength (Spray, 2010; Boneh et al., 2013).

At smaller scale, the constituent phases (crystals, glass or clasts) of rocks imparts different fracture toughness controlling wear and the mechanical response during slip (Spray, 1992, 2010). Local variations in weak vs strong phases (or asperities) along a fault plane leads to the preferential wear. In turn, at smaller scale, Hughes et al. (2020a) found that the porosity of the material imposes a key control on wear and thus on the mesoscopic evolution of fault roughness. The porosity of materials affects their strength (Al-Harthi et al., 1999; Heap et al., 2014b; Vasseur et al., 2015; A Bubeck et al., 2017) and imparts an inherent roughness of the contact surface at the scale of the dominant pore size, which modulates the true contact area and concentrates mechanical stresses, wear and frictional heating (e.g. Rapetto et al., 2009; Hughes et al., 2020a). The magnitude of wear has been theoretically investigated and

suggested to be proportional to the products of normal stress and slip distance and inversely proportional to the hardness of the softest component, a relationship commonly referred to as Archard's wear equation (Archard, 1953). However, it does not take into account the variable of slip velocity, which has been shown to be a controlling parameter in wear rates (Hirose et al., 2012; Hughes et al., 2020a) and is especially important when considering high slip rates where rate weakening is apparent.

3.1.3. Frictional heat and melting

The conversion of mechanical work into heat during frictional slip results in frictional heating of the slip interface and surrounding material. This heat is proportional to the rate of frictional heating against the rate of heat dissipation from the slip zone (e.g. Carslaw and Jaeger, 1959). Friction along natural faults is capable of generating heating, resulting in several hundreds of degrees Celsius of temperature increase, which may greatly influence the tribological properties of materials, as temperature impacts all of the rate weakening processes mentioned above (e.g. Spray, 2010). In particular, the heat may be sufficient to cause melting of the rocks along the slip interface, leading to the production of frictional melts which impact the resistance to shear (Hirose and Shimamoto, 2005b; Spray, 2010), and produce pseudotachylytes (features commonly used to infer the occurrence of seismogenic faulting activity; Sibson, 1975). The transience and potential high rate of frictional heating has been shown, not to be an equilibrium process, but to require selective melting of individual minerals (Shimamoto and Lin, 1994; Lin and Shimamoto, 1998; Wallace et al., 2019a). This results in physically and chemically evolving frictional melts (e.g. Wallace et al., 2019a) which impacts their resultant rheology and resistance to shear during slip (Hornby et al., 2015; Jiang et al., 2015; Wallace et al., 2019a; Hughes et al., 2020b). Silicate minerals have different melting temperatures, as such the amount of heat generated and the presence of different constituent minerals impacts the development of frictional melt chemistry and the fraction of restites (remaining unmelted crystals or clasts) in suspension. Both of these parameters control the resultant apparent effective viscosity that defines the shear resistance along a melt-bearing fault (Spray, 1993; Nielsen et al., 2010; Di Toro et al., 2011). Thermo-mechanical feedback during melt generation and evolution, enhanced by the non-Newtonian shear thinning rheology of such melts (Kendrick et al., 2014), determines the slip behaviour (Lin and Shimamoto, 1998; Wallace et al., 2019a), such that melt may either acts as a lubricating layer or as a viscous brake (Fialko and Khazan, 2005). Moreover, as silicate melts are viscoelastic bodies that abide to the glass transition, frictional melts may rupture during shear if the strain rates experienced exceeds the relaxation rate of the melt

structure (Dingwell and Webb, 1989). Frictional melt fragmentation has been demonstrated experimentally (Lavallée et al., 2015b) and evidence of its occurrence in nature is preserved in natural pseudotachylytes at the base of the Arequipa volcanic landslide deposit (Hughes et al., 2020b).

The basal frictional properties of landslides remains relatively unexplored. Wang et al. (2017) used material from the substratum of a landslide during laboratory experiments to assess the frictional properties of the basal shear zone but did not consider the fact that the lithologies along the slip plane are contrasting. This type of experimentation has never been conducted with coherent samples. To address this shortcoming, samples collected from the Arequipa volcanic landslide deposit (Hughes et al., 2020b) were used in the experimental investigation reported here to explore the frictional properties and behaviour of juxtaposed lithologies and evaluate whether contrasting material properties combine to produce low shear resistance favouring long runouts.

3.1.4 The Arequipa volcanic landslide deposit

The Arequipa volcanic landslide deposit covers an area of ~200 km^2 to the east of Arequipa (Peru) and originated from the collapse of the Pichu Pichu andesitic volcanic complex (Fig. 3.1). The runout distance of up to 27 km resulted in the eventual juxtaposition of contrasting lithologies along the basal fault contact. The deposit consists primarily of variably brecciated and coherent andesitic lavas transported and emplaced upon the basin infill of coherent rhyolitic ignimbrites known as the Sillar of Arequipa (Legros et al., 2000; Lebti et al., 2006). The palaeotopography, and thus the basal contact over which the debris avalanche propagated, is uneven and undulates on a scale of 10's of meters. Overall, the paleo-surface angle dips in a westward direction at an estimated average of 5 degrees (Hughes et al., 2020b).

The deposit evidences the partitioning of strain during transport, as shear zones have been identified along its base as well as within the rock mass, some ten of metres above the basal contact (Hughes et al., 2020b). The basal contact, exposed along deep river canyons that developed across the deposit, exhibits a spectrum of shear textures (Hughes et al., 2020b). In one instance, the basal shear zone consists of a narrow 1–2 cm thick layer of ultracataclasite and pseudotachylyte (Legros et al., 2000), containing fragments of a less evolved pseudotachylyte (See Fig. 3.1d). In other instances, the basal contact exhibits a shear zone, with variable width (< 40 cm wide) overprinted by, or laterally evolving into sub-parallel faults that would have localised strain (See Fig. 3.1e).

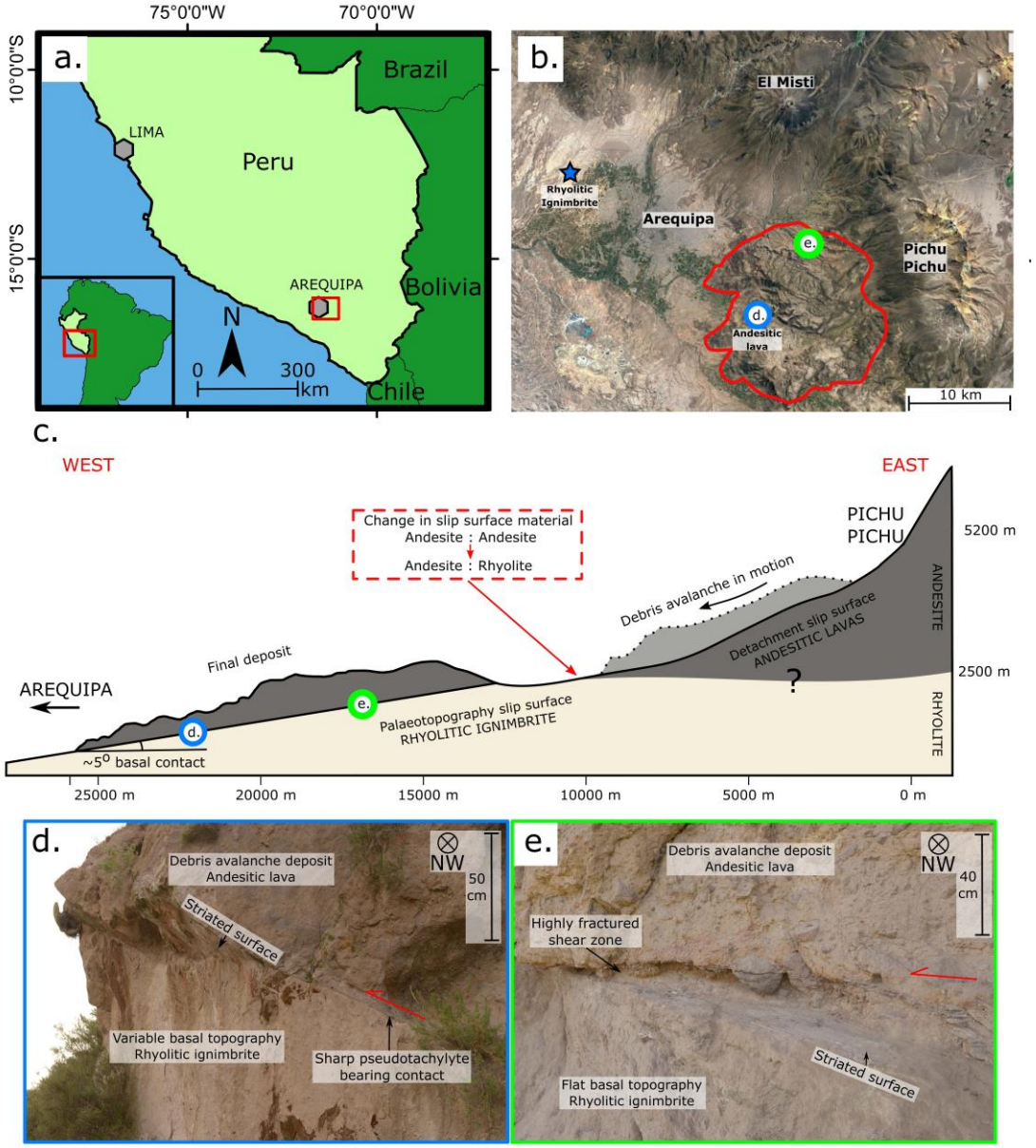

Figure 3.1. Locality map, idealised cross section and field photos of the studied Arequipa volcanic landslide deposit a) Map of southern Peru with inset of South America. b) Satellite image of Arequipa, Pichu Pichu, the debris avalanche deposit (red outline) and positions of ignimbrite sampling site, and 2 example localites two field localities (studied in Hughes et al. 2020) marked as (d) and (e). c) Idealised cross-sectional sketch of the Arequipa volcanic landslide deposit, originating from sector collapse of andesitic Pichu Pichu volcanic complex, and the basal ignimbritic substratum. The basal contact shows the juxtaposition of andesitic lavas against the rhyolitic ignimbrite with positions of (d) and (e). d) Basal contact showing the presence of pseudotachylyte in the shear zone, where it ramps up over a paleotopographic high. The deposit also reveals striations on the underlying surface of the andesitic lava debris avalanche deposit (located at 16°28'00"S 71°26'30"W). e) Flat, sub-horizontal, basal

contact exhibiting a diffuse shear zone (~40 cm thick), cross cut by a late fault, showing striation on the surface of the underlying rhyolitic ignimbrite (located at 16°25'15"S 71°24'07"W).

These basal contacts evidence the importance of contrasting lithology juxtapositions on fault processes. The chemical signature of the pseudotachylyte indicated localised melting and mixing of andesitic lava material from the debris avalanche with the underlying rhyolitic ignimbrite (Hughes et al., 2020b). Rheological analysis of the melt layer concluded that the melt would have acted as a viscous brake, owing to the bulk chemistry of each of the end-member components (Hughes et al., 2020b). Similarly, the basal shear contacts not hosting pseudotachylytes, show the importance and relative preference of wear of contrasting adjacent lithologies, which influences the degree of strain localisation. The spatial and inferred temporal evolution of basal shear processes during the Arequipa volcanic landside (Legros et al., 2000; Hughes et al., 2020b) point to the role of highly variable material properties in either localising or dissipating strain during mass movements.

3.2. Materials and methods

3.2.1. Materials

Samples were collected from the Arequipa volcanic landslide deposit to the east of Arequipa (Peru) (Fig. 3.1) (Legros et al., 2000; Hughes et al., 2020b) during a field campaign in 2017. The andesitic lava blocks were sampled from the basal section of the landslide, 24 km from the source volcano of Pichu Pichu. Samples were selected 22 m above the primary, basal shear zone to obtain coherent blocks with minimal fracture damage accumulated in shear zones during transport (Fig. 3.1d; see position in Fig 3.1b and description of Loc. 1 in Hughes et al., 2020b, 16°28'00"S 71°26'30"W). The andesitic lava block used in this study was previously described in Hughes et al. (2020b) including geochemical analysis and physical characterisation. The andesite is porphyritic, consisting of phenocrysts of plagioclase (up to 2 mm in size) and sometimes amphibole (up to 1 mm in size) and occasional pyroxene, as well as occasional glomerocrysts, in a groundmass rich in plagioclase microlites (Fig 3.2a & c; (Hughes et al., 2020b). The andesite exhibits a porosity of 7 to 12%, consisting of vesicles and microcracks.

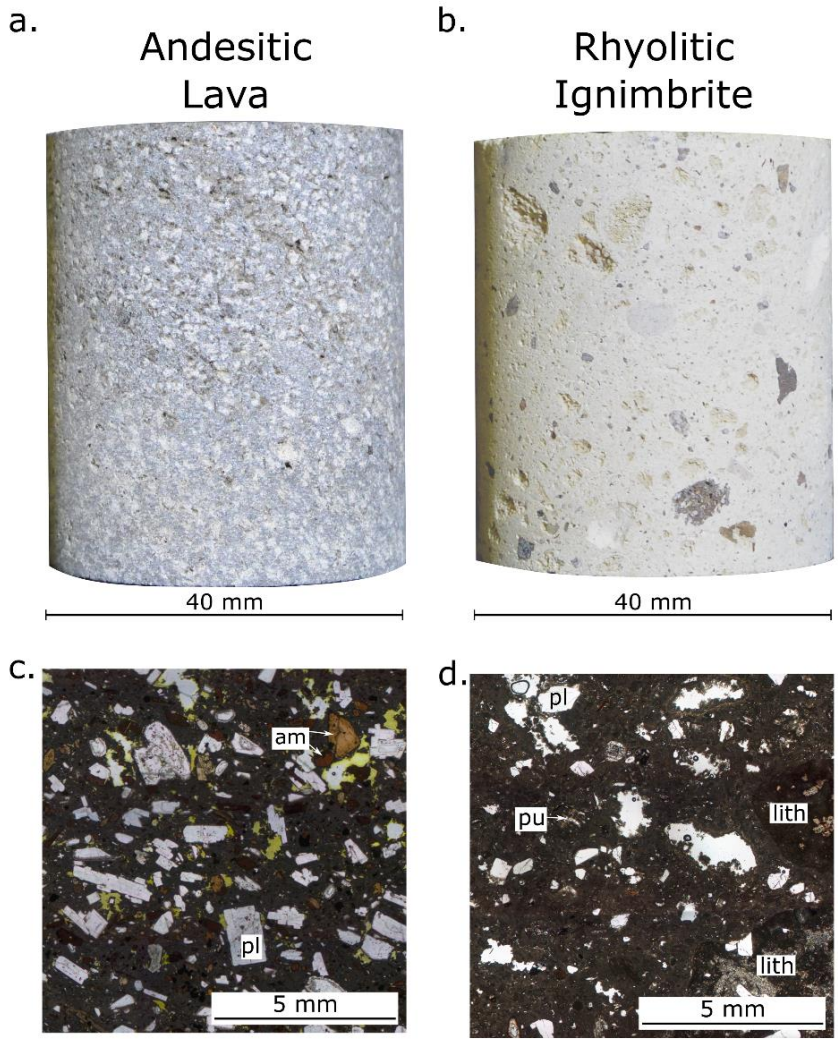

Figure 3.2. Pre-experimental textures of the two lithologies used in this study. Photos of experimental cores of a) andesitic lava and b) rhyolitic ignimbrite accompanied by photomicrographs taken in plane polarised light of c) the andesitic lava and d) the rhyolitic ignimbrite. Pl = plagioclase, am = amphibole, pu = pumice clast, lith = lithic clast.

The La Joya Ignimbrite (LJI) consists a series of variably welded lapilli tuffs containing crystals of quartz and sandine. The rhyolitic ignimbrite exposed beneath the landslide deposit (Fig. 3.1d & e; Lebti et al., 2006; Hughes et al., 2020b) was highly fractured and hydrothermally altered; moreover it is exposed by fluvial erosions and is subjected to seasonal submersion. The unit no longer has the attributes (e.g. coherence) that it would have had at the time of the landslide. In many areas the ignimbrite is draped with geomorphological phenomena such as lahar deposits (Hughes et al., 2020b). As the collection of pristine, coherent, unfractured, La Joya Ignimbrite was not possible for this experimental study, we referred to the work of Lebti et al. (2006) to source rocks with similar physico-chemical properties. The

nearby, younger Arequipa Airport Ignimbrite (AAI), specifically the older “white unit”, was selected as an alternative material as it is similar to the La Joya ignimbrite (i.e., the facies observed directly below the deposit) and it has been inferred to extend and directly underlie the distal north-western portion of the landslide deposit (Lebti et al. 2006).

The Arequipa Airport Ignimbrite (AAI) is formed of 2 distinct units: the lower “white” and upper “pink” units. The lower white unit, from which the material in this study was sampled, is a massive, indurated ash and lapilli tuff with similar mineral abundances to the La Joya Ignimbrite, but with less quartz and sandine free crystals (Lebti et al., 2006). Induration of the AAI occurred following the percolation of hot gas and vapour-phase crystallisation during the cooling of the deposit (Streck and Grunder, 1995; Lebti et al., 2006). [We refer the reader to Lebti et al. (2006) for an extensive comparison of the two ignimbrites.] The welding rank of the AAI white unit matches that of the medial and distal non-welded facies of the LJI, making this a suitable replacement for the LJI in this study.

The Arequipa Airport Ignimbrite is commonly used as building material in the Arequipa region and is readily available. For this study, large blocks of AAI (white unit) were sourced from a quarry (i.e., Canteras de Sillar) in Añashuayco, in the Cerro Colorado district, 2.5 km southwest from Rodríguez Ballón International Airport and northwest of the city of Arequipa (16º21’34”S 71º36’30”W; see Fig. 3.1b for location). The block used in this study is a massive, (devitrified) ash-rich ignimbrite containing 10 % undeformed pumice clasts (1-60 mm in size) and 15 % dense lithics (1-100 mm in size), its porosity ranges between 44 and 54 %, which confirms the rank of welding (rank II) of the selected samples, rather than the higher welding (rank III) that can also be observed in stratigraphically lower exposures within the AAI. The ignimbrite contains free crystals of plagioclase (up to 1.5 mm in size) predominantly, with occasional biotite (< 1 mm, Fig. 3.2b & d).

3.2.2. Methods

In this study, we conducted rotary shear experiments on the primary lithologies of The Arequipa volcanic landslide deposit. For this purpose, the collected rock samples were cored to produce cylindrical specimens with 40.0 mm diameter. In the case of the rhyolitic ignimbrite, which is heterogeneous and contains large clasts, any core with pumice or lithic clasts larger than 2 cm diameter were discarded for the experiments. The remaining samples were ground parallel to lengths between 30 and 48 mm. Finally, the centre of the cylindrical specimens were cored out to produce hollow cylinders with an inner diameter of 18.5 mm. Here, the smaller, central cores were used for porosity analysis, whilst the larger hollow cores were used for the rotary shear experiments.

3.2.2.1. Porosity

The smaller cores were used to determine the porosity of the materials. These porosities were determined by calculating the samples' bulk density (ρ_s):

$$\rho_s = \frac{m}{\pi r^2 h} \tag{3.2}$$

where h is sample height (in m), r is radius (in m) and m is the mass (in kg) for each core. Using an AccuPyc II 1340 helium pycnometer from Micromeritics, the solid phase density (ρ_0) of the samples was quantified by determining the sample skeletal volume (i.e., the solid phase fraction inaccessible by helium during pycnometric measurements) and its mass; the ratio of which was used as the solid phase density (ρ_0), assuming that no pores were isolated to helium during measurements. The fraction of connected porosity (ϕ) was estimated using:

$$\varphi = 1 - \frac{\rho_s}{\rho_0} \tag{3.3}$$

3.2.2.2. Rotary shear tests

To investigate the frictional behaviour of the rhyolitic ignimbrite and andesite lava samples under a range of conditions, direct shear experiments were performed using a (2nd generation) low- to high-velocity rotary shear apparatus at the University of Liverpool. The apparatus was manufactured by Marui instruments following the revised design of Prof. T. Shimamoto; the 1st generation apparatus was described in Shimamoto (1994) and Hirose and Shimamoto (2005b). The second generation uses the same principle but was developed to stand upright to improve stress distribution and alignment of the rotating axial column. The apparatus is capable of imposing variable rotational speeds (1 rotation per year to 1500 rotations per minute), allowing for the study of friction at a wide range of slip rates. The normal force (axial load) is applied by the lower loading column using a gas actuator and can reach 10 kN. The use of hollow cylindrical samples (created with a 40.0 mm outer diameter and an 18.5 mm inner diameter) minimises the slip rate gradient along the samples' contact, thus creating a 21.5 mm wide annular slip surface in this sample set up, with a surface area of 987.83 mm^2 (9.88 cm^2).

The rotary shear tests were conducted on pairs of hollow cylindrical samples from a given lithology (andesite-andesite and ignimbrite-ignimbrite) as well as from mixed lithologies (andesite-ignimbrite). Frictional and wear behaviour was tested at four normal stresses of 0.25, 0.5, 1 and 3 MPa (corresponding to axial loads of 0.25, 0.5, 1.0, 3.0 kN), following the experimental procedure described in Hughes et al. (2020a). Shear was applied by spinning

one sample axially against the other and controlling the rotation rate. Due to the variation in angular velocity across the slip surface created, the equivalent slip rate (V) was determined after Hirose and Shimamoto (2005):

$$V = \frac{4\pi R\,(r_1^2 + r_1 r_2 + r_2^2)}{3(r_1 + r_2)} \tag{3.4}$$

assuming constant shear across the slip surface, where R is the revolution rate, r_1 is the outer radius and r_2 is the inner radius. Slip rates of 0.01, 0.05, 0.1, 0.2, 0.3, 0.5, 1, 1.7 and 2.4 m s^{-1} were applied, targeting total slip distances of 10 m for slow slip rate tests (< 0.2 m s^{-1}) and 20 m for tests high slip rate tests, to ensure stabilisation of the shear response at contrasting rates. The torque, applied axial loads and number of rotations were monitored continuously. The cumulative slip distance was calculated using the product of the equivalent slip rate (V) and the slip duration, and the shear stress was calculated from torque following Hirose and Shimamoto (2005). During the test, the wear was constrained by analysing the sample shortening due to material removal along the slip plane by a linear variable differential transformer (LVDT) attached to the lower column.

The friction coefficient (μ) was calculated for each test from the ratio between the steady state shear stress (τ_{ss} in MPa) and the average normal stress (σ_n in MPa):

$$\mu = \frac{\tau}{\sigma_n} \tag{3.5}$$

The work per unit area was constrained to evaluate the evolution of wear. The work per unit area (W in MJ m^{-2}) was obtained by integrating the experimentally generated shear stress as a function of displacement along the slip surface (after Abercrombie and Rice, 2005; Di Toro et al., 2012; Kanamori and Rivera, 2013). To enable a comparison of the obtained work per unit area between experiments conducted at different slip rates, the total work per unit area during steady state was divided by the length of displacement during steady state (D_{ss} in m) to quantify the work per metre slip during the steady state period (W_M in MJ m^{-2} m^{-1}). D_{ss} is also where wear rates were calculated from so the values are comparable (For all values see Table. 1 in Appendix II, Table A.II.1).

The mean power density per unit area (P_D in MW m^{-2}) was calculated from the equivalent slip velocity (V) and the shear stress (τ_{ss}) during the period of steady state sliding (D_{ss}) to describe energy dissipation rate at the slip surface, via:

$$P_D = V\tau_{ss} \tag{3.6}$$

3.2.2.3. Thermographic monitoring

The experiments were recorded using a FLIR X600sc thermographic camera at 5 Hz for tests with slip velocity 0.01-0.5 m s^{-1} and 15 Hz for high velocity tests with slip velocity > 1 m s^{-1}. For all experiments the camera was placed at a distance of 70 cm from the sample set-up in order to monitor the surface temperature of the samples. The FLIR X600sc thermographic camera requires selection of a calibrated temperature range prior to recording; for this camera, the range options are 20-300 °C and 300-1500 °C. As we were anticipating that the temperature of the sample would generally remain below 300 °C, the lower calibrated temperature range was selected. In exceptional cases in which the samples unexpectedly heated beyond this value, the temperature data is inaccurate. All data was analysed with the FLIR IR Max software. The temperature is plotted with displacement using the pixel with the greatest temperature value at the slip surface for each frame of the thermal data.

3.2.2.4. Microstructural analysis

Thin sections were prepared perpendicular to the slip surface after testing. These samples were selected to illustrate differences in the damage zones created during shear of similar (andesite-andesite and ignimbrite-ignimbrite) and dissimilar (andesite-ignimbrite) lithologies as a function of applied normal stresses and slip rates. It was not possible however, to select samples from experiments with comparable displacements as experiments involving rhyolitic ignimbrite samples were often subjected to shorter displacements due to large wear rates or sample failure. Additionally, some experiments on pairs of andesitic lava samples were occasionally run for longer than the targeted displacement of 20 m at greater slip rates, to allow for stabilisation of shear stress after the formation of melt layers. Samples were impregnated in resin prior to cutting to attempt to preserve the fragile structures on the slip surfaces (especially in the weaker rhyolitic ignimbrite samples).

Thin section scans of the experimental material prior to testing (both the andesitic lava and rhyolitic ignimbrite) were obtained by a Leica DM2500P microscope using plane polarised light and a Leica DFC295 camera with pixel resolution of 5 x 5 µm. Images of post-experiment

slip surfaces were taken using a 12 megapixel, 26 mm, f/1.8 smartphone camera mounted to a Kyowa Tokyo monocular microscope.

3.3. Results

86 tests were undertaken in this study: 30 were conducted on pairs of andesite cores, 24 on pairs of ignimbrite cores, and 32 on mixed pairs of andesitic lava and rhyolitic ignimbrite. Tests conducted at the majority of loads and slip rates resulted in the wear and expulsion of gouge from the rock-rock interface; the detail of the monitored data is described below. Tests conducted on pairs of andesite cores at the highest slip rates and loads (> 1.7 m s^{-1} at 0.25 MPa, > 0.5 m s^{-1} at 1 MPa and > 0.3 m s^{-1} at 3MPa) initiated with wear of rocks and the expulsion of gouge, and eventually resulted in melting of rocks along the slip plane.

Slip initiation at the start of experiments is always associated with an instantaneous increase in shear stress (Fig. 3.3a). Upon further slip ($\lesssim$2 m), the shear stress then often reduces to a lower value, achieving a steady state. Simultaneously, wear and ejection of gouge from the slip surface resulted in sample shortening. All samples underwent pronounced shortening, and thus wear, upon initiation of slip, reducing to a lower rate as shear achieved steady state (Fig. 3.3a). Slip was accompanied by a nonlinear increase in temperature of the sample along the slip plane; the temperature increase tended to be greatest during the initial portion of slip, before establishing a maximum temperature upon extensive displacement (Fig 3.3a; For all mechanical and thermal data profiles see Appendix II, Figures A.II.1 – A.II.8). In the steady state regime, momentary jolts were occasionally observed in the monitored shear stress data (see Appendix II, Figures A.II.1 – A.II.8) These were commonly associated with simultaneous variations in wear rate and local temperature fluctuations along the slip plane.

The rotary shear experiments conducted on the three lithology pairings resulted in contrasting observations. Below we analyse these differences in terms of (3.1) frictional properties, (3.2) wear characteristics, (3.3) frictional heating (including a description of frictional melt-bearing fault slip), and (3.4) resultant microstructures considering the effects of applied normal stress and slip rate (See Appendix II, Table A.II.1).

3.3.1. Frictional properties

The rotary shear tests were conducted by controlling the slip rate and the normal stress acting on the slip plane, as such the resultant shear stress monitored is evaluated here to describe the frictional properties of rock pairs and constrain their frictional coefficient. To compare the influence of normal stress and slip rates, the obtained shear stress at steady state (τ_{ss}) is plotted against normal stress (Fig. 3.3b-d). The data show an increase in shear

resistance with normal stress for all lithology combinations tested. At the lowest normal stress (0.25 MPa), mixed lithology samples show lowest levels of variability in shear stress compared to single lithology samples. This variability increases with both normal stress and slip velocity for all tests that include the ignimbrite (as single or mixed lithology). For all mechanical and thermal data profiles see Appendix II, Figures A.II.1 – A.II.8). Experiments on single-lithology pairs of rhyolitic ignimbrite or andesitic lava show similar rates of increase of shear stress with normal stress (Fig. 3.3b-c), whereas tests on mixed lithology show a comparatively lower shear stress for a given normal stress (Fig. 3.3d) - values commonly lower than those suggested by Byerlee's friction relationship. Notably, the shear resistances of tests on andesitic lava that underwent frictional melting clearly exceeded that obtained when the andesite-andesite contact remained solid at the same normal stress (Fig. 3.3c).

To assess controls on frictional properties, we quantified the frictional coefficient as the gradient in shear to normal stress plotted in Figure 3b-c. and evaluated its dependence on slip rate (Fig. 4). [Note that experiments which resulted in frictional melting are not considered in this analysis.] Figure 4 shows that the friction coefficients resulting from tests on mixed lithology (μ = 0.45-0.6) tend to be lower than those obtained on single-lithology pairs (μ = 0.6-0.8). The friction coefficients appear to exhibit slight velocity strengthening at slow slip rates (< 0.01-0.3 m s^{-1}), although some non-systematic variability in the data due to heterogeneity prevents a more robust claim (see Appendix II, Figures A.II.1 – A.II.8). The rate of this transition in regime varies for each lithology combination.

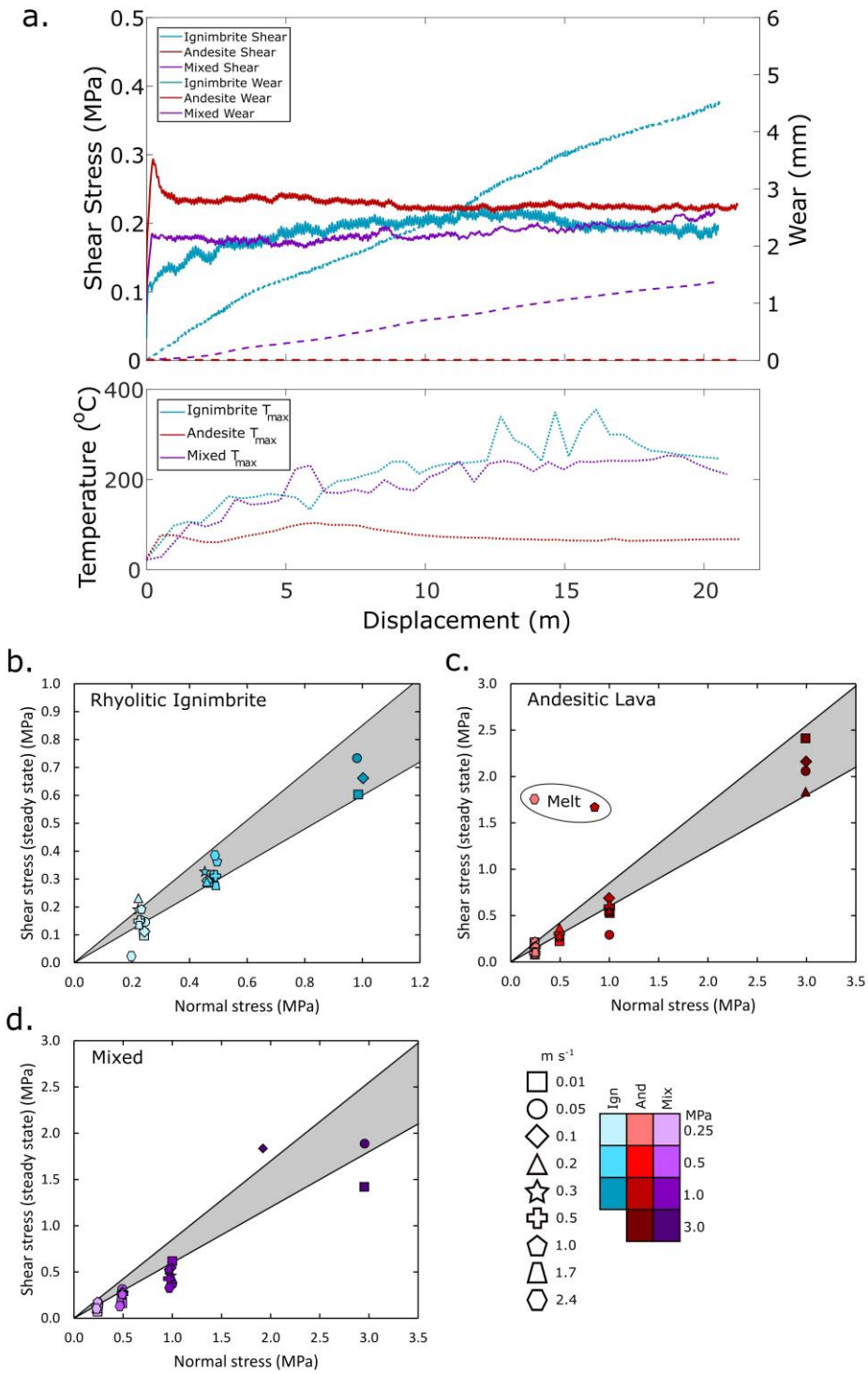

Figure 3.3. Mechanical data for the three lithology combinations. a) Example of shear stress, shortening (wear) and temperature evolution for shear experiments at 1 m s^{-1} and 0.25 MPa for all three lithology combinations tested (rhyolitic ignimbrite (blue), andesitic lava (red) and mixed lithology (purple)). T_{max} is the maximum temperature measured from the samples' outer slip surface at each thermographic image captured by the thermographic camera. Note the large initial peak in shear stress for tests on andesitic lava before attaining steady state values. b-d) Average steady state shear stress (τ_{ss}) plotted against normal stress for tests on pairs of b) rhyolitic ignimbrite, c) andesitic.

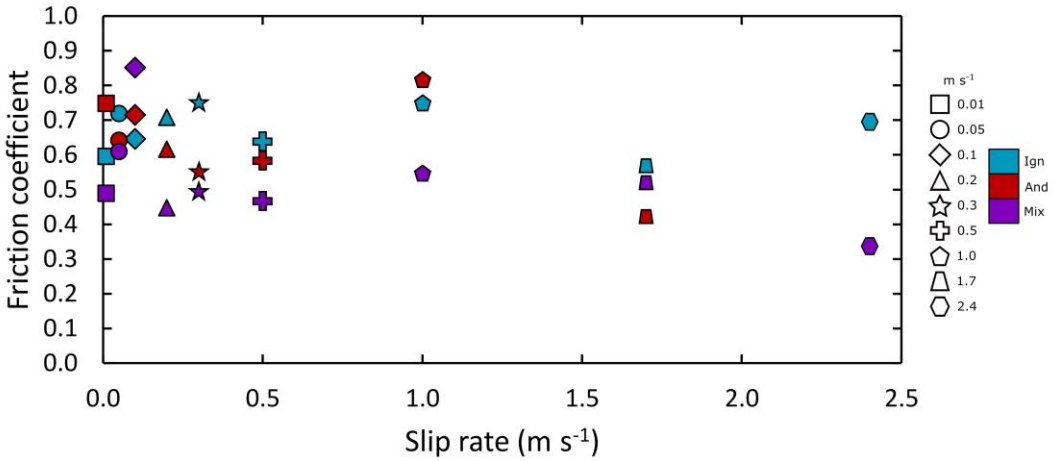

Figure 3.4. Friction coefficient for the three lithology combinations at every slip rate tested. The friction coefficient was calculated from the slope of the normal-shear stress relationship in Figures 3.3b-d. The colour denotes the lithology combination and the shape the slip rate. Note that friction coefficient is variable at low slip rates, but all lithology combinations exhibit rate weakening behaviour at slip rates greater than 1 m s^{-1}.

Though behaviour is complex at low slip rates (< 1 m s^{-1}) at higher slip rates there is a general weakening trend for experiments controlled by frictional sliding. However, there are fewer datapoints used for determining friction coefficient values for the andesitic lava due to onset of frictional melting. The lowest friction coefficient for andesitic lava of 0.42 occurs at 1.7 m s^{-1} (highest slip rate without melting). Mixed lithology also reduces to the lowest friction coefficient value of 0.34 at 2.4 m s^{-1}. For the fastest slip rate tested, 2.4 m s^{-1}, the rhyolitic ignimbrite exhibits a higher frictional coefficient than expected (higher than at 1.7 m s^{-1}), yet this is due to this value only representing two experiments at low normal stress (0.25 MPa and 0.5 MPa) because the samples could not sustain slip at higher loads at this velocity. Such results highlight the importance of taking a combined approach to exploring the frictional response of the heterogeneous ignimbrite: by analysing the mechanical data, wear rate and visual recordings from these 2 experiments, the differences at the 2 normal stresses can be determined. If friction is plotted separately for these 2 experiments (using the steady state shear value and normal stresses plotted in Figure 3.3. for each experiment (see also Appendix II, Table A.II.1) 0.25 MPa yields a friction coefficient of 0.12 and the test at 0.5 MPa has a friction coefficient of 0.79. At 0.25 MPa there is equal shortening of both samples, however at 0.5 MPa one sample resists wear resulting in one sided wear of the interface until the failure of one of the samples, suggesting that the sample was only precariously surviving the applied conditions. Hence, the value for 0.25 MPa where no variation in wear

rate and shear stress caused by sample heterogeneity, plots in a position that follows the previous velocity weakening behaviour expected at this high slip rate (2.4 m s^{-1}). This example shows the bias caused by inclusion of the result obtained at 0.5 MPa and 2.4 m s^{-1} in which the sample was visibly unable to sustain slip without breaking apart, despite appearing to depict a steady shear stress response.

3.3.2. Wear characteristics

All frictional tests resulted in wear along the sample interface. For the experiments involving the dense andesitic lava (whether in a mixed or single lithology pairs), the wear is greatest upon initiation of slip, then reduces to a lower value, as shear reached steady state (Fig. 3.3a). This behaviour is also observed in some rhyolitic ignimbrite pair experiments (< 0.2 m s^{-1} at 0.25 MPa) but differs at greater slip rates and normal stresses. In these cases, the initial high wear rate is maintained or continues to increase throughout the test. Many tests were stopped after 10 mm of shortening (beyond the measuring capability of the LVDT or due to failure of one or both core(s)). During slip, we observed variations in wear simultaneous with the jolts in shear stress. Occasionally, the wear slowed and plateaued, especially in mixed lithology tests.

To quantitively compare the impact of lithology on wear, we divided the total wear by the slip distance over the period of steady state (D_{ss}; previously used to define the shear stress at steady state). Below we detail the influence of lithologies, slip rate and normal stress on wear rate.

Generally, friction of the rhyolitic ignimbrite sample pairs displays the greatest wear rates followed by mixed lithology and then the dense andesitic lava samples for a given condition (Fig. 3.5), this was due to preferential wear of the porous ignimbrite, and contrastingly little wear of the dense lavas. The common rupture of ignimbrites at high loads resulted in an incomplete dataset for our comparison (e.g. only the dense lavas survived experiments at > 0.1 m s^{-1} at 1 MPa and at 3 MPa), making certain distinctions difficult. During tests, intense gouge expulsion, ruptures and plucking of clasts were observed to promote fluctuations in wear and occasionally, premature failure of the rhyolitic ignimbrite samples (especially at high applied normal stresses) preventing data comparison with other sample pairs at the same conditions.

For tests on mixed lithology, increased visible damage of the andesitic lava is associated with tests where clasts in the rhyolitic ignimbrite interacted with the slip zone for a significant displacement during sliding. The wear rate of rhyolitic ignimbrite pairs was not simply twice

that of mixed ignimbrite-andesite pairs which may be expected if the ignimbrite wear remained the same and the dense lava underwent no wear at the same parameters. At low slip rates and normal stresses, mixed lithology wear rates are more closely comparable to that of the wear rates of andesitic lava tests. At 0.25 MPa and < 0.5 m s^{-1}, the wear recorded is only slightly higher than that of andesitic lava tests. At 1-1.7 m s^{-1} the wear approximates half of the wear of rhyolitic ignimbrite and at 2.4 m s^{-1} rhyolitic ignimbrite lithology samples underwent near instantaneous failure. The mixed lithology wear rates throughout the experiments were complicated by the interaction of clasts with the slip zone, leading to a halting in wear followed by an abrupt acceleration to a wear rate similar to that observed for the 1 and 1.7 m s^{-1} tests after clast ejection. This is observed at a range of parameters and even multiple times in single experiments. At greater normal stresses (> 0.5 MPa), earlier failure of the rhyolitic ignimbrite samples both in ignimbrite only experiments and in the mixed lithology tests make patterns harder to discern. For mixed lithology tests at 0.5 MPa there is a sudden increase in wear rates between 1-1.7 m s^{-1} (from 0.02 to 0.14 mm m^{-1}) and at 1 MPa wear increases between 0.2-0.3 m s^{-1} (from 0.04 to 2.23 mm m^{-1}).

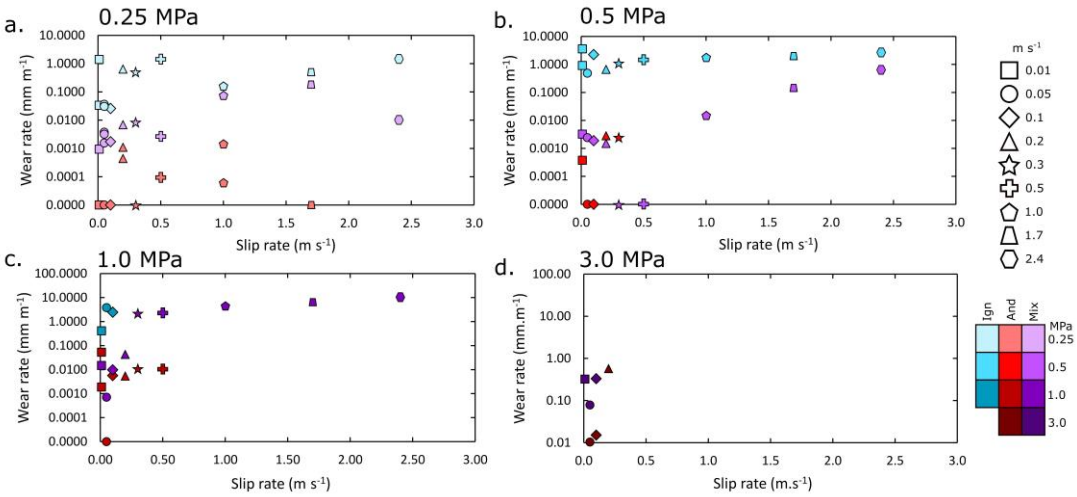

Figure 3.5. Steady state wear rate (i.e., mm of wear per meter of lateral slip) as a function of slip rate for each lithology combination at a) 0.25 MPa, b) 0.5 MPa, c) 1 MPa, and d) 3 MPa. The wear rates generally increase with applied load and are highest for the rhyolitic ignimbrite, followed by the mixed lithology and the andesitic lava. The rhyolitic ignimbrite was not tested at slip rates faster than 0.1 m s^{-1} at 1 MPa or any tests at 3 MPa as they underwent failure. With increasing slip rate, the wear rates during tests on mixed lithology tend to evolve towards values obtained on pairs of rhyolitic ignimbrite cores.

The wear rate generally increases with applied normal stress, for a given lithology pair and slip rate, but only slightly in the range of conditions tested here. Andesitic lava maintains near-negligible wear rates until high normal stresses (3 MPa) where wear rate increases to 0.57 mm m^{-1} (Fig. 3.5d). There is a more evident correlation of wear rate with slip rate. Generally, at slip rates greater than 0.5 m s^{-1}, wear rates increase with slip rates for all normal stresses applied, for all lithologies tested (Fig. 3.5). Below 0.5 m s^{-1} the data is more variable and wear rates are often negligible for tests on andesitic lava sample pairs. Only at slip rates greater than 0.2 m s^{-1} at 3 MPa does the wear rate become greater than 0.05 mm m^{-1}, a value exceeded by all experiments involving rhyolitic ignimbrite (as single- or mixed-lithology pairs) with slip rates > 0.2 m s^{-1} at the full range of normal stresses tested.

To further evaluate wear rate, we compare it to the associated friction coefficient, to the work per metre slip (W_M) and to the power density (P_D) (Fig. 3.6). This is done as the friction coefficient is a fundamental rock property, whilst W_M and P_D are both measures of energy at the slip surface for unit displacement and time, respectively. There is variability in the relationship between the wear rate and friction coefficient (Fig. 3.6a). In general, at low normal stresses (0.25 and 0.5 MPa), the rhyolitic ignimbrites undergo greater wear rates (0.03-3.7 mm m^{-1}) and have higher friction coefficients than the mixed lithology tests, with wear rates of 0.01-0.2 mm m^{-1}. Tests on mixed lithology at high slip rates and 1 MPa reaches the maximum wear rates of all experiments of 6 mm m^{-1} (equivalent tests on ignimbrite underwent failure). Experiments on dense andesitic lava sample pairs exhibit negligible wear at low normal stresses (0.25 and 0.5 MPa) despite a range of friction coefficients. Only at higher applied normal stresses does measurable wear rates in andesitic lava tests occur. The lower slip rates produce the lowest frictional coefficients and wear rates during tests on rhyolitic ignimbrite and mixed lithology. For higher slip rates, mixed lithology tests also have relatively low frictional coefficients but greater wear rates comparable to the rhyolitic ignimbrite values (accounting for complications arising from clast interaction).

Comparing wear rate and the work per meter slip (Fig. 3.6b), which gives an indication of the energy consumed by frictional sliding for each metre of slip during the steady state conditions, we observed more systematic relationships than for wear rate and friction coefficient (Fig. 3.6b). The range of work rates is similar for all lithologies however, the corresponding wear rates are dependent on lithology type and normal stress. Generally, the wear rate is higher for experiments involving rhyolitic ignimbrite at a given W_M. The correlation between wear rate and work rate per metre slip is the weakest for tests on mixed

lithology. At high normal stress (3 MPa) we observe a much higher work rate (Fig. 3.6b) for both mixed and andesite lava pairs.

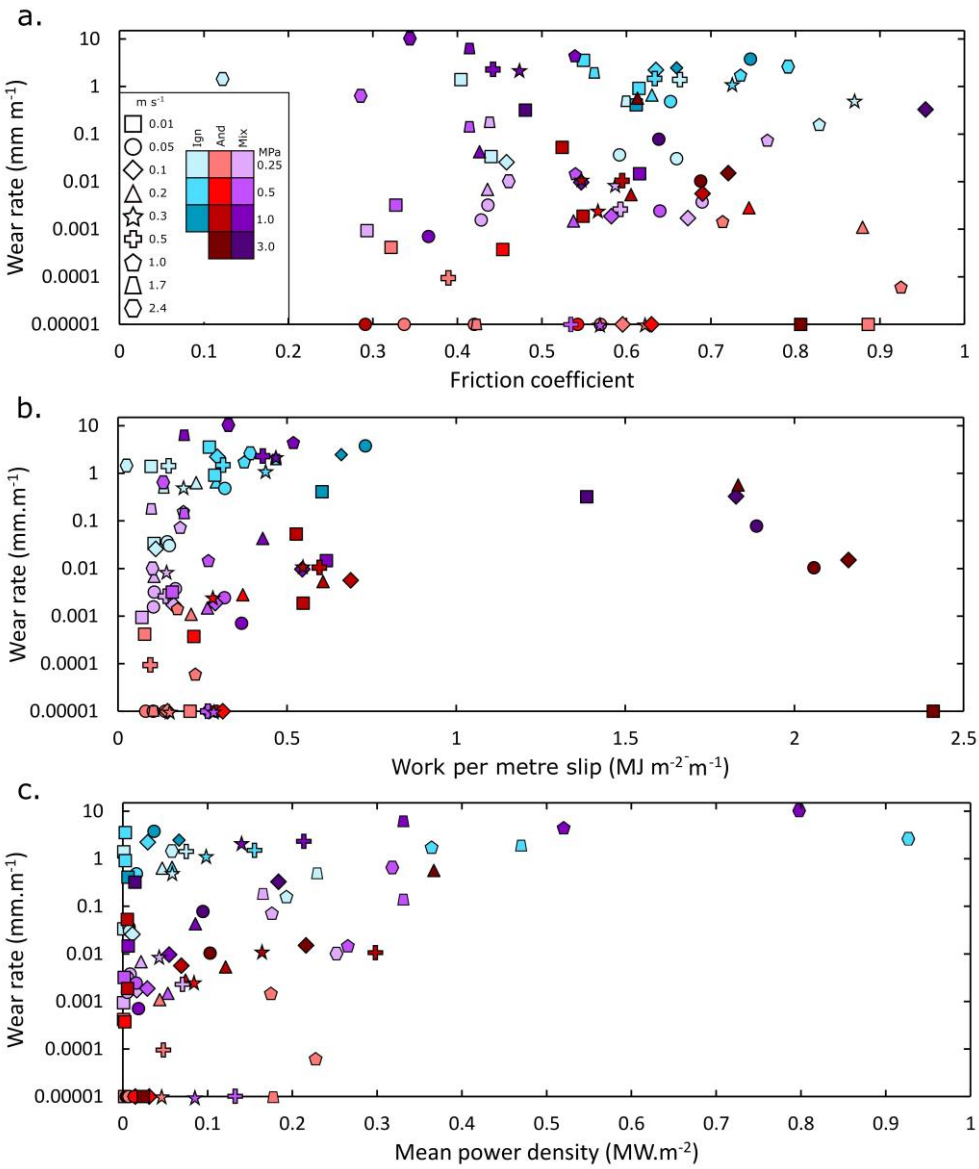

Figure 3.6. Dynamic controls on wear rate. Steady state wear rate (mm of wear per meter of lateral slip) as a function of a) friction coefficient, b) work per metre slip, and c) Mean power density. a) Wear rate is greatest during shear between rhyolitic ignimbrite samples, followed by mixed lithology pairs and finally andesitic lava, with overlapping ranges of friction coefficients. Each lithology combination plots distinctly in terms of wear rate in panels b and c, and for each lithology higher W_M and P_D are associated with greater wear rates (except where melting occurs).

Comparing wear rate and the mean power density, which gives a measure of energy dissipation per unit time, leads to a marked narrowing of the data spread. There is a slight positive correlation between wear rate and P_D for each of lithologies tested, with the

greatest wear rates associated with the tests with the greatest P_D within a given lithology (Fig. 3.6c). The lithologies do, however, follow distinct trends. For the same P_D, experiments on pairs of andesitic lava samples had the lowest corresponding wear rates followed by mixed lithology, then the rhyolitic ignimbrite. Slip at high velocity (> 1 m s^{-1}) on mixed lithology pairs exhibited the highest wear rates recorded and the highest power densities.

3.3.3. Frictional heating

The temperature of the samples' surface was continuously monitored during experiments using a thermographic camera. This did not permit direct measurement along the slip plane, except for the very edge of the sample contact. The initiation of slip generates a high initial heating rate which tends to decrease after further displacement (around 2 m) to a lower rate of heating that is maintained for the duration of the test (Fig. 3.3a, see also Appendix II, Figures A.II.1 – A.II.8).

The generation of frictional heat and heat dissipation away from the slip plane is different for each lithology pairs tested. Figures 3.8 and 3.9 shows how the maximum temperature evolves with slip (T_{max}) for all lithologies. At lower slip rates, friction on andesitic lava samples generally results in the lowest temperature accumulated along the outer edge of the slip plane, compared to tests on both mixed and rhyolitic ignimbrite pairs. At greater slip rates, however, we observe that the andesitic lava samples reach higher temperatures than tests involving the rhyolitic ignimbrite. The thermographic imagery indicates that the preferential wear of ignimbrite, and the subsequent ejection of the material, brings cooler materials along the slip plane. This results in a net temperature reduction, contributing to lower maximum values of T_{max} when ignimbrite is present. In contrast, the limited wear and ejection of hot gouge from the slip plane on andesitic lava sample pairs keeps the material at the slip plane hot for a longer duration (both in time and displacement) and so can reach greater temperatures. At 3 MPa, andesitic lava consistently shows much higher temperatures reached (and faster) than mixed lithology. Andesitic lava samples are also capable of accommodating longer displacement tests without failure compared to mixed lithology tests at this high normal stress, allowing for continued heating. At some conditions frictional heating is great enough to result in the melting of the andesitic lava pairs at lower slip rates, with melting occurring at slip rates equal to or greater than 1.7 m s^{-1} at 0.25 MPa, 0.5 m s^{-1} at 1 MPa and 0.3 ms^{-1} at 3MPa. Additionally, with increasing slip rates, melting occurs at shorter displacement distances as the temperatures required for melt generation are achieved faster.

Frictional heat is generated along the slip plane and is conducted away through time. The andesitic lava sample pairs generally show a broader heating zone, and some phenocrysts have been observed to get hotter than the surrounding groundmass. Similarly, the dense lithics present along the slip plane of rhyolitic ignimbrite samples tend to preferentially heat during slip due to concentration of shear stress and lack of heat transfer to the surrounding material. For tests on mixed lithology pairs, we observed heterogeneous heat concentrations as frictional heat typically accumulates in the andesitic lava more than in the rhyolitic ignimbrite, arguably as the ignimbrite wears and the gouge is ejected.

The wear of the rhyolitic ignimbrite material systematically brings clasts to the slip surface. Once a clast is at the slip surface, shear stress peaks are seen to occur due to the sudden strength increase (Fig. 3.7a, also see Appendix II, Figures A.II.1 – A.II.8). Additionally, as wear continues on the surrounding, weaker material, the clasts become proud of the wall rock and can directly interact with asperities on the other side of the gouge material layer. The protrusion of such clasts into the slip zone results in a concentrated temperature increase observed in the thermal recordings. To illustrate this phenomenon, an occurrence of clast interaction from an experiment run at 2.4 m s^{-1} at 0.25 MPa, is used to identify different types of slip experienced by the same heterogeneous mixed sample pair. This is monitored throughout the duration of the experiment in terms of mechanical and thermal data (Fig. 3.7). Initially, after a brief peak in shear stress and wear in the first 5-10 m of slip, shear stress reduces to ~0.1 MPa, a friction coefficient of approximately 0.4 (see position 1. in Fig. 3.7). This is below that experienced at any of the lower slip rates (Fig. 3.4). At approximately 80 m displacement there is a destabilisation of shear away from steady state values, accompanied by an increase in the rate of wear, an increase in temperature and the observation of incandescent material at the slip surface (see position 2. in Fig. 3.7). Immediately after this (see position 3. in Fig. 3.7), wear reduces to near-zero, shear stress rises to ~0.2 (Fig. 3.7a) (a friction coefficient ~0.8) and a single hot spot on the surface of the ignimbrite sample exceeds 460 °C (Fig 3.7a & c). This localisation of heating and reduction in wear is due to a larger clast within the ignimbritic material, identified in sample photos, interacting with the slip surface. This clast is seen to be ejected, an event which is succeeded with much greater wear rates and eventual sample failure (see position 4. in Fig. 3.7). In this experiment alone, the effects of clasts both aiding and inhibiting wear rates (points 2. and 3. respectively in Figure 3.7) are observed.

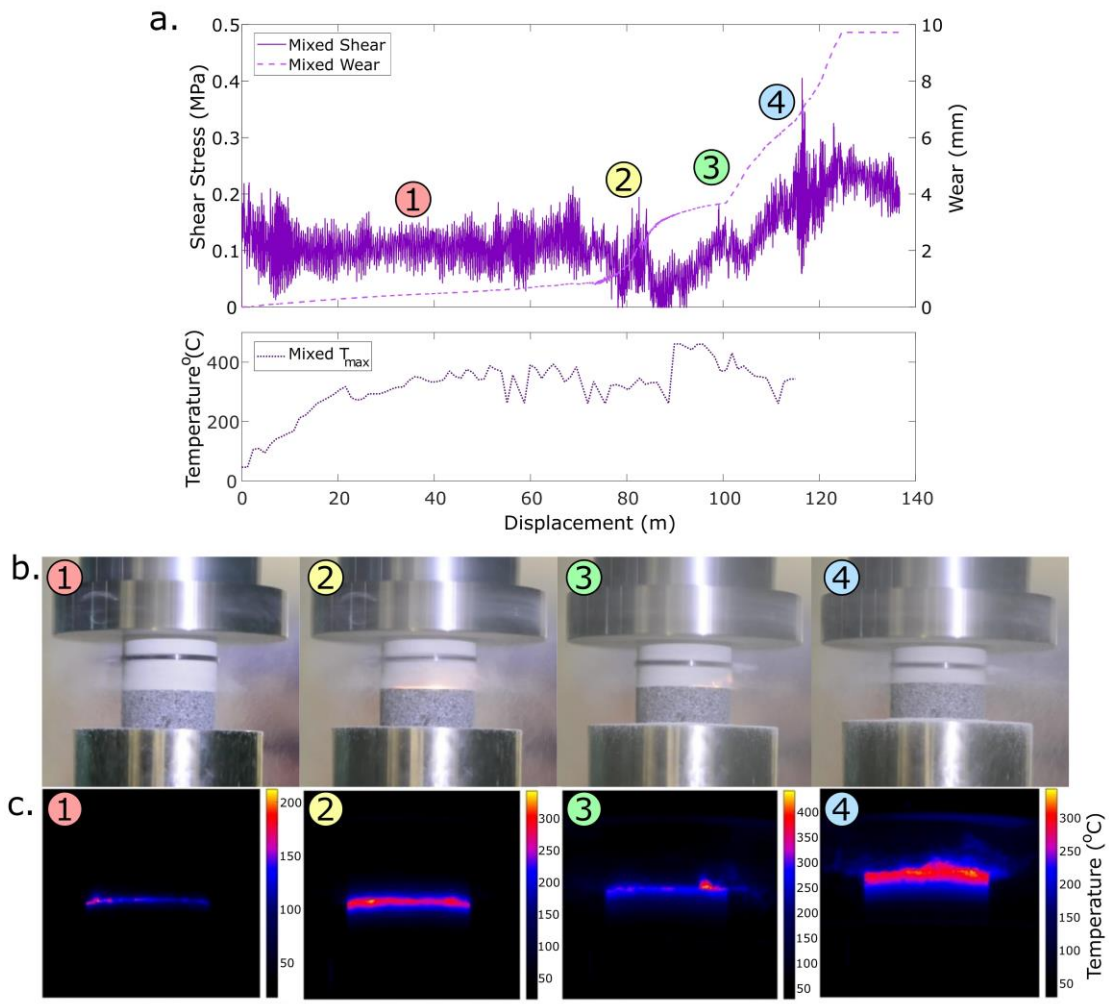

Figure 3.7. a) Mechanical and thermal data along with snapshots obtained using the b) optical and c) thermographic cameras for a test conducted on a mixed lithology pair at 2.4 m s^{-1} and 0.25 MPa. This experiment highlights the impact of wear and lithic clast interaction with the slip zone, before being ejected during frictional sliding. a) evolution of shear stress (MPa), shortening (in mm) associated with wear, and temperature throughout the experiment. The data shows variable wear rates and expulsion of clasts which result in fluctuations in shear resistance and thermal output. b-c) snapshots taken from 4 key events (labelled in panel a): 1) Steady state conditions during early sliding. 2) Destabilisation of shear with increased wear and incandescence in slip zone. 3) Near-zero wear with greater shear stress and concentration of heat to clast at slip surface. 4) Sudden onset of wear rate and shear stress increase, temperature of slip zone reduces.

The maximum temperature generated by frictional heating is described as a function of slip rate and normal applied stress. For direct comparison of frictional heat between experiments we report the maximum temperature during the steady state phase of slip, following Hughes et al. (2020a). However, due to the highly variable position of T_{max} during the test and the heating and subsequent ejection of comminuted features such as clasts, a

heating rate for the period of steady state sliding could not be determined to be directly compared to the wear rates, work per metre slip and power density calculated from the same period in each test. The behaviour leading to changes in heating profiles are therefore best observed in the raw mechanical data (Fig 3.3a & 3.7a, see also Appendix II, Figures A.II.1 – A.II.8) where heating profiles may be directly compared to shear stress and wear evolution to elucidate the mechanism linked to the variability.

If T_{max} is taken as a single value of the hottest recorded pixel during the duration of the entire experiment (excluding the frame depicting sample failure), some inferences can be made as to the effects of normal stress and slip rate in relation to lithology combinations. To constrain the thermal output of shear in our experiments, we evaluate its relationship with slip rate (Fig. 3.8-3.9). Looking at the results obtained for each lithology separately (Fig. 3.8), we observe that for andesitic lava pairs, T_{max} is linearly proportional with slip rates – a relationship accentuated with normal stress (Fig. 3.8a). The andesite lava is the only lithology to reach sufficient temperatures to undergo frictional melting. For the rhyolitic ignimbrite pairs, T_{max} scales with slip rate, but decreases with normal stress (Fig. 3.8b). It must be noted that tests are generally shorter than other lithologies due to very high wear rates and premature failure of samples. For tests on the mixed lithology samples, the relationships between T_{max} and slip rate, and between T_{max} and normal stress, are not systematic (Fig. 3.8c). At low slip rates (≤ 1m s^{-1}) T_{max} increases with normal stress, but at higher slip rates (1.7 and 2.4 m s^{-1}) we observed the opposite relationship, arguably due to the important observed ejection of hot materials due to wear. Tests on mixed lithology pairs at 2.4 m s^{-1} and 0.25 MPa normal stress resulted in incandescence during a period of slip where a lithic clast in the ignimbrite was in direct contact with the slip surface of the paired andesite, and temperatures were observed to exceed 460 °C (experiment shown in Fig 3.7).

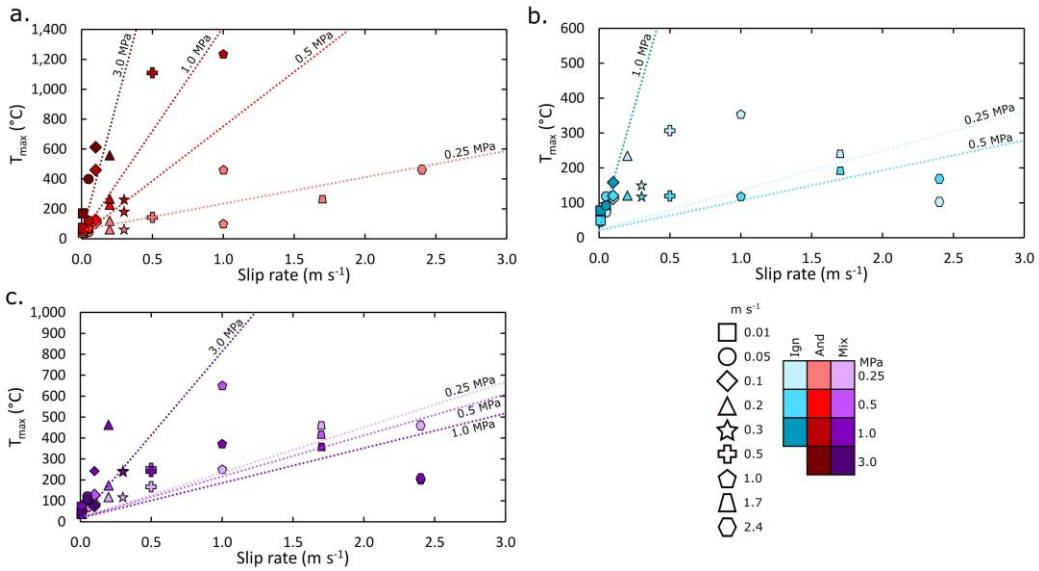

Figure 3.8. Maximum temperature (T_{max}) achieved during slip as a function of slip rate for test as a function of normal stress. a) Andesitic lava shows systematic increase in T_{max} with slip rate (for a given normal stress) and increase in T_{max} with normal stress (for a given slip rate). In contrast, the b) Rhyolitic ignimbrite and c) mixed lithology show less systematic behaviour, with T_{max} tending to increase with slip rate (at given normal stress) but not always with normal stress. Note the different vertical scales for each lithology.

To resolve the influence of lithology pairing on the maximum temperature reached during slip, we evaluate the data at different normal stresses (Fig. 3.9). For both tests on rhyolitic ignimbrite and mixed lithology there is an observed plateau or reversal in T_{max} values with increased slip rate (Fig. 3.9). This pattern is best observed in the data for the mixed lithology tests (Fig. 3.9c). At 0.25 MPa T_{max} plateaus at around 460 °C at 1.7 – 2.4 m s^{-1}. At 0.5 MPa, T_{max} is higher for larger slip rates until it reaches a maximum of 650 °C in the 1 m s^{-1} test, subsequent to that, the greater slip rates (1.7 and 2.4 m s^{-1}) produce maximum T_{max} values lower than the tests at 1 m s^{-1}. At 1 MPa, a reversal in T_{max} is observed to occur at tests with slip rates > 1 m s^{-1} after reaching a maximum of 374 °C. A similar pattern is observed in the T_{max} data from the rhyolitic ignimbrite data, and the onset for the plateau or reversal occurs at lower slip rates and lower peak T_{max} values for tests with greater normal stresses. Though the behaviour is complex it must be noted that the onset of the plateau or reversal in T_{max} trends are always associated with the initiation of greater rates of wear at that slip rate and higher slip rates at that set normal stress (compare with Fig. 3.5).

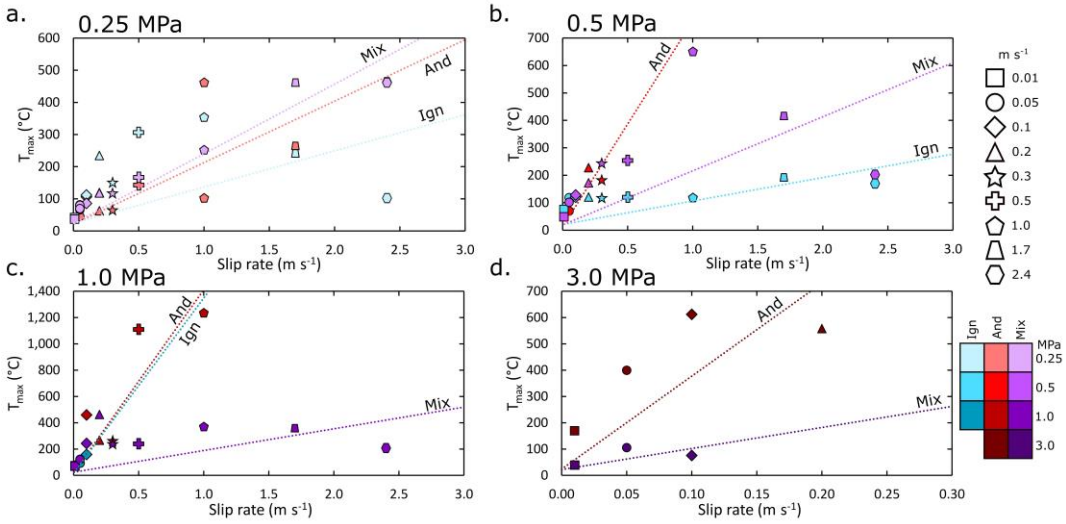

Figure 3.9. Maximum temperature (T_{max}) achieved during slip as a function of slip rate for tests a) 0.25 MPa, b) 0.5 MPa, c) 1 MPa and d) 3 MPa of applied normal stress. T_{max} generally increases with normal stress for each slip rate tested, the data show that the andesitic lava generally reaches the highest temperature for tests conducted at normal stresses equal or exceeding 0.5 MPa; at 0.25MPa however, the data shows more scatter but tests on andesite-andesite and on mixed pairs generated similar thermal output. Note the different vertical scales for each normal stress.

3.3.4. Microstructural characteristics

Samples with slip surfaces preserved after testing were selected for thin sectioning and microstructural analysis to provide insight into the acting deformation mechanisms and processes. Observations made during the experiments and inspection of the sample surfaces after experiments revealed differences in the associated damage at different slip rates and normal stresses for each lithology combination tested. Due to the range in strengths and frictional behaviours, samples were run to different slip distances (either due to premature failure, excessive wear or instabilities in shear stress lengthening the duration to achieve steady state). As such, the microstructural comparisons drawn between experimentally generated damage zones is only analysed qualitatively.

3.3.4.1. Mixed lithology pairs

We compare microstructures from preserved slip surfaces generated during tests on juxtaposed andesitic lava and rhyolitic ignimbrite samples. Andesitic lava samples record more damage at the slip surfaces than the ignimbrite sample that formed the opposing wall rock, despite the visible concentration of wear to the ignimbrite. It is difficult to determine how much damage may have been induced on the ignimbrite during the process of thin section preparation, which may have caused the loss of evidence of experimentally accumulated damage; however, 5 of the 7 ignimbrite samples (from both ignimbrite only

and mixed lithology experiments) recorded at least partial damage zones at the slip surface. Below, we proceed to detail the microstructure generated by comparing, first, the effect of slip rates, and second, the effect of normal stress.

Here we compare tests conducted at 0.25 MPa and 1.7 vs 2.4 m s^{-1}. At the lowest rate, a rough slip surface is observed in the ignimbrite sample with some preserved riedel R shear fractures extending 0.08 mm into the sample (Fig. 3.10a). In the opposing andesitic lava sample, a 0.12 mm thick fracture zone is observed at the slip surface (Fig. 3.10b-c). Thickening of this damage zone occurs where crystals are present to preferentially wear at the slip surface; this is especially the case when amphibole crystals are present, in which a denser fracture pattern is observed (Fig. 3.10d). The damage across the surface occurs as riedel shear fractures with a range of angles (15°- 30°) with respect to the primary slip surface. This fracture orientation is consistent with sinistral (left lateral) slip observed in the presented photomicrograph. The angle of these fractures tends to shallow and become subparallel to the slip surface as the fracture propagates into the material. There is no observed deformation within the wall rock further away from the damaged zone.

In comparison to this, the mixed lithology sample pair generated at 2.4 m s^{-1} shows increased evidence of damage (Fig. 3.10e-h). In the ignimbrite, and in contrast to the ignimbrite from the test with slower slip rate, multiple areas of damage zone are preserved (Fig. 3.10e). These damage patches are 0.12 mm thick with 30° riedel shear fractures which propagate linearly into the sample without curving as observed in the andesitic lava samples for both slip rates. In the andesitic lava sample, the damage zone, which is 0.16 mm thick, is more densely fractured than the lower slip rate sample, with both low angle R and higher angle R' fractures. These fractures are more aligned, and the majority have comparable geometries (Fig. 3.10f-g). Again, damage zones thicken slightly where large crystals are present along the slip plane (Fig. 3.10h) and R fractures shallow to become slip surface sub parallel. Despite the thicker damage zone and greater intensity of fracturing, the surface of the sample remains relatively smooth with little evidence of material entrainment (Fig. 3.10f-g).

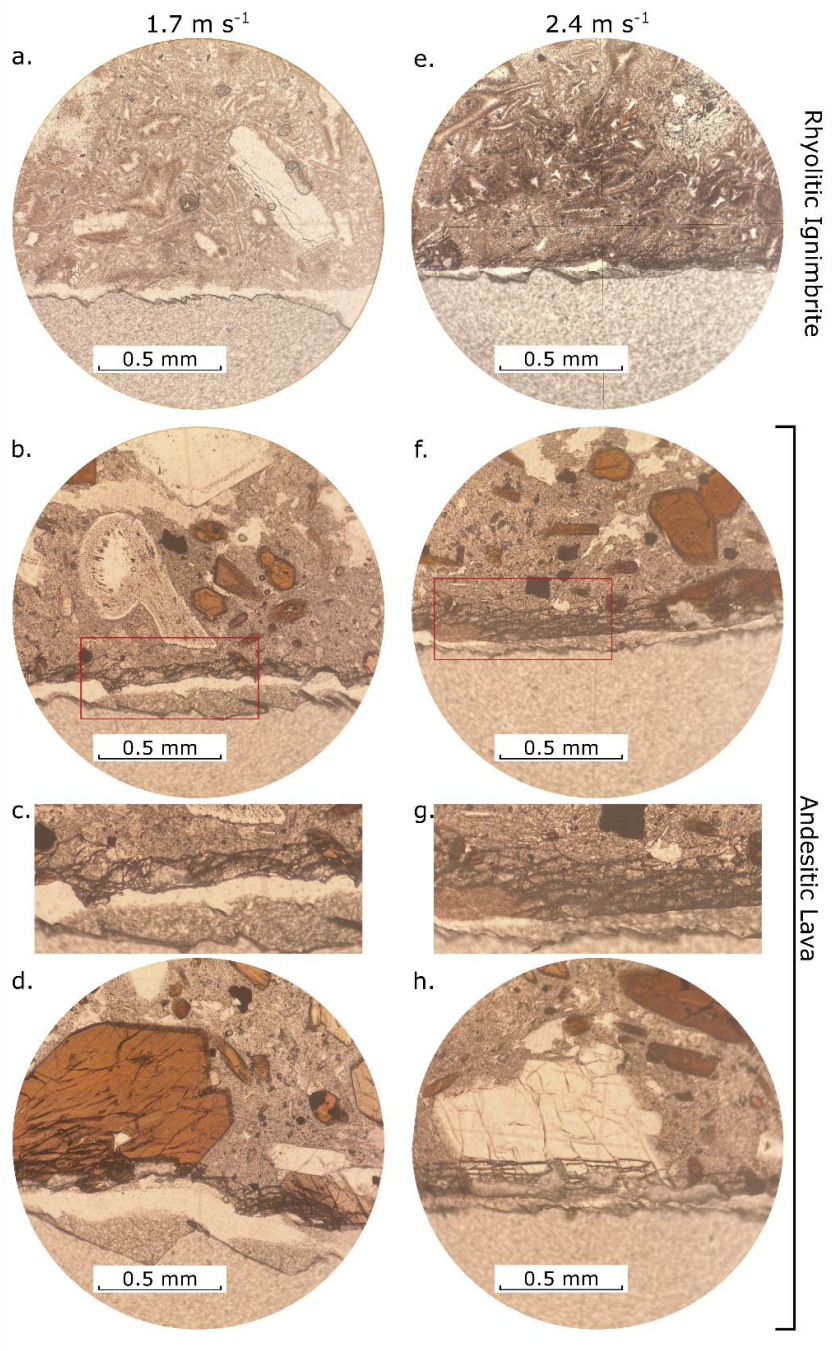

Figure 3.10. Photomicrographs of slip surface and damage zones from friction tests on mixed andesitic lava and rhyolitic ignimbrite sample pairs at 0.25 MPa normal stress and a-d) 1.7 m s^{-1} and e-h) 2.4 m s^{-1} slip rates. The damage zones in andesite are thicker despite material removal being concentrated in the rhyolitic ignimbrite. a) Areas of riedel fracturing in ignimbrite sample. b & c) Damage in the andesite (area of c marked by red rectangle in b) d) Increased damage accumulation in a hornblende crystal (from the andesitic lava) towards the slip surface. e) Thick damage zone in ignimbrite sample at 2.4 m s^{-1} (thicker than in tests at 1.7 m s^{-1} as shown in a). f & g) Damage zone in andesite, thicker than that produced at 1.7 m s^{-1} shown in b (area of g marked by red rectangle in f). h) Increased damage accumulation in a plagioclase crystal (from the andesite) towards the slip surface.

We contrast the above by analysis of the sample pair that underwent 2.4 m s^{-1} slip rate at the higher normal stress of 0.5 MPa (Fig. 3.11). The ignimbrite sample did not preserve damage away from the slip plane (Fig. 3.11d) compared to the ignimbrite undergoing slip at lower slip rates (Fig. 3.11a). The andesite exhibits a rough surface suggesting material removal (Fig. 3.11e-f) unlike the surfaces preserved at lower normal stresses. The damage zone is 0.09 mm thick with a thin layer of intense fracturing (0.04 mm) of thicker and larger fractures extending 0.11 mm into the wall rock. As the majority of wear in mixed lithology tests is concentrated in the rhyolitic ignimbrite, it is not possible to quantify the difference in wear in the andesitic lava sample of the pair between different slip rates.

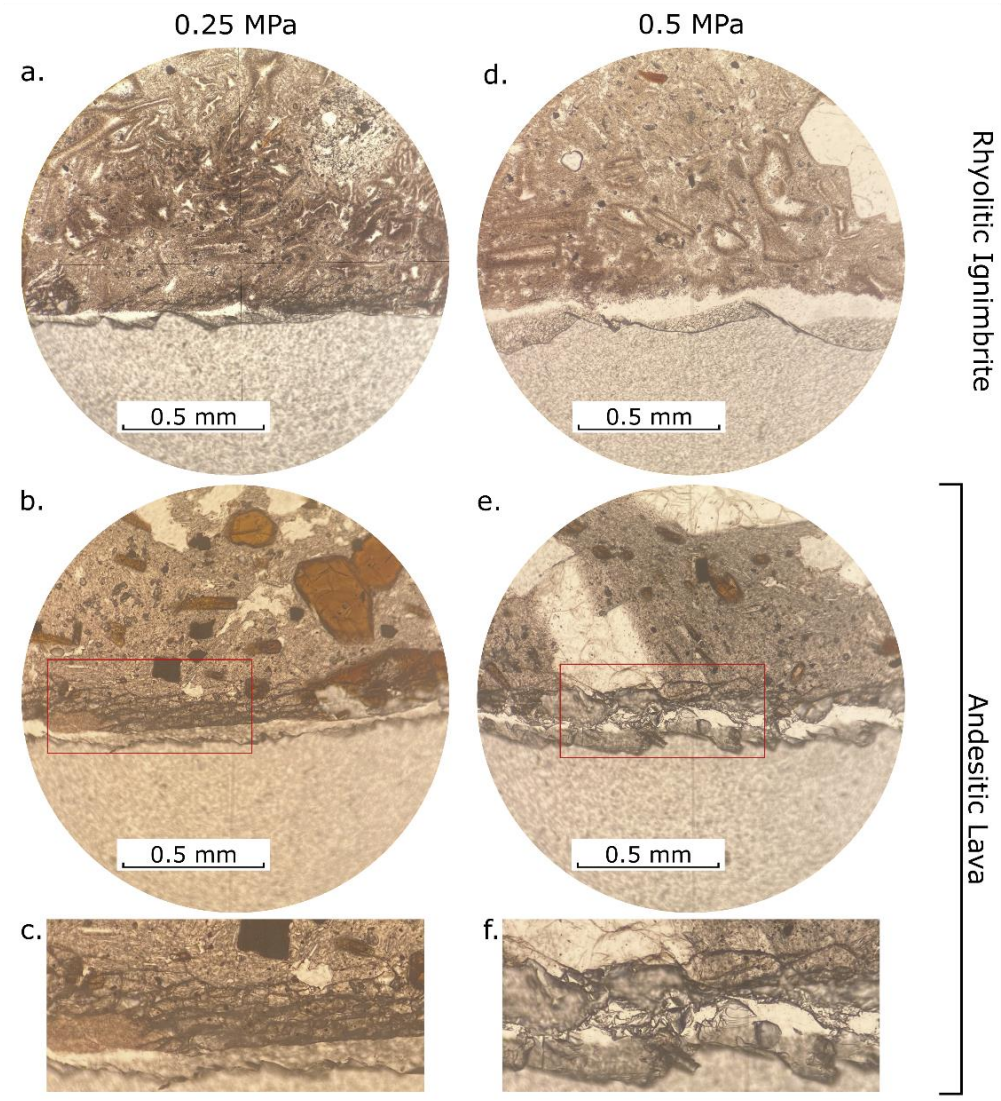

Figure 3.11. Photomicrographs of slip surface and damage zones from friction tests at 2.4 m s^{-1} and a-c) 0.25 MPa and d-f) 0.5 MPa normal, both at 2.4 m s^{-1} for contrast of damage microstructures. a-c) see Figure 3.9, repeated here for contrast against d-f. d) slip surface with no visible damage zone in ignimbrite sample. e-f) Contrasting damage zone in andesite (area of e marked by red rectangle).

3.3.4.2. Single lithology pairs

The microstructure generated during shear of single lithology sample pairs were subjected to the same analysis and comparisons as for the mixed lithology pairs. First, we compare the effects of slip rates and second, the effects of normal applied stress.

The slip zone preserved from an experiment on a rhyolitic ignimbrite pair at 0.01 m s^{-1} and 0.25 MPa normal stress shows a 0.12-mm thick damage zone with faint fractures, sub-parallel and that do not appear to necessarily originate from the slip surface (Fig. 3.12a-b). The fractures may be low angle riedel shear fractures, but lack of 3D exposure prevents a conclusive assessment. In contrast, the slip surface from an experiment run at the same normal stress (0.25 MPa) but higher slip rate of 1.7 m s^{-1}, does not preserve a damage zone and only exhibits obvious fractures within phenocrysts (e.g. plagioclase) interacting with the slip surface (Fig. 3.12c-d).

The ignimbrite displaying the most observed damage is from the test run at 1 m s^{-1} and 0.5 MPa (Fig. 3.12e-f). It hosts the thickest damage zone at 0.21 mm and the greatest abundances of fractures. All observed fractures within the glassy groundmass were low angle riedel shears; with more complex fracture patterns were observed in plagioclase crystals at the slip surface (Fig. 3.12e-f). [Note that similar thickness of damage zones in andesitic lava samples from mixed lithology tests generally have a higher concentration of fractures, with ignimbrite samples exhibiting lower abundances of small fractures in the damage zone. Additionally, the fractures are linear rather than curves as observed in andesitic samples from mixed lithology experiments (Fig 3.9 & 3.10).] For the slip surface generated at 1.7 m s^{-1} and a greater normal stress of 0.5 MPa, we observe an extremely thin damage zone, 0.04 mm thick, with dispersed fractures (Fig. 3.12g-h). At a lower normal stress (0.25 MPa) and same slip rate (1.7 m s^{-1}) no damage zone was preserved, and only isolated free crystals exhibit fractures (Fig. 3.12c-d). In contrast at the same normal stress (0.5 MPa) and lower slip rate (1 m s^{-1}) the damage zone is thicker than that observed from experiments with the same normal stress but lower slip rate (Fig. 3.12e-f).

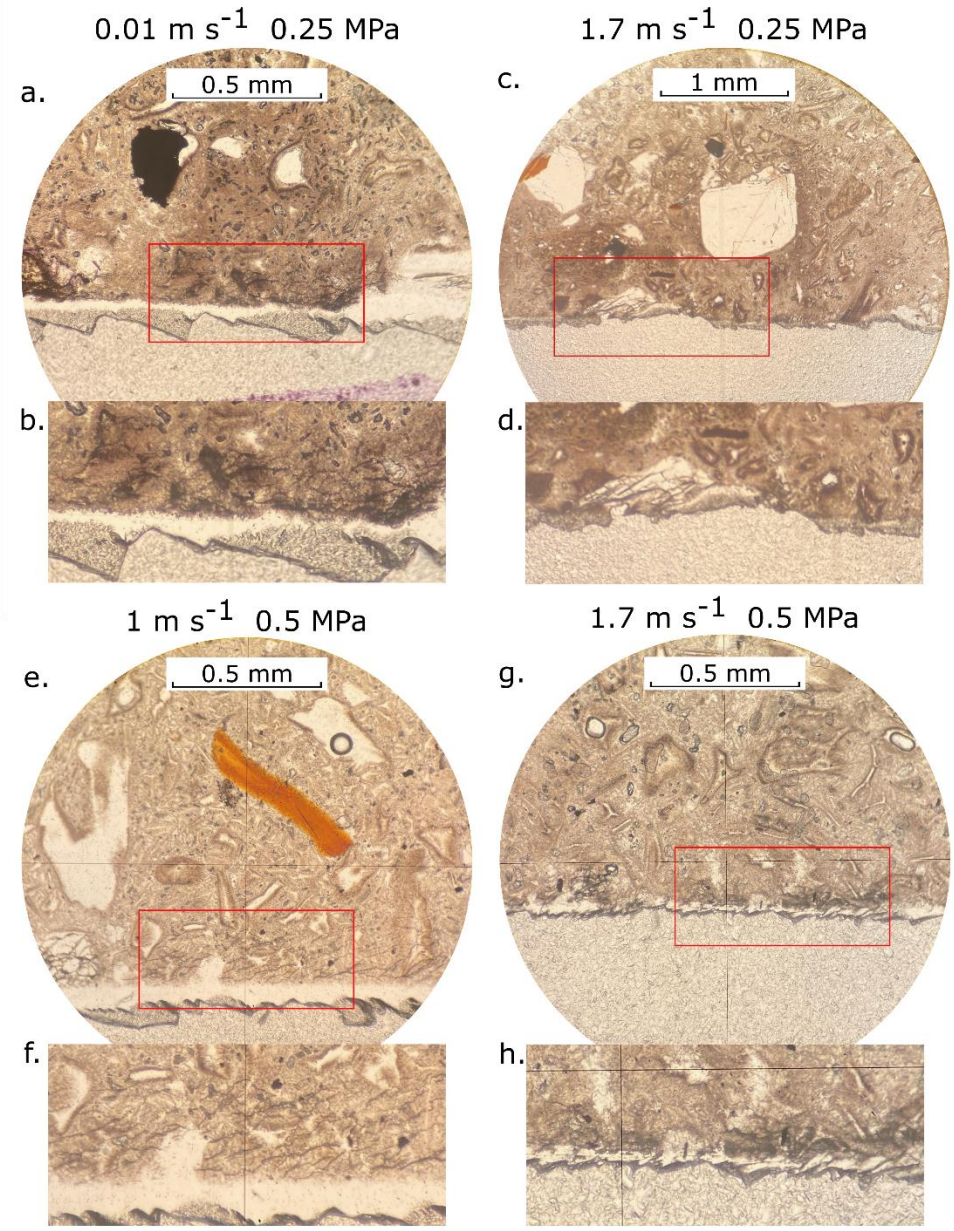

Figure 3.12. Photomicrographs of four contrasting slip surface and damage zone morphologies developed during rhyolitic ignimbrite-ignimbrite friction tests at different conditions. a & b) Tests at 0.01 m s^{-1} and 0.25 MPa resulted in a thick damage zone. The origin of (b) is marked by a red rectangle in (a). c & d) Tests at 1.7 m s^{-1} and 0.25 MPa resulted in negligible damage zone but for fractured crystals along the slip surface. The location of (d) is marked by a red rectangle in (c). e & f) Tests at 1 m s^{-1} and 0.5 MPa promoted a thick fracture zone with low fracture density (compared to similar thickness zones in andesitic lava (Fig. 3.10 & 3.11)). g & h) Test at 1.7 m s^{-1} and 0.5 MPa produced narrow damage zone, compared to tests at a lower rate of 1 m s^{-1} at the same normal stress, but thicker than that generated at same slip rate and lower normal stress.

3.3.4.3. Experimentally generated pseudotachylytes

The only experiment that resulted in frictional melting that welded the samples is that conducted on andesite samples at 0.25 MPa and 2.4 m s^{-1}. The resultant pseudotachylyte exhibits a glass-bearing layer with variable thickness from 0.3 mm to 0.4 mm across the section cut for analysis (Fig. 3.13a-c). Within the layer there is an abundance of angular fragments of plagioclase restites (Fig. 3.13c). The crystal-bearing pseudotachylyte is seen to form embayment's along the wall rock contact. Where the leading edge of plagioclase crystals have become cracked, the pseudotachylyte intrudes into the wall rock by way of these fractured minerals. Plagioclase crystals in contact with the pseudotachylyte only show limited evidence of melting and often stand proud from the wall rock material and remain locally intact within the pseudotachylyte layer. Figure 3.13d-e shows a large plagioclase glomerocryst interacting with the pseudotachylyte. In this area of the slip layer the thickness of the preserved pseudotachylyte is reduced to approximately 0.15 mm.

The wall rocks along the pseudotachylyte are marked by dark-brown zones of alteration seen in plane polarised and cross-polarised light (Fig. 3.13). Within these zones, plagioclase microlites are orientated sub-parallel to the direction of shearing. One large plagioclase phenocryst is also deformed and bent towards this alignment (Fig. 3.13c). Hornblende crystals present in this zone within the andesitic lava exhibit dark coronas in cross-polarised light in comparison to further away from the slip zone, in the undeformed areas of the sample (Fig. 3.13).

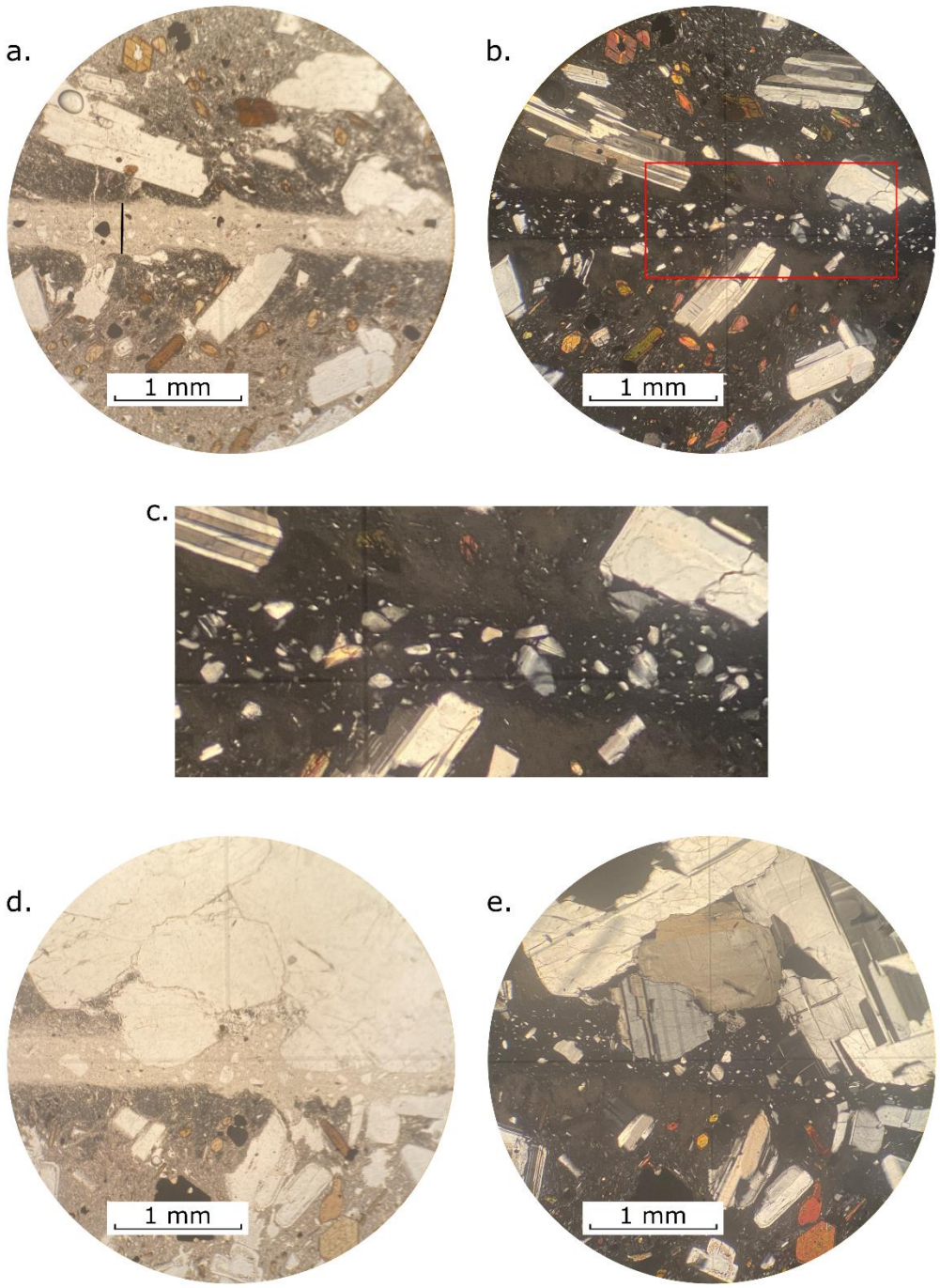

Figure 3.13. Photomicrographs of the pseudotachylyte-bearing shear zone produced by frictional melting of andesitic lava samples during slip at 2.4 m s^{-1} and 0.25 MPa. a) plane polarised and b) cross polarised images showing the texture of the pseudotachylyte and alteration zone of the wall rock (i.e., the dark brown areas on either side of the pseudotachylyte). c) The zoomed-in image shows the alignment of crystals with the shearing direction in alteration zone on either side of the pseudotachylyte. The location of (c) is marked by a red rectangle in (b). d) plane polarised and e) cross polarised images showing local variation in pseudotachylyte thickness due to preference wear of large crystals or glomerocrysts interacting with the melting zone.

3.4. Interpretation and discussion

By combining analyses of the evolving shear resistance, wear and frictional heat, we interpret the frictional behaviour of juxtaposed rocks of differing material properties, and the role of heterogeneities on the tribological evolution during slip. We can then infer how these factors may influence slip in natural examples of juxtaposed materials including the case study of the Arequipa volcanic landslide.

The steady state shear resistance (at a given normal stress) obtained during tests on single lithology pairs adhere to Byerlee's friction relationship (Byerlee, 1978) despite contrasting physical properties, including porosities. Experiments on mixed lithology pairs show shear resistances below those expected by Byerlee (1978) and lower than those obtained for both constituent lithology types independently. The combination of lithologies in this case leads to a reduction in friction and favourable slip conditions at a range of slip rates.

It must be noted however, that the variation in wear rates and frictional heating profiles highlight the differences in behaviour between the andesitic lava and rhyolitic ignimbrite which must be considered when discussing the slip properties of the two materials, in order to adequately determine the processes dominating during shear on contrasting juxtaposed lithologies.

3.4.1. The role of sample heterogeneity on slip dynamics

Variability during the experiments observed in shear stress, wear and frictional heating can be attributed, in part, to the interaction of lithic fragments and free crystals with the slip surface. This variation occurs in both experimental suites containing the rhyolitic ignimbrite (single and mixed lithology pairs). The lithic clasts and occasional large free crystals of plagioclase present in the rhyolitic ignimbrite impart local strength variances as they are more resistant to wear during shear (Archard, 1953; Spray, 2010). Protrusion of these clasts and crystals into the slip zone, due to the relative resistance to wear compared to the host rock, results in the bypassing of the potential lubricating effect of the gouge layer (Reches and Lockner, 2010; Boneh and Reches, 2018) and focuses the shear on these heterogeneities. As the clasts are harder to fracture, less energy is consumed by surface energy creation associated with fractures, and the measured shear stress increases. Lack of wear and concentration of shear stress to these resistant asperities causes heterogeneous heating of these clasts, leading to uneven heat distribution across the slip surface. The longer

the clast interacts with the surface without being destroyed by wear, or plucked and removed from the ignimbrite matrix, the greater the temperature the clasts can reach.

As previously introduced when describing Figure 3.7, steady wear generally results in steady-state shear resistance (see position 1 in Fig. 3.7). However, when an area of the shear zone starts to wear preferentially, exposing the hotter inner regions of the slip plane, the shear resistance starts to fluctuate and briefly decreases (see position 2in Fig. 3.7). As shear eventually causes the plucking of a clast from the slip plane (observed as a locally high temperature region on Fig 3.7b, position 3), the rate of wear varies further causing further fluctuations and increases in shear resistance (see position 3 in Fig. 3.7). As slip continues and shear resistance fluctuates, further clasts were seen to interact with the slip plane, causing trivial wear and localised heating exceeding 460 °C (position 4 in Fig. 3.7). The array of behaviours shown in Figure 3.7 demonstrates the different effects rocks with mineralogical and mechanical heterogeneities can have on the tribological properties during a sliding event. Most critically, during the sliding phase at position 3 in Figure 3.7, the shear resistance associated with clast interaction counteracts the velocity weakening observed at the start of the test and in other experiments at > 1m s^{-1}. This increased the friction coefficient to values generally anticipated for tests at greater normal stresses and slip rates (and consequently lower work rates per metre slip and power density; Fig. 3.4). By searching for periods of reduced wear rates and increased shear stress and increased temperatures in the dataset, we can identify occurrences of clast interaction with the slip plane in a multitude of tests in this study (see Appendix II, Figures A.II.1 – A.II.8).

Commonly, after clast failure or ejection, there is a period of increased wear and even fragmentation as the fragments are entrained into, and abrade, the slip zone, either by ploughing or rotational grinding (e.g. Hutchings and Shipway, 2017) as observed in Figure 3.7. Considering the implication of these observations for the case of the Arequipa volcanic landslide, a scaled-up version of the abrasion from strong clasts could lead to enhanced damage and entrainment of the basal, weaker ignimbrite lithology by large and coherent blocks of andesite within the debris avalanche. These blocks or clasts interacting with the shear zone could speed up the mechanical wear occurring along the base of large debris avalanches.

In addition to strong clasts in the ignimbrite, weak pumice fragments are also present but their impacts on wear, shear resistance and temperature are less evident. However, there were small periods of noted increases in wear rates during pumice clast interaction with the

slip zone due to the high porosity (and hence lower strength) of these structures, allowing for the fast fracturing and comminution of the glassy material, increasing gouge production speeds.

3.4.2. Frictional behaviour

The complicated pattern of velocity strengthening and weakening at low slip rates and velocity weakening at slip rates greater than 1 m s^{-1} suggests a weakening mechanism, likely gouge production, that is triggered at a critical work rate. This is supported by observations by Reches and Lockner (2010), where formation of a critical body of gouge formed at 0.01–0.05 m s^{-1} in homogenous granite experiments was linked with velocity weakening, and in Hughes et al. (2020a) where similar weakening mechanisms were interpreted to have been triggered at 0.2-0.4 m s^{-1} in homogenous, variably porous glass samples. Due to the mineralogical and textural differences of the samples (i.e., the crystalline nature of the andesitic lava vs the variably indurated glassy matrix of rhyolitic ignimbrite) the same mechanism identified in these studies may also occur here, but at more variable low slip rates and normal stresses. An observed variability in wear rates for rhyolitic ignimbrite and mixed lithology tests between low slip rates (Fig. 3.5) may account for the delayed onset of this weakening compared with the andesitic lava (Fig. 3.4).

This study, Reches and Lockner (2010) and Hughes et al. (2020a) all identified unstable slip and velocity strengthening occurring at 1 m s^{-1} but the previous studies did not conduct experiments at higher slip rates to investigate whether a second phase of weakening would occur. In this study, we observed rate weakening behaviour beyond 1 m s^{-1}, which is likely attributable to the onset of thermally activated dynamic weakening mechanisms, along with a certain degree of wear and/or rupture.

3.4.3. Comminution and wear

Application of greater normal stresses (leading to greater shear stresses) increases physical interactions and resultant wear rate. There is also an overall correlation between wear rate and work rate as well as power density, where the greater energy exerted during slip (per metre or per second of slip respectively) promotes fracturing at the slip surface. However, the correlation between friction and wear rate in the case of these materials is less clear. Weakening of the materials at higher slip rates and the complication of clasts at the slip surface in both ignimbrite and mixed lithology tests can result in both lower and higher frictional values than friction coefficients suggested by Byerlee (1978), respectively.

At low slip rates wear rates are variable, but above 0.5 m s^{-1} the rate of wear increases with slip rate, with the exception of tests conducted on single lithology andesitic lava samples at the lowest normal stress of 0.25 MPa. The andesitic lava does not typically experience wear rates greater than 0.001 mm m^{-1} at any slip rate at 0.25 MPa due to the high strength of the material, although at higher normal stresses (1 and 3 MPa) the wear rate increases with slip rates as did other rocks. The rhyolitic ignimbrite exhibits much lower increase in wear rates as a function of slip rates as the material is so weak; wear is significant at all conditions tested, even at slow slip rates. This is highlighted in Figure 3.6c where even tests experiencing low power densities exhibit very high wear rates; hence, it suggests that less energy is required for fracturing and comminution of the rhyolitic ignimbrite during shear. From this, the inference is that where the active wall rock along a fault exhibits contrasting strengths, rupture and generation of gouge (Matsu'ura et al., 1992; Reches and Lockner, 2010) may form quicker and at lower slip rates, aided by wear concentration on the weakest materials.

When analysing the wear rates (Fig. 3.6a), we note that often the highest rates (> 2 mm m^{-1}) experienced by the mixed lithology at high slip rates were linked with the lowest frictional coefficient values of 0.3-0.5, especially at higher normal stresses. The equivalent tests on rhyolitic ignimbrite experienced higher frictional values of 0.6-0.8 and sometimes underwent failure. The greatest wear rates experienced by andesite in high normal stress tests were associated with friction coefficient values between 0.5-0.7 (Fig. 3.6a).

Complete material failure, often observed in high normal stress experiments, is not regarded as wear at the scale of our laboratory experiments, but as a rupture events. In nature however, these rupture events may rapidly modify the componentry in the fault zone by adding large amounts of fragmental material; it also results in momentary dilation of the slipping surface. However, our experiments are not confined, and therefore we cannot comment on the prevalence of such processes in naturally confined settings. The process does however draw parallels to behaviour inferred at the base of debris avalanches and landslides, where undulations in the slip surface and spatially contrasting basal textures are observed and could result from local dilation or failure of adjacent material. For example, the large scale failure of weak basal rocks has been noted in catastrophic mass movements including the Pichu-Pichu case study, where the La Joya ignimbrite is highly fractured for several metres below the Arequipa volcanic debris avalanche deposit (Hughes et al., 2020). Additionally, the larger Markagunt gravity slide in southern Utah has multiple basal shear zone exposures involving a range of juxtaposed materials due to large scale ramping of the

gravity slide and many exhibit large scale damage of the underlying rocks (Hacker et al., 2014; Biek et al., 2019).

3.4.4. Frictional heating

Throughout the tests, especially those involving heterogenous material, we note the transience of frictional heating. Many experiments showed momentary fluctuations in temperature due to the ejection of hot material and clasts, resulting in a net loss of heat from the slip zone. The frictional heat generated during shear of andesitic lava pairs exhibits the lowest variation due to its relative homogeneity, which ensured it remained coherent throughout the test. As such, these samples reached greater T_{max} values (proportional to normal stress and slip rate) due to the greater work done at the slip surface (Fig. 3.9) and more conduction of heat away from the slip zone into the samples. In contrast, as slip on rhyolitic ignimbrite sample pairs resulted in substantial wear at high normal stresses, higher temperatures were reached at the lowest applied normal stresses due to the longer test duration possible at these conditions. These displayed very little conduction of heat away from the slip surface. The thermal evolution of the slip plane during tests on the mixed lithology were more complex: at low slip rates, higher temperatures were reached at greater normal stresses, but at higher slip rates (> 0.5 m s^{-1}) higher temperatures were reached at the lower normal stresses. This is due to the longer interaction of clasts at the slip surface (than in rhyolitic ignimbrite sample pairs) and greater displacements due to lower wear rates and less incidents of failure. In mixed lithology pairs the prolonged interaction of clasts with the andesitic lava slowed the rate of wear (Fig. 3.7 and Appendix II, Figures A.II.1 – A.II.8). In tests on rhyolitic ignimbrite single lithology pairs, however, clast interactions either ploughed through the weaker opposing ignimbrite material or caused their sudden plucking and removal (due to shear stress exceeding their strength when in direct contact), leading to either failure or rapid shortening. The low shear resistances and work rates experienced during such ignimbrite tests resulted in only limited heating.

For both the mixed lithology and rhyolitic ignimbrite sample suites, plateauing or reversal of T_{max} was identified at high slip rates (Fig. 3.9). In these cases, the high slip rates resulted in either shorter slip distances due to high wear or failure, or due to the faster removal of heated material and clasts from the surface in tests with greater W_M and P_D. This limitation of frictional heating by increased wear was also identified in tests on homogenous porous glass samples in Hughes et al. (2020a), although they witnessed lower wear rates and less common sample failure (see Chapter 4). In this study on glass analogues, slip distances of experiments had less variation and so it is likely that the high wear rates of both the high

porosity glass analogues in that study and the high porosity rhyolitic ignimbrite tested in this study act to keep slip surface temperatures low due to intense wear, regardless of slip distance.

3.4.5. Slip surface processes

The damage zones experimentally generated allow for the identification of the wear mechanisms that are not evident from the mechanical data alone. In tests on mixed lithology pairs, an increase in slip rate is seen to increase the thickness and fracture density of damage zones in both rocks, but an increase in normal stress appears necessary to promote material removal and wear of the andesitic wall rock. This has important inferences in natural slip surfaces, as although wear of the weaker wall rock produces a gouge layer, the inclusion of the stronger andesite material within this layer increases abrasion, and resultant wear rate, due to increased ploughing of the weaker wall rock by strong, resistant fragments of andesite in the gouge layer. This may also be inferred from the experimental products, as the ignimbrite wall rock from the higher normal stress tests does not exhibit a damage zone suggesting that fragmental material was removed readily, preventing damage accumulation within the sample. At low slip rates and normal stresses, and thus lower mean power density (P_D), the surficial interaction and the removal of asperities lessened (Bhushan, 1998; Bowden and Tabor, 2001). Upon the application of greater normal stresses, interaction is increased, resulting in greater energy and producing larger damage zones, which in the case of the rhyolitic ignimbrite, commonly leads to failure.

Where free crystals are observed at the slip surface, they preferentially contain fractures (Fig. 3.10d & h). The crystallographic structure of minerals promotes the propagation of fractures within them, thus conspiring to generate wider damage zones. In these cases, damage may be preserved within crystals as ploughing and wear of the weak ignimbrite matrix would only impart fractures in these crystals rather than through the grinding comminution of the weakly indurated groundmass. This is observed in the experiments on rhyolitic ignimbrite pairs at high velocity where cracking in the plagioclase is the only surviving evidence of surface damage (Fig. 3.12c-d), this is in contrast to slow slip rate tests and high normal stress tests where damage of the material precedes the removal and comminution. The variation between material removal/damage zone fracturing has implications for the relative generation and propagation of damage zones and the removal and comminution of surface material in slip zones, in turn determining their architecture and longer term behaviour (e.g. Scholz, 2019).

The only material observed in this study to produce frictional melting is the andesitic lava. Hence the damage in andesitic lava samples from tests at similar slip rates as the previously discussed mixed lithology tests is not comparable, having been overprinted by pseudotachylyte generation. With increasing normal stress, the andesitic lava is able to melt at slower slip rates, although at a similar amount of work per meter slip. When melting occurs, the shear resistance of the melt layer is much higher than that expected of rock-rock frictional contacts (Fig. 3.3b). This high shear resistance suggests that the melt layer acted as a viscous brake (e.g. Fialko and Khazan, 2005). The viscosity and thus shear resistance of frictional melts (which influences whether the melt will act as a brake or lubricant) is dependent on temperature and the melt's chemical composition (e.g. Hess and Dingwell, 1996; Giordano et al., 2008), as well as the fraction of bubbles and crystals/lithics in suspension and strain rate (Lejeune and Richet, 1995b; Caricchi et al., 2007; Lavallée et al., 2007).

The chemistry and rheology of the frictional melt, preserved as pseudotachylyte, at the base of the Arequipa volcanic landslide deposit was analysed to assess whether it acted as a lubricating or viscous brake in Hughes et al., 2020b. It was determined that the pseudotachylyte was a product of melting of both the andesitic debris and the basal ignimbrite, as the silica content was greater than the bulk composition of the andesite. In this study, only experiments on andesite-andesite rock friction resulted in frictional melting, so a rheological comparison is unfortunately not possible.

The experimental pseudotachylyte contained a large proportion of plagioclase fragments that failed to melt (i.e., restites). Additionally, where a large glomerocryst of plagioclase interacts with the slip zone, the melt layer thins, suggesting that despite having > 40 m of slip, the melt never reached the required temperatures to effectively melt the plagioclase it was in contact with. The natural pseudotachylyte contains an even larger proportion of plagioclase restites (Hughes et al., 2020b), and thus may have experienced a slightly lower temperature than our experiments. As the shear resistance experienced in the presence of a frictional melt layer was so much greater than the measured rock-rock shear stress (Fig. 3.3c), we concluded that the melts from these intermediate to evolved melts likely act as viscous brakes at shallow crustal conditions, as suggested by Hughes et al. (2020b). This is despite the abundance of OH-bearing amphiboles in the andesite that would preferentially melt and favour the generation of hydrous melt with relatively low viscosities (Hornby et al., 2015; Wallace et al., 2019a).

As described in Hughes et al. (2020b) the melt layer formed adjacent to layer of ultracataclasite within the basal shear zone in which strain was primarily accommodated. In this case it is evident that despite cataclasis of solid rocks, high temperatures required for melting were reached. Hughes et al. (2020b) postulated that the increased normal stress from the interaction of the debris flow with topographic barriers formed localised areas of extreme compression that led to high shear resistance and thus thermal output along the basal contact, which promoted frictional melting locally. In the experiments in this study, which had no lateral confinement, the continuous ejection of hot gouge persistently outbalanced the frictional heat generated. It must be noted that the presence of strong clasts may minimise wear and enable further localised frictional heating whilst causing high shear resistance. This suggests that the presence of strong components in weak rocks could favour the development of local heat anomalies along the slip surface, potentially leading to melting.

3.5. Conclusions

Here we present the results of controlled laboratory experiments investigating the frictional properties of single and mixed lithology pairs to resolve how faults with extensive slip (and lithologically contrasting wall rock) is sustained. Specifically, we relate our findings to the case of the Arequipa volcanic landslide deposit, following sector collapse of the predominantly andesitic Pichu Pichu volcanic complex, forming a debris avalanche that travelled for ~27 km over a rhyolitic ignimbrite substratum.

By performing tests on the rhyolitic ignimbrite and andesitic lavas in both single lithology and mixed lithology pairs in a direct shear apparatus, we explored how juxtaposed lithologies influence frictional sliding. We found that slip on juxtaposed contrasting lithologies can lead to lower frictional coefficients, than during tests on single lithology rock pairs, due to the preferential fracture and wear of the weakest materials which experience greater wear rates. This may promote the rapid formation of gouge layers, potentially limiting the magnitude of frictional heating, due to an increased proportion of energy consumed by rupture, and thus impacting the occurrence of thermally activated processes and potential weakening mechanisms (e.g. melting).

Heterogeneity present in rocks, in the form of strong clasts, causes a concentration of stress and discrete damage along the slip surface that may result in momentary and localised increases in shear resistance, that may exceed (and thus counteract) the contribution of shear rate weakening mechanisms active at high slip rates. These heterogeneities can cause

both increases and decreases in wear rates, either by strengthening the weaker material slip surface, or becoming entrained into the slip zone and acting as effective asperities by material ploughing. In extreme cases, strong asperities may abrade the adjacent rock before being plucked and entrained in the slip zone. The increased shear stress and potentially reduced wear rates created by strong clast asperities causes localised heating along the slip surface, which may result in localised thermally activated weakening mechanisms and even melting at slip conditions at which melting would not otherwise be expected to occur. The wear of weak porous clasts such as pumices ensure slip surface roughness (at the scale of pores) that favours wear resulting in momentary lower shear resistance.

In relation to the debris avalanche near Arequipa, we suggest that the juxtaposition of andesitic lava material against the weak basal rhyolitic ignimbrite during transport may have favoured wear that promoted long runout distance by reducing the basal shear resistance. The rhyolitic ignimbrite's propensity to high wear rates and rupture under low normal stresses would have favoured cataclasis and material entrainment in the basal shear zone. Localised strength variations from large clasts may too have produced transient variations in shear resistance and thus frictional heating that may have aided the generation of the laterally non-continuous pseudotachylyte layers.

Chapter 4: Frictional behaviour, wear and comminution of synthetic porous geomaterials

Abstract

During shearing in geological environments, frictional processes, including the wear of sliding rock surfaces, control the nature of the slip events. Multiple studies focusing on natural samples have investigated the frictional behaviour of a large suite of geological materials. However, due to the varied and heterogeneous nature of geomaterials, the individual controls of material properties on friction and wear remain unconstrained. Here, we use variably porous synthetic glass samples (8, 19 and 30 % porosity) to explore the frictional behaviour and development of wear in geomaterials at low normal stresses (≤ 1 MPa). We propose that porosity provides an inherent roughness to material which wear and abrasion cannot smooth, allowing material at the pore margins to interact with the slip surface. This results in an increase in measured friction coefficient from < 0.4 for 8 % porosity, to < 0.55 for 19 % porosity and 0.6–0.8 for 30 % porosity for the slip rates evaluated. For a given porosity, wear rate reduces with slip rate due to less asperity interaction time. At higher slip rates, samples also exhibit slip weakening behaviour, either due to evolution of the slipping zone or by the activation of temperature-dependent microphysical processes. However, heating rate and peak temperature may be reduced by rapid wear rates as frictional heating and wear compete. The higher wear rates and reduced heating rates of porous rocks during slip may delay the onset of thermally triggered dynamic weakening mechanisms such as flash heating, frictional melting and thermal pressurisation. Hence porosity, and the resultant friction coefficient, work, heating rate and wear rate, of materials can influence the dynamics of slip during such events as shallow crustal faulting or mass movements.

4.1. Introduction

A spectrum of geohazards and anthropogenic processes are associated with shear, rupture and slip on faults or other slip surfaces. These include earthquakes, volcanic activity, landslides, glacier flow and induced seismicity. Hence, an understanding of the frictional behaviour of geomaterials is essential to resolve the development of faulting events in a variety of environments. Geomaterials vary greatly in their mineralogy and texture, which range from sedimentary and volcaniclastic rocks formed by the deposition, compaction and cementation of grains or fragments during lithification (Lewis, 1984), to igneous rocks formed through cooling with variable degrees of crystallisation and vitrification, causing a range of textures with diverse glass, crystal and bubble contents (e.g. Le Bas and Streckeisen, 1991), and metamorphic rocks formed through recrystallisation (e.g. Schumacher, 1999). This textural and chemical variety leads to differing mechanical properties of rocks as each of the constituent phases have different strength and fracture toughness, dictating the rocks' mechanical response to slip and comminution (Spray, 1992; 2010). It is therefore difficult to determine the control each of these variables exerts onto the frictional response of the material. Furthermore, fault slip can generate a substantial amount of frictional heating (Carslaw and Jaeger, 1959). The thermal conductivities and, where relevant, decomposition, breakdown or melting temperatures of each constituent phase of the material also determine the progression of frictional heating during sliding (e.g. Spray, 2010; Wallace et al., 2019a). It is the pairing of comminution with the production and conduction of frictional heat away from the slip interface, determined by the nature of the material, that acts to dissipate the energy of slip events (e.g. Lavallée and Kendrick, 2020 and references therein).

The frictional behaviour of rocks has been studied extensively using field observations (e.g. Sibson, 1994; Di Toro and Pennacchioni, 2005; Di Toro et al., 2005; Mitchell et al., 2016; Hughes et al., 2020), controlled laboratory experiments (e.g. Byerlee, 1978; Marone, 1998; Scholz, 1998; Hirose and Shimamoto, 2005a, 2005b; Di Toro et al., 2006, 2011; Kendrick et al., 2014; Hornby et al., 2015; Wallace et al., 2019a), and modelling (e.g. Nielsen et al., 2008; Weng and Yang, 2018). In an early attempt to reconcile laboratory data, Byerlee (1978) advanced that at low slip velocities and shallow crustal conditions (< 200 MPa normal stress), the shear resistance (τ) of rocks during slip is proportional to the normal stress (σ_n), such that:

$$\tau = \mu\sigma_n \tag{4.1}$$

where μ is the coefficient of friction. At low normal stresses (< 200 MPa), coefficients of friction vary around 0.85 with very large scatter (e.g. 0.3 < μ < 3.0 at σ_n = 5 MPa) and high dependence on surface roughness (Byerlee, 1978). With higher normal stresses (> 200 MPa), the friction coefficients of rocks decrease to approximately 0.6 with lower scatter (e.g. 0.57 < μ < 0.62: Byerlee, 1978), unless the rocks are clay-rich, in which case μ may be significantly lower (e.g. Collettini et al., 2009, 2019; Ikari et al., 2009). Yet, faulting events are dynamic, and as such friction is often expressed via the rate-and-state friction constitutive law, which includes consideration of time, slip velocity and displacement (Dieterich, 1979; Ruina, 1983). This description is particularly important at velocities associated with seismic events, as a rate weakening response has been observed in a variety of rock types. In some instances, high slip rates may promote frictional coefficients even lower than 0.1 (Di Toro et al., 2011). Such occurrences have been attributed to a range of physical and chemical processes that are dependent on both rock type and slip conditions, including: thermal pressurisation of pore fluids (e.g. Sibson, 1973; Rice, 2006); flash heating (e.g. Rice, 2006); chemical decomposition (e.g. Han et al., 2007); production of gouge by material wear, abrasion and comminution (e.g. Matsu'ura et al., 1992); formation of silica gel (from water quartz interaction; e.g. Di Toro et al., 2004); and frictional melting (Hirose and Shimamoto, 2005b; Di Toro et al., 2006).These processes are determined primarily by the nature and evolution of the contact surface of the slip interface. Within geomaterials, widely ranging fractions of void space in the form of pores (vesicles) and fractures (cracks) concentrate stress and localise fracture nucleation, ultimately reducing the strength (Al-Harthi et al., 1999; Heap et al., 2014b; Vasseur et al., 2015; A Bubeck et al., 2017). The presence of pores and fractures in contact with the slip interface acts to increase the roughness of the surface and reduce the potential contact area (e.g. Rapetto et al., 2009), which results in locally higher stresses that concentrate the mechanical wear and frictional heating to a smaller surface area (Engelder and Scholz, 1976; Scholz and Engelder, 1976; Bhushan, 1998). Greater normal stresses increase the geometric interaction of rough surfaces by asperity deformation (Bhushan, 1998; Bowden and Tabor, 2001).

Fracturing and wear of slip surfaces can create a cataclastic gouge layer with diminishing grain size upon attrition (Engelder, 1974; Mair and Abe, 2011), and generally, gouge zone thickness increases with increasing slip distance (Scholz, 1987). The generation of gouge influences the frictional behaviour by the removal of surface asperities (Matsu'ura et al., 1992) and the introduction of a layer of particles with differing frictional behaviour (Sibson,

1994; Niemeijer et al., 2010; Lavallée et al., 2014). Field and structural observations of natural faults exhibiting large amounts of gouge and cataclasite often indicate lower apparent frictional coefficients than those with rock-rock contact surfaces (Sibson, 1994; Townend, 2006), which is supported by experimental investigations of gouge samples (Ikari et al., 2009; Niemeijer et al., 2010; Lavallée et al., 2014; Faulkner et al., 2018). There are many examples of the products of frictional sliding preserved in the rock record, the nature of which are determined by the lithologies involved and the conditions at which slip occurred. In the brittle regime in near surface shear zones, gouge and cataclasite layers and zones are preserved (Engelder, 1974; Sibson, 1977; Wallace et al., 2019b). At greater pressures, ductile mylonites are formed (Sibson, 1977) and in cases of extreme heating during slip, pseudotachylytes, solidified frictional melts, occur (Sibson, 1977; Di Toro et al., 2011; Kendrick et al., 2012; Mitchell et al., 2016) and are often used as evidence for the occurrence of coseismic slip (Sibson, 1975; Cowan, 1999), though they have also been recorded in mass movements (e.g. Masch et al., 1985; Grunewald et al., 2000; Hacker et al., 2014; Hughes et al., 2020a).

Although friction coefficient is relatively easy to calculate from experiments and model from natural faults, explaining the active mechanisms, their temporal occurrence, competing influence and evolution is more difficult (e.g. Rutter et al., 2001). Transience of multiple conditions such as cohesion, composition, interface geometry (roughness), loading, saturation and the presence of lubricating layers (such as melt, gouge, nanoparticles or silica gel) ultimately determine the evolution of slip behaviour (Scholz, 2019) . Friction and wear are considered linked processes in tribology and are often studied in conjunction with one another as they can elucidate temporal transitions (Yoshioka, 1986; Wang and Scholz, 1994; Hirose et al., 2012; Boneh et al., 2013; Boneh and Reches, 2018). Wear is largely controlled by the failure of asperity contacts (Archard, 1953; Rabinowicz, 1965; Bowden and Tabor, 2001) and results from a mix of complex mechanisms: adhesive, effective at asperity contacts (Archard, 1953); abrasive, from asperity ploughing (Moore and King, 1980); delamination, where damage occurs away from the sliding surface (Fleming and Suh, 1977); fatigue, from repeating events (Rozeanu, 1963); and corrosive due to chemical weakening (Watson et al., 1995). Archard (1953) studied the global wear of faults and introduced Archard's equation. This is given as:

$$G = KD\left(\frac{\sigma_n}{H}\right) \tag{4.2}$$

where the cumulative wear volume (G) from two surfaces with a given normal stress (σ_n) is calculated after a given slip distance (D), considering the wear coefficient (K) in units of m^2, and the hardness of the softer of the two materials in contact (H). However, it was later noted that this only considers steady state wear, whereas experimental data also suggests an initial transient running-in phase, with elevated wear rates (Queener et al., 1965). The transient running-in phase is linked with initial asperity removal, whilst steady state wear rates are associated with the continued removal of material at the surface (Wang and Scholz, 1994). Additionally, Archard's model fails to consider the effect of slip velocity, which has been shown to have a large impact on wear rates (Hirose et al., 2012; Boneh et al., 2013). Boneh and Reches (2018) found wear rate to increase with slowness (inverse slip velocity) for a range of lithologies (sandstones, granites and carbonates) tested, a phenomena also noted in ceramics at slip velocities up to 1 m s^{-1} (Conway et al., 1988; Al-Qutub et al., 2008).

As asperities and roughness on slip surface interfaces have a key control on wear, friction and on the nucleation of seismic ruptures (i.e., relations between critical slip distance and asperity size; e.g. Dieterich, 1979), numerous geophysical/geological studies have investigated roughness and evolution of roughness along sliding surfaces with increasing cumulative slip (Scholz, 1987; Power et al., 1988; Sagy et al., 2007; Candela et al., 2012; Brodsky et al., 2016). Investigations have found that fault surfaces are fractal in nature, being self-similar to self-affine (Power et al., 1988; Sagy et al., 2007), with roughness evolving to smoother forms with increasing slip via abrasion and fracturing, forming fault rock products such as gouge (Sagy et al., 2007). During experimentation the scale of investigation is often limited due to experimental geometric constraints, where roughness of samples cannot replicate the fractal nature of large fault surfaces observed in nature. As a result, natural faults have been shown to exhibit a broader range of wear rates during slip than their experimental counterparts (Scholz, 1987; Boneh et al., 2013; Boneh and Reches, 2018).

Multiple studies have used natural or synthetic gouge samples to investigate the frictional properties of gouge layers during slip events (e.g. Numelin et al., 2007; Lavallée et al., 2014; Togo et al., 2016). However, such studies do not quantify the early comminution of material at the onset of slip and the formation of a layer of cataclasite or gouge. During the onset of slip, frictional sliding is dominated by the interaction of asperities (controlled by normal stress and slip rate) so that roughness is a key parameter, as opposed to in the presence of a gouge layer, which produces a three-body system consisting of two wall rock surfaces and a granular layer (Matsu'ura et al., 1992; Sagy et al., 2007).

Due to the complex and heterogeneous nature of natural rock samples, it is difficult to compare the influence of individual variables on the wear and frictional responses of rocks. As such, the use of synthetic proxies for geomaterials, specifically variably indurated glass beads, may be used to systematically and independently vary properties such as porosity in order to determine their role (Wadsworth et al., 2016; Ryan et al., 2019).

4.2. Methods and Materials

In order to test the influence of porosity on frictional behaviour, wear and comminution, we elected to use glass beads sintered to three target porosities (8, 19 and 30 %). These porosities were chosen because they represent realistic values for a range of natural geomaterials found in shallow, structurally active settings (e.g. Wheaton, 2016). During sintering above the glass transition temperature (T_g), porosity of the viscous droplets (glass beads) reduces according to a characteristic timeframe, driven by surface tension (Wadsworth et al., 2016). The porosity reduction is repeatable and predictable for a given temperature, thus by controlling temperature and dwell time, the target porosity can be achieved. We used soda lime silica glass spheres (Spheriglass® A-glass Solid Glass Microspheres, product number 1922, Potters Industries Inc) as a starting material which has well constrained properties, including a known T_g value of 824 K (551°C; at 10 °C min^{-1}). Product 1922 has a bead size range of 45–90 µm with a particle size distribution mean between 60 and 70 µm, as used in Wadsworth et al. (2016). Samples with 6–11 % and 28–32 % porosities (hereafter known as 8 % and 30 % porosity sample sets) were made at Ludwig-Maximilians-Universität, where microspheres were loosely packed into ceramic trays with dimensions 20 cm by 15 cm and 5 cm deep and heated to 663°C for 2.5 or 13 hours (respectively for the 30 % and 8 % porosity samples), with a heating and cooling rate of 10 °C min^{-1}, following existing protocols and models (see Wadsworth et al., 2016, 2017). The slow heating and cooling rate minimised thermal gradients across the sample, and the relatively low temperature (relative to T_g) ensured that the sintering was slow, minimising the possibility for local heterogeneities. The trays were rotated 180° halfway through the heating process to eliminate any effect of temperature gradients within the furnace. The low depth of the tray ensured that sintering occurred in the scale-independent surface-tension dominated regime, and not the pressure-sintering regime which could induce basal compaction due to overburden (Wadsworth et al., 2019). This process created bricks of sintered material with only slight porosity gradients and packing inconsistencies and a 3-4 % porosity variability (at the sample scale) across the slabs; this gradient was negligible in the

direction of coring from the side of the sample block and therefore did not affect individual samples.

The 19 % porosity samples were made at the University of Liverpool to obtain a sample set between the other two porosity ranges. Beads were loaded into cylindrical ceramic crucibles 5 cm in height and heated to 725°C and dwelled for 25 minutes with a heating and cooling rate of 10 °C min^{-1} (total time during which sintering was active above T_g was 60 minutes). Single samples were then cored from each crucible and the porosity was found to be repeatable using this method, although slight, repeatable gradients existed from top (denser) to bottom, likely due to slight temperature gradients. It was ensured that the slip surface for the test was cut at the same height within each sample where the porosity was 18-20 % porosity (hereafter called the 19 % porosity sample set).

Porosities of all samples were determined by constraining the sample density (ρ_s):

$$\rho_s = \frac{m}{\pi r^2 h} \tag{4.3}$$

where m is mass (in kg), h is height and r is radius (both in m) for each core. Then, determining the solid phase density (ρ_0) of the sample by measuring the inaccessible volume of each core in an AccuPyc II 1340 helium pycnometer from Micromeritics, so that porosity (φ) can be estimated by:

$$\varphi = 1 - \frac{\rho_s}{\rho_0} \tag{4.4}$$

A total of 44 friction experiments were performed on a 2nd generation low to high velocity rotary shear apparatus (LHVR) from Marui instruments at the University of Liverpool, a successor to the 1st generation apparatus designed and described by Shimamoto (1994). The LHVR uses a concentric sample geometry and is capable of a rotational speed range of 1 rotation per year to a maximum of 1500 rotations per minute (rpm) and normal force (axial load) of up to 10 kN as described in Ma et al. (2014). Hollow samples with 25.0 mm outer diameter and 8.5 mm inner diameters were cored from each of the three porosity sample groups (8, 19 and 30 %), resulting in an 8.25 mm wide annular slip surface. The axial load was applied using a gas actuator controlling the position of, and stress exerted by, the lower column. Three normal stresses of 0.25, 0.5 and 1 MPa were applied to the specimens, with normal stress (MPa) calculated by dividing applied force (kN) by the slip surface area. During each experiment torque was used to calculate shear stress (τ, see details in Hirose and

Shimamoto, 2005b) and an LVDT attached to the lower column recorded the axial shortening, used here as a measure of wear.

To examine the effects of slip rate on frictional behaviour, wear and comminution, we used a range of constant slip rates. Tests were conducted at 0.1, 0.2, 0.3, 0.4, and 0.5 m s^{-1} at each of the normal stresses; 0.25, 0.5 and 1 MPa. Additional 1.0 m s^{-1} tests were also conducted at 1 MPa for each of the sample sets. Due to variations in angular velocity across the slip surface, an equivalent slip rate (V) was calculated after Hirose and Shimamoto (2005b), assuming constant shear stress across the slip surface:

$$V = \frac{4\pi R\,(r_1^2 + r_1 r_2 + r_2^2)}{3(r_1 + r_2)} \tag{4.5}$$

where R is the revolution rate of the motor, r_1 is outer radius and r_2 is inner radius.

Cumulative rotations recorded via a tachometer on the rotating upper column were used to calculate cumulative and total slip distance (hereafter termed displacement) of the experiments using the equivalent slip rate (V in m s^{-1}). Most experiments were performed to displacements of 9-10 m with the exception of samples that failed, and samples with very high wear rates that were halted once wear rates and shear stresses had stabilised. All data for each test (torque, normal stress, rpm and axial shortening) was recorded at 100 Hz.

For each test friction coefficient (μ) was calculated from normal stress (σ_n in MPa) and shear stress (τ in MPa) using:

$$\mu = \frac{\tau}{\sigma_n} \tag{4.6}$$

Work per unit area (W in MJ m^{-2}) of the slip surface was calculated by the integration of the experimentally generated shear stress curve (after Abercrombie and Rice, 2005; Di Toro et al., 2012; Kanamori and Rivera, 2013). In order to compare this to both wear and heating rates, the work during steady state slip (W_{ss} in MJ m^{-2}) was calculated and divided by the displacement over which steady state conditions were measured (D_{ss}; see Table 1) to produce the work per metre slip during the steady state period (W_M in MJ m^{-2} m^{-1}).

In order to evaluate the combined effect of slip rate and normal stress, the mean power density per unit area (P_D in MW m^{-2}) of the slip surface was calculated for all tests for the period of steady state shear stress (τ_{ss}) and wear to describe the energy dissipation rate at the slip surface, via:

$$P_D = V\tau_{ss} \tag{4.7}$$

where τ_{ss} is the mean shear stress during the period of steady state sliding (from which shortening rates and heating rates were also calculated).

All experiments were recorded using a FLIR X6000sc thermographic infrared camera at 20 Hz. The camera was placed at a distance of 70 cm to monitor sample surface temperature of the slip zone and adjacent wall material due to frictional heating at a pixel size of approximately 0.15 mm. The data was analysed with the FLIR IR Max software.

A thermomechanical analyser (TMA) 402F1 Hyperion (Netzsch GmbH) was used to measure the coefficient of thermal expansion of the three glasses with different porosities.

The analysis was performed on 6 mm diameter cores, 5 mm in height and at a heating rate of 10 °C min^{-1} with a constant normal force of 0.5 N. To accurately determine the expansion coefficient of our samples, a cylinder of standard alumina, of equal dimension to our porous glasses, was first heated using the pre-determined temperature and loading profile to obtain a baseline of sample assembly expansivity; length changes are monitored at a resolution of 0.125 nm. Once completed, the same temperature and loading profile was applied to the porous glass samples, and the thermal expansion constrained in the baseline run was subtracted to the sample run to accurately determine the expansion coefficient (with trivial measurement errors of < 0.2 %).

Table 4.1. Mechanical and Temperature data for all experiments

Sample name	Sample set porosity	Applied normal stress	Slip rate	Rotations	Total displacement	Wear rate	Measured normal stress	Peak shear stress	Steady-state shear stress	Steady-state shear standard deviation	Steady-state shear stress standard error	Friction coeff.	Friction coeff. standard deviation	Friction coeff. standard error	Steady state conditions	Power density	Work per metre slip	T_{max}	Heating rate
	%	MPa	m s^{-1}	n	m	mm m^{-1}	MPa	MPa	MPa	MPa	MPa				m	MW m^{-2}	J m^{-2} m^{-1}	ºC	°C m^{-1}
SINT_GLASS_6		0.25	0.1	350.0	19.98	0.0020	0.2361	0.2058	0.0283	0.0678	0.0005	0.1198	0.358953	0.002907	4.42-19.57	0.0028	0.3362	60	5.0410
SINT_GLASS_8		0.25	0.1	159.0	9.08	0.0024	0.2311	0.0694	0.0022	0.0553	0.0007	0.0095	0.291967	0.00369	2.36-8.58	0.0002	0.0136	25	3.9234
SINT_GLASS_9		0.25	0.2	182.9	10.39	0.0022	0.2449	0.0987	0.0577	0.0492	0.0011	0.2357	0.231047	0.00515	4.00-8.00	0.0115	0.2312	29	2.3984
SINT_GLASS_10		0.25	0.3	157.1	8.90	0.0027	0.2351	0.0975	0.0837	0.0420	0.0016	0.3560	0.222271	0.008574	4.00-6.00	0.0251	0.1672	28	1.4738
SINT_GLASS_11		0.25	0.4	162.5	9.91	0.0008	0.2506	0.0896	0.0329	0.0370	0.0016	0.1313	0.157813	0.00703	4.00-6.00	0.0132	0.0658	28	1.1594
SINT_GLASS_12		0.25	0.5	165.0	9.31	0.0000	0.2432	0.0302	0.0202	0.0856	0.0035	0.0831	0.363994	0.014811	3.00-6.00	0.0101	0.0600	27	2.0200
SINT_GLASS_13	6 to 11	0.51	0.1	157.1	8.96	0.0024	0.5032	0.0475	0.0061	0.0570	0.0009	0.0121	0.115566	0.001822	4.00-8.00	0.0006	0.0244	32	3.3594
SINT_GLASS_14		0.51	0.2	160.5	9.11	0.0013	0.4991	0.0882	0.0395	0.0484	0.0012	0.0791	0.099179	0.002553	3.00-6.00	0.0079	0.1185	32	2.7479
SINT_GLASS_15		0.51	0.3	164.1	9.30	0.0037	0.4945	0.1326	0.0779	0.0432	0.0010	0.1576	0.090828	0.002072	2.27-8.00	0.0234	0.4460	33	7.0655
SINT_GLASS_16		0.51	0.4	162.0	9.16	0.0028	0.5045	0.0756	0.0459	0.0393	0.0017	0.0909	0.078778	0.003509	2.00-4.00	0.0184	0.0917	40	5.8805
SINT_GLASS_17		0.51	0.5	211.8	11.97	0.0091	0.5013	0.0681	0.0280	0.1043	0.0052	0.0559	0.211374	0.010529	1.00-3.00	0.0140	0.1353	48	9.0544
SINT_GLASS_9		1.02	0.1	158.9	9.04	0.0100	0.9743	0.1214	0.0609	0.0555	0.0010	0.0625	0.05768	0.001049	5.00-8.00	0.0061	0.1826	52	8.9277
SINT_GLASS_10		1.02	0.2	157.5	8.94	0.0032	1.0136	0.2543	0.1672	0.0483	0.0011	0.1650	0.048795	0.001087	4.00-8.00	0.0334	0.6691	54	-2.7280

SINT_GLASS_11		1.02	0.3	149.7	8.48	0.0023	1.0118	0.4468	0.3013	0.0456	0.0018	0.2978	0.047227	0.001822	3.00-5.00	0.0904	0.6034	90	2.1196
SINT_GLASS_7		1.02	1.0	43.0	2.31	0.0342	1.0025	1.6075	0.3933	0.1268	0.0211	0.3924	0.121517	0.020253	0.54-0.92	0.3933	0.1490	188	11.1297
SINT_GLASS_16	18 to 20	0.25	0.1	176.1	10.08	0.0123	0.2384	0.1065	0.0506	0.0503	0.0009	0.2123	0.237388	0.00433	3.00-6.00	0.0051	0.1519	83	7.8169
SINT_GLASS_12		0.25	0.1	175.4	10.00	0.0046	0.2224	0.1340	0.0872	0.0536	0.0008	0.3921	0.299025	0.004717	4.00-8.00	0.0087	0.3487	41	3.3868
SINT_GLASS_13		0.25	0.2	178.2	10.08	0.0074	0.2391	0.1710	0.0814	0.0452	0.0011	0.3405	0.22476	0.005362	6.32-9.82	0.0163	0.2850	53	4.1109
SINT_GLASS_14		0.25	0.3	175.7	9.97	0.0009	0.2288	0.1478	0.0723	0.0423	0.0012	0.3161	0.214733	0.005864	4.00-8.00	0.0217	0.2894	85	-30.7739
SINT_GLASS_15		0.25	0.4	176.4	9.98	0.0187	0.2400	0.1349	0.0593	0.0405	0.0013	0.2469	0.178786	0.005637	4.00-8.00	0.0237	0.2369	128	5.6241
SINT_GLASS_17		0.25	0.5	176.7	9.98	0.0243	0.2444	0.1048	0.0674	0.1026	0.0036	0.2757	0.435778	0.015359	4.00-8.00	0.0337	0.4275	165	2.1613
SINT_GLASS_15		0.51	0.1	175.8	10.07	0.0096	0.5168	0.4380	0.2353	0.0507	0.0008	0.4554	0.110318	0.001744	4.00-8.00	0.0235	0.9412	94	2.1795
SINT_GLASS_18		0.51	0.1	175.9	10.08	0.0754	0.5117	0.3232	0.1599	0.0588	0.0010	0.3125	0.12346	0.002116	6.20-9.55	0.0160	0.5368	120	49.8186
SINT_GLASS_19		0.51	0.2	176.6	10.06	0.0210	0.5193	0.4150	0.1645	0.0429	0.0010	0.3168	0.092248	0.002059	4.00-8.00	0.0329	0.6580	129	31.3364
SINT_GLASS_20		0.51	0.3	176.8	10.04	0.0174	0.5214	0.4164	0.1609	0.0436	0.0012	0.3086	0.090577	0.002474	2.00-6.00	0.0483	0.6439	169	62.1597
SINT_GLASS_14		0.51	0.4	179.0	10.14	0.0151	0.5209	0.2185	0.1162	0.0360	0.0013	0.2231	0.071523	0.002605	7.00-10.00	0.0465	0.3482	119	20.5676
SINT_GLASS_21		0.51	0.5	179.5	10.15	0.0076	0.5178	0.1795	0.1125	0.0930	0.0033	0.2172	0.181074	0.006378	4.00-8.00	0.0562	0.4506	76	10.7325
SINT_GLASS_16		1.02	0.1	150.6	8.64	0.0490	1.0150	0.9210	0.3556	0.0583	0.0013	0.3503	0.061164	0.001367	2.00-4.00	0.0356	0.7112	138	22.3711
SINT_GLASS_16		1.02	0.2	105.5	5.97	0.0311	1.0076	0.9855	0.6234	0.0438	0.0020	0.6187	0.054745	0.002439	0.50-1.50	0.1247	0.6225	260	30.2604
SINT_GLASS_13		1.02	1.0	57.2	3.06	0.3148	1.0338	0.6042	0.5591	0.0233	0.0053	0.5409	0.022564	0.005177	0.50-1.00	0.5591	0.2817	206	102.8708
SINT_GLASS_8	28 to 32	0.25	0.1	89.7	5.11	0.3892	0.2415	0.2981	0.1274	0.1014	0.0018	0.5276	0.623988	0.01136	2.00-5.00	0.0127	0.8267	55	15.7095
SINT_GLASS_4		0.25	0.2	85.8	4.79	0.3017	0.2249	0.3366	0.1413	0.0872	0.0027	0.6280	0.802306	0.025295	2.00-4.00	0.0283	0.2821	57	13.1761
SINT_GLASS_5		0.25	0.3	162.7	9.22	0.0467	0.2432	0.2745	0.1721	0.0924	0.0036	0.7074	0.426612	0.016469	4.00-6.00	0.0516	0.3438	76	8.4231
SINT_GLASS_6		0.25	0.4	115.4	6.51	0.0937	0.2447	0.3242	0.1945	0.0999	0.0036	0.7949	0.595399	0.021669	2.00-5.00	0.0778	0.5834	76	22.2166

SINT_GLASS_7		0.25	0.5	126.2	7.09	0.0456	0.2378	0.3385	0.1987	0.1187	0.0059	0.8355	0.534798	0.026607	2.50-4.50	0.0993	0.3977	111	31.4377
SINT_GLASS_9		0.51	0.1	151.1	8.62	0.2890	0.4961	0.7017	0.3172	0.1740	0.0032	0.6394	0.369796	0.006732	4.00-7.00	0.0317	0.9521	103	24.4157
SINT_GLASS_10		0.51	0.2	213.6	12.14	0.2377	0.4708	0.6754	0.3352	0.2083	0.0046	0.7120	0.461912	0.0103	4.00-8.00	0.0670	1.3403	120	18.1324
SINT_GLASS_12		0.51	0.3	208.7	11.84	0.0763	0.5009	0.7447	0.4198	0.0998	0.0031	0.8380	0.225777	0.007122	4.49-7.49	0.1259	1.2592	182	58.0135
SINT_GLASS_3		0.51	0.4	157.1	8.87	0.0767	0.4924	0.5231	0.3494	0.0992	0.0036	0.7097	0.21795	0.007932	2.00-5.00	0.1398	1.0474	241	52.8097
SINT_GLASS_5		0.51	0.5	161.2	9.08	0.0441	0.4783	0.5505	0.2893	0.1103	0.0055	0.6049	0.237924	0.011837	6.00-8.00	0.1447	0.5785	253	52.1852
SINT_GLASS_6		1.02	0.1	78.9	4.46	0.1625	0.9903	1.0238	0.5653	0.1876	0.0048	0.5709	0.19323	0.004959	2.50-4.00	0.0565	0.8487	155	38.1039
SINT_GLASS_7		1.02	0.2	49.6	2.79	0.2827	0.9839	1.4830	0.8833	0.2239	0.0141	0.8977	0.233766	0.014697	1.50-2.00	0.1767	0.4413	222	18.0725
SINT_GLASS_2		1.02	1.0	25.8	1.44	0.7895	0.9130	1.1108	0.5605	0.0921	0.0147	0.6139	0.106696	0.017085	0.20-0.60	0.5605	0.2142	230	172.9855

The thermal expansivity determination, combined with the thermographic data, was used to model the effect of thermal expansion on the monitored axial displacement during frictional sliding, and to correct the axial shortening data, used to calculate wear accurately. Thermal expansion was identified during frictional testing by a phenomenon where some experiments showed net lengthening of the sample despite wear products being observed (due to the expansion outweighing comminution). To correct the length change for thermal expansion, first the temperature of each 0.15 mm pixel along a profile of the sample, perpendicular to the slip zone was measured for each frame of thermal data. Then, the net expansion of the sample was calculated by determining the length change experienced along this profile by summing the individual expansions according to the temperature in each pixel (obtained from the thermal expansion profiles of the materials measured using the TMA). The net expansion was then subtracted from the measured shortening throughout the test to identify the true shortening (wear) and rate of wear (see Appendix III, Figures A.III.2 – A.III.4). As the thermographic data used in this correction was measured from the outer surface of the sample it is a minimum estimate of slip zone temperature (due to not accounting for potentially higher temperatures within the sample). Therefore, despite the high accuracy of samples' thermal expansivity determined by TMA (i.e., <0.2 %), the modelled thermal expansivity at any point during slip is likely underestimated due to underestimation of the slip zone temperature caused by surface monitoring (to date, no direct slip zone temperature measurements are possible).

Following the experiments, selected samples were dissected and analysis of microstructures was conducted on a benchtop Hitachi TM3000 scanning electron microscope (SEM) with a 15 kV accelerating voltage and a 10 mm working distance. Images were acquired using the Bruker Quantax 70 software.

4.3. Results

During rotary shear experiments at different slip rate and normal stress conditions the shear resistance of variably porous synthetic rock analogues varied, and consequently the friction coefficient, wear rate and frictional heating differed. These three phenomena are explored via (a) evolution during slip, (b) the influence of normal stress and (c) the effect of slip rate, each as a function of porosity. Mechanical and thermal data for all experiments are displayed in Table 1 along with the standard deviation and standard error analysis of the mechanical data.

4.3.1. Frictional behaviour

When slip on a plane initiated, we immediately observed a rapid increase in shear stress for all tests, which was followed by a subsequent reduction in shear stress with increasing displacement (slip distance). This often plateaued at lower shear stress values, referred to as steady state (τ_{ss}) conditions, after 0.5 – 2.0 meters and remained steady throughout the duration of slip (Fig. 4.1a, Appendix III, Figures A.III.2 – A.III.4). In conjunction with the initial stress peak, wear rate was elevated. The rapid initial wear rate during the running-in phase decreased to a constant lower rate as shear stresses reduced to steady state conditions. The rate of evolution of both the shear stress and the wear rate was variable between sample porosities and slip conditions. The lowest porosity samples (8 %) evolved from initial peak friction and wear rates to steady state in the shortest slip distance whereas the 30 % porosity samples took longer to reach steady state, and, in many cases, the interpreted steady state areas were punctuated by multiple shear stress peaks occurring throughout the test, a phenomenon that was less commonly observed at lower porosity. Peaks in shear stress were often accompanied by changes in wear rates and temperature increases. At lower normal stress (i.e., 0.25 MPa), the reduction in shear stress and wear rate to steady state occurs over a longer distance than at higher normal stresses and at lower slip rates this distance also appears to be longer. In most experiments, shear stress response follows a similar pattern as presented in Figure 4.1a (see Appendix III, Figures A.III.2 – A.III.4), where increasingly higher porosities exhibit higher shear stresses and wear (Fig. 4.1a) for a given slip condition. Higher temperatures are also achieved in the higher porosity samples. Temperature profiles for the tests show that heating rates for all samples have an initial rapid increase in temperature. Both 8 % and 19 % porosity samples then achieved a relatively stable slow rate of increase, or temperature stabilised entirely. However, the highest porosity samples (30 %) typically maintained higher rates of heating throughout slip (Fig. 4.1a, Appendix III Figures A.III.2 – A.III.4).

To better compare the influence of normal stress and slip rate on frictional behaviour, steady state shear stress (τ_{ss}) can be plotted against normal stress (σ_n; Fig. 4.1b-d). The gradients of the plots represent the friction coefficient and show the dependence of shear resistance on normal stress. For each given porosity, shear stress increases with normal stress. However, 8 % porosity samples showed a lower sensitivity to normal stress increase, especially from 0.25 to 0.5 MPa (Fig. 4.1b) and had a lower rate of increase to 1 MPa than the other, higher porosity suites (Fig. 4.1c-d). The most porous samples (30 %) had the highest dependence of shear stress on normal stress (Fig. 4.1d).

Correspondingly, the lowest porosity glass samples (8 %) had the lowest shear resistance and associated frictional coefficients for all conditions tested ranging from 0.05 to 0.40 (Fig. 4.1b), reaching a maximum at 0.3 m s^{-1}, which is in the lower end of the friction coefficient values expected for geomaterials at low normal stresses (< 5 MPa; Fig. 3 in Byerlee, 1978). At intermediate porosity (19 %) the friction coefficients were slightly higher, ranging from 0.23 to 0.54 (Fig. 4.1c). At the highest porosity (30 %), the steady state friction coefficient of the samples ranged from 0.57 to 0.81 (calculated from the linear fit of the steady state shear stress), which are typical Byerlee's friction values for rocks (Fig. 4.1d). Experiments conducted at 1 MPa and at 0.4 and 0.5 m s^{-1} for all samples, and at 0.3 m s^{-1} for the 8 and 19 % porosity samples produced a shear stress that exceeded the strength of all the three porosity sample sets and the samples failed, resulting in no test data for these conditions.

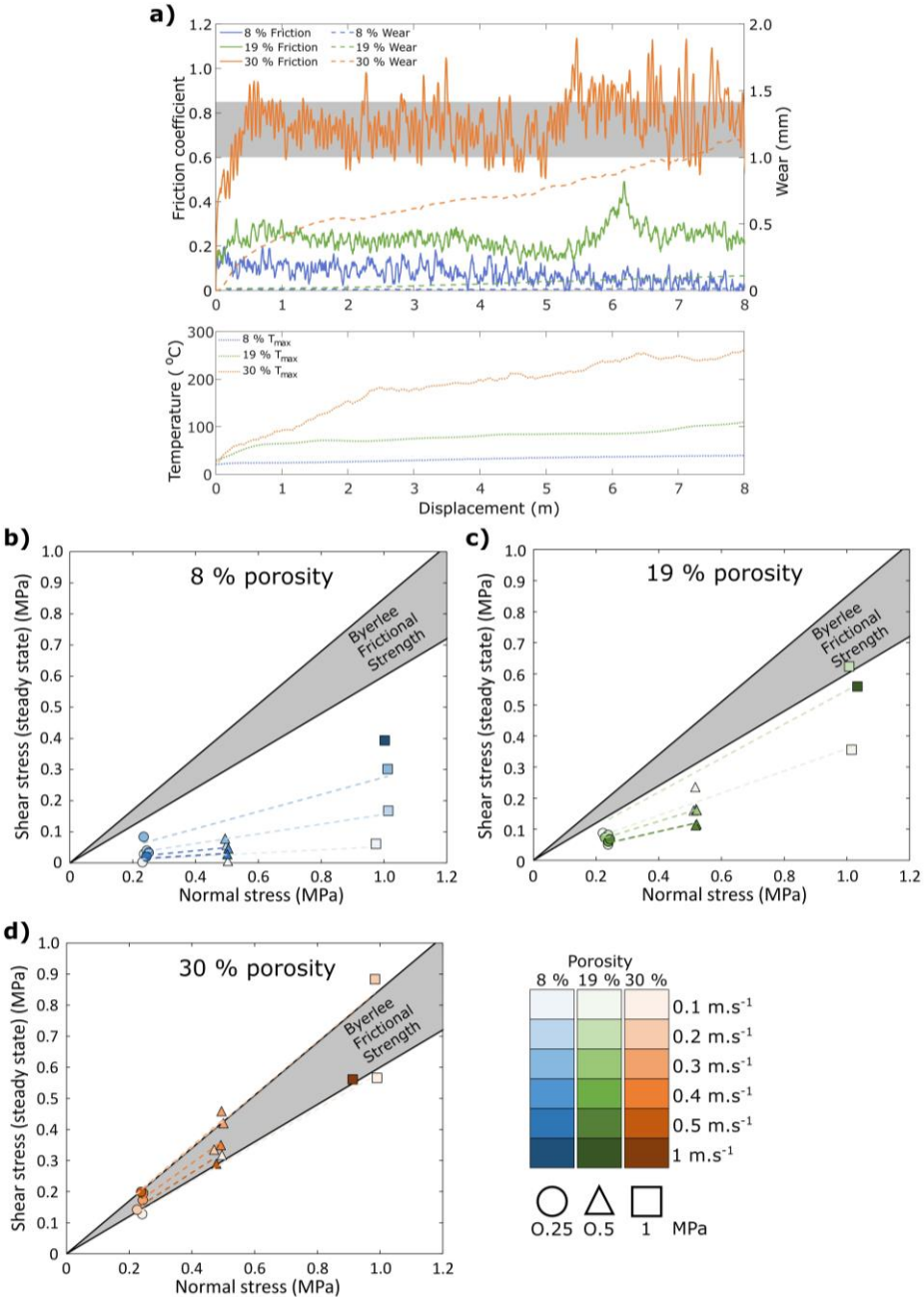

Figure 4.1. Mechanical data for glass analogues with different porosities. a) Example evolution of friction coefficient, shortening (wear) and temperature for slip parameters 0.4 m s^{-1} and 0.5 MPa for the suite of porosities tested (8 % blue, 19 % green and 30 % orange). T_{max} is the peak temperature measured by the thermographic camera in any given frame. Note initially heightened friction coefficients and faster wear at the initiation of slip and subsequent reduction to steady state conditions after approximately 0.5 – 2.0 metres of slip. b-d) Average steady state shear stress (τ_{ss}) plotted against normal stress for b) 8 %, c) 19 % and d) 30 % porosity – see Table 1 for slip distances over which this was measured. The Byerlee friction range 0.6-0.85 is highlighted in grey for reference. Darker colour shades indicate increasing slip rate and shape indicates normal stress. The 30 % porosity sample approximates Byerlee frictional behaviour, and with decreasing porosity the samples' response deviates further.

Shear stress, and hence friction coefficients show a dependence on slip rate (Fig. 4.1b-d). Friction coefficients initially increase with higher slip rates (at low slip rates) but switch to decreasing friction coefficients at faster slip rates, shown in Figure 4.2 (which plots friction coefficients calculated for each slip rate using the gradients in Fig. 4.1b-d, see Appendix III, Table A.III.1). In detail, samples exhibit velocity strengthening up to 0.2 -0.3 m s^{-1}, followed by the onset of velocity weakening behaviour at around 0.3-0.4 m s^{-1} for all porosities tested, resulting in lower frictional coefficients until 0.5 m s^{-1}. Results for high-velocity tests of 1 m s^{-1} for each porosity sample set show another increase in friction coefficient for 8 and 19 % porosity samples, and stabilisation for the 30 % porosity sample (Fig. 4.2), though it should be noted that 1 m s^{-1} tests were only conducted at 1 MPa.

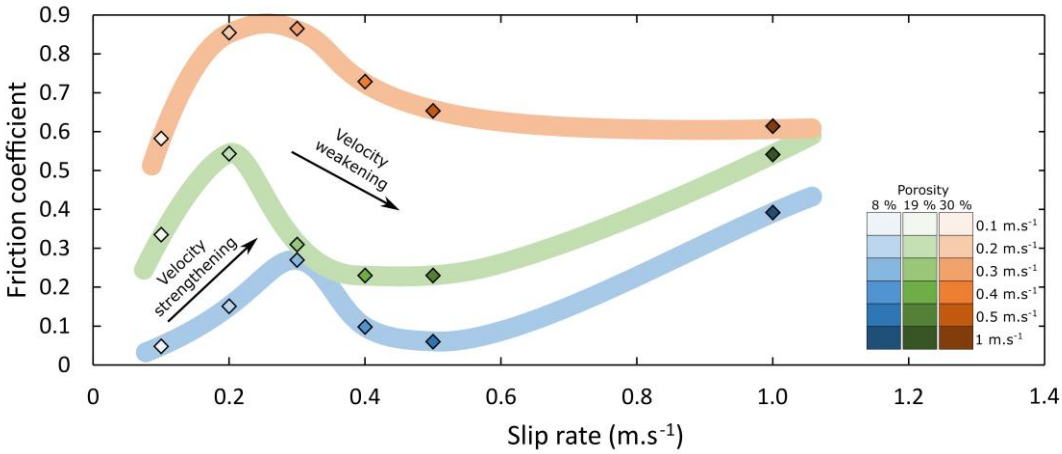

Figure 4.2. Friction coefficient for each porosity material (8, 19 and 30 %) calculated from data displayed in Figure 4.1b-d and plotted against slip rate for all porosities (colour denotes porosity, shade is slip rate from 0.1 – 1.0 m s^{-1}). Note that friction coefficients increase at rates up to 0.3 m s^{-1} and decrease with increasingly higher slip rates as marked with sketch lines.

4.3.2. Wear rate

The initiation of slip and the early slip phase are associated with initially high wear rate that gradually decreases to a steady rate over a period of running in described above (Fig. 4.1a, Appendix II, Figures A.III.2 – A.III.4). Once steady state wear rate is achieved, it is greater for higher porosity samples for each given slip rate and normal stress (Fig. 4.3). Both 8 % and 19 % porosity samples show much lower wear rates than 30 % porosity samples at the same conditions (Fig. 4.3). The 30 % porosity samples have more variable wear rates throughout slip, though an overall reduction in rate to a steady state value is still observed (Fig. 4.1a) and perturbations in wear rate often coincide with variations (peaks) in shear stress (Fig. 4.1a, Appendix II, Figures A.III.2 – A.III.4).

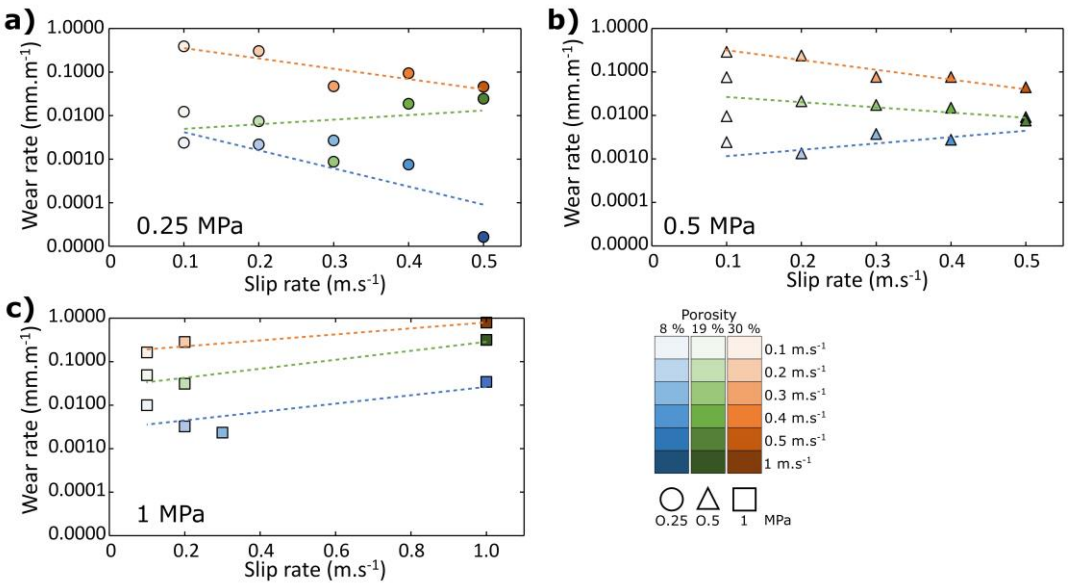

Figure 4.3. Wear rate as a function of slip rate for samples of each porosity (8, 19 and 30 %), at a) 0.25 MPa, b) 0.5 MPa, c) 1.0 MPa normal stress. Wear rates generally increase with increasing axial load and are highest for the 30 %, followed by 19 % and finally 8 % porosity samples. At normal stresses of 0.25 and 0.5 MPa the 30 % porosity samples show reduction in wear rate with higher slip rates, with a reversed trend at 1.0 MPa. 8 and 19 % porosity exhibit negligible wear rates at 0.25 MPa and 0.5 MPa (Fig. 4.1b). 1 m s^{-1} test show much higher wear rates than low slip rate experiments. All wear rates have been corrected for thermal expansion using coefficient of expansion and thermal data recorded during tests.

In order to compare wear across different slip conditions we define wear rate during the steady state period of slip as wear per unit slip distance (mm m^{-1}). Comparing these wear rates (Fig. 4.3), we observe that at all conditions (of normal stress and slip rate) wear rate is highest in the most porous samples (30 %), intermediate in the mid-porosity samples (19 %) and lowest in the low porosity samples (8 %). Additionally, we note that wear rate varies with normal stress (Fig. 4.3). Wear rate is negligible (i.e., < 0.04 mm m^{-1}) at low porosity across all normal stresses tested (0.25, 0.5 and 1.0 MPa), but is still slightly dependent on normal stress, being greater at higher normal stresses for a given slip rate for both the 8 % and 19 % samples, especially at low slip rates. Conversely, 30 % samples exhibited comparable or slightly lower wear rates at higher normal stresses (Fig. 4.3).

In comparing wear rates for each porosity at differing slip rates, we note that the effect is dissimilar at different normal stresses. Wear rate generally reduces with higher slip rates at 0.25 and 0.5 MPa normal stress for all porosities with one exception, the 19 % porosity sample at 0.25 MPa (Fig. 4.3). This observation is supported by visual inspection of the amount of material ejected from the slip surface during experiments, which was seen to be

lower for tests with higher slip rates. The largest reduction in steady state wear rates occurs between 0.2 and 0.3 m s^{-1} (Fig. 4.3a-b), most notably for the 30 % porosity sample experiments. Beyond 0.3 - 0.4 m s^{-1} slip rate, the wear rate stabilises or increases slightly. At 1 MPa, we similarly see that wear rates reduce with increasing slip rates for the lower porosity samples (8 and 19 %) at low velocity (< 0.3 m s^{-1}), yet the 30 % sample shows a reverse trend (it should be noted that these samples experienced very high shear stresses and were stopped prematurely due to accumulating damage). For all porosities the high slip rate tests conducted at 1 m s^{-1} (at 1.0 MPa) show much greater wear rates for all porosities than at any other condition, indicating (as at the lower normal stresses) a reversal in the trend of reducing wear rate with increasing slip rate above ~0.3 m s^{-1} (Fig. 4.3c).

To further investigate the factors controlling wear rate, we evaluate it as a function of friction coefficient, work per metre slip (W_M) and power density (P_D) in Figure. 4.4. Both W_M and P_D are used to evaluate the energy at the slip surface over displacement and time respectively. We note a systematic positive correlation between friction coefficient and wear rate across all sample suites and normal stresses, with each sample suite plotting distinctly but contributing to the larger trend (Fig. 4.4a). This positive correlation is also noted between work per metre slip and wear rate; W_M is seen to be greater for tests with higher normal stress, producing greater wear rates; W_M is typically greater for higher porosity, also resulting in higher wear rates, though the effect of velocity is variable. Overall, wear rate is higher for higher porosity samples for a given W_M (Fig. 4.4b). We note a weaker positive correlation between power density and wear rate for the full experimental suite, but note that each porosity sample set plots with their own distinct trend and that the highest wear rates for each porosity correspond with the highest P_D. Moreover, we note that for the same P_D, wear rates are higher in the most porous samples (Fig. 4.4c). Experiments with negligible wear rates (typically low porosity, low slip rates and low normal stresses) had the lowest power density, work per metre slip and friction coefficients (Fig. 4.4).

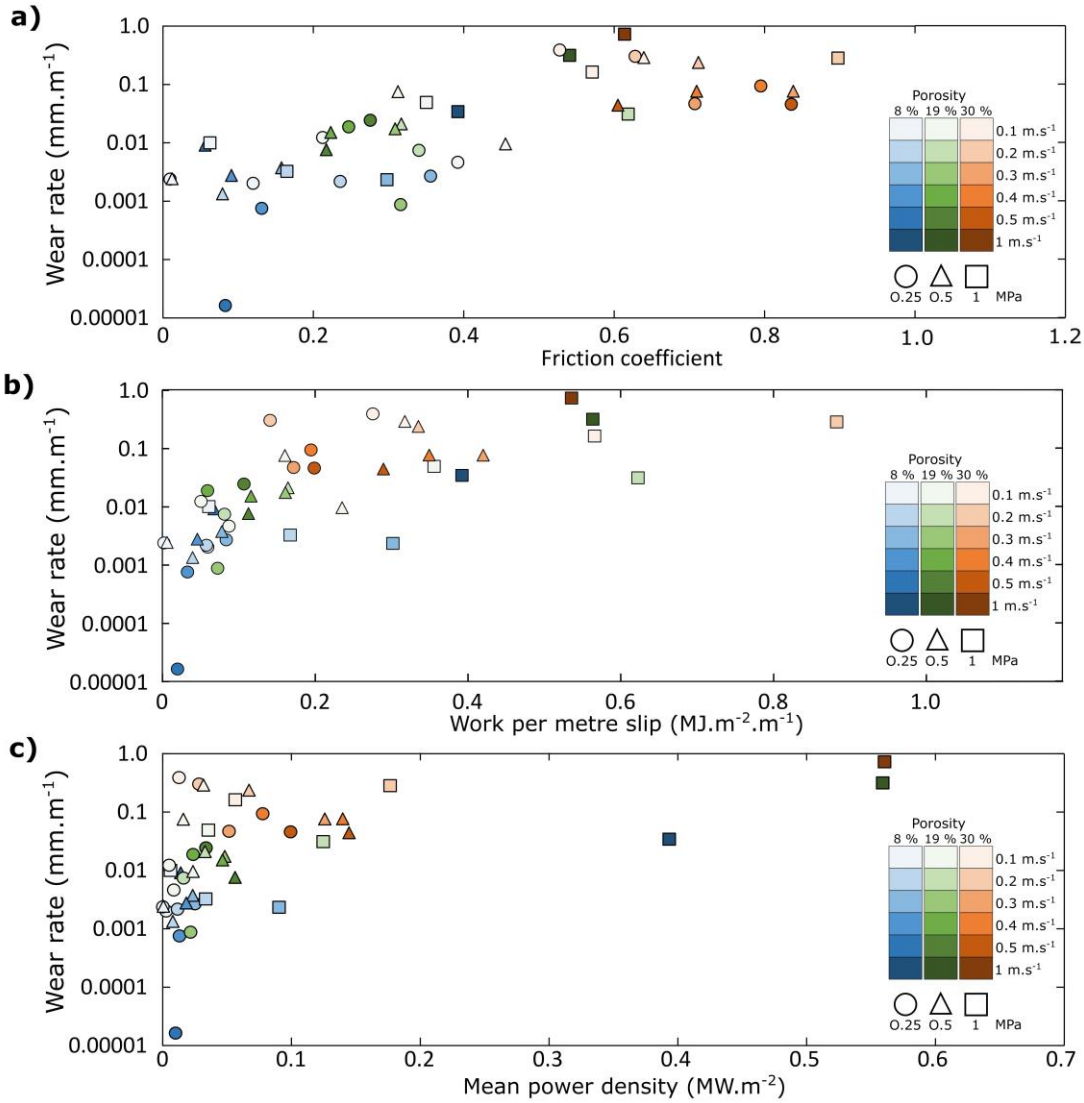

Figure 4.4. Mechanical controls on wear rates achieved during slip. a) Wear rate related to friction coefficient for all tests. High porosity results in higher frictional coefficients and higher wear rates. b) Wear rate as a function of work per metre slip (W_M). c) Wear rate as a function of power density (P_D). Higher W_M and P_D associated with higher porosities and higher wear rates. All wear rates have been corrected for thermal expansion using coefficient of expansion and thermal data recorded during tests.

4.3.3. Frictional heating

Sample surface temperature was monitored continuously using a thermographic camera during experiments. Similar to wear rates, the initiation of slip and running-in period generates a high initial rate of frictional heating which then often decreases to a lower rate of heating after approximately 0.5 – 3.0 m (Fig. 4.1a, Appendix II, Figures A.III.2 – A.III.4). The plateau in temperature was achieved later for the higher porosity sample, in which steady state temperature was occasionally not reached in the slip distance tested. For each given experimental condition (slip rate and normal stress) temperatures on the slip surface at any

point during slip were typically highest in the most porous samples (30 %), intermediate in the mid-porosity samples (19 %) and lowest in the low porosity samples (8 %; Fig. 4.5a-c), though in just over half the conditions tested at the onset of slip (< 3 m) temperature generation in the 19 % sample exceeded the more porous sample, and in a few cases temperature remained higher throughout (Fig. 4.1a, Appendix III, Figures A.III.2 – A.III.4). Variations in heating rate correlate with fluctuations in friction coefficient, though excursions in temperature are typically shorter-lived. As most experiments were halted at a similar slip distance (8-10 m) and because peak temperatures often plateaued, we defined the maximum temperature for each experiment (T_{max}) as a means to systematically compare the effect of each variable (normal stress, slip rate, porosity) on frictional heating [we acknowledge that this approach provides only an indication of the energy dissipated by frictional heating, and provide the details of all temperature data in the Appendix III]. T_{max} shows correlation with normal stress, porosity and slip rate (Fig. 4.5): for a given porosity and slip rate, maximum temperature increases with normal stress (Fig 4.5d-f); and for a given porosity and normal stress, temperature increases with slip rate (Fig. 4.5a-c). The latter being minor in the lowest porosity samples (8 %) at lowest load (0.25 MPa), which show little variation in temperature with increasing slip rate (Fig. 4.5a-b), whereas the 19 % and 30 % porosity samples show a systematic positive trend of greater frictional heating with increasing slip rate at all loads tested (Fig. 4.5d-f). As also seen in the temperature profiles, T_{max} in the 19 % porosity samples sometimes exceed those in the 30 % porosity samples (Fig. 4.5), though it should be noted that tests were stopped after shorter slip distances for the more porous samples due to excessive wear (reaching the apparatus limit; see Appendix III Table A.III.1 and Appendix III, Figures A.III.2 – A.III.4).

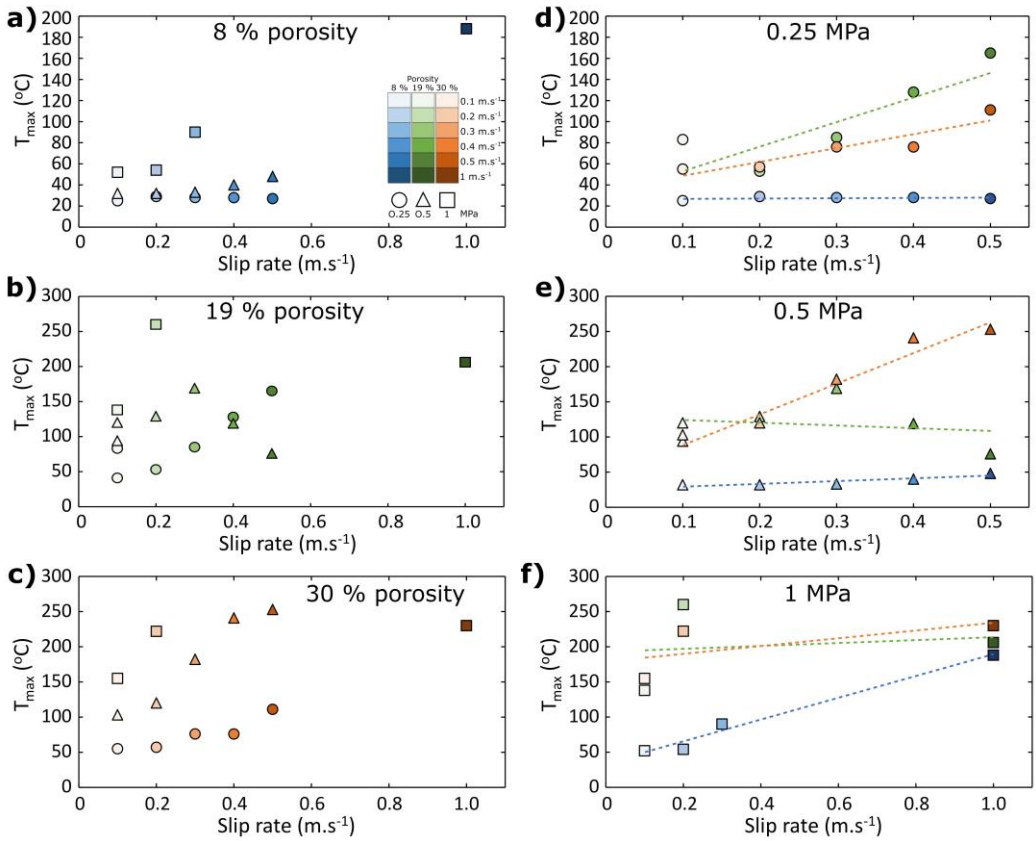

Figure 4.5. Maximum temperature (T_{max}) achieved during slip as a function of slip rate. a-c) The effect of normal stress (0.25, 0.5 and 1.0 MPa) for each of the sample porosities tested, showing higher T_{max} at higher slip rate and at higher normal stress. d-f) The effect of porosity (8, 19 and 30 %) at each of the normal stresses, showing increasing T_{max} with increasing slip rate for all porosities, but a complex impact of porosity on Tmax, where 19 % porosity samples result in higher maximum temperatures than 30 % porosity. Note that T_{max} may occur at different slip distance for each test, a complete temperature record of all experiments is provided in Appendix III.

To further explore the controls on frictional heating we calculated the heating rate per meter of slip during the steady state slip period (the change in peak temperature during τ_{SS}). This heating rate is plotted against both friction coefficient and work per metre slip over the same period for each test (Fig. 4.6a & b). As we found with wear rate, the heating rate shows a positive correlation with friction coefficient across all porosities and experimental parameters, with each porosity plotting distinctly but contributing to the overall trend (Fig. 4.6a). We also see positive correlation between work per metre slip and heating rate, with W_M greater for tests with larger applied normal stress, and for a given normal stress tests with greater slip rates resulted in greater heating rates. Unlike wear rate, each porosity of sample does not have a distinct trend of heating rate as a function of W_M and instead clustering of different porosity samples is observed to contribute to the overall trend (Fig.

4.6b). In comparing heating rates and wear rates, which both positively correlate with friction coefficient and W_M, we note a distinction in the trends (Figs. 4.4 & 4.6). The most porous samples have typically higher W_M and higher wear rates, but not always the highest heating rates, which suggests high wear rates may limit temperature production, as also seen by lower T_{max} for tests with the highest wear rates (Appendix III, Figure A.III.5). We also plot T_{max} against P_D (Fig. 4.6c), noting that each porosity shows a separate positive trend of increasing T_{max}, with the 19 % sample typically having the highest T_{max} for a given P_D.

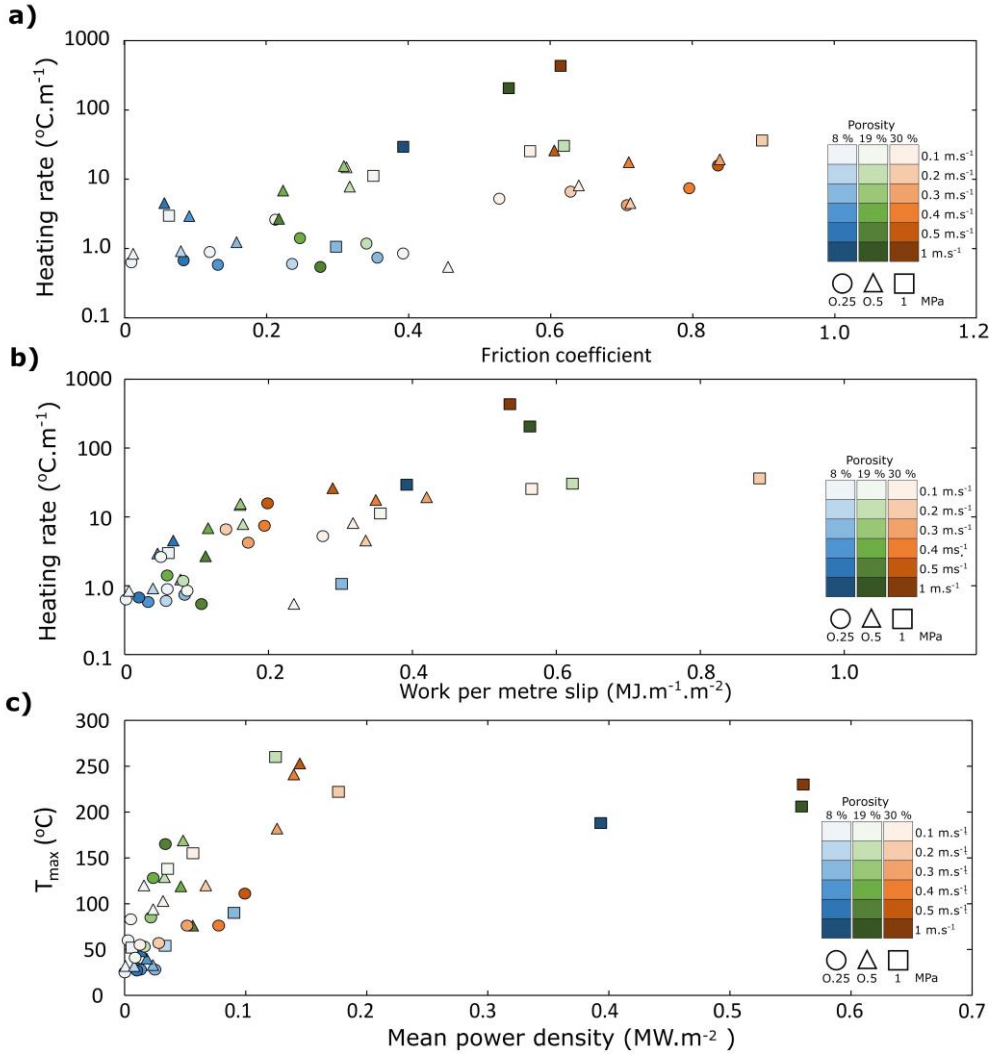

Figure 4.6. Mechanical controls on frictional heat achieved during slip. a) Heating rate plotted against friction coefficient for all tests, showing positive correlation. b) Heating rate plotted against work per metre slip also showing positive correlation, with more work produced per metre of slip resulting in greater heating rates c) T_{max} plotted against mean power density. Note that T_{max} may occur at different slip distances for each test. A complete temperature record of all experiments is provided in the Appendix III.

4.3.4. Comminution and wear mechanisms

Visual inspection of samples after testing revealed notable differences in the damage associated with mechanical wear for each porosity (for original pore structures see Fig. 4.7a-c). Samples that experienced slip at similar conditions (8 % and 19 % samples at 0.1 m s^{-1} at 1 MPa and a 30 % sample at 0.2 m s^{-1} at 1 MPa) were selected and cut perpendicular to the slip direction to expose the damage zone for SEM analysis (Fig. 4.7d-g; for thin section orientation in relation to the experimental set up see Fig. 4.7h). Due to the slight differences in slip rate of the samples, the damage zones were only analysed qualitatively for fracturing style.

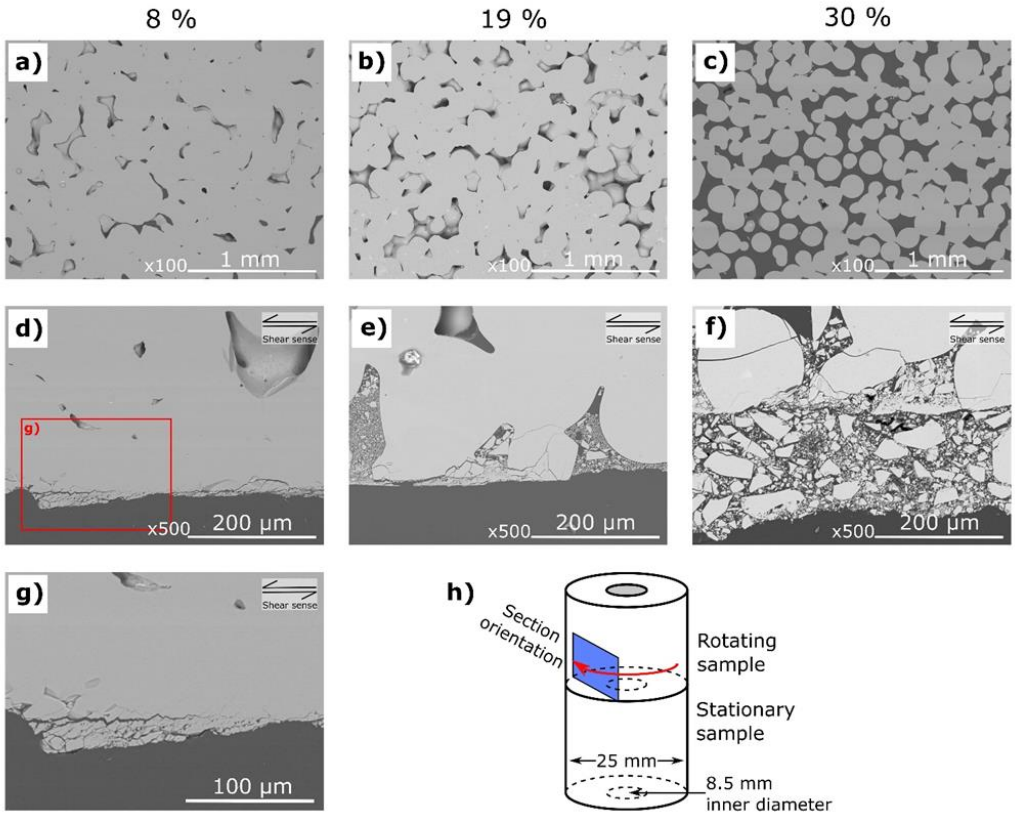

Figure 4.7. Backscattered electron (BSE) images of samples with different porosity. Texture of the sintered glass samples highlighting pore structure prior to testing for a) 8 %, b) 19 % and c) 30 % porosity samples. d) Damage zone of an 8 % porosity sample that experience 9.04 m of slip at 1 MPa at 0.1 m s^{-1} showing minimal penetration of damage (< 50 µm) and Riedel shearing. e) Damage zone of a 19 % porosity sample that experienced 8.64 m of slip at 1 MPa at 0.1 m s^{-1} with more fracturing at pore edges and accumulation of fine-grained (maximum 50 µm to smaller than 1 µm) gouge material within pores. f) Damage zone and gouge of a 30 % porosity sample that experience 2.79 m of slip at 1 MPa at 0.2 m s^{-1} with large fragments up to 100 µm in size in a gouge layer up to 350 µm thick. g) Zoomed area of panel d (shown by the red inset box) at higher magnification to highlight

Riedel structures and the absence of gouge. h) A schematic of thin section orientation (same for all samples) within the sample assembly. Shear for panels d-g is left-lateral (sinistral) as indicated by the schematic.

Increasing the porosity of materials slipping along a fault plane results in a larger zone of damage. The 8 % porosity samples exhibit only a narrow area of damage < 50 µm (Fig. 4.7d, g). Damage presents as Riedel (R) fractures at ~15-30° to the slip surface. These fractures splay into en-echelon R shears and higher angle R' shear fractures propagating into the glass. Where the observed damage zone is thicker, duplexing of R shear fracturing occurs, bounding highly fractured material. On the interior edge of the damage zone, fracturing decreases to single discrete R' fracture sets extending 10-15 µm into the solid glass material (Fig. 4.7g).

The 19 % porosity samples exhibit a similar style of Riedel shear fracturing, though with a thicker damage zone of up to 100 µm is present, with longer fractures (Fig. 4.7e). Unlike the 8 % samples, 19 % samples had multiple pore spaces that interacted with the slip surface and damage zone. Gouge particles were preserved in these pores, with particle sizes ranging from < 1 µm up to 40-50 µm angular fragments (Fig. 4.7e). High angle R' fractures extend further into the glass, especially around pores; Figure 4.7e shows a fracture extending ~100 µm into the glass from the trailing edge of the pore relative to slip direction and several in-place angular fragments of ~10 µm.

The most porous sample (30 %) has the largest gouge layer and damage zone, comprising a 200-300 µm thick layer of gouge with a range of fragment sizes from < 1 µm up to the largest observed fragments at around 90 µm in size (Fig. 4.7f). Fracturing within the grains in the gouge layer indicates that the fragment size is reduced during comminution with a reduction of angularity. The structure of the glass material at 30 % porosity shows the original glass bead shape with necking where grains were in contact during sintering (Fig. 4.7c, f). Fractures in the damaged zone of sintered glass are observed at these necks between grains, as well as across the grains at their widest point and as chips off the side of the grains.

4.4. Discussion

By combining analysis of friction coefficient, work and power density with wear rates, temperature monitoring and microstructural data, we can make many observations regarding the interplay between material properties and the tribological responses of variably porous media. Inferences can then be made on the role of porosity in slip behaviour of natural geomaterials in frictional regimes.

The results of the frictional investigation show that porosity has a significant control on fault slip. We show that the 30 % porosity sintered glass samples abide by Byerlee's law, and that with decreasing porosity the reduction in shear resistance means friction coefficients approach the lower end of the expected variability in friction coefficient values for geomaterials at low normal stresses (Byerlee, 1978) (Fig. 4.1b-d). This suggests that most natural geomaterials, which are texturally heterogeneous and fully crystalline, behave differently during frictional sliding to amorphous glass samples of the same porosity. Differences in mineral strength and the addition of heterogeneous stress distributions from textural features such as crystal boundaries, cleavage planes and differences in cementation in granular material (e.g. Saadati et al., 2018) promote stress concentrations and weaknesses that alter the strength and as a consequence, frictional behaviour. Yet understanding the response of glassy materials to fault slip is vital to numerous settings, including volcanic environments that include glass-bearing lavas and ignimbrites, and which are prone to faulting and gravitational instabilities (Elsworth et al., 2007; Hacker et al., 2014; Lavallée et al., 2015) .

The low porosity glass samples lack the textural heterogeneity to experience comminution and wear, as evidenced by the lack of fault gouge (Fig. 4.7). With increasing porosity there was an increase in ability to comminute, such that steady state shear stress and frictional coefficients approached more typical values that were predicted by Byerlee, with the 30 % porosity samples behaving in a similar manner to the majority of natural geomaterials. Increasing roughness is shown to increase friction (Byerlee, 1978) as asperities interact on the surfaces. We interpret that at higher porosity the presence of pores at the slip surface provides a surface roughness, enhancing interactions between the surfaces and localising stress concentrations. Additionally, porosity has been shown to reduce material strength across a range of lithologies (e.g. Dunn et al., 1973; Al-Harthi et al., 1999; Rajabzadeh et al., 2012; Bubeck et al., 2017; Coats et al., 2018) and porous glasses alike (Vasseur et al., 2013). This enables fractures to more readily propagate into the material, increasing damage and wear of the surfaces.

The granular texture of the more porous material allows more material removal from the host due to each fracture, as evidenced by the SEM analysis (Fig. 4.7) which shows larger fractures and larger clasts in the cataclasite and variable, higher friction coefficients throughout the experiments (Fig. 4.1a and Appendix III, Figures A.III.2 – A.III.4). In contrast, the 8 % samples that had very few pores intersecting with the slip surface had less concentration of stress on discrete points and so fractures are distributed along the surface

in Riedel patterns that produce only a thin damage zone (50 µm thick) and very little fragmented material is incorporated into the slip zone between the wall rock interfaces. Not only is more volume of material removed in more porous samples, but also larger fragments that are subsequently comminuted in the gouge layer. These larger fracturing events are observed as shear stress peaks and slip zone dilation in the axial displacement of the samples during the tests. Some large fragments are preserved in the damage zone and gouge layer of the 30 % porosity sample slip surfaces (Fig. 4.7f) and can be compared to the smaller grain sizes preserved in the pores on the surface of the 19 % porosity samples (Fig. 4.7e). This style of fracturing and gouge layer formation would not be possible with the smaller fractures in the damage zone observed with the 8 % porosity samples. This variation in wear mechanism, from small scale damage zones to larger fracturing events (Fig. 4.7), also causes the differences in run-in time for the materials to achieve steady state sliding. High initial wear rates observed during early phases of slip (Fig. 4.1a) are caused by the initial failure of asperities, smoothing of the surface and, in the more porous samples, the production of a gouge layer. The higher porosity samples experienced longer running-in phases due to the higher roughness caused by pore-surface interaction, and they had to generate thick gouge layers to achieve quasi-stable slip (Fig. 4.7). As several studies have previously noted, a continuous gouge layer can dramatically reduce shear stress by halting rock-on-rock, two-body system behaviour in favour of a three-body system with granular medium with the capability of adopting a shear weakening rheology (e.g. Ikari et al., 2009; Niemeijer et al., 2010).

Natural fractures and slip surfaces have a fractal roughness, self-similar across a range of scales (Power et al., 1988), these rough slip surfaces tend towards smoother profiles across scales (self-affine) with increasing slip due to the fracturing and comminution of asperities and other slip surface features (Brodsky et al., 2016). However, where roughness is induced by porosity on a planar surface, this is not the case because as the surface material is removed due to wear, additional pores are uncovered at increasing distance from the original slip plane. As a result, roughness at the scale of porosity (micron to cm) cannot reduce effectively leading to large amounts of interlocking asperity contacts beyond the initial running in period. The roughness at the scale of the porosity is therefore a property of the material itself, an inherent roughness, that cannot be smoothed by abrasion, though it may be buffered by the presence of a gouge layer, with gouge also infilling pores at the surface. This would suggest that for a given normal stress, faults in more porous materials maintain higher roughness as well as having higher wear rates and potentially higher friction

coefficients for longer slip displacements, which may prevent attainment of stable slip conditions (Fig. 4.3 and Fig. 4.4).

An increase in normal stress results in higher shear stresses. As normal stress is increased, so too does the geometric interaction of roughness and this results in higher shear resistance along the slip surface. The shear resistance to normal stress relationships define the friction coefficient for each given slip velocity (Fig. 4.1b-d). In this study, we observed that the highest porosity sample exhibits the highest friction coefficient, as locally increased normal stress (at the points of contact) has the largest impact on promoting geometric interaction for the most porous sample (i.e., shear stress has the highest dependence on normal stress; Fig 4.1b-d) due to deformation, either elastic or plastic of the asperities on the slip surface (Bhushan, 1998; Bowden and Tabor, 2001). Meanwhile, for the lowest porosity samples (8 % porosity), little surface roughness exists due to the lack of pores and material heterogeneity and therefore the increase in normal stress does not so dramatically increase asperity interactions, and the additional normal stress is distributed over a larger area instead of at discrete asperity contact points. In detail, for low porosity samples (8 and 19 % porosity), at a given slip rate, an increase in normal stress is associated with higher wear resulting from a greater amount of fracturing and damage. Shorter running-in periods to the attainment of steady sliding are also noted at higher normal stresses due to the enhanced wear rates and early asperity removal (see Appendix II, Figures A.III.2 – A.III.4). At 30 % porosity, the effect of an increase in normal stress is not simple (Fig. 4.3). The generation of thicker gouge layers may be the cause of a lower sensitivity of wear rate to normal stress, since gouge has differing frictional behaviour to rock-rock contacts (Matsu'ura et al., 1992; Sibson, 1994; Sagy et al., 2007; Niemeijer et al., 2010). SEM analysis of the 30 % porosity sample slip zone showed a relatively thick (200-300 µm) layer of cataclasite, which kept the sample interfaces separated during sliding (Fig. 4.7f).

Steady state friction coefficients increase and subsequently decrease with increasing slip rates (Fig. 4.2). This suggests an initial velocity strengthening behaviour transitioning to velocity weakening behaviour (*m* decreases with increasing *V*) at higher slip rates. This transition occurs for all porosities tested at around 0.2 m s^{-1} to 0.4 m s^{-1} (Fig. 4.2). A weakening mechanism is therefore triggered after an increase in slip rate, across all porosities tested, and independent of normal stress, which has been attributed to the time-dependent interaction of the surfaces (Dieterich, 1979; Ruina, 1983). The restrengthening observed at 1 m s^{-1} for the 8 and 19 % samples may be related to partial welding of the slip surface which is supported by a black/brown material observed on the slip surface after

these experiments. Fault healing (welding due to viscous remobilization of glass (or glass-rich rocks) causes higher frictional coefficients (due to strengthening e.g. Lamur et al., 2019) and instability during slip (Lavallée et al., 2015b). The 30 % porosity sample did not exhibit the increased friction or darkening of the slip surface prior to failure, and a correspondingly lower T_{max} was recorded. In most cases wear rate also decreases with increasing slip velocity during the initial velocity strengthening portion up to around 0.3 m s^{-1} and then achieves a plateau during the faster slip rates where materials are velocity weakening. This reliance of wear rate on slip rate disagrees with Archard's original law (Archard, 1953) that states that wear rate increases with increasing normal stress, but fails to include response to slip rates. However, such reliance on slip rate has been noted by numerous studies on natural rock samples (Hirose et al., 2012; Boneh et al., 2013; Boneh and Reches, 2018) and ceramics (Conway et al., 1988; Al-Qutub et al., 2008).

There is an overall positive correlation across all experiments between friction coefficient and wear rate, with each porosity clustering (largely due to the distinct ranges of friction coefficients for each porosity material) but contributing to the overall trend (Fig. 4.4a) indicating that wear rate may be determined from friction coefficients without further knowledge about the fault rock porosity. Negligible wear rates also correspond to the lowest work per metre slip values and power densities (Fig. 4.4b & c), suggesting there was not enough energy per unit slip distance or unit time to damage the samples surfaces in order to produce wear products. Interestingly, the relationship between wear rate and W_M and by extension, P_D is porosity-specific, which indicates that lower energy during slip is required to induce damage in the (weaker) more porous samples. Thus porosity may be a contributing factor in the observation that whilst damage zone thickness scales with slip displacement, it varies by over three orders of magnitude for given displacement when considering different geomaterials and settings (Shipton et al., 2006).

The normal stress also controls the generation of frictional heat during sliding; at higher normal stress the heat generated is greater for a given slip rate for materials of each porosity (Fig. 4.5a-c). Maximum surface temperatures observed generally (but with exceptions) increase with porosity for a given slip rate and normal stress (Fig. 4.5). In the more porous materials, the roughness caused by porosity more effectively enhance stress concentration, increasing the shear resistance and work done at the slip surface, leading to a greater amount of energy dissipated as heat. Thus, higher porosities generally result in higher friction coefficients, wider damage zones, enhanced wear and more temperature release compared to the less porous counterparts (Fig. 4.1-4.4; Fig. 4.7). Higher slip rates also

resulted in higher temperatures (Fig. 4.5) and heating rates (Fig. 4.6a & b) with the exception of experiments on the 19 % porosity samples at 0.5 MPa at 0.4 and 0.5 m s^{-1} (Fig. 4.5b & e) where T_{max} was lower than that of tests at lower slip rates. We attribute this to the observed lack of initial peak in shear stress data recorded (Appendix III Fig. A.III.3e-f and Fig 4.1a), perhaps due to the initial heterogeneous surface conditions that resulted in less initial work, which retarded heating and reduced the maximum temperature reached (though heating rate during the steady state period followed the expected trend). The increase in heating rates with slip rates corresponds with greater W_M (Fig. 4.6b) implying greater mechanical energy dissipation per unit of displacement. This is mirrored in the correlation of T_{max} with P_D (Fig. 4.6c) with greater energy per unit time due to increased displacement experienced per second of slip acting to increase temperatures at the slip surface due to faster mechanical energy dissipation than the wall rock material capability to conduct or radiate heat away.

Wear rate and temperature may be sensitive to slip velocity for the same reason as friction coefficient, as asperities have less time to interact when slip is more rapid. Boneh and Reches (2018) relate wear rate to the mechanical impulse, derived from asperity contact period which is proportional to slip rate and describes the relationship between contact time and asperity failure; at higher slip rates, individual asperities spend less time interacting, hence less shear stress is generated, and the likelihood of fracture or failure is reduced. An implication of this could be that faults that maintain higher friction coefficients due to the persistent roughness imposed by the presence of high porosity, could overcome the high friction conditions if slip rate becomes rapid enough to reduce interaction time of each point of stress concentration, lowering shear resistance. However, as asperities interact at greater and greater slip rates they have higher impact energy and thus increased power density and energy for heating, and thus frictional heat may still increase with slip rate even when friction coefficient and wear rate do not increase, as is observed here above ~0.3 m s^{-1} (Fig. 4.6).

Thermal weakening of the surface material may also act to reduce the strength of asperities (e.g. Sleep, 2019), a mechanism that would be material-dependent between different rocks and mineral assemblages with varying strengths. It must be noted that wear rates also influence the temperatures achieved at the slip surface (Fig. 4.4 & 4.6, Appendix III Figure A.III.5); when wear rates are high, this may counteract the attainment of high temperatures. Specifically, for low porosity samples with low wear rates heating is in competition with heat dissipation away from the slip zone yet heat generated largely remains on the slip surface. However, the most porous samples (30 %) with highest shortening rates have lower early

slip zone temperatures and, in some experiments, lower temperatures throughout than the intermediate porosity samples, an effect which may be due to a combination of: (1) introduction of cooler (distal) material along the slip zone due wear and removal of (proximal) material originally along the slip plane, (2) more energy consumed during fracturing (due to surface area creation); (3) more effective heat dissipation to the atmosphere from the porous media; and (4) loss of hot particles from the slip zone during rapid wear and comminution as heated fractured material is expelled. So, it may be that these processes hamper heat generation as well as the ability to accumulate heat in the slip zone. Where wear rates are more rapid, the heated zone around the slip surface is narrower as wear rate exceeds the rate of conduction of heat away from the slip zone.

As the rates of heating on slip surfaces control the timing of various weakening mechanisms in natural faults, the data here would suggest that slip surfaces with high wear rates may not necessarily heat substantially as abundant fracturing and pervasive damage zones may be favoured instead. This could potentially delay the onset of thermal weakening mechanisms such as flash heating, thermal pressurisation and frictional melting that are methods of lubricating faults and allowing slip to occur with low friction coefficient. In nature, the addition of pore fluids in an interconnected porosity may also act to reduce normal stress and remove heat from the slip surface, further decreasing the opportunity for thermal weakening compared to denser materials (all else being equal). It is worth noting however that mature faults contain substantial gouge, which shows that fragmental products can accumulate in the slip zone. In these cases of confined slip planes, ejection of material would be less than that observed in the unconfined experiments in this study, and hot, comminuted fragments that are trapped may continue heating, contributing to thermal weakening. In nature, the addition of a through-going and perpetuating gouge layer prevents the direct interaction of slip surfaces, after which the friction (and wear) in the fault core would not be related to asperity wear from direct surface interaction but the properties of the gouge itself(e.g. Niemeijer et al., 2010). As such, wear rate during direct interaction of shear surfaces may only be comparable to new ruptures, where gouge layers are yet to be formed and developed (Sagy et al., 2007).

An example in which interaction of shear surfaces is maintained is during landslides or sector collapses. These events are controlled, especially in the early phases, by the initial wear and friction parameters, impacting the extent of initial collapse controlling the velocity of the mass movement (e.g. Legros, 2002) and the runout distance (often greater than predicted by simple friction models; e.g. Scheidegger, 1973).Such large displacement events often

juxtapose lithologies of differing porosities, in which case predominant damage and wear of the more porous rocks contributes to cataclasis and material entrainment, potentially leading to a reduction in basal friction (Hughes et al., 2020b).

A distinction between laboratory experiments and natural faults is the fractal nature of natural fault roughness. Here we examine inherent roughness in the form of porosity, yet the surface roughness of samples cannot replicate the fractal nature of natural fault surfaces and as a result, wear rate in natural faults demonstrably varies by more than their experimental counterparts (Scholz, 1987; Boneh et al., 2013; Boneh and Reches, 2018), as such the differences in wear rate as a function of porosity observed here may be exaggerated in a natural faulting environment. It must also be noted here that these experiments are conducted at low normal stresses and are unconfined. As such, they elucidate conditions in events occurring at upper crustal conditions (e.g. mass movements and landslides, glacier abrasion, volcanic edifice collapses and volcanic spine extrusion). To investigate lower crustal conditions, confinement of the sample would be necessary to test samples at higher normal stresses without failure. In these deeper conditions the natural porosity range may also be smaller due to greater lithostatic pressures preventing the existence of high porosity rocks.

4.5. Conclusions

Here we report on controlled experiments to study the impact of porosity on slip behaviour, wear and heat generation. Porosity in geomaterials acts to form an inherent roughness that cannot be removed by mechanical wear with accumulated slip. The roughness formed where pore margins interact with planar slip surfaces acts to increase shear resistance and friction coefficient. Porous samples also have higher wear rates compared to low porosity samples due to the increased asperity removal, producing higher levels of fractured material. Normal stress serves to promote asperity interaction, increasing shear resistance, wear rate and temperature.

The glass samples used have frictional coefficients in the lower range of Byerlee's frictional behaviour expected for natural geomaterials at low normal stresses, especially at lower porosity, due to a lack of compositional and textural heterogeneity. This highlights the importance of other variables such as varying crystal strength and textural weaknesses along crystal and grain boundaries but allows for the isolation of the role of porosity on the frictional and tribological behaviour of geomaterials.

Friction coefficient and wear rate increase with increasing slip rate, then decrease beyond a velocity of ~0.3 m s^{-1}. The observed change in behaviour to slip weakening at higher slip rates may be a result of reduced asperity interaction times or of thermally activated weakening mechanism. It is likely this relates to the work per metre slip at the slip surface, defining a specific energy required for activation.

We observe a reduction in maximum recorded temperatures produced by frictional heating in some experiments with high wear rates (i.e., high porosity), which we attribute to an increased proportion of energy consumed in fracturing, enhanced heat dissipation from porous material and the removal of heated material from the slip zone due to wear and ejection. The interplay of frictional coefficient, work per metre slip, power density, wear rate and heating rate suggest that in some natural conditions (e.g. at shallow crustal depths), such as in porous host rocks, the onset of thermally activated weakening mechanisms may be delayed due to reduced frictional heating rates in the slip zone undergoing wear.

Chapter 5: Conclusions and future work

This thesis investigated and experimentally evaluated the primary fault controls, tribological properties and deformation mechanisms active during the collapse and transport of large volcanic mass movements. Each chapter provides new insights into the frictional properties of volcanic rocks pertaining to the hazardous occurrence of large volcanic sector collapses and the debris avalanches they produce, which have the potential for long runout distances. In Chapter 2, field-based observations of a large volcanic debris avalanche deposit near Arequipa (Peru) revealed how strain was partitioned between the primary basal contact and intra-deposit secondary shear zones. The generation of shearing products (e.g. by frictional melting, brecciation, comminution, cataclasis and abrasion) was found to vary spatially and temporally in association with changes in paleo-topographic relief. Guided by these field observations, in Chapter 3, laboratory experiments were undertaken to investigate the frictional properties of the rocks involved in the Arequipa debris avalanche, including juxtaposed mixed lithology experiments, to evaluate the role of variable material properties at basal contacts with differing substratum rock types, revealing the important role of heterogeneities, including porosity. A further study in Chapter 4 evaluated the development of wear in analogue porous materials involved in the transport of volcanic debris avalanches, to quantitatively probe the effects of porosity (of which there is a high range in volcanic products) on the slip dynamics within volcanic shear zones including the propagation of mass movements.

5.1. Summary of outcomes

5.1.1. Examination of a volcanic debris avalanche

In Chapter 2, I investigated the role of shear localisation during volcanic landslides using field observations, as well as textural and geochemical analysis of samples collected from the Arequipa volcanic landslide deposit (south Peru). I identified new basal contacts as well as intra-deposit slip planes that displayed different types of fault rocks with varying levels of shear localisation. In one locality (initially identified by Legros et al. 2000) there was evidence of intense shear localisation to a 1–2 cm thick ultracataclasite layer containing pseudotachylyte. In another instance, basal shearing was distributed across a 40 cm thick basal shear zone, with multiple overprinting sub-parallel faults, localising strain. At multiple

localities, evidence of secondary shear surfaces within the body of the flow deposit were identified, which would have acted to partition the strain within the lower flow away from the basal contact.

I found that frictional melting at the basal contact of the debris avalanche was possible where the shear localisation was extreme, but did not occur in the more diffuse basal shear zones. Frictional melting in areas of high shear localisation is also identified in other, previously studied field examples of melt generation at the base of landslides (Erismann, 1979; Masch et al., 1985; Biek et al., 2019). Using microstructural and geochemical analysis, I determined that there had been at least 2 distinct frictional melting events along the basal contact: an early event which was subsequently fragmented and incorporated back into the granular slip products, and a later event which remained intact. Using geochemical and mineralogical constraints, I applied rheological modelling to evaluate the viscosity and rheological limits (e.g. slip rate) that controlled the development of both fragments of the early melt-bearing layer and the later intact layer. This revealed that neither melting episode appears to have had the capacity for lubrication of basal shear resistance due to the high viscosities of the frictional melts caused by high silica contents (e.g. Giordano et al., 2008), and exacerbated by high fractions of entrained solid particles (e.g. Caricchi et al., 2007).

Modelling was also used to determine the velocity at which either survival of the frictional melt or brittle failure would occur (e.g. Lavallée et al., 2015), and from this, the velocity of the original event could be estimated. The fragmentation of the first identified generation of melt suggested slip rates exceeded ~31 m s^{-1}. In contrast, the intact nature of the late melt layer (i.e., not having undergone brittle failure during transport) suggests that the debris avalanche slowed to < 9 m s^{-1} by the time of its generation and preservation. The brittle failure of an early frictional melt layer, followed by preservation of another phase of melting, suggests that frictional melting may recur multiple times during the extensive runout of debris avalanches. Hence, the presence of melt may be temporally and spatially transient, with the generation of melt layers occurring in certain topological areas of the basal plane with favourable conditions, but with the potential for subsequent destruction as conditions change or the strain rate exceeds that which the layer can accommodate.

The process of strain partitioning by the formation of new slip surfaces, either in the lower portion of the flow or within the diffusely sheared basal granular zone was also described in this chapter. This indicates a mechanism acting to delocalise strain away from the basal shear plane if resistance is too large, such as in the case of topographic barriers observed at the

field location with a pseudotachylyte-bearing basal shear zone. Such de-localisation may result in more favourable slipping conditions at the base of the flow. This process is also seen in the much larger scale generation of new shear zones in the Koefels landslide (Austria) upon encountering a significant topographic barrier (Erismann, 1979). Occasionally, a similar process occurs at the basal contact, whereby new rupture planes cut through undulating existing contacts, a process which reduces topological complexity and which can incorporate basal rocks into the debris avalanche by extending below the original contact. In such cases, the mechanism reduces topographic variation on a cm to m scale, acting in a similar manner to asperity removal in faulting (e.g. Boneh et al., 2014). Evidence of this process illustrates the temporal variation of shear localisation during the event at a single locality.

I identified and examined clastic dykes that propagated into the avalanche deposit from the basal contact. Here, the meso-structure of the dykes preserved evidence of fragmented materials transported in a pressurised fluid mixture. In these areas no defined boundary between the basal and avalanche lithologies could be identified. This may be due to the increased entrainment of material through injection from a fluidised basal layer and subsequent turbulent mixing which may have hindered the localisation of shear to a single basal layer. There was some non-continuous localisation to discrete secondary slip surfaces identified within the lower portion of the flow. Where these occurred, the interaction with the clastic dyking showed that active slip on these surfaces acted as a barrier to material injection from the fluidised basal layer, but that the shear plane, once inactive, was cross-cut by dyking.

5.1.2. Natural volcanic materials' response to fault slip

In Chapter 3, I used natural materials collected from the Arequipa volcanic landside deposit, described in Chapter 2, to experimentally investigate the frictional properties of the materials present along the basal contact. These samples were of a rhyolitic ignimbrite which forms the paleo-substratum and andesitic lava from the collapsed Pichu Pichu volcano, which was the main rock type identified in the collapse deposit. The investigation involved performing a series of direct shear experiments using a low to high velocity rotary shear apparatus, both on the two lithology types independently (i.e., ignimbrite-ignimbrite friction and andesite-andesite contact surfaces) and on a mixed lithology pair of the two materials (i.e., ignimbrite-andesite contact). By doing this, I investigated the effects of juxtaposing rocks with varying mechanical properties compared to the individual lithology behaviour during slip (unlike most rock mechanics studies which are performed on single lithology contacts).

I discovered that the juxtaposition of dissimilar rocks with contrasting porosities and strengths, commonly found along the base of landslides and large tectonic faults, results in lower frictional coefficients than that of either of the rocks tested independently. Mixed lithology experiments exhibited low frictional coefficients of 0.45 – 0.6 compared to values of 0.6 - 0.8 for slip within a single lithology. In these experiments, the wear was concentrated primarily in the weak, porous rhyolitic ignimbrite, with little wear or damage observed in the stronger, denser, andesitic lava samples. All lithology pairings, whether single or mixed, exhibited rate weakening at high slip rates (> 1 m s^{-1}, as was identified for a range of other lithologies compiled in Di Toro et al., 2011) due to the evolution of the shear zones and increased frictional heating.

The rate of wear was found to generally increase with slip rates, although the primary variable controlling wear was porosity. For instance, the dense andesitic lava's wear rates remained negligible at all slip conditions tested, whereas the porous rhyolitic ignimbrite's wear rates reached a high, steady rate of wear at high slip rates. The low material strength of the rhyolitic ignimbrite promoted fracturing and wear of the material at lower work rates compared to the stronger andesitic lava. The acting normal stress, scaling with the overburden (or thickness) of a debris avalanche, also influenced wear. I found that greater normal stresses (> 1 MPa) could be sustained in dense lavas which revealed wear at increasing rates, but not in ignimbrite samples which underwent rupture under the same imposed conditions. The heating rates measured at the slip zone showed spatial and temporal fluctuations but generally increased during slip to a quasi-steady-state, reaching higher temperatures at higher normal stresses and resultant shear stresses. The data indicates that the maximum slip surface temperatures reached in all materials was lower for tests with greater wear rates.

The heterogeneous nature of ignimbrite, containing porous indurated volcanic ash as well as vesicular lapilli and dense lithics (primarily andesitic), was noted to result in a wide range of wear behaviours. For instance, the presence of strong clasts along the slip plane initially reduced the wear rate during slip, but plucking and incorporation of the clast into the slip zone subsequently caused an abrupt increase in wear rates whilst the clasts acted as strong effective asperities, prompting material ploughing (Reches and Lockner, 2010). Shear stress and temperature also peaked in such events, before returning to pre-entrainment conditions once clasts were expelled. In heterogeneous materials such as ignimbrites, wear recurrently exposes internal clasts to the slip surface during sustained sliding events, resulting in discontinuous, erratic fluctuations in wear and frictional properties. I analysed the resulting

fluctuations in the tribological parameters of friction, wear and frictional heating during slip to better understand frictional sliding in heterogenous natural conditions such as debris avalanches.

5.1.3. The role of porosity in friction and wear

In Chapter 4, I built upon the field and laboratory observations seen in Chapters 2-3, which indicated that the presence of porous volcanic rocks, such as ignimbrite, along a slip plane influence the wear, frictional properties and thermo-mechanical response of fault zones. Consequently, I further investigated the role of porosity on fault slip using volcanic rock analogues with controlled physical properties, without the textural heterogeneities of crystals or clasts present in natural samples. This was done by fabricating a glass analogue material with a range of porosities (8, 19 and 30 % porosity) utilising the viscous sintering of glass beads (after Wadsworth et al., 2016). These samples were then tested under direct shear conditions using the low to high velocity rotary shear apparatus and analysed using the same methods as in Chapter 3.

Pores impart an inherent roughness to the material, which scales with their size, which cannot be abraded to achieve smoother surfaces. Porosity is therefore both a material property and a variable in the surface conditions during slip, suggesting that porosity must be considered in the description of geotribological variables (Boneh and Reches, 2018). The presence of pores reduces the contact area between the solid fractions, thus concentrating stress, wear, and heat generation onto a smaller true contact area. During slip between two porous materials, any given area of solid rock will be in contact with another area of solid rock or not (when adjacent to a pore), which influences the stability of fault slip. The application of greater normal stresses to opposing rough interfaces causes greater surface interaction and increases the shear resistance to slip. Porous samples displayed higher wear rates compared to denser samples. This is due not only to surface interaction, but also to the lower strength of the porous material (Lavallée and Kendrick, 2021) leading to increased fracturing, material comminution and eventual ejection from the slip plane. Generally, at low normal stresses and slip rates, wear rate reduced with slip rate, differing from the trend seen in natural samples in Chapter 3. For each porosity the wear rate was the greatest at high velocity (1 m s^{-1} due to the greater mean power density).

The porous rock analogues used in this study highlighted the importance of material properties on the frictional behaviour of geomaterials. High-density glass samples showed markedly low friction coefficient values (< 0.4) and wear rates, as they lacked the micro-

textural heterogeneity of crystalline materials (such as crystallographic structures and grain boundaries) that facilitates rupture, comminution and wear along the slip surface. All of the porous samples tested exhibited an evolution to velocity weakening behaviour occurring at moderate slip rates (0.2-0.4 m s^{-1}) suggesting a weakening mechanism independent of porosity; potentially the generation of a sufficient gouge layer (Reches and Lockner, 2010). High velocity tests (1 m s^{-1}) on the denser materials (8 % and 19 % porosity) may have caused sufficient heat to prompt glass viscous remobilisation. This would have resulted in some degrees of welding of the slip interface, leading to strengthening of the samples and enabling large-scale sample failure, similar to that observed in dense glasses by Lavallée et al. (2015).

In this study, the homogeneity of the samples used revealed the role of pores on frictional heating and wear rates, without the complication of the material heterogeneities observed in Chapter 3, that obscured direct correlation of observations to materials' porosity. Indeed, the results of this study confirmed that high wear rates hinder frictional heating, as the removal of hot material from the slip plane exposes colder rock to slip, thus lowering the magnitude of heat accumulated. During frictional testing of dense, low-porosity samples characterised by low wear rates, the frictional heat at the slip surface was determined by the competing contributions of mechanical energy conversion to heat and heat dissipation away from the slip zone by heat conduction through the sample. However, during friction of porous samples characterised by high wear rates, the slip zone reached lower temperatures as the increased removal of heated material via fracturing and ejection (which was faster than heat conduction), and greater energy consumed during fracturing, combined to minimise the magnitude of heat accumulated in the slip zone.

5.2. Implications of the findings

5.2.1. Wear and the evolution of frictional controls on volcanic debris avalanches

The long runout distance of the Arequipa volcanic landslide described in Chapter 2 and in the formative work of Legros et al. (2000) require a reduction in basal shear resistance from values predicted of rock friction in nature (Legros, 2002; van Wyk de Vries and Davies, 2015). In Chapter 3, the frictional properties of the materials sampled from the deposit were experimentally determined at slip velocities between 0.01 and 2.4 m s^{-1}. These indicated that the rocks exhibit a rate weakening behaviour, yet it is worthwhile noting that the experimental conditions did not achieve the very high velocities expected in nature, thus the result should be considered cautiously. For instance, Siebert et al. (1987) suggested that large volume landslides may reach ~100 m s^{-1} and in my rheological evaluation of the

frictional melt behaviour, I constrained that the landslide must have been transported at a velocity in excess of 31 m s^{-1}. Hence there is an uncertainty pertaining to the behaviour of these materials at ultra-fast slip rates experienced during the debris avalanche. If velocity weakening scales linearly from the slip rate experimentally tested to that anticipated in natural events (e.g. 31-100 m s^{-1}, a range beyond the current scope of friction experiments), then I would correspondingly expect very low basal friction coefficient values. The presence of weak basal rocks, with higher likelihood of failure, has been identified as a cause of gravitational deformation of large-scale volcanic structures worldwide. These basal rocks are not all volcanic in origin (e.g. van Wyk de Vries and Davies, 2015). Clay rich lithologies are known to have inherently low friction coefficients (Byerlee, 1978), and their presence can facilitate a reduction in basal friction and resulting slip where they occur beneath volcanic structures (Murray et al., 2018). Whilst this is a possible contributor, the study of wear and friction of mixed lithologies undertaken in this study in Chapter 3 suggests that friction between the two different rock types tested results in lower frictional coefficient than if we considered each lithology separately. This could also facilitate slip at a range of slip rates, including the high slip rates associated with mass movements, as the frictional coefficients are observed to be lower for all slip rates at the low normal stresses tested.

In addition to the importance of basal friction during transport of debris avalanches, the evolution of the fault rocks and frictional behaviour must also be considered from the onset of failure until deposition. In particular, the extent of wear increases with slip distance and thus modifies the materials present along the fault. By analysing the rate of wear from both porous natural materials (Chapter 3) and analogues (Chapter 4), it is possible to make inferences on the effects of gouge and faulting products accumulated in the localised basal shear zone. Volcanic sector collapses result from failure of (or parts of) an edifice along a basal detachment. In many instances, such as in the first occurrence of a sector collapse event at a volcanic edifice, these fault surfaces are freshly developed, rich in asperity contacts and thus contain no pre-existing wear products. The tribological properties of the evolving slip interface therefore determines the dynamics of slip immediately after failure. There have been instances where a volcanic sector collapse initiates, but is aborted with only a small amount of movement; for example at El Hierro (Canary Islands) where the inactive San Andres fault system has been identified as evidence of an aborted landslide event with a few tens of metres displacement at ~250 ka (Day et al., 1997), and in 2010 at Pacaya (Guatemala) where the edifice flank underwent a rapid, but mere ~4 m of movement as a coherent mass (Schaefer et al., 2017). Such failed collapse events suggest that unfavourable

slip conditions due to high frictional resistance may have prevented the generation of debris avalanches from continued movement and disaggregation of the mass. The generation of wear, shown in experiments to affect the frictional resistance in the running-in phases leading to steady state friction and wear, may contribute to the attainment of slip stability following slip initiation along the basal detachment.

Chapters 3 and 4 show that the generation of wear products is aided by the materials' weakness and surface roughness, imparted by the porous structure of the materials, and causes fine gouge in the fault zone which reduces the shear resistance. These observations are in agreement with previous findings (e.g. Matsu'ura et al., 1992; Reches and Lockner, 2010). In the case of dense, low-porosity and high-strength lithologies (e.g. the andesitic lava in Chapter 3), gouge may be slow to form due to limited pores, and thus asperities which enables wear; so high friction coefficients may be sustained along the slip interfaces.

Additionally, as shown in Chapter 3, the presence of strong clasts within otherwise weak lithological units in which failure may be preferential, can act to momentarily increase the shear resistance along the slip surface. Upscaling of this laboratory observation may be argued for, via consideration of lithological heterogeneities at the volcanic edifice scale. For instance, dense, coherent lavas emplaced within thick successions of volcaniclastic deposits may act in a similar way to "strong clasts" within experimental-scale fault slip, which would not preferentially wear when in contact with weaker material along the slip plane at the debris avalanche scale. In the Arequipa landslide deposit (Chapter 2), I observed the preferential wear of the ignimbrite in contact with dense andesite blocks in the overlying debris avalanche deposit, thus supporting the importance of considering large-scale lithological heterogeneities when resolving frictional properties to model the transport of volcanic debris avalanches.

Finally, as evidenced in Chapter 4, high levels of comminution of the fragments of analogue material included into the slip zone acted to maintain high shear resistance to sliding, despite high wear rates and large damage zones. Here, the large-scale failure at the slip surface of the analogue material impeded the effects of wear products to reduce friction coefficients, maintaining high shear throughout. Fragmentation of the rhyolitic ignimbrite samples during experiments detailed in Chapter 3 also suggests that a weak substrate material could result in the entrainment of the basal ignimbrite into the shear zone. Any entrained material would undergo further comminution, effecting shear resistance.

5.2.2 Frictional melting and shear localisation during collapse events

The presence of pseudotachylyte in fault zones is commonly used to infer a seismogenic event of significance (e.g. Sibson, 1975). Although vestiges of pseudotachylytes were observed in the basal outcrop of the Arequipa volcanic landslide deposit, frictional melting did not occur in any of the experiments conducted on the natural materials within the range of conditions tested. This lack of melting may be due to the relatively low slip rates tested (i.e., < 2.4 m s^{-1}) compared to that arguably experienced in the natural example - at least 31 m s^{-1} based on the rheological modelling conducted in Chapter 2 and typically > 10 m s^{-1} in the case of catastrophic collapse events (Siebert et al., 1987; McGuire, 1996). The unconfined nature of the experiments also resulted in the ejection of hot material from the slip plane rather than the continued comminution and heating of wear products to temperatures sufficient to induce melting. The non-ubiquitous distribution of pseudotachylyte along the base of the natural deposits would also suggest that the slip conditions and evolution of the slip zone may vary spatially and temporally, thus impacting the thermal output necessary to generate frictional melt at the base of the landslide.

In the Arequipa volcanic landslide deposit (Chapter 2), the degree of strain localisation was observed to be greatest where the basal shear zone interacted with an uphill ramp in basal topographic height. This obstacle locally diverted the direction of material movement due to the resistance to flow of the lower metres of material. The angle of the basal contact with regards to flow direction influences the resultant normal and shear stresses as illustrated in Figure 2.13. These increased stresses acting on the basal shearing zone, in cases where the debris avalanche needs to ramp up to overcome a paleo-topographic high, would have favoured the localisation of shear to a discrete layer. This causes the compaction of the highly fragmented material and the prolonged rock-rock frictional interactions required for the generation of sufficient heat to melt a portion of the rocks along the basal contact. In areas where the paleo-topographic relief was relatively flat or where the debris avalanche encountered a trough which permitted dilation of the shear zone, the preserved basal shear zone exhibits evidence of multiple slip surfaces rather than the single surface observed in the pseudotachylyte bearing basal contact. In these areas, the basal shear zone did not experience the same degree of localisation, which would have lessened the thermal output, meaning these areas were likely incapable of reaching melting conditions. This is mimicked by the friction experiments in Chapters 3 and 4 that linked the removal of material from the active slip zone to an overall decrease in heating rates and slip surface temperature, which prevented frictional melting despite the high transport rate. These differing basal contacts

indicated that where strain was localised, increasing rock-rock frictional interactions, melting was more likely to occur, and potentially topological variations had a primary control on this difference.

The packing of the granular material formed in the basal shear zone could have implications for both the shear resistance to flow and the occurrence of frictional melting. The wear of material from volcanic rock erases natural textures and void space, and further comminution reduces fragment size in the shear zone, producing a closely packed granular layer. This is evident in highly porous rocks, such as the ignimbrites described in Chapters 2 and 3, and in the most porous glass samples in Chapter 4. Additionally, and unique to volcanic rocks with high glass content, the frictional heating may result in the further densification of the glass phase by viscous remobilisation. If temperatures within the granular shear zone exceed the glass transition temperature, as they did in some of my experiments, molten particles may viscously sinter (Vasseur et al., 2013; Wadsworth et al., 2014, 2019). Sintering increases the coherence between grains, reduces porosity and impacts the ability of individual grains (i.e., molten fragments) to move past one another in a granular flow due to potential agglutination, leading to increased resistance to flow. This process results in an increase in frictional heating and the potential for melting within the shearing layer.

Although the degree of strain localisation contributes to the amount of mechanical work converted to heat and influences frictional melting, there is also evidence of processes acting against localisation and therefore against the conditions required for the generation of frictional heating sufficient to generate frictional melting. This may explain the rarity of preserved pseudotachylytes observed in the Arequipa volcanic landslide deposit and other deposits worldwide. In cases where the morphology of the substratum leads to unfavourable slip conditions along the basal contact, strain may shift elsewhere in the debris avalanche, as supported by the observation of secondary shear zones within the debris avalanche mass (Chapter 2). If these secondary shear zones then become localised sufficiently to form faults, the frictional heating on these surfaces will be enhanced and could promote frictional melting (as suggested by the modelling conducted by De Blasio and Elverhøi, 2008). This was noted in the generation of ultracataclasite layers described in Chapter 2.4.1.2 that showed a high degree of localisation but lacking evidence of any resultant melting, suggesting either that durations or slip distances on these secondary surfaces may have been insufficient to generate the heat required for melting.

Additionally, where the basal contact was identified to have a fluidised granular layer indicated by injected clastic dykes, the injection and mixing of materials prevented the localisation of shear to a discrete basal layer. The presence of discrete, localised secondary shear zones in these areas may act as barriers to the injection of fluidised material, as evidenced by the cross-cutting relationship of slip surfaces and clastic dykes observed in the field. The presence of pressurised fluids in such materials may also prevent frictional melting, whilst reducing the normal stress acting on the slip plane. Pore pressurisation of fault rocks is dependent on the permeability of the surrounding material, which controls whether fluids remain in, or leave the fault zone (e.g. Byerlee, 1978; Goren et al., 2010).

In the case of shear zones with preserved pseudotachylyte, the independent formation of small, unhomogenised melt filaments (schlieren) within the granular shear zone indicates that variable conditions at the basal contact may have prevented coalescence of the filaments to form a continuous melt layer. The melt bearing layer described in Chapter 2 had discontinuous frictional melt and contained a large fraction of intermixed clastic material, increasing the effective viscosity of the suspension (Costa et al., 2009; Cordonnier et al., 2012). Formation and preservation of pseudotachylyte layers may therefore be more common in block facies found in the centre of deposits (Glicken, 1991), and in the proximal areas of the deposits where large block sliding is more common (van Wyk de Vries and Davies, 2015) forming solid rock interfaces. Frictional melting from localised shear zones in compacted highly granular basal facies may be rarer, however field evidence proves that these shear zones can also produce melting (Chapter 2).

Where pseudotachylytes are preserved, multiple studies have assumed that the presence of frictional melt during shear would have led to lubricating properties, lowering the shear resistance (Erismann, 1979; De Blasio and Elverhøi, 2008). However, rheological modelling in Chapter 2 determined that the frictional melt at the base of the debris avalanche had a relatively high viscosity (for the temperature range constrained) and would have been unlikely to have acted as a lubricant. So, the increased shear resistance generated by frictional melting, as well as variations in the topography of the substratum, may have contributed to the partitioning of shear into a secondary shear plane across the base of the debris avalanche. I therefore suggest that further studies analysing pseudotachylytes should undertake the same rigorous rheological analysis outlined in Chapter 2 wherever possible to adequately understand the effects of the frictional melt on the shear resistance in basal shear zones. Pseudotachylytes have been rarely identified in the deposits of debris avalanches despite dynamic conditions, including high transport velocities. The discovery of

pseudotachylyte fragments in the vicinity of the preserved pseudotachylyte-bearing basal shear zone due to brittle failure of the melt during intense shearing (Chapter 2), provides evidence of yet another process preventing the preservation of pseudotachylytes in nature. The addition of this affinity for syn-emplacement destruction of frictional melts along with the frequently inferred chemical and textural overprinting of pseudotachylytes (including recrystallisation, alteration and deformation; Kendrick et al., 2012; Kirkpatrick and Rowe, 2013), results in the low probability of preservation of pseudotachylytes from such events. It is likely, based on the discovery of brittle failure due to intense shearing, that frictional melting in rapid landslide events is more common than the preservation (and exhumation and identification of such outcrops) would suggest.

5.3. Outlook and further work

In this thesis, I have investigated the frictional and tribological response to slip in volcanic settings, specifically during debris avalanche transport associated with volcanic flank collapse events. This was done through the careful examination of field evidence to target key mechanisms for quantification via controlled laboratory experiments and the concepts of friction, wear, and frictional heating.

I examined basal shear experienced by the Arequipa volcanic landslide (described in Chapter 2) and recreated key deformation mechanisms by juxtaposing the primary lithologies using controlled friction experiments (Chapter 3), and further explored the role of porosity on friction using analogue materials (Chapter 4); yet further aspects remain to be investigated. In Chapter 2, I described the presence of clastic dyke intrusion into the lower portion of the debris avalanche deposit, suggesting the presence of a fluidised layer present at the base of the debris avalanche in some areas. Pore pressure is known to reduce the normal stress, thus reducing the resistance to shear and enabling long transport distances, both in faults (Byerlee, 1978) and in large mass movements (Ferri et al., 2011; Mitchell et al., 2015). It is possible to apply a pore pressure during rotary shear experiments on existing apparatuses (Ma et al., 2014), and a suite of such experiments could reveal the role of pore fluid pressure during the active shearing at the base of mass movements. In the specific case of Arequipa volcanic landslide, the basal rhyolitic ignimbrite has a high porosity and correspondingly high permeability and may not be able to sustain pore fluid pressures sufficient to reduce shear resistance when tested individually. If tested as part of a mixed lithology pair, however, the much lower permeability of the opposing andesitic lava may sufficiently increase pore pressures at the slip interface to lower shear stresses.

In Chapter 3, I investigated the frictional behaviour and properties of juxtaposed materials with differing frictional coefficients, strengths and resistances to wear in shearing environments and showed the impact of rapid wear and failure of the weaker lithology on the frictional properties of faults with different rock types. Due to the common presence of weak basal rocks below volcanic edifices (van Wyk de Vries and Davies, 2015) and their observed role in volcanic structure deformation, there is a need for experimental investigation into the role of relative geomaterial strength on friction coefficient. This is required to understand slip mechanics in all environments with multiple rock types, not just limited to volcanic settings. In addition to material strength, the juxtaposition of rock types that are known to have different weakening mechanisms (such as thermal decomposition of carbonate fault rocks) may result in a combination of weakening mechanisms not previously observed in experimental data.

In the experiments described in Chapter 3 (on natural materials) and in Chapter 4 (on glass analogues), I noted that high wear rates acted to reduce heating rates, due in part to the removal of heated material from the slip zone. In a different experimental set up, Teflon rings could be used to confine and retain fragmental material in the slip surface, maintaining a layer of wear products (gouge) which would experience further comminution and could potentially enable the accumulation of frictional heat. These tests would further permit determination of a stronger relationship between slip conditions, wear rate and frictional heating to evaluate the ability of the fault gouge to undergo frictional melting from grain contacts at low normal stresses as it occurred in pseudotachylyte bearing basal contact as described in Chapter 2. Further experiments would also better constrain the most probable range of conditions required for frictional melting at the base of debris avalanches and large mass movements. In Chapter 3, I investigated the tribological responses of variably porous materials and noted that the entrainment of strong low-porosity clasts within the slip zone could facilitate much faster wear of the weaker lithology via ploughing. If the experiments were to be conducted with a confining ring, this effect may be magnified as the clasts would remain in the slip zone rather than being ejected from the interface.

In both Chapters 3 and 4 during rotary shear experiments, the slip surface is not visible, thus it is impossible to directly observe the dominant deformation mechanisms at any given time during shear. Instead, I relied on the preserved evidence of these processes in post-mortem samples and in the mechanical data collected. Previous studies have performed multiple shear experiments at the same conditions to variable slip distances to constrain the evolution of fault surfaces (Hirose and Shimamoto, 2005a; Wallace et al., 2019a). However,

during sample extraction from the experimental setup (involving the separation of the sample pairs) and during preparation of thin sections, there is inevitable loss of a portion of the wear material, (partial) destruction of textures within such layers, and (in weaker rocks such as the rhyolitic ignimbrite described in Chapter 3) the removal of fractured damage zone material due to sample fragmentation during experiments. The recent development of rotary shear testing in combination with non-destructive x-ray computed tomography imaging now allows for the continuous real time analysis of the faults surface evolution during slip, including surface roughness, wear mechanisms, and true contact area (Zhao et al., 2017, 2018).

In Chapter 2, the latest rheological models were used to determine both the slip velocities and possible strain rates experienced at the base of debris avalanches, as well as to assess whether the frictional melt acted as a lubricating layer or viscous brake. Physico-chemical controls including melt viscosity and the fraction of suspended particles, as well as the rate of deformation, impacts the potential for lubrication versus viscous brake effect. This means that frictional melt suspensions can provide both higher or lower shear resistance to that coined by Byerlee's friction law for brittle shear zones. The work in Chapter 2 showed that the frictional melt in the Arequipa volcanic landslide deposit was unlikely to have lubricated slip due to its physical and chemical attributes. Such rigorous rheological modelling should be attempted on other, well-documented pseudotachylytes, as it uniquely holds information to constrain the ranges of probable conditions occurring in natural settings, not otherwise attainable with direct monitoring.

The high temperature of rocks present in active volcanic systems may not necessarily respond like cold rocks and may be more prone to frictional melting. In fact, the literature has an important gap in knowledge on the frictional properties of hot rocks. Preliminary experiments have indicated that high starting temperatures can serve to increase the width of frictional melt zones compared to the same conditions at low starting temperatures (Wallace et al., 2019b). However, it is unclear whether this results from melting which more closely approaches equilibrium conditions and leads to low suspended particle (restite) fractions or due to the viscous remobilisation interstitial glass in the adjacent wall rocks at temperatures above the glass transition. Experiments using low to high rotary shear apparatus equipped with a furnace are required to provide constraints on the impact of rock temperature on their frictional properties, as it may radically change how we view certain shear processes in volcanic or near magmatic environments. Additionally, further work is required to adequately describe the behaviour of glassy materials under such conditions,

and how viscous remobilisation, potential densification, and welding within a shear zone modifies the tribological behaviours controlling the development slip.

In the last few years, as I was conducting this study, multiple new occurrences of frictional melting generated by mass movements have been identified by others at sites around the world (e.g. Bernard and van Wyk de Vries, 2017; Biek et al., 2019). This suggests that even with a preservation bias (e.g. Kirkpatrick and Rowe, 2013) there has also been a past failure to identify the small scale pseudotachylyte layers in large scale collapse deposits. A re-evaluation of large landslide deposits may show that despite the spatial variability of pseudotachylytes along the basal contact, frictional melting may not be as rare as commonly inferred at the base of large debris avalanches. Further identification and physico-chemical analysis of existing pseudotachylyte-bearing basal shear zones, and identification and characterisation of secondary shear zones (as observed in this study) may provide us with more robust rheological constraints to simulate the transport of debris avalanche and improve our ability to mitigate their risk, with a greater understanding of the processes leading to the long runout of large volcanic debris avalanches.

…Until a brand new world takes shape

-Earth, Sleeping At Last

Bibliography

Abercrombie, R.E., Rice, J.R., 2005. Can observations of earthquake scaling constrain slip weakening? Geophysical Journal International 162, 406–424. https://doi.org/10.1111/j.1365-246X.2005.02579.x

Acocella, V., Neri, M., 2003. What makes flank eruptions? The 2001 Etna eruption and its possible triggering mechanisms. Bulletin of Volcanology 65, 517–529. https://doi.org/10.1007/s00445-003-0280-3

Acocella, V., Puglisi, G., 2010. Hazard Mitigation of Unstable Volcanic Edifices. EOS Transactions 91. https://doi.org/10.1029/2010EO400002

Aguilar Contreras, R., Thouret, J.-C., Samaniego Eguiguren, P., 2016. Actividad eruptiva en sistemas de larga duración: relaciones entre el complejo post-caldérico Chachani y las ignimbritas Plio-cuaternarias de la cuenca de Arequipa (Perú). Instituto Geológico, Minero y Metalúrgico – INGEMMET.

Al-Harthi, A.A., Al-Amri, R.M., Shehata, W.M., 1999. The porosity and engineering properties of vesicular basalt in Saudi Arabia. Engineering Geology 54, 313–320. https://doi.org/10.1016/S0013-7952(99)00050-2

Al-Qutub, A.M., Allam, I.M., Abdul Samad, M.A., 2008. Wear and friction of Al–Al2O3 composites at various sliding speeds. Journal of Materials Science 43, 5797–5803. https://doi.org/10.1007/s10853-008-2867-8

Alvarado, G.E., Soto, G.J., 2002. Pyroclastic flow generated by crater-wall collapse and outpouring of the lava pool of Arenal Volcano, Costa Rica. Bulletin of Volcanology 63, 557–568. https://doi.org/10.1007/s00445-001-0179-9

An, M., Zhang, F., Zhang, L., Fang, Y., 2018. Effects of Normal Stress and Clay Content on the Frictional Properties of Reservoir Rocks Under Fully Saturated Conditions. 220–231. https://doi.org/10.1007/978-981-13-0113-1_25

Anders, M., Fouke, B., Zerkle, A., Tavarnelli, E., Alvarez, W., Harlow, G., 2010. The Role of Calcining and Basal Fluidization in the Long Runout of Carbonate Slides: An Example from the Heart Mountain Slide Block, Wyoming and Montana, U.S.A. Journal of Geology 118. https://doi.org/10.1086/656383

Ando, M., 1979. “The Hawaii Earthquake of November 29, 1975: Low dip angle faulting due

to forceful injection of magma"'. Journal of Geophysical Research: Solid Earth 84, 7616–7626. https://doi.org/https://doi.org/10.1029/JB084iB13p07616

Andrews, D.J., 2002. A fault constitutive relation accounting for thermal pressurization of pore fluid. Journal of Geophysical Research: Solid Earth 107, ESE 15-1-ESE 15-8. https://doi.org/https://doi.org/10.1029/2002JB001942

Arabnia, O., Sklar, L., 2016. Experimental Study of Particle Size Reduction in Geophysical Granular Flows. International Journal of Erosion Control Engineering 9, 122–129. https://doi.org/10.13101/ijece.9.122

Archard, J.F., 1953. Contact and Rubbing of Flat Surfaces. Journal of Applied Physics 24, 981–988. https://doi.org/10.1063/1.1721448

Ashby, M.F., Sammis, C.G., 1990. The damage mechanics of brittle solids in compression. Pure and Applied Geophysics 133, 489–521. https://doi.org/10.1007/BF00878002

Balme, M.R., Rocchi, V., Jones, C., Sammonds, P.R., Meredith, P.G., Boon, S., 2004. Fracture toughness measurements on igneous rocks using a high-pressure, high-temperature rock fracture mechanics cell. Journal of Volcanology and Geothermal Research 132, 159–172. https://doi.org/https://doi.org/10.1016/S0377-0273(03)00343-3

Barrett, R., Lebas, E., Ramalho, R., Klaucke, I., Kutterolf, S., Klügel, A., Lindhorst, K., Gross, F., Krastel, S., 2020. Revisiting the tsunamigenic volcanic flank collapse of Fogo Island in the Cape Verdes, offshore West Africa. Geological Society, London, Special Publications 500, 13–26. https://doi.org/10.1144/SP500-2019-187

Belousov, A., Belousova, M., Voight, B., 1999. Multiple edifice failures, debris avalanches and associated eruptions in the Holocene history of Shiveluch volcano, Kamchatka, Russia. Bulletin of Volcanology 61, 324–342. https://doi.org/10.1007/s004450050300

Benson, P., Heap, M.J., Lavallée, Y., Flaws, A., Hess, K.-U., Selvadurai, P., Dingwell, D., Schillinger, B., 2012. Laboratory simulations of tensile fracture development in a volcanic conduit via cyclic magma pressurisation. Earth and Planetary Science Letters s 349–350, 231–239. https://doi.org/10.1016/j.epsl.2012.07.003

Bernard, K., van Wyk de Vries, B., 2017. Volcanic avalanche fault zone with pseudotachylite and gouge in French Massif Central. Journal of Volcanology and Geothermal Research 347, 112–135. https://doi.org/10.1016/J.JVOLGEORES.2017.09.006

Bhushan, B., 1998. Contact mechanics of rough surfaces in tribology: multiple asperity

contact. Tribology Letters 4, 1–35. https://doi.org/10.1023/A:1019186601445

Biek, R.F., Rowley, P.D., Hacker, D.B., 2019. The Gigantic Markagunt and Sevier Gravity Slides Resulting from Mid-Cenozoic Catastrophic Mega-Scale Failure of the Marysvale Volcanic Field, Utah, USA. https://doi.org/10.1130/FLD056

Boneh, Y., Chang, J., Lockner, D., Reches, Z., 2014. Evolution of Wear and Friction Along Experimental Faults. Pure and Applied Geophysics 171, 3125–3141. https://doi.org/10.1007/s00024-014-0801-3

Boneh, Y., Reches, Z., 2018. Geotribology - Friction, wear, and lubrication of faults. Tectonophysics 733, 171–181. https://doi.org/10.1016/J.TECTO.2017.11.022

Boneh, Y., Sagy, A., Reches, Z., 2013. Frictional strength and wear-rate of carbonate faults during high-velocity, steady-state sliding. Earth and Planetary Science Letters 381, 127–137. https://doi.org/10.1016/J.EPSL.2013.08.050

Borgia, A., Delaney, P.T., Denlinger, R.P., 2000. Spreading Volcanoes. Annual Review of Earth and Planetary Sciences 28, 539–570. https://doi.org/10.1146/annurev.earth.28.1.539

Bowden, F.P., Tabor, D., 2001. The Friction and Lubrication of Solids, International series of monographs on physics. Clarendon Press.

Brodsky, E.E., Kanamori, H., 2001. Elastohydrodynamic lubrication of faults. Journal of Geophysical Research: Solid Earth 106, 16357–16374. https://doi.org/10.1029/2001JB000430

Brodsky, E.E., Kirkpatrick, J.D., Candela, T., 2016. Constraints from fault roughness on the scale-dependent strength of rocks. Geology 44, 19–22. https://doi.org/10.1130/G37206.1

Browning, J., Meredith, P., Gudmundsson, A., 2016. Cooling-dominated cracking in thermally stressed volcanic rocks. Geophysical Research Letters 43, 8417–8425. https://doi.org/10.1002/2016GL070532

Bubeck, A., Walker, R.J., Healy, D., Dobbs, M., Holwell, D.A., 2017. Pore geometry as a control on rock strength. Earth and Planetary Science Letters 457, 38–48. https://doi.org/10.1016/J.EPSL.2016.09.050

Bubeck, A, Walker, R.J., Healy, D., Dobbs, M., Holwell, D.A., 2017. Pore geometry as a

control on rock strength. Earth and Planetary Science Letters 457, 38–48. https://doi.org/http://dx.doi.org/10.1016/j.epsl.2016.09.050

Bullock, R.J., De Paola, N., Holdsworth, R.E., Trabucho-Alexandre, J., 2014. Lithological controls on the deformation mechanisms operating within carbonate-hosted faults during the seismic cycle. Journal of Structural Geology 58, 22–42. https://doi.org/https://doi.org/10.1016/j.jsg.2013.10.008

Buocz, I., Rozgonyi-Boissinot, N., Török, Á., Görög, P., 2014. Direct shear strength test on rocks along discontinuities, under laboratory conditions. Pollack Periodica 9, 139–150. https://doi.org/10.1556/pollack.9.2014.3.15

Byerlee, J., 1978. Friction of Rocks. Pure and Applied Geophysics 116, 615–626. https://doi.org/10.1007/bf00876528

Byerlee, J.D., 1967. Frictional characteristics of granite under high confining pressure. Journal of Geophysical Research (1896-1977) 72, 3639–3648. https://doi.org/https://doi.org/10.1029/JZ072i014p03639

Calder, E.S., Luckett, R., Sparks, R.S.J., Voight, B., 2002. Mechanisms of lava dome instability and generation of rockfalls and pyroclastic flows at Soufrière Hills Volcano, Montserrat. Geological Society, London, Memoirs 21, 173–190. https://doi.org/10.1144/GSL.MEM.2002.021.01.08

Campbell, C.S., Cleary, P.W., Hopkins, M., 1995. Large-scale landslide simulations: Global deformation, velocities and basal friction. Journal of Geophysical Research: Solid Earth 100, 8267–8283. https://doi.org/10.1029/94JB00937

Campbell, L.R., Menegon, L., Fagereng, Å., Pennacchioni, G., 2020. Earthquake nucleation in the lower crust by local stress amplification. Nature Communications 11, 1322. https://doi.org/10.1038/s41467-020-15150-x

Candela, T., Renard, F., Klinger, Y., Mair, K., Schmittbuhl, J., Brodsky, E.E., 2012. Roughness of fault surfaces over nine decades of length scales. Journal of Geophysical Research: Solid Earth 117. https://doi.org/10.1029/2011JB009041

Caricchi, L., Burlini, L., Ulmer, P., Gerya, T., Vassalli, M., Papale, P., 2007. Non-Newtonian rheology of crystal-bearing magmas and implications for magma ascent dynamics. Earth and Planetary Science Letters 264, 402–419. https://doi.org/10.1016/j.epsl.2007.09.032

Caricchi, L., Giordano, D., Burlini, L., Ulmer, P., Romano, C., 2008. Rheological Properties of Magma From the 1538 Eruption of Monte Nuovo (Phlegrean Fields, Italy). Chemical Geology 256, 158–171. https://doi.org/10.1016/j.chemgeo.2008.06.035

Carslaw, H.S., Jaeger, J.C., 1959. Conduction of heat in solids. Clarendon Press, Oxford.

Cecchi, E., van Wyk de Vries, B., Lavest, J.-M., 2004. Flank spreading and collapse of weak-cored volcanoes. Bulletin of Volcanology 67, 72–91. https://doi.org/10.1007/s00445-004-0369-3

Chen, X., Elwood Madden, A.S., Reches, Z., 2017. Friction Evolution of Granitic Faults: Heating Controlled Transition From Powder Lubrication to Frictional Melt. Journal of Geophysical Research: Solid Earth 122, 9275–9289. https://doi.org/https://doi.org/10.1002/2017JB014462

Chester, F.M., Chester, J.S., 1998. Ultracataclasite structure and friction processes of the Punchbowl fault, San Andreas system, California. Tectonophysics 295, 199–221. https://doi.org/https://doi.org/10.1016/S0040-1951(98)00121-8

Chester, F.M., Logan, J.M., 1986. Implications for mechanical properties of brittle faults from observations of the Punchbowl fault zone, California. Pure and Applied Geophysics 124, 79–106. https://doi.org/10.1007/BF00875720

Christie, J.M., Griggs, D.T., Heuer, A.H., Nord, J.L, J., Radcliffe, S.V., Lally, J.S., Fisher, R.M., 1973. Electron petrography of Apollo 14 and 15 breccias and shock-produced analogs. Lunar and Planetary Science Conference Proceedings 4, 365–382.

Cimarelli, C., Costa, A., Mueller, S., Mader, H.M., 2011. Rheology of magmas with bimodal crystal size and shape distributions: Insights from analog experiments. Geochemistry, Geophysics, Geosystems 12. https://doi.org/https://doi.org/10.1029/2011GC003606

Clavero, J., Sparks, R.S.J., Huppert, H., WB, D., 2002. Geological constraints on the emplacement mechanism of the Parinacota debris avalanche, Northern Chile. Bulletin of Volcanology 64, 40–54. https://doi.org/10.1007/s00445-001-0183-0

Clough, C.T., Maufe, H.B., Bailey, E.B., 1909. The Cauldron-Subsidence of Glen Coe, and the Associated Igneous Phenomena. Quarterly Journal of the Geological Society 65, 611–678. https://doi.org/10.1144/GSL.JGS.1909.065.01-04.35

Coats, R., Kendrick, J., Wallace, P., Miwa, T., Hornby, A., Ashworth, J., Matsushima, T., Lavallée, Y., 2018. Failure criteria for porous dome rocks and lavas: A study of Mt.

Unzen, Japan. Solid Earth 9, 1299–1328. https://doi.org/10.5194/se-9-1299-2018

Collettini, C., Niemeijer, A., Viti, C., Marone, C., 2009. Fault zone fabric and fault weakness. Nature 462, 907–910. https://doi.org/10.1038/nature08585

Collettini, C., Tesei, T., Scuderi, M.M., Carpenter, B.M., Viti, C., 2019. Beyond Byerlee friction, weak faults and implications for slip behavior. Earth and Planetary Science Letters 519, 245–263. https://doi.org/10.1016/J.EPSL.2019.05.011

Conway, J.C., Pangborn, R.N., Cohen, P.H., Love, D.A., 1988. Dry sliding wear behavior of an Si-Al-O-N ceramic. Wear 126, 79–90. https://doi.org/https://doi.org/10.1016/0043-1648(88)90110-X

Cordonnier, B., Caricchi, L., Pistone, M., Castro, J., Hess, K.-U., Gottschaller, S., Manga, M., Dingwell, D.B., Burlini, L., 2012. The viscous-brittle transition of crystal-bearing silicic melt: Direct observation of magma rupture and healing. Geology 40, 611–614. https://doi.org/10.1130/G3914.1

Costa, A., Caricchi, L., Bagdassarov, N., 2009. A model for the rheology of particle-bearing suspensions and partially molten rocks. Geochemistry, Geophysics, Geosystems 10. https://doi.org/10.1029/2008GC002138

Cowan, D.S., 1999. Do faults preserve a record of seismic slip? A field geologist's opinion. Journal of Structural Geology 21, 995–1001.

Craddock, J.P., Geary, J., Malone, D.H., 2012. Vertical injectites of detachment carbonate ultracataclasite at White Mountain, Heart Mountain detachment, Wyoming. Geology 40, 463–466. https://doi.org/10.1130/G32734.1

Dade, B.W., Huppert, H.E., 1998. Long-runout rockfalls. Geology 26, 803–806. https://doi.org/10.1130/0091-7613(1998)026<0803:LRR>2.3.CO;2

Davies, T., McSaveney, M., Kelfoun, K., 2010. Runout of the Socompa volcanic debris avalanche, Chile: a mechanical explanation for low basal shear resistance. Bulletin of Volcanology 72, 933–944. https://doi.org/10.1007/s00445-010-0372-9

Davies, T.R., McSaveney, M.J., 2009. The role of rock fragmentation in the motion of large landslides. Engineering Geology 109, 67–79. https://doi.org/https://doi.org/10.1016/j.enggeo.2008.11.004

Davies, T.R.H., 1982. Spreading of rock avalanche debris by mechanical fluidization. Rock

Mechanics 15, 9–24. https://doi.org/10.1007/BF01239474

Day, S.J., 1996. Hydrothermal pore fluid pressure and the stability of porous, permeable volcanoes. Geological Society, London, Special Publications 110, 77–93. https://doi.org/10.1144/gsl.sp.1996.110.01.06

Day, S.J., Carracedo, J.C., Guillou, H., 1997. Age and geometry of an aborted rift flank collapse: the San Andres fault system, El Hierro, Canary Islands. Geological Magazine 134, 523–537. https://doi.org/DOI: 10.1017/S0016756897007243

De Blasio, F.V., 2011. Landslides in Valles Marineris (Mars): A possible role of basal lubrication by sub-surface ice. Planetary and Space Science 59, 1384–1392. https://doi.org/10.1016/J.PSS.2011.04.015

De Blasio, F.V., Elverhøi, A., 2008. A model for frictional melt production beneath large rock avalanches. Journal of Geophysical Research: Earth Surface 113, n/a-n/a. https://doi.org/10.1029/2007JF000867

De Paola, N., Hirose, T., Mitchell, T., Di Toro, G., Viti, C., Shimamoto, T., 2011. Fault lubrication and earthquake propagation in thermally unstable rocks. Geology 39, 35–38. https://doi.org/10.1130/G31398.1

de Silva, S.L., Francis, P.W., 1990. Potentially active volcanoes of Peru-Observations using Landsat Thematic Mapper and Space Shuttle imagery. Bulletin of Volcanology 52, 286–301. https://doi.org/10.1007/BF00304100

Di Toro, G., Goldsby, D.L., Tullis, T.E., 2004. Friction falls towards zero in quartz rock as slip velocity approaches seismic rates. Nature 427, 436–439. https://doi.org/10.1038/nature02249

Di Toro, G., Han, R., Hirose, T., De Paola, N., Nielsen, S., Mizoguchi, K., Ferri, F., Cocco, M., Shimamoto, T., 2011. Fault lubrication during earthquakes. Nature 471, 494–498.

Di Toro, G., Hirose, T., Nielsen, S., Pennacchioni, G., Shimamoto, T., 2006. Natural and experimental evidence of melt lubrication of faults during earthquakes. Science 311, 647–649. https://doi.org/10.1126/science.1121012

Di Toro, G., Mittempergher, S., Ferri, F., Mitchell, T., Pennacchioni, G., 2012. The contribution of structural geology, experimental rock deformation and numerical modelling to an improved understanding of the seismic cycle Preface to the Special Volume “Physico-chemical processes in seismic faults.” Journal of Structural Geology

38, 3–10. https://doi.org/10.1016/j.jsg.2012.01.025

Di Toro, G., Nielsen, S., Pennacchioni, G., 2005. Earthquake rupture dynamics frozen in exhumed ancient faults. Nature 436, 1009–1012. https://doi.org/10.1038/nature03910

Di Toro, G., Pennacchioni, G., 2005. Fault plane processes and mesoscopic structure of a strong-type seismogenic fault in tonalites (Adamello batholith, Southern Alps). Tectonophysics 402, 55–80. https://doi.org/10.1016/J.TECTO.2004.12.036

Dieterich, J.H., 1992. Earthquake nucleation on faults with rate-and state-dependent strength. Tectonophysics 211, 115–134. https://doi.org/10.1016/0040-1951(92)90055-b

Dieterich, J.H., 1979. Modeling of rock friction: 1. Experimental results and constitutive equations. Journal of Geophysical Research: Solid Earth 84, 2161–2168. https://doi.org/10.1029/JB084iB05p02161

Dieterich, J.H., Kilgore, B.D., 1994. Direct observation of frictional contacts: New insights for state-dependent properties. Pure and Applied Geophysics 143, 283–302. https://doi.org/10.1007/BF00874332

Dingwell, D.B., 1996. Volcanic Dilemma--Flow or Blow? Science 273, 1054 LP – 1055. https://doi.org/10.1126/science.273.5278.1054

Dingwell, D.B., Webb, S.L., 1989. Structural relaxation in silicate melts and non-Newtonian melt rheology in geologic processes. Physics and Chemistry of Minerals 16, 508–516. https://doi.org/10.1007/bf00197020

Douillet, G.A., Tsang-Hin-Sun, È., Kueppers, U., Letort, J., Pacheco, D.A., Goldstein, F., Von Aulock, F., Lavallée, Y., Hanson, J.B., Bustillos, J., Robin, C., Ramón, P., Hall, M., Dingwell, D.B., 2013. Sedimentology and geomorphology of the deposits from the August 2006 pyroclastic density currents at Tungurahua volcano, Ecuador. Bulletin of Volcanology 75, 765. https://doi.org/10.1007/s00445-013-0765-7

Dufresne, A., Boesmeier, A., Prager, C., 2016. Sedimentology of rock avalanche deposits – Case study and review. Earth-Science Reviews 163, 234–259. https://doi.org/10.1016/j.earscirev.2016.10.002

Dunn, D.E., LaFountain, L.J., Jackson, R.E., 1973. Porosity dependence and mechanism of brittle fracture in sandstones. Journal of Geophysical Research (1896-1977) 78, 2403–

2417. https://doi.org/10.1029/JB078i014p02403

Einstein, A., 1906. Eine neue Bestimmung der Moleküldimensionen. Annalen Der Physik 324, 289–306. https://doi.org/https://doi.org/10.1002/andp.19063240204

Elsworth, D., Voight, B., Taron, J., 2007. Contemporary views of slope instability on active volcanoes, Volcanic Rocks. Taylor & Francis Ltd, London.

Engelder, J.T., 1974. Cataclasis and the Generation of Fault Gouge. Bulletin of the Geological Society of America 85, 1515–1522. https://doi.org/10.1130/0016-7606(1974)85<1515:CATGOF>2.0.CO;2

Engelder, J.T., Scholz, C.H., 1976. The role of asperity indentation and ploughing in rock friction—II: Influence of relative hardness and normal load. International Journal of Rock Mechanics and Mining Sciences & Geomechanics Abstracts 13, 155–163. https://doi.org/10.1016/0148-9062(76)90820-2

Erismann, T., Abele, G., 2001. Dynamics of Rockslides and Rockfalls. https://doi.org/10.1007/978-3-662-04639-5

Erismann, T.H., 1979. Mechanisms of large landslides. Rock Mechanics 12, 15–46. https://doi.org/10.1007/bf01241087

Faulkner, D.R., Sanchez-Roa, C., Boulton, C., den Hartog, S.A.M., 2018. Pore Fluid Pressure Development in Compacting Fault Gouge in Theory, Experiments, and Nature. Journal of Geophysical Research: Solid Earth 123, 226–241. https://doi.org/10.1002/2017JB015130

Ferri, F., Di Toro, G., Hirose, T., Han, R., Noda, H., Shimamoto, T., Quaresimin, M., de Rossi, N., 2011. Low- to high-velocity frictional properties of the clay-rich gouges from the slipping zone of the 1963 Vaiont slide, northern Italy. Journal of Geophysical Research: Solid Earth 116. https://doi.org/10.1029/2011JB008338

Fialko, Y., Khazan, Y., 2005. Fusion by earthquake fault friction: Stick or slip? Journal of Geophysical Research 110. https://doi.org/10.1029/2005JB003869

Fisher, R. V., 1995. Decoupling of pyroclastic currents: hazards assessments. Journal of Volcanology and Geothermal Research 66, 257–263. https://doi.org/10.1016/0377-0273(94)00075-R

Fleming, J.R., Suh, N.P., 1977. Mechanics of crack propagation in delamination wear. Wear

44, 39–56. https://doi.org/10.1016/0043-1648(77)90083-7

Floyd, M.A., Walters, R.J., Elliott, J.R., Funning, G.J., Svarc, J.L., Murray, J.R., Hooper, A.J., Larsen, Y., Marinkovic, P., Bürgmann, R., Johanson, I.A., Wright, T.J., 2016. Spatial variations in fault friction related to lithology from rupture and afterslip of the 2014 South Napa, California, earthquake. Geophysical Research Letters 43, 6808–6816. https://doi.org/https://doi.org/10.1002/2016GL069428

Frictional melting in magma and lava., n.d.

Giampiccolo, E., Cocina, O., De Gori, P., Chiarabba, C., 2020. Dyke intrusion and stress-induced collapse of volcano flanks: The example of the 2018 event at Mt. Etna (Sicily, Italy). Scientific Reports 10, 6373. https://doi.org/10.1038/s41598-020-63371-3

Giordano, D., Russell, J.K., Dingwell, D.B., 2008. Viscosity of magmatic liquids: A model. Earth and Planetary Science Letters 271, 123–134. https://doi.org/10.1016/J.EPSL.2008.03.038

Glicken, H., 1998. Rockslide-debris avalanche of May 18, 1980, Mount St. Helens Volcano, Washington. Bulletin of the Geological Survey of Japan 49, 96–677.

Glicken, H., 1991. Sedimentary Architecture of Large Volcanic-Debris Avalanches., Sedimentation in Volcanic Settings. https://doi.org/10.2110/pec.91.45.0099

Glicken, H., 1990. The Rockslide -Debris Avalanche of the May 18, 1980, Eruption of Mount St. Helens — 10th Anniversary Perspectives. Geoscience Canada 17.

Goldsby, D.L., Tullis, T.E., 2002. Low frictional strength of quartz rocks at subseismic slip rates. Geophysical Research Letters 29, 24–25. https://doi.org/https://doi.org/10.1029/2002GL015240

Goren, L., Aharonov, E., Anders, M.H., 2010. The long runout of the Heart Mountain landslide: Heating, pressurization, and carbonate decomposition. Journal of Geophysical Research: Solid Earth 115. https://doi.org/10.1029/2009JB007113

Grunewald, U., Sparks, R.S.J., Kearns, S., Komorowski, J.C., 2000. Friction marks on blocks from pyroclastic flows at the Soufriere Hills volcano, Montserrat: Implications for flow mechanisms. Geology 28, 827–830. https://doi.org/10.1130/0091-7613(2000)28<827:FMOBFP>2.0.CO;2

Erismann, T., Abele, G., 2001. Dynamics of Rockslides and Rockfalls.

https://doi.org/10.1007/978-3-662-04639-5

Hacker, D.B., Biek, R.F., Rowley, P.D., 2014. Catastrophic emplacement of the gigantic Markagunt gravity slide, southwest Utah (USA): Implications for hazards associated with sector collapse of volcanic fields. Geology 42, 943–946. https://doi.org/10.1130/G35896.1

Hall, M.L., Robin, C., Beate, B., Mothes, P., Monzier, M., 1999. Tungurahua Volcano, Ecuador: structure, eruptive history and hazards. Journal of Volcanology and Geothermal Research 91, 1–21. https://doi.org/https://doi.org/10.1016/S0377-0273(99)00047-5

Han, R., Hirose, T., Shimamoto, T., 2010. Strong velocity weakening and powder lubrication of simulated carbonate faults at seismic slip rates. Journal of Geophysical Research: Solid Earth 115. https://doi.org/https://doi.org/10.1029/2008JB006136

Han, R., Kim, J.-S., Kim, C.-M., Hirose, T., Jeong, J.O., Jeong, G.Y., 2019. Dynamic weakening of ring faults and catastrophic caldera collapses. Geology 47, 107–110. https://doi.org/10.1130/G45687.1

Han, R., Shimamoto, T., Hirose, T., Ree, J.-H., Ando, J., 2007. Ultralow Friction of Carbonate Faults Caused by Thermal Decomposition. Science 316, 878 LP – 881. https://doi.org/10.1126/science.1139763

Harnett, C.E., Kendrick, J.E., Lamur, A., Thomas, M.E., Stinton, A., Wallace, P.A., Utley, J.E.P., Murphy, W., Neuberg, J., Lavallée, Y., 2019. Evolution of Mechanical Properties of Lava Dome Rocks Across the 1995–2010 Eruption of Soufrière Hills Volcano, Montserrat. Frontiers in Earth Science 7, 7. https://doi.org/10.3389/feart.2019.00007

Heap, M.J., Farquharson, J.I., Baud, P., Lavallée, Y., Reuschlé, T., 2015. Fracture and compaction of andesite in a volcanic edifice. Bulletin of Volcanology 77, 55. https://doi.org/10.1007/s00445-015-0938-7

Heap, M.J., Faulkner, D.R., Meredith, P.G., Vinciguerra, S., 2010. Elastic moduli evolution and accompanying stress changes with increasing crack damage: implications for stress changes around fault zones and volcanoes during deformation. Geophysical Journal International 183, 225–236. https://doi.org/10.1111/j.1365-246X.2010.04726.x

Heap, M.J., Lavallée, Y., Petrakova, L., Baud, P., Reuschlé, T., Varley, N.R., Dingwell, D.B.,

2014a. Microstructural controls on the physical and mechanical properties of edifice-forming andesites at Volcán de Colima, Mexico. Journal of Geophysical Research: Solid Earth 119, 2925–2963. https://doi.org/https://doi.org/10.1002/2013JB010521

Heap, M.J., Villeneuve, M., Albino, F., Farquharson, J.I., Brothelande, E., Amelung, F., Got, J.-L., Baud, P., 2020. Towards more realistic values of elastic moduli for volcano modelling. Journal of Volcanology and Geothermal Research 390, 106684. https://doi.org/https://doi.org/10.1016/j.jvolgeores.2019.106684

Heap, M.J., Wadsworth, F.B., Xu, T., Chen, C., Tang, C., 2016. The strength of heterogeneous volcanic rocks: A 2D approximation. Journal of Volcanology and Geothermal Research 319, 1–11. https://doi.org/https://doi.org/10.1016/j.jvolgeores.2016.03.013

Heap, M.J., Xu, T., Chen, C., 2014b. The influence of porosity and vesicle size on the brittle strength of volcanic rocks and magma. Bulletin of Volcanology 76, 856. https://doi.org/10.1007/s00445-014-0856-0

Hess, K.-U., Dingwell, D., 1996. Viscosities of hydrous leucogranitic melts: A non-Arrhenian model. American Mineralogist 81, 1297–1300.

Hirose, T., Mizoguchi, K., Shimamoto, T., 2012. Wear processes in rocks at slow to high slip rates. Journal of Structural Geology 38, 102–116. https://doi.org/10.1016/J.JSG.2011.12.007

Hirose, T., Shimamoto, T., 2005a. Growth of molten zone as a mechanism of slip weakening of simulated faults in gabbro during frictional melting. Journal of Geophysical Research: Solid Earth 110, B05202. https://doi.org/10.1029/2004jb003207

Hirose, T., Shimamoto, T., 2005b. Slip-Weakening Distance of Faults during Frictional Melting as Inferred from Experimental and Natural Pseudotachylytes. Bulletin of the Seismological Society of America 95, 1666–1673. https://doi.org/10.1785/0120040131

Holland, T.H., 1900. The charnockite series, a group of Archaean hypersthenic rocks in Peninsular India. Mem Geol Surv India 28, 119–249.

Hornby, A.J., Kendrick, J.E., Lamb, O.D., Hirose, T., De Angelis, S., von Aulock, F.W., Umakoshi, K., Miwa, T., Henton De Angelis, S., Wadsworth, F.B., Hess, K.-U., Dingwell, D.B., Lavallée, Y., 2015. Spine growth and seismogenic faulting at Mt. Unzen, Japan.

Journal of Geophysical Research: Solid Earth 2014JB011660. https://doi.org/10.1002/2014JB011660

Hornby, A.J., Lavallée, Y., Kendrick, J.E., De Angelis, S., Lamur, A., Lamb, O.D., Rietbrock, A., Chigna, G., 2019. Brittle-Ductile Deformation and Tensile Rupture of Dome Lava During Inflation at Santiaguito, Guatemala. Journal of Geophysical Research: Solid Earth 124, 10107–10131. https://doi.org/https://doi.org/10.1029/2018JB017253

Hoskins, E.R., Jaeger, J.C., Rosengren, K.J., 1968. A medium-scale direct friction experiment. International Journal of Rock Mechanics and Mining Sciences & Geomechanics Abstracts 5, 143–152. https://doi.org/https://doi.org/10.1016/0148-9062(68)90030-2

Hughes, A., Kendrick, J.E., Lamur, A., Wadsworth, F.B., Wallace, P.A., Di Toro, G., Lavallée, Y., 2020a. Frictional Behaviour, Wear and Comminution of Synthetic Porous Geomaterials. Frontiers in Earth Science 8, 488. https://doi.org/10.3389/feart.2020.562548

Hughes, A., Kendrick, J.E., Salas, G., Wallace, P.A., Legros, F., Di Toro, G., Lavallée, Y., 2020b. Shear localisation, strain partitioning and frictional melting in a debris avalanche generated by volcanic flank collapse. Journal of Structural Geology 140, 104132. https://doi.org/https://doi.org/10.1016/j.jsg.2020.104132

Hunt, J.E., Cassidy, M., Talling, P.J., 2018. Multi-stage volcanic island flank collapses with coeval explosive caldera-forming eruptions. Scientific Reports 8, 1146. https://doi.org/10.1038/s41598-018-19285-2

Hutchings, I., Shipway, P., 2017. 6 - Wear by hard particles. In: Hutchings, I., Shipway, P. (Eds.), Tribology (Second Edition). Butterworth-Heinemann, 165–236. https://doi.org/https://doi.org/10.1016/B978-0-08-100910-9.00006-4

Ikari, M.J., Saffer, D.M., Marone, C., 2009. Frictional and hydrologic properties of clay-rich fault gouge. Journal of Geophysical Research: Solid Earth 114. https://doi.org/10.1029/2008JB006089

Iverson, R.M., George, D.L., Allstadt, K., Reid, M.E., Collins, B.D., Vallance, J.W., Schilling, S.P., Godt, J.W., Cannon, C.M., Magirl, C.S., Baum, R.L., Coe, J.A., Schulz, W.H., Bower, J.B., 2015. Landslide mobility and hazards: implications of the 2014 Oso disaster. Earth and Planetary Science Letters 412, 197–208. https://doi.org/10.1016/J.EPSL.2014.12.020

Jiang, H., Lee, C.-T.A., Morgan, J.K., Ross, C.H., 2015. Geochemistry and thermodynamics of an earthquake: A case study of pseudotachylites within mylonitic granitoid. Earth and Planetary Science Letters 430, 235–248. https://doi.org/https://doi.org/10.1016/j.epsl.2015.08.027

Johnson, B.C., Campbell, C.S., Melosh, H.J., 2016. The reduction of friction in long runout landslides as an emergent phenomenon. Journal of Geophysical Research: Earth Surface 121, 881–889. https://doi.org/10.1002/2015JF003751

Kanamori, H., Rivera, L., 2013. Energy Partitioning During an Earthquake. Earthquakes: Radiated Energy and the Physics of Faulting. American Geophysical Union (AGU), 3–13. https://doi.org/10.1029/170GM03

Kaneoka, I., Guevara, C., 1984. K-Ar determinations of late Tertiary and Quaternary Andean volcanic rocks, Southern Peru. GEOCHEMICAL JOURNAL 18, 233–239. https://doi.org/10.2343/geochemj.18.233

Kawamura, S., Miura, S., 2013. Rainfall-induced failures of volcanic slopes subjected to freezing and thawing. Soils and Foundations 53, 443–461. https://doi.org/10.1016/J.SANDF.2013.04.006

Kendrick, J.E., Lavallée, Y., Hess, K.-U., De Angelis, S., Ferk, A., Gaunt, E., Dingwell, D., Leonhardt, R., 2014. Seismogenic frictional melting in the magmatic column. Solid Earth 5, 199–208. https://doi.org/10.5194/se-5-199-2014

Kendrick, J.E., Lavallée, Y., Hirose, T., Di Toro, G., Hornby, A.J., De Angelis, S., Dingwell, D.B., 2014. Volcanic drumbeat seismicity caused by stick-slip motion and magmatic frictional melting. Nature Geosci 7, 438–442. https://doi.org/10.1038/ngeo2146 http://www.nature.com/ngeo/journal/v7/n6/abs/ngeo2146.html#supplementary-information

Kendrick, J.E., Lavallée, Y., Ferk, A., Perugini, D., Leonhardt, R., Dingwell, D.B., 2012. Extreme frictional processes in the volcanic conduit of Mount St. Helens (USA) during the 2004–2008 eruption. Journal of Structural Geology 38, 61–76. https://doi.org/10.1016/j.jsg.2011.10.003

Kendrick, J.E., Smith, R., Sammonds, P., Meredith, P.G., Dainty, M., Pallister, J.S., 2013. The influence of thermal and cyclic stressing on the strength of rocks from Mount St. Helens, Washington. Bulletin of Volcanology 75, 728.

https://doi.org/10.1007/s00445-013-0728-z

Kennedy, F., 2000. Frictional heating and contact temperatures. Modern Tribology Handbook: Volume One: Principles of Tribology. 235–272.

Kirkpatrick, J.D., Rowe, C.D., 2013. Disappearing ink: How pseudotachylytes are lost from the rock record. Journal of Structural Geology 52, 183–198. https://doi.org/10.1016/J.JSG.2013.03.003

Klein, J., Mueller, S.P., Castro, J.M., 2017. The Influence of Crystal Size Distributions on the Rheology of Magmas: New Insights From Analog Experiments. Geochemistry, Geophysics, Geosystems 18, 4055–4073. https://doi.org/10.1002/2017GC007114

Kohlstedt, D.L., Holtzman, B.K., 2009. Shearing Melt Out of the Earth: An Experimentalist's Perspective on the Influence of Deformation on Melt Extraction. Annual Review of Earth and Planetary Sciences 37, 561–593. https://doi.org/10.1146/annurev.earth.031208.100104

Kohlstedt, D.L., Zimmerman, M.E., Mackwell, S.J., 2010. Stress-driven Melt Segregation in Partially Molten Feldspathic Rocks. Journal of Petrology 51, 9–19. https://doi.org/10.1093/petrology/egp043

Kokelaar, P., 2007. Friction melting, catastrophic dilation and breccia formation along caldera superfaults. Journal of the Geological Society 164, 751 LP – 754. https://doi.org/10.1144/0016-76492006-059

Lagmay, A.M.F., van Wyk de Vries, B., Kerle, N., Pyle, D.M., 2000. Volcano instability induced by strike-slip faulting. Bulletin of Volcanology 62, 331–346. https://doi.org/10.1007/s004450000103

Lamur, A., Kendrick, J.E., Wadsworth, F.B., Lavallée, Y., 2019. Fracture healing and strength recovery in magmatic liquids. Geology 47, 195–198. https://doi.org/10.1130/G45512.1

Lamur, A., Lavallée, Y., Iddon, F.E., Hornby, A.J., Kendrick, J.E., von Aulock, F.W., Wadsworth, F.B., 2018. Disclosing the temperature of columnar jointing in lavas. Nature Communications 9, 1432. https://doi.org/10.1038/s41467-018-03842-4

Lavallée, Y., de Silva, S.L., Salas, G., Byrnes, J.M., 2009. Structural control on volcanism at the Ubinas, Huaynaputina, and Ticsani Volcanic Group (UHTVG), southern Peru. Journal of Volcanology and Geothermal Research 186, 253–264.

https://doi.org/10.1016/J.JVOLGEORES.2009.07.003

Lavallée, Y., Dingwell, D.B., Johnson, J.B., Cimarelli, C.., Hornby, A.J., Kendrick, J.., von Aulock, F.W., Kennedy, B.M., Andrews, B.., Wadsworth, F.., Rhodes, E., Chigna, G., 2015a. Thermal vesiculation during volcanic eruptions. Nature 528, 544–547. https://doi.org/10.1038/nature16153

Lavallée, Y., Hess, K.U., Cordonnier, B., Dingwell, D.B., 2007. Non-Newtonian rheological law for highly crystalline dome lavas. Geology 35, 843–846.

Lavallée, Y., Hirose, T., Kendrick, J.E., De Angelis, S., Petrakova, L., Hornby, A.J., Dingwell, D.B., 2014. A frictional law for volcanic ash gouge. Earth and Planetary Science Letters 400, 177–183. https://doi.org/http://dx.doi.org/10.1016/j.epsl.2014.05.023

Lavallée, Y., Hirose, T., Kendrick, J.E., Hess, K.-U., Dingwell, D.B., 2015b. Fault rheology beyond frictional melting. Proceedings of the National Academy of Sciences 112.

Lavallée, Y., Kendrick, J.E., 2020. A review of the physical and mechanical properties of volcanic rocks and magmas in the brittle and ductile fields. In: Vol. Ed. Papale, P., series Ed. Shroder, J.F. (Ed.), Forecasting and Planning for Volcanic Hazards, Risks, and Disasters. Elsevier Hazards and Disasters series, 214.

Lavallée, Y., Kendrick, J.E., 2021. Chapter 5 - A review of the physical and mechanical properties of volcanic rocks and magmas in the brittle and ductile regimes. In: Papale, P. (Ed.), Forecasting and Planning for Volcanic Hazards, Risks, and Disasters, Hazards and Disasters. Elsevier, 153–238. https://doi.org/https://doi.org/10.1016/B978-0-12-818082-2.00005-6

Lavallée, Y., Mitchell, T.M., Heap, M.J., Vasseur, J., Hess, K.-U., Hirose, T., Dingwell, D.B., 2012. Experimental generation of volcanic pseudotachylytes: Constraining rheology. Journal of Structural Geology 38, 222–233. https://doi.org/10.1016/j.jsg.2012.02.001

Le Bas, M.J., Streckeisen, A.L., 1991. The IUGS systematics of igneous rocks. Journal of the Geological Society 148, 825–833. https://doi.org/10.1144/gsjgs.148.5.0825

Lebti, P.P., Thouret, J.-C., Wörner, G., Fornari, M., 2006. Neogene and Quaternary ignimbrites in the area of Arequipa, Southern Peru: Stratigraphical and petrological correlations. Journal of Volcanology and Geothermal Research 154, 251–275. https://doi.org/https://doi.org/10.1016/j.jvolgeores.2006.02.014

Legros, F., 2002. The mobility of long-runout landslides. Engineering Geology 63, 301–331.

https://doi.org/10.1016/S0013-7952(01)00090-4

Legros, F., Cantagrel, J., Devouard, B., 2000. Pseudotachylyte (Frictionite) at the Base of the Arequipa Volcanic Landslide Deposit (Peru): Implications for Emplacement Mechanisms. The Journal of Geology 108, 601–611. https://doi.org/doi:10.1086/314421

Lejeune, A.-M., Richet, P., 1995a. Rheology of crystal-bearing silicate melts: An experimental study at high viscosities. Journal of Geophysical Research: Solid Earth 100, 4215–4229. https://doi.org/10.1029/94JB02985

Lejeune, A.-M., Richet, P., 1995b. Rheology of crystal-bearing silicate melts: An experimental study at high viscosities. Journal of Geophysical Research: Solid Earth 100, 4215–4229. https://doi.org/10.1029/94JB02985

Lesher, C.E., Spera, F.J., 2015. Chapter 5 - Thermodynamic and Transport Properties of Silicate Melts and Magma. In: Sigurdsson, H.B.T.-T.E. of V. (Second E. (Ed.). Academic Press, Amsterdam, 113–141. https://doi.org/https://doi.org/10.1016/B978-0-12-385938-9.00005-5

Lewis, D.W., 1984. Practical sedimentology. Hutchinson Ross.

Lin, A., 2007. Fossil Earthquakes: The Formation and Preservation of Pseudotachylytes, Lecture Notes in Earth Sciences. Springer Berlin Heidelberg.

Lin, A., 1999. Roundness of clasts in pseudotachylytes and cataclastic rocks as an indicator of frictional melting. Journal of Structural Geology 21, 473–478. https://doi.org/https://doi.org/10.1016/S0191-8141(99)00030-9

Lin, A., Chen, A., Liau, C.-F., Lee, C.-T., Lin, C.-C., Lin, P.-S., Wen, S.-C., Ouchi, T., 2001. Frictional fusion due to coseismic landsliding during the 1999 Chi-Chi (Taiwan) ML 7.3 Earthquake. Geophysical Research Letters 28, 4011–4014. https://doi.org/10.1029/2001GL013253

Lin, A.M., Shimamoto, T., 1998. Selective melting processes as inferred from experimentally generated pseudotachylytes. JOURNAL OF ASIAN EARTH SCIENCES 16, 533–545. https://doi.org/10.1016/S0743-9547(98)00040-3

Lipman, P.W., Mullineaux, D.R., 1981. The 1980 eruptions of Mount St. Helens, Washington, Professional Paper. https://doi.org/10.3133/pp1250

Loughlin, S., Sparks, S., Brown, S., Jenkins, S., Vye-Brown, C., 2015. Global Volcanic Hazards and Risk. Cambridge University Press, Cambridge. https://doi.org/DOI: 10.1017/CBO9781316276273

Lucchitta, B.K., 1987. Valles Marineris, Mars: Wet debris flows and ground ice. Icarus 72, 411–429. https://doi.org/10.1016/0019-1035(87)90183-7

Ma, S., Shimamoto, T., Yao, L., Togo, T., Kitajima, H., 2014. A rotary-shear low to high-velocity friction apparatus in Beijing to study rock friction at plate to seismic slip rates, Earthquake Science. https://doi.org/10.1007/s11589-014-0097-5

Maccaferri, F., Richter, N., Walter, T.R., 2017. The effect of giant lateral collapses on magma pathways and the location of volcanism. Nature Communications 8, 1097. https://doi.org/10.1038/s41467-017-01256-2

Maddock, R.H., 1986. Frictional melting in landslide-generated frictionites (hyalomylonites) and fault-generated pseudotachylytes-discussion. Tectonophysics 128, 151–153. https://doi.org/https://doi.org/10.1016/0040-1951(86)90316-1

Magloughlin, J.F., 2011. Bubble Collapse Structure: A Microstructural Record of Fluids, Bubble Formation and Collapse, and Mineralization in Pseudotachylyte. The Journal of Geology 119, 351–371. https://doi.org/10.1086/659143

Magloughlin, Jerry F., Spray, J.G., 1992. Frictional melting processes and products in geological materials: introduction and discussion. Tectonophysics 204, 197–204. https://doi.org/10.1016/0040-1951(92)90307-R

Magloughlin, Jerry F, Spray, J.G., 1992. Frictional melting processes and products in geological materials: introduction and discussion. Tectonophysics 204, 197–204. https://doi.org/https://doi.org/10.1016/0040-1951(92)90307-R

Mair, K., Abe, S., 2011. Breaking Up: Comminution Mechanisms in Sheared Simulated Fault Gouge, Pure and Applied Geophysics. https://doi.org/10.1007/s00024-011-0266-6

Marone, C., 1998. Laboratory-derived friction laws and their application to seismic faulting. Annual Review of Earth and Planetary Sciences 26, 643–696. https://doi.org/10.1146/annurev.earth.26.1.643

Masch, L., Wenk, H.R., Preuss, E., 1985. Electron microscopy study of hyalomylonites—evidence for frictional melting in landslides. Tectonophysics 115, 131–160. https://doi.org/10.1016/0040-1951(85)90103-9

Mase, C.W., Smith, L., 1984. Pore-fluid pressures and frictional heating on a fault surface. Pure and Applied Geophysics 122, 583–607. https://doi.org/10.1007/BF00874618

Matsu'ura, M., Kataoka, H., Shibazaki, B., 1992. Slip-dependent friction law and nucleation processes in earthquake rupture. Tectonophysics 211, 135–148. https://doi.org/10.1016/0040-1951(92)90056-C

Matthews, A.J., Barclay, J., 2004. A thermodynamical model for rainfall-triggered volcanic dome collapse. Geophysical Research Letters 31. https://doi.org/https://doi.org/10.1029/2003GL019310

McGuire, W.J., 2003. Volcano instability and lateral collapse. Revista 1, 33–45.

McGuire, W.J., 1996. Volcano instability: a review of contemporary themes. Geological Society, London, Special Publications 110, 1–23.

McGuire, W.J., Pullen, A.D., Saunders, S.J., 1990. Recent dyke-induced large-scale block movement at Mount Etna and potential slope failure. Nature 343, 357–359. https://doi.org/10.1038/343357a0

Melosh, H.J., 2005. The Mechanics of Pseudotachylite Formation in Impact Events. In: Koeberl, C., Henkel, H. (Eds.), Impact Tectonics. Springer Berlin Heidelberg, Berlin, Heidelberg, 55–80. https://doi.org/10.1007/3-540-27548-7_2

Melosh, H.J., 1986. The physics of very large landslides. Acta Mechanica 64, 89–99. https://doi.org/10.1007/BF01180100

Melosh, H.J., 1979. Acoustic fluidization: A new geologic process? Journal of Geophysical Research: Solid Earth 84, 7513–7520. https://doi.org/10.1029/JB084iB13p07513

Mitchell, T.M., Smith, S.A.F., Anders, M.H., Toro, G. Di, Nielsen, S., Cavallo, A., Beard, A.D., 2015. Catastrophic emplacement of giant landslides aided by thermal decomposition: Heart Mountain, Wyoming. Earth and Planetary Science Letters 411, 199–207. https://doi.org/https://doi.org/10.1016/j.epsl.2014.10.051

Mitchell, T.M., Toy, V., Di Toro, G., Renner, J., Sibson, R.H., 2016. Fault welding by pseudotachylyte formation. Geology 44, 1059–1062. https://doi.org/10.1130/G38373.1

Mohr, O., 1914. Abhandlungen aus dem Gebiete der technischen Mechanik. W. Ernst & Sohn, Berlin.

Moore, D.E., Lockner, D.A., 2011. Frictional strengths of talc-serpentine and talc-quartz mixtures. Journal of Geophysical Research B: Solid Earth 116. https://doi.org/10.1029/2010JB007881

Moore, M.A., King, F.S., 1980. Abrasive wear of brittle solids. Wear 60, 123–140. https://doi.org/10.1016/0043-1648(80)90253-7

Morohashi, S., Sawahata, Y., Yashima, S., 1973. Effect of Operational Conditions on the Formation of Ultra Fine Powders by a Reciprocating Friction Mill. Journal of the Society of Materials Science, Japan 22, 689–692. https://doi.org/10.2472/jsms.22.689

Mueller, S., Llewellin, E., Mader, H., 2011. The effect of particle shape on suspension viscosity and implications for magmatic flows. Geophysical Research Letters - GEOPHYS RES LETT 38. https://doi.org/10.1029/2011GL047167

Mueller, S., Llewellin, E.W., Mader, H.M., 2010. The rheology of suspensions of solid particles. Proceedings of the Royal Society A: Mathematical, Physical and Engineering Sciences 466, 1201–1228. https://doi.org/10.1098/rspa.2009.0445

Murray, J.B., van Wyk de Vries, B., Pitty, A., Sargent, P., Wooller, L., 2018. Gravitational sliding of the Mt. Etna massif along a sloping basement. Bulletin of Volcanology 80, 40. https://doi.org/10.1007/s00445-018-1209-1

Nielsen, S., Di Toro, G., Hirose, T., Shimamoto, T., 2008. Frictional Melt and Seismic Slip. Journal of Geophysical Research: Solid Earth 113, B01308. https://doi.org/doi:10.1029/2007JB005122.

Nielsen, S., Mosca, P., Giberti, G., Di Toro, G., Hirose, T., Shimamoto, T., 2010. On the transient behavior of frictional melt during seismic slip. Journal of Geophysical Research-Solid Earth 115, 17. https://doi.org/B1030110.1029/2009jb007020

Niemeijer, A., Marone, C., Elsworth, D., 2010. Frictional strength and strain weakening in simulated fault gouge: Competition between geometrical weakening and chemical strengthening. Journal of Geophysical Research: Solid Earth 115. https://doi.org/10.1029/2009JB000838

Niemeijer, A.R., Di Toro, G., Nielsen, S., Di Felice, F., 2011. Frictional melting of gabbro under extreme experimental conditions of normal stress, acceleration and sliding velocity. Journal of Geophysical Research: Solid Earth 116, B07404.

Numelin, T., Marone, C., Kirby, E., 2007. Frictional properties of natural fault gouge from a

low-angle normal fault, Panamint Valley, California. Tectonics 26. https://doi.org/10.1029/2005TC001916

Paguican, E.M.R., van Wyk de Vries, B., Lagmay, A.M.F., 2014. Hummocks: how they form and how they evolve in rockslide-debris avalanches. Landslides 11, 67–80. https://doi.org/10.1007/s10346-012-0368-y

Paterson, M.S., Wong, T.-F., 2005. Experimental Rock Deformation - The Brittle Field.

Phan, S.-E., Russel, W.B., Zhu, J., Chaikin, P.M., 1998. Effects of polydispersity on hard sphere crystals. The Journal of Chemical Physics 108, 9789–9795. https://doi.org/10.1063/1.476453

Phillips, N.J., Williams, R.T., 2021. To D or not to D? Re-evaluating particle-size distributions in natural and experimental fault rocks. Earth and Planetary Science Letters 553, 116635. https://doi.org/https://doi.org/10.1016/j.epsl.2020.116635

Philpotts, A.R., 1964. Origin of pseudotachylites. American Journal of Science 262, 1008–1035. https://doi.org/10.2475/ajs.262.8.1008

Power, W.L., Tullis, T.E., Weeks, J.D., 1988. Roughness and wear during brittle faulting. Journal of Geophysical Research: Solid Earth 93, 15268–15278. https://doi.org/10.1029/JB093iB12p15268

Pudasaini, S.P., Miller, S.A., 2013. The hypermobility of huge landslides and avalanches. Engineering Geology 157, 124–132. https://doi.org/https://doi.org/10.1016/j.enggeo.2013.01.012

Queener, C.A., Smith, T.C., Mitchell, W.L., 1965. Transient wear of machine parts. Wear 8, 391–400. https://doi.org/10.1016/0043-1648(65)90170-5

Rabinowicz, E., 1965. Friction and wear of materials. Wiley, New York.

Rajabzadeh, M.A., Moosavinasab, Z., Rakhshandehroo, G., 2012. Effects of Rock Classes and Porosity on the Relation between Uniaxial Compressive Strength and Some Rock Properties for Carbonate Rocks. Rock Mechanics and Rock Engineering 45, 113–122. https://doi.org/10.1007/s00603-011-0169-y

Rapetto, M.P., Almqvist, A., Larsson, R., Lugt, P.M., 2009. On the influence of surface roughness on real area of contact in normal, dry, friction free, rough contact by using a neural network. Wear 266, 592–595. https://doi.org/10.1016/J.WEAR.2008.04.059

Reches, Z., Lockner, D.A., 2010. Fault weakening and earthquake instability by powder lubrication. Nature 467, 452-U102. https://doi.org/10.1038/nature09348

Reid, M.E., 2004. Massive collapse of volcano edifices triggered by hydrothermal pressurization. Geology 32, 373–376. https://doi.org/10.1130/G20300.1

Reid, M.E., Sisson, T.W., Brien, D.L., 2001. Volcano collapse promoted by hydrothermal alteration and edifice shape, Mount Rainier, Washington. Geology 29, 779–782. https://doi.org/10.1130/0091-7613(2001)029<0779:VCPBHA>2.0.CO;2

Reid, Mark, E., Keith, Terry, E.C., Kayen, Robert, E., Iverson, Neal, R., Richard, M., Brien, Dianne, L., 2010. Volcano collapse promoted by progressive strength reduction: new data from Mount St. Helens. Springer, Heidelberg, Germany.

Reimold, W.U., 1995. Pseudotachylite in impact structures — generation by friction melting and shock brecciation?: A review and discussion. Earth-Science Reviews 39, 247–265. https://doi.org/https://doi.org/10.1016/0012-8252(95)00033-X

Rice, J.R., 2006. Heating and weakening of faults during earthquake slip. Journal of Geophysical Research: Solid Earth 111. https://doi.org/10.1029/2005JB004006

Roscoe, R., 1952. The viscosity of suspensions of rigid spheres. British Journal of Applied Physics 3, 267–269. https://doi.org/10.1088/0508-3443/3/8/306

Rowe, C.D., Moore, J.C., Meneghini, F., McKeirnan, A.W., 2005. Large-scale pseudotachylytes and fluidized cataclasites from an ancient subduction thrust fault. Geology 33, 937–940. https://doi.org/10.1130/G21856.1

Rozeanu, L., 1963. Fatigue wear as a rate process. Wear 6, 337–340. https://doi.org/10.1016/0043-1648(63)90201-1

Ruina, A., 1983. Slip Instability and State Variable Friction Laws. Journal of Geophysical Research 88.

Rust, A.C., Manga, M., 2002. Effects of bubble deformation on the viscosity of dilute suspensions. Journal of Non-Newtonian Fluid Mechanics 104, 53–63. https://doi.org/https://doi.org/10.1016/S0377-0257(02)00013-7

Rutter, E.H., Holdsworth, R.E., Knipe, R.J., 2001. The nature and tectonic significance of fault-zone weakening: an introduction. Geological Society, London, Special Publications 186, 1 LP – 11. https://doi.org/10.1144/GSL.SP.2001.186.01.01

Ryan, A.G., Kolzenburg, S., Vona, A., Heap, M.J., Russell, J.K., Badger, S., 2019. A proxy for magmatic foams: FOAMGLAS®, a closed-cell glass insulation. Journal of Non-Crystalline Solids: X 1, 100001. https://doi.org/https://doi.org/10.1016/j.nocx.2018.100001

Saadati, M., Forquin, P., Weddfelt, K., Larsson, P., Hild, F., 2018. On the Mechanical Behavior of Granite Material With Particular Emphasis on the Influence From Pre-Existing Cracks and Defects. In: Mitchell, M.R. (Ed.), Journal of Testing and Evaluation 46, 33–45. https://doi.org/10.1520/JTE20160072

Sagy, A., Brodsky, E.E., Axen, G.J., 2007. Evolution of fault-surface roughness with slip. Geology 35, 283–286. https://doi.org/10.1130/G23235A.1

Sammis, C.G., Ashby, M.F., 1986. The failure of brittle porous solids under compressive stress states. Acta Metallurgica 34, 511–526. https://doi.org/https://doi.org/10.1016/0001-6160(86)90087-8

Sarkar, A., Chattopadhyay, A., 2020. Microstructure and geochemistry of pseudotachylyte veins from Sarwar-Junia Fault Zone, India: Implications for frictional melting process in a seismic fault zone. Geological Journal 55, 7687–7715. https://doi.org/https://doi.org/10.1002/gj.3900

Sarkar, A., Chattopadhyay, A., Singh, T., 2019. Roundness of survivor clasts as a discriminator for melting and crushing origin of fault rocks: A reappraisal. Journal of Earth System Science 128, 51. https://doi.org/10.1007/s12040-019-1072-2

Schaefer, L.N., Kendrick, J.E., Oommen, T., Lavallée, Y., Chigna, G., 2015. Geomechanical rock properties of a basaltic volcano ., Frontiers in Earth Science .

Schaefer, L.N., Wang, T., Escobar-Wolf, R., Oommen, T., Lu, Z., Kim, J., Lundgren, P.R., Waite, G.P., 2017. Three-dimensional displacements of a large volcano flank movement during the May 2010 eruptions at Pacaya Volcano, Guatemala. Geophysical Research Letters 44, 135–142. https://doi.org/https://doi.org/10.1002/2016GL071402

Scheidegger, A.E., 1973. On the prediction of the reach and velocity of catastrophic landslides. Rock Mechanics 5, 231–236. https://doi.org/10.1007/BF01301796

Schneider, C.A., Rasband, W.S., Eliceiri, K.W., 2012. NIH Image to ImageJ: 25 years of image analysis. Nature Methods 9, 671–675. https://doi.org/10.1038/nmeth.2089

Scholz, C.H., 2019. The Mechanics of Earthquakes and Faulting. Cambridge University Press. https://doi.org/10.1017/9781316681473

Scholz, C.H., 1998. Earthquakes and friction laws. Nature 391, 37–42. https://doi.org/10.1038/34097

Scholz, C.H., 1987. Wear and gouge formation in brittle faulting. Geology 15, 493–495. https://doi.org/10.1130/0091-7613(1987)15<493:WAGFIB>2.0.CO;2

Scholz, C.H., Engelder, J.T., 1976. The role of asperity indentation and ploughing in rock friction — I: Asperity creep and stick-slip. International Journal of Rock Mechanics and Mining Sciences & Geomechanics Abstracts 13, 149–154. https://doi.org/10.1016/0148-9062(76)90819-6

Schumacher, J.C., 1999. Introduction to Metamorphic Textures, 2nd edition, by A. J. Barker. Stanley Thornes, Cheltenham, 1998. 264 pp. ISBN 0748739858. Paperback. £29.95. Journal of Petrology 40, 1745. https://doi.org/10.1093/petroj/40.11.1745

Schwarzkopf, L., Schmincke, H.-U., Troll, V., 2001. Pseudotachylite on impact marks of block surfaces in block-and-ash flows at Merapi volcano, Central Java, Indonesia. International Journal of Earth Sciences 90, 769–775. https://doi.org/10.1007/s005310000171

Scott, J.S., Drever, H.I., 1954. X.—Frictional Fusion Along a Himalayan Thrust. Proceedings of the Royal Society of Edinburgh. Section B. Biology 65, 121–142. https://doi.org/10.1017/S0080455X00012078

Shand, S.J., 1916. The Pseudotachylyte of Parijs (Orange Free State), and its Relation to {\textquoteleft}Trap-Shotten Gneiss{\textquoteright} and {\textquoteleft}Flinty Crush-Rock{\textquoteright}. Quarterly Journal of the Geological Society 72, 198–221. https://doi.org/10.1144/GSL.JGS.1916.072.01-04.12

Shea, T., van Wyk de Vries, B., 2008. Structural analysis and analogue modeling of the kinematics and dynamics of rockslide avalanchesShea and van Wyk de Vries. Geosphere 4, 657–686. https://doi.org/10.1130/GES00131.1

Shea, T., Van Wyk de Vries, B., 2010. Collapsing volcanoes: the sleeping giants' threat. Geology Today 26, 72–77. https://doi.org/https://doi.org/10.1111/j.1365-2451.2010.00750.x

Sherrod, D.R., Scott, W.E., Stauffer, P.H., 2008. A volcano rekindled: The renewed eruption

of Mount St. Helens, 2004-2006, Professional Paper. https://doi.org/10.3133/pp1750

Shimamoto, T., Lin, A., 1994. Is frictional melting equilibrium melting or non-equilibrium melting? Struct. Geol. (J. Tect. Res. Gro. Japan) 39, 79–84.

Shimamoto, T., Tsutsumi, A., 1994. A new rotary-shear high-speed frictional testing machine : its basic design and scope of research. Jour. Tectonic Res. Group of Japan 39, 65–78.

Shipton, Z.K., Soden, A.M., Kirkpatrick, J.D., Bright, A.M., Lunn, R.J., 2006. How Thick is a Fault? Fault Displacement-Thickness Scaling Revisited., Earthquakes: Radiated Energy and the Physics of Faulting, Geophysical Monograph Series. https://doi.org/doi:10.1029/170GM19

Shreve, R.L., 1968. The Blackhawk Landslide. In: Shreve, R.L. (Ed.), The Blackhawk Landslide. Geological Society of America, 0. https://doi.org/10.1130/SPE108-p1

Sibson, R.H., 1994. An assessment of field evidence for `Byerlee' friction. Pure and Applied Geophysics 142, 645–662. https://doi.org/10.1007/BF00876058

Sibson, R.H., 1977. Fault rocks and fault mechanisms. Journal of the Geological Society 133, 191–213. https://doi.org/10.1144/gsjgs.133.3.0191

Sibson, R.H., 1975. Generation of Pseudotachylyte by Ancient Seismic Faulting. Geophysical Journal of the Royal Astronomical Society 43, 775–794. https://doi.org/10.1111/j.1365-246X.1975.tb06195.x

Sibson, R.H., 1973. Interactions between Temperature and Pore-Fluid Pressure during Earthquake Faulting and a Mechanism for Partial or Total Stress Relief. Nature Physical Science 243, 66–68. https://doi.org/10.1038/physci243066a0

Sibson, R.H., Toy, V.G., 2006. The Habitat of Fault-Generated Pseudotachylyte: Presence vs. Absence of Friction-Melt. Earthquakes: Radiated Energy and the Physics of Faulting. American Geophysical Union (AGU), 153–166. https://doi.org/https://doi.org/10.1029/170GM16

Siebert, L., 1992. Threats from debris avalanches. Nature 356, 658–659. https://doi.org/10.1038/356658a0

Siebert, L., 1984. Large volcanic debris avalanches: Characteristics of source areas, deposits, and associated eruptions. Journal of Volcanology and Geothermal Research

22, 163–197. https://doi.org/10.1016/0377-0273(84)90002-7

Siebert, L., Glicken, H., Ui, T., 1987. Volcanic hazards from Bezymianny- and Bandai-type eruptions. Bulletin of Volcanology 49, 435–459. https://doi.org/10.1007/BF01046635

Sleep, N.H., 2019. Thermal Weakening of Asperity Tips on Fault Planes at High Sliding Velocities. Geochemistry, Geophysics, Geosystems 20, 1164–1188. https://doi.org/10.1029/2018GC008062

Spray, J., 2010. Frictional Melting Processes in Planetary Materials: From Hypervelocity Impact to Earthquakes. Annu. Rev. Earth Planet. Sci 38, 221–254. https://doi.org/10.1146/annurev.earth.031208.100045

Spray, J.G., 1998. Localized shock- and friction-induced melting in response to hypervelocity impact. Geological Society, London, Special Publications 140, 195 LP – 204. https://doi.org/10.1144/GSL.SP.1998.140.01.14

Spray, J.G., 1997. Superfaults. Geology 25, 579–582. https://doi.org/10.1130/0091-7613(1997)025<0579:S>2.3.CO;2

Spray, J.G., 1993. Viscosity determinations of some frictionally generated silicate melts: Implications for fault zone rheology at high strain rates. Journal of Geophysical Research: Solid Earth 98, 8053–8068. https://doi.org/10.1029/93JB00020

Spray, J.G., 1992. A physical basis for the frictional melting of some rock-forming minerals. Tectonophysics 204, 205–221. https://doi.org/10.1016/0040-1951(92)90308-S

Spray, J.G., 1988. Generation and crystallization of an amphibolite shear melt: an investigation using radial friction welding apparatus. Contributions to Mineralogy and Petrology 99, 464–475. https://doi.org/10.1007/BF00371937

Spray, J.G., 1987. Artificial generation of pseudotachylyte using friction welding apparatus: simulation of melting on a fault plane. Journal of Structural Geology 9, 49–60. https://doi.org/https://doi.org/10.1016/0191-8141(87)90043-5

Streck, M.J., Grunder, A.L., 1995. Crystallization and welding variations in a widespread ignimbrite sheet; the Rattlesnake Tuff, eastern Oregon, USA. Bulletin of Volcanology 57, 151–169. https://doi.org/10.1007/BF00265035

Swanson, D.A., Duffield, W.A., Fiske, R.S., 1976. Displacement of the south flank of Kilauea Volcano; the result of forceful intrusion of magma into the rift zones, Professional

Paper. https://doi.org/10.3133/pp963

Thouret, J.-C., Finizola, A., Fornari, M., Legeley-Padovani, A., Suni, J., Frechen, M., 2001. Geology of El Misti volcano near the city of Arequipa, Peru. GSA Bulletin 113, 1593–1610. https://doi.org/10.1130/0016-7606(2001)113<1593:GOEMVN>2.0.CO;2

Togo, T., Yao, L., Ma, S., Shimamoto, T., 2016. High-velocity frictional strength of Longmenshan fault gouge and its comparison with an estimate of friction from the temperature anomaly in WFSD-1 drill hole, Journal of Geophysical Research: Solid Earth. https://doi.org/10.1002/2016JB012880

Townend, J., 2006. What do faults feel? Observational constraints on the stresses acting on seismogenic faults. In: Abercrombie, R., McGarr, A., Di Toro, G., Kanamori, H. (Eds.), Earthquakes : Radiated Energy and the Physics of Faulting. American Geophysical Union, Washington, D.C., 313–327.

Truby, J.M., Mueller, S.P., Llewellin, E.W., Mader, H.M., 2015a. The rheology of three-phase suspensions at low bubble capillary number. Proceedings of the Royal Society A: Mathematical, Physical and Engineering Sciences 471, 20140557. https://doi.org/10.1098/rspa.2014.0557

Truby, J.M., Mueller, S.P., Llewellin, E.W., Mader, H.M., 2015b. The rheology of three-phase suspensions at low bubble capillary number. Proceedings of the Royal Society A: Mathematical, Physical and Engineering Sciences 471, 20140557. https://doi.org/10.1098/rspa.2014.0557

Tsutsumi, A., Shimamoto, T., 1997. High-velocity frictional properties of gabbro. Geophysical Research Letters 24, 699–702. https://doi.org/https://doi.org/10.1029/97GL00503

van Wyk de Vries, B., Davies, T., 2015. Chapter 38 - Landslides, Debris Avalanches, and Volcanic Gravitational Deformation. In: Sigurdsson, H. (Ed.), The Encyclopedia of Volcanoes (Second Edition). Academic Press, Amsterdam, 665–685. https://doi.org/https://doi.org/10.1016/B978-0-12-385938-9.00038-9

van Wyk de Vries, B., Francis, P.W., 1997. Catastrophic collapse at stratovolcanoes induced by gradual volcano spreading. Nature 387, 387–390. https://doi.org/10.1038/387387a0

Vasseur, J., Wadsworth, F.B., Lavallée, Y., Bell, A.F., Main, I.G., Dingwell, D.B., 2015.

Heterogeneity: The key to failure forecasting. Scientific Reports 5, 13259. https://doi.org/10.1038/srep13259

Vasseur, J., Wadsworth, F.B., Lavallée, Y., Hess, K.-U., Dingwell, D.B., 2013. Volcanic sintering: Timescales of viscous densification and strength recovery. Geophysical Research Letters 40, 5658–5664. https://doi.org/10.1002/2013GL058105

Ventura, G., Vilardo, G., Bruno, P.P., 1999. The role of flank failure in modifying the shallow plumbing system of volcanoes: An example from Somma-Vesuvius, Italy. Geophysical Research Letters 26, 3681–3684. https://doi.org/https://doi.org/10.1029/1999GL005404

Violay, M., Di Toro, G., Gibert, B., Nielsen, S., Spagnuolo, E., Del Gaudio, P., Azais, P., Scarlato, P.G., 2014. Effect of glass on the frictional behavior of basalts at seismic slip rates. Geophysical Research Letters 41, 348–355. https://doi.org/10.1002/2013GL058601

Voight, B., 2000. Structural stability of andesite volcanoes and lava domes. Philosophical Transactions of the Royal Society of London 358, 1663–1703.

Voight, B., Elsworth, D., 1997. Failure of volcano slopes. Géotechnique 47, 1–31. https://doi.org/10.1680/geot.1997.47.1.1

Vries, B.V.W. De, Borgia, A., 1996. The role of basement in volcano deformation. Geological Society, London, Special Publications 110, 95 LP – 110. https://doi.org/10.1144/GSL.SP.1996.110.01.07

Wadsworth, F., Vasseur, J., Von Aulock, F., Hess, K.-U., Scheu, B., Lavallée, Y., Dingwell, D., 2014. Nonisothermal viscous sintering of volcanic ash. Journal of Geophysical Research: Solid Earth 119, 8792–8804. https://doi.org/10.1002/2014JB011453

Wadsworth, F.B., Vasseur, J., Llewellin, E.W., Dobson, K.J., Colombier, M., von Aulock, F.W., Fife, J.L., Wiesmaier, S., Hess, K.-U., Scheu, B., Lavallée, Y., Dingwell, D.B., 2017. Topological inversions in coalescing granular media control fluid-flow regimes. Phys. Rev. E 96, 33113. https://doi.org/10.1103/PhysRevE.96.033113

Wadsworth, F.B., Vasseur, J., Llewellin, E.W., Schauroth, J., Dobson, K.J., Scheu, B., Dingwell, D.B., 2016. Sintering of viscous droplets under surface tension. Proceedings of the Royal Society A: Mathematical, Physical and Engineering Science 472. https://doi.org/10.1098/rspa.2015.0780

Wadsworth, F.B., Vasseur, J., Schauroth, J., Llewellin, E.W., Dobson, K.J., Havard, T., Scheu, B., von Aulock, F.W., Gardner, J.E., Dingwell, D.B., Hess, K.-U., Colombier, M., Marone, F., Tuffen, H., Heap, M.J., 2019. A general model for welding of ash particles in volcanic systems validated using in situ X-ray tomography. Earth and Planetary Science Letters 525, 115726. https://doi.org/https://doi.org/10.1016/j.epsl.2019.115726

Wallace, P.A., De Angelis, S.H., Hornby, A.J., Kendrick, J.E., Clesham, S., von Aulock, F.W., Hughes, A., Utley, J.E.P., Hirose, T., Dingwell, D.B., Lavallée, Y., 2019a. Frictional melt homogenisation during fault slip: Geochemical, textural and rheological fingerprints. Geochimica et Cosmochimica Acta 255, 265–288. https://doi.org/10.1016/J.GCA.2019.04.010

Wallace, P.A., Kendrick, J.E., Miwa, T., Ashworth, J.D., Coats, R., Utley, J.E.P., De Angelis, S.H., Mariani, E., Biggin, A., Kendrick, R., Nakada, S., Matsushima, T., Lavallée, Y., 2019b. Petrological architecture of a magmatic shear zone: A multidisciplinary investigation of strain localisation during magma ascent at Unzen volcano, Japan. Journal of Petrology 60, 791–826. https://doi.org/10.1093/petrology/egz016

Walter, T.R., Haghshenas Haghighi, M., Schneider, F.M., Coppola, D., Motagh, M., Saul, J., Babeyko, A., Dahm, T., Troll, V.R., Tilmann, F., Heimann, S., Valade, S., Triyono, R., Khomarudin, R., Kartadinata, N., Laiolo, M., Massimetti, F., Gaebler, P., 2019. Complex hazard cascade culminating in the Anak Krakatau sector collapse. Nature Communications 10, 4339. https://doi.org/10.1038/s41467-019-12284-5

Wang, C., Goodman, R.E., Sundaram, P.N., 1975. Variations of VP and VS in granite premonitory to shear rupture and stick-slip sliding: Application to earthquake prediction. Geophysical Research Letters 2, 309–311. https://doi.org/https://doi.org/10.1029/GL002i008p00309

Wang, W., Scholz, C.H., 1994. Wear processes during frictional sliding of rock: A theoretical and experimental study. Journal of Geophysical Research: Solid Earth 99, 6789–6799. https://doi.org/10.1029/93JB02875

Wang, Y.F., Dong, J.J., Cheng, Q.G., 2017. Velocity-dependent frictional weakening of large rock avalanche basal facies: Implications for rock avalanche hypermobility? Journal of Geophysical Research: Solid Earth 122, 1648–1676. https://doi.org/10.1002/2016JB013624

Watson, S.W., Friedersdorf, F.J., Madsen, B.W., Cramer, S.D., 1995. Methods of measuring wear-corrosion synergism. Wear 181–183, 476–484. https://doi.org/10.1016/0043-1648(95)90161-2

Webb, S.L., Dingwell, D.B., 1990. The onset of non-Newtonian rheology of silicate melts. Physics and Chemistry of Minerals 17, 125–132. https://doi.org/10.1007/BF00199663

Weidinger, J.T., Korup, O., 2009. Frictionite as evidence for a large Late Quaternary rockslide near Kanchenjunga, Sikkim Himalayas, India — Implications for extreme events in mountain relief destruction. Geomorphology 103, 57–65. https://doi.org/10.1016/J.GEOMORPH.2007.10.021

Weng, H., Yang, H., 2018. Constraining Frictional Properties on Fault by Dynamic Rupture Simulations and Near-Field Observations. Journal of Geophysical Research: Solid Earth 123, 6658–6670. https://doi.org/10.1029/2017JB015414

Wenk, H.-R., Johnson, L.R., Ratschbacher, L., 2000. Pseudotachylites in the Eastern Peninsular Ranges of California. Tectonophysics 321, 253–277. https://doi.org/https://doi.org/10.1016/S0040-1951(00)00064-0

Wheaton, R., 2016. Chapter 2 - Basic Rock and Fluid Properties. In: Wheaton, R.B.T.-F. of A.R.E. (Ed.). Gulf Professional Publishing, 5–57. https://doi.org/https://doi.org/10.1016/B978-0-08-101019-8.00002-8

Yamasato, H., Kitagawa, S., Komiya, M., 1998. Effect of rainfall on dacitic lava dome collapse at Unzen volcano, Japan. Papers in Meteorology and Geophysics 48, 73–78. https://doi.org/10.2467/mripapers.48.73

Yoshioka, N., 1986. Fracture energy and the variation of gouge and surface roughness during frictional sliding of rocks. Journal of Physics of the Earth 34, 335–355. https://doi.org/10.4294/jpe1952.34.335

Zhao, Q., Tisato, N., Grasselli, G., 2017. Rotary shear experiments under X-ray micro-computed tomography. Review of Scientific Instruments 88, 15110. https://doi.org/10.1063/1.4974149

Zhao, Q., Tisato, N., Kovaleva, O., Grasselli, G., 2018. Direct Observation of Faulting by Means of Rotary Shear Tests Under X-Ray Micro-Computed Tomography. Journal of Geophysical Research: Solid Earth 123, 7389–7403. https://doi.org/https://doi.org/10.1029/2017JB015394

Appendix I – (Chapter 2)

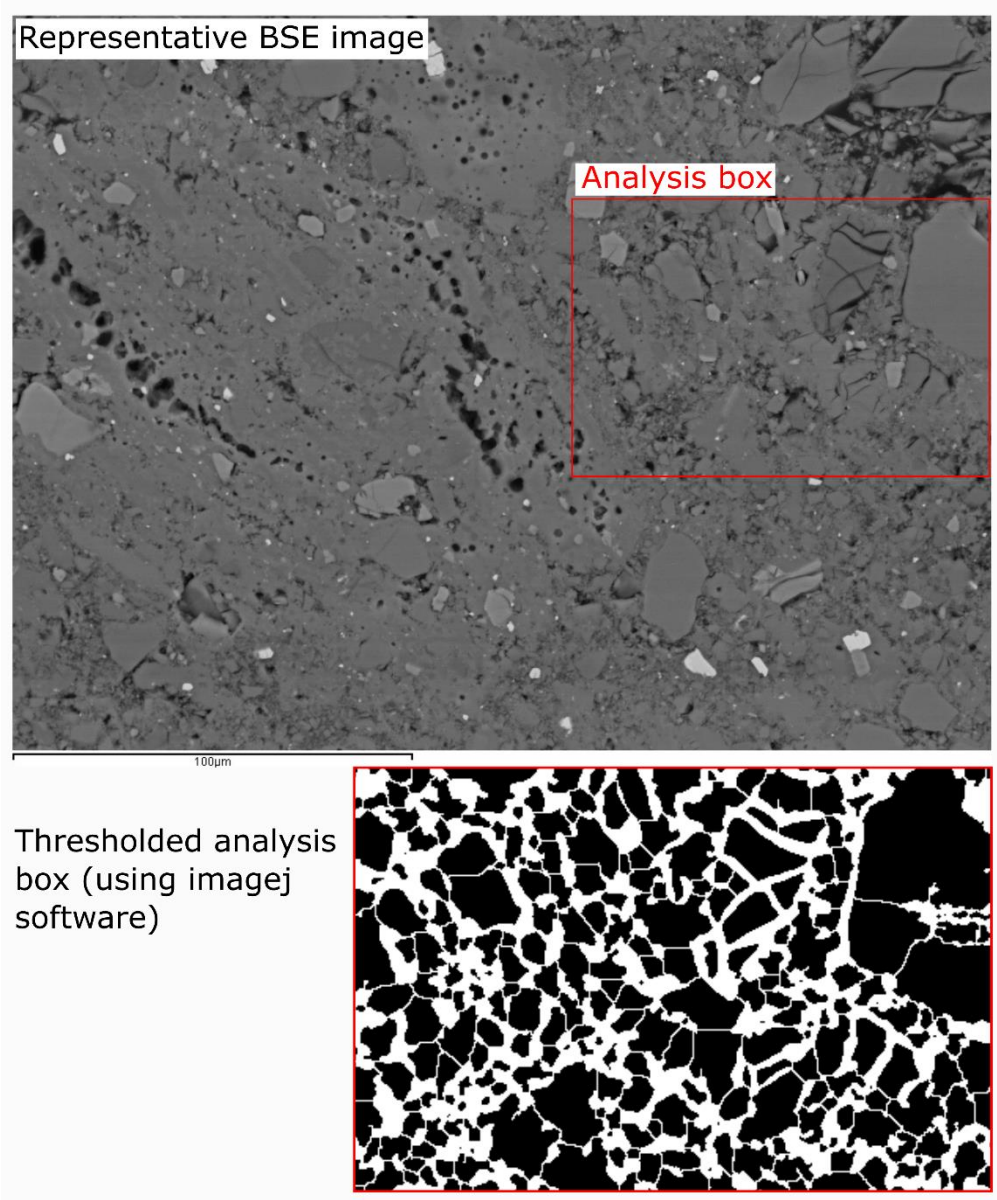

Supplementary figure A.I.1. a) Representative BSE image from basal layer at Locality 1. (See Figure 2.8). Red box shows area of analysis. b) Image of thresholding output from ImageJ software. Each black section is identified as a separate particle from which area, perimeter, major and minor axis length, circularity and aspect ratio are measured (see Supplementary Tables AI.7-8 for dataset).

Supplementary Table A.I.1. Data from electron microprobe analysis (EPMA).

Locality	Locality descriptor	Sample	Point descriptor	Glass/crystal	Beam size (µm)	Na_2O	MgO	K_2O	SiO_2	FeO	MnO	Al_2O_3	TiO_2	CaO	TOTAL
1_1	Glass-bearing Basal contact	1_1.1	Glass-bearing basal layer	Glass	10	4.59911	1.67194	3.33597	64.5256	3.31613	0.097253	16.3338	0.523044	3.70315	98.106
1_1	Glass-bearing Basal contact	1_1.1	Glass-bearing basal layer	Glass	10	3.87935	1.79395	3.85571	64.4783	2.63214	0.055223	17.0692	0.326302	3.86705	97.9572
1_1	Glass-bearing Basal contact	1_1.1	Glass-bearing basal layer	Glass	10	5.01769	0.705737	2.89786	65.8447	1.52795	-0.00762	17.5204	0.253663	3.88363	97.644
1_1	Glass-bearing Basal contact	1_1.1	Glass-bearing basal layer	Glass	10	5.88836	0.400882	2.93221	68.2377	1.02292	0.017704	16.567	0.081359	2.31725	97.4654
1_1	Glass-bearing Basal contact	1_1.1	Glass-bearing basal layer	Glass	10	4.27954	0.920914	2.83025	66.8916	1.49003	0.079477	16.4563	0.303118	3.86472	97.116
1_1	Glass-bearing Basal contact	1_1.1	Glass-bearing basal layer	Glass	10	4.70996	0.575099	5.46843	65.9338	1.07106	0.034655	17.0819	0.135223	2.03971	97.0498
1_1	Glass-bearing Basal contact	1_1.1	Glass-bearing basal layer	Glass	10	3.87387	1.04195	3.08405	67.7912	1.93967	0.037942	15.567	0.300826	3.323	96.9595
1_1	Glass-bearing Basal contact	1_1.1	Glass-bearing basal layer	Glass	10	4.57453	0.774694	3.14707	64.7223	1.60703	0.07757	17.6317	0.257002	4.01947	96.8114
1_1	Glass-bearing Basal contact	1_1.1	Glass-bearing basal layer	Glass	10	3.87487	1.50203	3.91766	67.5163	2.34459	0.08298	14.7076	0.369485	2.47178	96.7873
1_1	Glass-bearing Basal contact	1_1.1	Glass-bearing basal layer	Glass	10	4.26139	1.84427	3.28781	63.441	3.37278	0.096214	16.1351	0.551853	3.78542	96.7758
1_1	Glass-bearing Basal contact	1_1.1	Glass-bearing basal layer	Glass	10	4.34457	1.38562	3.68919	64.591	2.54724	0.063705	16.2973	0.407953	3.42366	96.7502
1_1	Glass-bearing Basal contact	1_1.1	Glass-bearing basal layer	Glass	10	4.09738	1.00601	2.72654	65.7247	2.14644	0.062841	16.5863	0.376696	3.97328	96.7002
1_1	Glass-bearing Basal contact	1_1.1	Glass-bearing basal layer	Glass	10	3.96188	0.618492	2.80212	68.5556	1.85148	0.039161	15.205	0.267477	3.38792	96.6891
1_1	Glass-bearing Basal contact	1_1.1	Glass-bearing basal layer	Glass	10	3.7033	1.5954	3.17579	64.9659	2.64263	0.121051	16.3059	0.319482	3.63099	96.4604
1_1	Glass-bearing Basal contact	1_1.1	Glass-bearing basal layer	Glass	10	3.83968	0.290448	5.77432	67.8241	0.837856	-0.00979	15.6113	0.164302	1.96988	96.3021
1_1	Glass-bearing Basal contact	1_1.1	Glass-bearing basal layer	Glass	10	5.62226	0.409406	3.25809	65.7874	1.34525	0.010523	16.9085	0.307504	2.61457	96.2635
1_1	Glass-bearing Basal contact	1_1.1	Glass-bearing basal layer	Glass	10	4.1819	1.77133	3.20183	62.8099	2.46706	0.05795	16.7324	0.390108	4.60294	96.2154
1_1	Glass-bearing Basal contact	1_1.1	Glass-bearing basal layer	Glass	10	3.67693	0.750006	3.86639	69.0001	1.41531	0.032293	14.7501	0.20726	2.46496	96.1634

1_1	Glass-bearing Basal contact	1_1.1	Glass-bearing basal layer	Glass	10	4.23995	0.866289	2.02223	65.2607	1.43837	0.048641	16.8706	0.217828	5.06595	96.0306
1_1	Glass-bearing Basal contact	1_1.1	Glass-bearing basal layer	Glass	10	3.77849	0.644084	3.03936	66.3634	1.73149	0.09469	16.0934	0.322698	3.94847	96.0161
1_1	Glass-bearing Basal contact	1_1.1	Glass-bearing basal layer	Glass	10	3.75946	0.364748	3.81862	71.9843	1.09098	0.076642	13.0553	0.195577	1.58636	95.932
1_1	Glass-bearing Basal contact	1_1.1	Glass-bearing basal layer	Glass	10	4.23805	0.890835	3.13727	65.4891	1.95137	0.041694	15.9786	0.524035	3.63129	95.8822
1_1	Glass-bearing Basal contact	1_1.1	Glass-bearing basal layer	Glass	10	3.56619	0.870752	3.77811	68.7644	1.29798	0.039927	14.7228	0.171721	2.54518	95.757
1_1	Glass-bearing Basal contact	1_1.1	Glass-bearing basal layer	Glass	10	3.64883	0.136049	4.37141	70.7838	0.815289	0.049019	13.9207	0.315322	1.68009	95.7206
1_1	Glass-bearing Basal contact	1_1.1	Glass-bearing basal layer	Glass	10	4.05895	0.498085	3.83779	68.1983	1.08676	0.018161	15.309	0.193259	2.47458	95.6749
1_1	Glass-bearing Basal contact	1_1.1	Glass-bearing basal layer	Glass	10	4.3228	0.919083	3.29284	64.7143	2.09267	0.038045	16.4383	0.397854	3.37384	95.5898
1_1	Glass-bearing Basal contact	1_1.1	Glass-bearing basal layer	Glass	10	3.95037	0.736859	3.20037	67.749	1.84568	0.053313	14.8487	0.315319	2.73475	95.4343
1_1	Glass-bearing Basal contact	1_1.1	Glass-bearing basal layer	Glass	10	4.15561	1.51105	3.37036	65.3749	1.97552	0.092371	15.6272	0.278492	2.8964	95.2819
1_1	Glass-bearing Basal contact	1_1.1	Glass-bearing basal layer	Glass	10	3.92437	0.932035	3.30594	65.601	1.69161	0.03626	15.9372	0.326746	3.50384	95.259
1_1	Glass-bearing Basal contact	1_1.1	Glass-bearing basal layer	Glass	10	4.76856	0.650765	2.81445	64.8757	1.44184	0.051345	16.4254	0.350064	3.74526	95.1234
1_1	Glass-bearing Basal contact	1_1.1	Glass-bearing fragment	Glass	10	5.13657	0.422693	2.1722	60.1451	1.08785	0.039128	21.4224	0.189603	6.13635	96.751894
1_1	Glass-bearing Basal contact	1_1.1	Glass-bearing fragment	Glass	10	4.08039	0.748541	3.7579	66.7968	1.44008	0.014148	15.5642	0.263312	3.04244	95.7079
1_1	Glass-bearing Basal contact	1_1.1	Glass-bearing fragment	Glass	10	4.65782	0.806052	2.72595	64.6983	1.66227	0.014503	16.8203	0.513378	3.80228	95.7009
1_1	Glass-bearing Basal contact	1_1.1	Glass-bearing fragment	Glass	10	4.11248	1.21101	3.66903	67.0491	2.21121	0.077878	14.6115	0.311519	2.39149	95.6452
1_1	Glass-bearing Basal contact	1_1.1	Glass-bearing fragment	Glass	10	3.503	1.09688	3.59105	69.8819	2.04831	0.041712	12.9294	0.368217	2.12256	95.583
1_1	Glass-bearing Basal contact	1_1.1	Glass-bearing fragment	Glass	10	4.06665	0.677862	2.95887	68.0271	1.60372	0.051521	14.5767	0.26843	2.98831	95.2192
1_1	Glass-bearing Basal contact	1_1.1	Glass-bearing fragment	Glass	10	4.259485	0.827173	3.14583333	66.0997167	1.67557333	0.039815	15.9874167	0.3190765	3.413905	95.7680157
1_1	Glass-bearing Basal contact	1_1.1	Glass-bearing fragment	Glass	10	4.42601	1.01124	3.31801	64.5076	1.86847	0.043111	16.032	0.319911	3.35942	94.8858
1_1	Glass-bearing Basal contact	1_1.1	Glass-bearing fragment	Glass	10	4.20433	1.30604	3.34329	60.6365	5.22112	0.085374	15.0267	1.72717	2.93464	94.4851

1_1	Glass-bearing Basal contact	1_1.1	Glass-bearing fragment	Glass	10	3.36971	0.781706	2.90891	68.0488	1.44169	0.020701	14.3858	0.308217	2.98946	94.255
1_1	Glass-bearing Basal contact	1_1.1	Glass-bearing fragment	Glass	10	4.08469	1.30571	3.58202	62.1566	2.31446	0.034753	16.2672	0.367256	3.92276	94.0355
1_1	Glass-bearing Basal contact	1_1.1	Glass-bearing fragment	Glass	10	4.32695	1.43259	3.31745	61.613	4.06656	0.097523	15.3839	0.514975	3.0911	93.844
1_1	Glass-bearing Basal contact	1_1.1	Glass-bearing fragment	Glass	10	3.89864	0.762812	3.18518	64.3048	1.82097	0.064186	16.0206	0.291655	3.34981	93.6987
1_1	Glass-bearing Basal contact	1_1.1	Glass-bearing fragment	Glass	10	3.41307	1.41691	3.27036	59.0627	7.05242	0.08724	14.7661	0.989242	3.24406	93.3021
1_1	Glass-bearing Basal contact	1_1.1	Cataclasite within layer	Fragmented material	10	0.651751	0.035252	0.731033	95.0828	0.217865	0.010604	2.86573	0.030431	0.424495	100.05
1_1	Glass-bearing Basal contact	1_1.1	Cataclasite within layer	Fragmented material	10	1.33995	13.8475	1.58152	55.6822	15.5511	0.359142	5.78029	0.431155	1.65318	96.226
1_1	Glass-bearing Basal contact	1_1.1	Cataclasite above layer	Fragmented material	0	10.0837	0.003814	0.911145	64.5994	0.365724	0.001863	22.4168	0.018434	3.45109	101.852
1_1	Glass-bearing Basal contact	1_1.1	Cataclasite above layer	Fragmented material	0	4.37981	0.003948	10.5739	66.4982	0.294015	-0.01153	18.6917	0.023107	0.146724	100.6
1_1	Glass-bearing Basal contact	1_1.1	Cataclasite below layer	Plagioclase	0	6.9409	0.021786	0.426516	57.2651	0.288373	-0.00037	25.315	0.017305	8.09877	98.3734
1_1	Glass-bearing Basal contact	1_1.1	Cataclasite below layer	Plagioclase	0	6.79847	0.009723	0.41437	57.5859	0.280655	0.010894	25.5892	0.01762	8.16086	98.8677
1_1	Glass-bearing Basal contact	1_1.1	Cataclasite below layer	Plagioclase	0	7.78822	0.01092	0.472019	59.4198	0.352616	0.001397	24.2677	0.036204	6.5768	98.9256
1_1	Glass-bearing Basal contact	1_1.1	Cataclasite below layer	Plagioclase	0	7.21222	0.027628	0.49746	57.7514	0.286965	0.007358	24.7992	0.022642	7.52074	98.1256
1_1	Glass-bearing Basal contact	1_1.1	Restites in glass-bearing layer	Plagioclase	0	7.78773	0.004933	0.473187	59.7705	0.211001	0.011405	24.6792	0.005771	6.83145	99.7752
1_1	Glass-bearing Basal contact	1_1.1	Restites in glass-bearing layer	Plagioclase	0	7.27479	0.016568	0.427835	59.3873	0.240591	-0.00838	25.0703	0.003578	7.33973	99.7523
1_1	Glass-bearing Basal contact	1_1.1	Restites in glass-bearing layer	Ca Pyroxene	0	0.454902	14.9221	0.016748	50.1625	8.90715	0.239597	2.91029	0.907879	20.1606	98.6818
1_1	Glass-bearing Basal contact	1_1.1	Restites in glass-bearing layer	Ca Pyroxene	0	0.387978	14.9832	0.003212	51.0654	7.94041	0.25171	2.46259	0.607033	20.5101	98.2116
1_1	Glass-bearing Basal contact	1_1.1	Restites in glass-bearing layer	Ca Pyroxene	0	0.358772	15.1063	0.002704	50.2691	7.98236	0.201216	2.95849	0.738124	21.0678	98.685

1_1	Glass-bearing Basal contact	1_1.1	Restites in glass-bearing layer	Ca Pyroxene	0	0.348271	15.2663	0.001614	50.5754	8.22421	0.23404	2.84381	0.604021	20.9302	99.0279
1_1	Glass-bearing Basal contact	1_1.1	Restites in glass-bearing layer	Mg-Fe Pyroxene	0	0.020279	23.6513	0.0052	52.4195	19.2661	1.46195	1.05625	0.163065	0.608884	98.6525
1_1	Glass-bearing Basal contact	1_1.1	Restites in glass-bearing layer	Mg-Fe Pyroxene	0	0.029247	23.7116	0.013035	52.5986	19.2071	1.11123	0.81242	0.158854	0.943324	98.5854
1_1	Glass-bearing Basal contact	1_1.1	Restites in glass-bearing layer	Mg-Fe Pyroxene	0	0.013358	23.8871	-0.00149	52.2529	18.8631	1.26216	0.979873	0.142739	0.775885	98.1756
1_1	Glass-bearing Basal contact	1_1.1	Andesite clasts below layer	Lithic groundmass	10	4.07043	0.775438	4.29349	71.8417	2.18863	0.045603	13.8128	0.454999	1.63375	99.1168
1_1	Glass-bearing Basal contact	1_1.1	Andesite clasts below layer	Lithic groundmass	10	4.62627	1.45455	3.05785	69.3506	3.39461	0.114119	14.3312	0.40926	2.2036	98.942
1_1	Glass-bearing Basal contact	1_1.1	Andesite clasts below layer	Lithic groundmass	10	4.922	0.142771	3.96127	70.8411	1.32062	0.013107	15.8915	0.41661	2.29244	99.8014
1_1	Glass-bearing Basal contact	1_1.1	Andesite clasts below layer	Lithic groundmass	10	5.27305	0.399198	3.06932	69.4751	1.7392	0.025437	16.496	0.357838	3.1703	100.006
1_1	Glass-bearing Basal contact	1_1.1	Andesite clasts below layer	Lithic groundmass	10	2.53865	0.004151	4.61149	73.7638	0.30413	0.064482	11.8155	0.25755	0.634371	93.9941
1_1	Glass-bearing Basal contact	1_1.1	Andesite clasts below layer	Lithic groundmass	10	1.57502	0.059253	5.52803	74.9448	0.397063	0.029644	10.3459	0.293458	0.175661	93.3488
1_1	Glass-bearing Basal contact	1_1.1	Andesite clasts below layer	Lithic groundmass	10	3.59265	0.019948	4.13454	71.5756	0.301001	0.012591	14.0089	0.227853	1.34809	95.2212
1_5	Secondary shear surface	1_5.3	Cataclasite above 2ndary surface	Fragmented material	0	2.13434	0.596476	0.309761	85.5207	0.540698	0.027354	7.987	0.102559	1.577	98.7958
1_5	Secondary shear surface	1_5.3	Clasts above 2ndary surface	Ca Pyroxene	0	0.325182	16.5325	-0.00192	51.4757	6.69088	0.168726	2.63934	0.428173	20.1167	98.3753
1_5	Secondary shear surface	1_5.3	Clasts above 2ndary surface	Ca Pyroxene	0	0.388578	15.3177	0.000742	49.7938	6.78718	0.133566	4.13758	0.657073	20.9921	98.2082
1_5	Secondary shear surface	1_5.8	Andesite block	Amphibole	0	2.22008	14.5557	0.622807	41.9951	11.0257	0.120862	12.7153	2.456	11.3508	97.0624
1_5	Secondary shear surface	1_5.8	Andesite block	Amphibole	0	2.33374	14.872	0.633233	41.7672	10.4441	0.110543	12.7571	2.46402	11.2875	96.6695
1_5	Secondary shear surface	1_5.8	Andesite block	Amphibole	0	2.31748	13.5146	0.595857	41.362	12.2044	0.226477	12.6348	2.49483	11.0836	96.4341
1_5	Secondary shear surface	1_5.8	Andesite block	Amphibole	0	2.1474	13.6125	0.642777	43.1691	13.1879	0.307349	10.8258	2.5455	10.8851	97.3233
1_5	Secondary shear surface	1_5.8	Andesite block	Amphibole	0	2.28696	13.3755	0.602368	42.5514	12.7461	0.267963	10.8842	2.54892	10.88	96.1433

1_5	Secondary shear surface	1_5.8	Andesite block	Amphibole		1.89356	15.0234	0.440367	44.936	12.4179	0.354168	9.20461	1.89437	10.5396	96.7039
1_5	Secondary shear surface	1_5.8	Andesite block	Amphibole		1.89565	14.5024	0.458269	44.6785	12.8316	0.386839	9.44566	1.91995	10.4484	96.5672
1_5	Secondary shear surface	1_5.8	Andesite block	Amphibole		1.88446	14.7005	0.497062	44.5078	12.9151	0.403083	9.30253	1.98893	10.6677	96.8671
1_5	Secondary shear surface	1_5.8	Andesite block	Plagioclase		6.32413	0.021829	0.30151	56.6426	0.246322	0.006334	26.614	-0.00058	9.1767	99.3328

Supplementary Table A.I.2. Data from XRF analysis (major element analyses).

Locality	Locality descriptor	Sample	Sample descriptor	SiO_2	TiO_2	Al_2O_3	Fe_2O_3	MnO	MgO	CaO	Na_2O	K_2O	P_2O_5	SO_3	LOI	Total
1_4	Glass-bearing basal contact	PPA1_4_1	Basal Ignimbrite	74.07	0.21	13.53	1.52	0.071	0.42	1.15	4.09	4.591	0.024	0.015	0.58	100.28
1_5	Secondary shear surface	PPA1_5_8	Andesite block	59.54	0.73	17.23	6.18	0.100	2.71	5.71	3.90	2.245	0.299	0.007	0.65	99.30
2_1	Clastic dyking	PPA2_1_4	Clastic dyke	71.15	0.25	13.00	1.83	0.094	0.81	1.35	4.32	4.213	0.048	0.007	2.48	99.54
2_3	Blocky flow interior (north bank)	PPA2_3_1	Andesite block	58.73	0.72	17.52	6.29	0.096	3.28	6.15	3.85	2.150	0.234	0.049	1.20	100.26
2_4	Blocky flow interior (south bank)	PPA2_4_1B	Andesite block	58.44	0.82	18.12	7.09	0.087	3.22	6.22	3.89	1.951	0.214	0.007	0.46	100.51
2_5	Road to Loc. 2	PPA2_5_1	Andesite block	60.55	0.76	18.13	6.37	0.095	2.48	5.54	3.93	2.293	0.268	0.004	0.43	100.85
3_1	Cataclastic basal contact	PPA3_1_3_14	Basal shear zone	56.91	0.57	15.27	12.89	0.038	0.78	2.26	2.77	2.104	0.176	0.077	5.39	99.23

Table AI.3. Data from XRF analysis (minor element analyses)

Loc.	Loc. descriptor	Sample	Sample descriptor	As	Ba	Ce	Co	Cr	Cs	Cu	Ga	La	Mo	Nb	Nd	Ni	Pb	Rb	Sb	Sc	Se	Sn	Sr	Th	U	V	W	Y	Zn	Zr
1_4	Glass-bearing basal contact	PPA1_4_1	Basal Ignimbrite	12.9	708.4	65.6	2.5	13.6	5.1	1.2	15.3	44.5	1.7	13.0	26.1	2.7	16.9	188.2	<0.9	3.1	<0.5	<0.8	136.4	34.3	5.8	17.7	2.7	16.9	29.6	149.6
2_1	Clastic dyking	PPA2_1_4	Clastic dyke	14.4	656.2	67.4	4.6	11.5	6.9	14.7	14.5	42.2	2.4	12.0	26.7	4.8	21.4	165.4	1.4	4.3	<0.5	2.4	189.7	29.4	6.3	22.0	1.3	17.6	36.6	144.8
3_1	Cataclastic basal contact	PPA3_1_3_14	Basal shear zone	21.4	998.7	45.9	25.4	18.3	<1.7	44.5	17.6	24.4	2.7	6.6	14.6	5.7	14.2	52.0	<1.1	10.9	<0.5	<1.0	538.4	3.8	1.6	101.7	<1.7	7.8	85.3	135.0

Supplementary Table A.I.4. Working standard (Glass (Rhyolite) VG-568) from electron microprobe analysis (EPMA) for accuracy and precision, standard was visited continuously throughout data collection. (bdl = below detection limits).

Material	Location	Na_2O	MgO	K_2O	SiO_2	FeO	MnO	Al_2O_3	TiO_2	CaO
Glass (Rhyolite) VG-568	Yellowstone Nat. Park, WY	3.87973	0.032002	4.78059	77.6405	1.04295	0.051671	12.0087	0.092079	0.410648
Glass (Rhyolite) VG-568	Yellowstone Nat. Park, WY	3.98298	0.037657	4.88528	77.8063	1.08286	0.023476	12.1606	0.083124	0.409628
Glass (Rhyolite) VG-568	Yellowstone Nat. Park, WY	3.82929	0.048775	4.86639	76.7732	1.1511	0.043715	12.122	0.083017	0.426032
Glass (Rhyolite) VG-568	Yellowstone Nat. Park, WY	3.54416	0.012795	4.83818	77.631	1.07041	0.019881	11.8495	0.109706	0.443308
Glass (Rhyolite) VG-568	Yellowstone Nat. Park, WY	3.81632	0.037673	4.73153	77.6594	1.12923	0.01698	11.9422	0.087097	0.425018
Glass (Rhyolite) VG-568	Yellowstone Nat. Park, WY	4.07865	0.027273	4.87301	77.8394	1.12017	0.045259	12.0565	0.065362	0.44237
Glass (Rhyolite) VG-568	Yellowstone Nat. Park, WY	3.93904	0.029908	4.87358	78.0952	1.07031	0.023906	12.0475	0.078612	0.375966
Glass (Rhyolite) VG-568	Yellowstone Nat. Park, WY	3.81588	0.023164	4.84229	77.4544	1.0183	0.007634	12.0127	0.093941	0.407648
Glass (Rhyolite) VG-568	Yellowstone Nat. Park, WY	3.82439	0.024848	4.70158	77.4133	1.10408	0.028344	12.1573	0.107968	0.447586
Glass (Rhyolite) VG-568	Yellowstone Nat. Park, WY	3.72393	0.032364	4.67116	77.5835	1.18444	0.031235	12.1004	0.075493	0.420068
Glass (Rhyolite) VG-568	Yellowstone Nat. Park, WY	3.91303	0.022896	4.97795	77.7686	0.952983	0.027617	12.1392	0.07653	0.418402
Glass (Rhyolite) VG-568	Yellowstone Nat. Park, WY	4.09847	0.008853	4.85377	77.5932	1.1157	0.043246	12.0238	0.103168	0.461061
Glass (Rhyolite) VG-568	Yellowstone Nat. Park, WY	3.87176	0.031364	4.86612	77.541	1.09148	0.020703	12.2413	0.113175	0.428987
Glass (Rhyolite) VG-568	Yellowstone Nat. Park, WY	4.07548	0.034381	4.65163	78.399	1.03749	-0.00073	11.8547	0.090632	0.424448
Glass (Rhyolite) VG-568	Yellowstone Nat. Park, WY	3.83845	0.020384	4.86603	77.9859	0.892956	0.044016	12.086	0.073188	0.396459
Glass (Rhyolite) VG-568	Yellowstone Nat. Park, WY	3.89553	0.039286	4.7197	77.2007	1.14644	0.02727	11.948	0.067703	0.450305
Glass (Rhyolite) VG-568	Yellowstone Nat. Park, WY	3.86803	0.025654	4.77632	77.2877	1.09306	0.033434	12.2334	0.08703	0.437674
Glass (Rhyolite) VG-568	Yellowstone Nat. Park, WY	3.87587	0.001315	4.93324	77.3756	1.02408	0.065822	11.938	0.043051	0.419658

Glass (Rhyolite) VG-568	Yellowstone Nat. Park, WY	3.70316	0.04493	4.7521	77.8027	1.19689	0.015634	12.0109	0.088542	0.436127
Glass (Rhyolite) VG-568	Yellowstone Nat. Park, WY	3.76135	0.036275	4.85325	77.5864	1.04637	0.04217	12.0848	0.098276	0.447826
Glass (Rhyolite) VG-568	Yellowstone Nat. Park, WY	4.1662	0.040839	4.83058	77.297	1.11418	0.021819	12.1059	0.078706	0.406992
Glass (Rhyolite) VG-568	Yellowstone Nat. Park, WY	3.98864	0.026882	4.86139	77.5971	1.06157	0.027998	12.1729	0.077978	0.420306
Glass (Rhyolite) VG-568	Yellowstone Nat. Park, WY	3.76814	0.041931	4.76284	78.0752	1.17436	0.013822	12.03	0.080701	0.451081
	Known reference value	**3.75**	**bdl**	**4.89**	**76.71**	**1.23**	**bdl**	**12.06**	**0.12**	**0.50**
	Average	3.88080348	n/a	4.81602217	77.6263609	1.08353952	n/a	12.0576652	0.08500343	0.4264173
	StDv	0.13914628	n/a	0.0814	0.33366696	0.0700669	n/a	0.10377955	0.01549583	0.01972587
	% Rel. StDv	3.5855019	n/a	1.69019148	0.42983718	6.46648294	n/a	0.86069359	18.2296515	4.62595341
	Dev. from ref. value	0.13	n/a	0.07	0.92	0.15	n/a	0.00	0.03	0.07
	% Dev. from ref. value	3.48809275	n/a	1.51283898	1.19457811	11.907356	n/a	0.01935972	29.1638043	14.7165391

Supplementary Table A.I.5. Working standard (Albite) from electron microprobe analysis (EPMA) for accuracy and precision, standard was visited continuously throughout data collection. (bdl = below detection limits).

Material	Location	Na_2O	MgO	K_2O	SiO_2	FeO	MnO	Al_2O_3	TiO_2	CaO
Albite	Rutherford Mine, VA	11.6029	-0.01134	0.154523	68.9443	0.023868	-0.01736	19.5154	-0.01788	0.144755
Albite	Rutherford Mine, VA	11.7039	-0.00132	0.158867	68.7489	-0.00502	0.018797	19.6188	-0.01398	0.192914
Albite	Rutherford Mine, VA	11.6495	0.008039	0.134028	68.5074	0.026395	0.001448	19.3947	-0.01965	0.137542
Albite	Rutherford Mine, VA	11.5504	-0.00576	0.145048	69.7186	-0.00754	-0.05646	19.8071	0.037985	0.16648
Albite	Rutherford Mine, VA	11.8922	-0.01772	0.187198	69.0201	-0.01131	0.003259	19.6292	-0.00235	0.196255
Albite	Rutherford Mine, VA	11.9062	0.023177	0.123932	69.1044	0.001042	0.006886	19.4289	-0.01883	0.092184
Albite	Rutherford Mine, VA	11.9125	-0.01087	0.181111	67.8577	0.048114	0.007265	19.4609	-0.01088	0.131768
Albite	Rutherford Mine, VA	11.6314	0.001898	0.123584	68.0173	0.001015	0.002908	19.4453	-0.0079	0.091185
Albite	Rutherford Mine, VA	11.6394	0.002289	0.167292	68.4824	0.00445	-0.00182	19.0379	0.011548	0.143478
Albite	Rutherford Mine, VA	11.9147	0.00594	0.142692	68.2948	-0.00503	-0.00218	19.5199	0.003203	0.132858
Albite	Rutherford Mine, VA	12.0367	0.008422	0.117417	67.7817	0.012812	-0.00763	19.2915	-0.00492	0.156129
Albite	Rutherford Mine, VA	11.7537	0.020651	0.169652	67.7729	0.005621	0.021804	19.3252	0.014116	0.073742
Albite	Rutherford Mine, VA	11.7276	0.000707	0.181288	68.0221	-0.02386	-0.00255	19.0621	-0.03906	0.145918
Albite	Rutherford Mine, VA	11.8565	-0.00425	0.169253	68.0009	-0.03389	0.015634	19.0838	-0.02673	0.127713
Albite	Rutherford Mine, VA	11.6548	-0.00373	0.213641	67.9058	0.002996	0.00618	19.4033	0.019608	0.233304
Albite	Rutherford Mine, VA	12.0147	0.002841	0.192143	68.0198	-0.00752	0.042533	19.4345	-0.01064	0.22212
Albite	Rutherford Mine, VA	11.9919	-0.00891	0.220248	68.4014	0.011022	0.01127	19.5629	0.02415	0.231358
Albite	Rutherford Mine, VA	11.8306	-0.01398	0.170036	67.8824	-0.00125	0.010179	19.3481	-0.00861	0.229779
Albite	Rutherford Mine, VA	11.5587	0.006044	0.191462	68.6797	-0.00625	0.005094	19.5505	0.017495	0.214085
Albite	Rutherford Mine, VA	11.6481	0.006651	0.18891	68.9801	-0.02626	-0.00546	19.4828	-0.00302	0.200687
Albite	Rutherford Mine, VA	12.4526	-0.00357	0.183325	68.4763	0.004723	0.00936	21.7814	0.002886	0.197329
Albite	Rutherford Mine, VA	12.9523	-0.00158	0.184659	68.1798	0.009583	-0.0102	21.3537	0.003444	0.21888

Albite	Rutherford Mine, VA	11.7659	0.003849	0.199223	68.6581	-0.03382	0.001697	19.6532	0.020125	0.228125
Albite	Rutherford Mine, VA	11.7651	0.006577	0.183326	68.3174	0.005434	-0.03228	19.4411	-0.00519	0.190814
Albite	Rutherford Mine, VA	11.0558	-0.01937	0.179237	69.336	0	-0.00846	19.8112	0.011969	0.206516
Albite	Rutherford Mine, VA	9.89594	-0.02014	0.178758	69.5909	0.040352	-0.00339	19.8664	-0.00555	0.222076
Albite	Rutherford Mine, VA	8.56364	0.003933	0.209243	69.9496	0.070382	-0.0098	19.8602	0.000786	0.203739
Albite	Rutherford Mine, VA	7.95004	-0.00707	0.196277	70.5273	0.012211	0.007788	19.8465	0.013817	0.188253
Albite	Rutherford Mine, VA	7.1214	-0.00216	0.189888	70.1592	0.00758	0.016874	20.1933	0.022504	0.208203
Albite	Rutherford Mine, VA	6.80199	0.003848	0.196467	70.7945	-0.01853	-0.01848	20.2942	-0.03018	0.197968
	Known reference value	**11.4**	**bdl**	**0.3**	**68.2**	**bdl**	**bdl**	**19.8**	**bdl**	**0.2**
	Average	11.2	n/a	0.2	68.7	n/a	n/a	19.7	n/a	0.2
	StDv	1.50051839	n/a	0.02625858	0.8248599	n/a	n/a	0.58002648	n/a	0.04490893
	% Rel. StDv	13.4054208	n/a	14.8198828	1.20001044	n/a	n/a	2.94676993	n/a	25.0564729
	Dev. from ref. value	0.2	n/a	0.1	0.6	n/a	n/a	0.1	n/a	0.1
	% Dev. from ref. value	2.15585373	n/a	31.8520099	0.86240157	n/a	n/a	0.48803505	n/a	22.0735344

Supplementary Table A.I.6. XRF analysis reference materials (for accuracy and precision).

Measurement	Reference ID	Reference material	SiO_2 (wt.%)	TiO_2 (wt.%)	Al_2O_3 (wt.%)	Fe_2O_3 (wt.%)	MnO (wt.%)	MgO (wt.%)	CaO (wt.%)	Na_2O (wt.%)	K_2O (wt.%)	P_2O_5 (wt.%)
AFUS748	BH-1	Bardon Hill microgranodiorite	68.48	0.41	14.36	5.83	0.14	2.66	3.60	3.68	0.84	0.07
AFUS747	BH-1	Bardon Hill microgranodiorite	68.44	0.41	14.31	5.74	0.13	2.66	3.58	3.67	0.84	0.07
AFUS744	BH-1	Bardon Hill microgranodiorite	68.47	0.41	14.32	5.83	0.14	2.67	3.57	3.71	0.84	0.07
AFUS741	BH-1	Bardon Hill microgranodiorite	68.34	0.42	14.33	5.82	0.14	2.66	3.57	3.68	0.84	0.07
AFUS736	BH-1	Bardon Hill microgranodiorite	68.31	0.41	14.32	5.83	0.14	2.64	3.56	3.69	0.83	0.07
		Known reference value	**68.07**	**0.43**	**14.35**	**5.81**	**0.14**	**2.50**	**3.53**	**3.94**	**0.87**	**0.07**
		Average	*68.41*	*0.41*	*14.33*	*5.81*	*0.14*	*2.66*	*3.58*	*3.69*	*0.84*	*0.07*
		StDv	*0.1*	*0.0*	*0.0*	*0.0*	*0.0*	*0.0*	*0.0*	*0.0*	*0.0*	*0.0*
		% Rel. StDv	*0.1*	*1.0*	*0.1*	*0.7*	*0.6*	*0.4*	*0.4*	*0.4*	*0.3*	*1.2*
		Dev. from ref.	*0.3*	*0.0*	*0.0*	*0.0*	*0.0*	*0.2*	*0.0*	*0.3*	*0.0*	*0.0*
		% Dev. from ref.	*0.5*	*4.6*	*0.2*	*0.0*	*3.3*	*6.0*	*1.3*	*6.9*	*3.8*	*4.0*
AFUS748	WS-1	Whin Sill dolerite	51.89	2.52	13.94	13.55	0.17	5.38	8.78	2.84	1.33	0.31
AFUS747	WS-1	Whin Sill dolerite	51.53	2.52	13.98	13.46	0.17	5.36	8.79	2.82	1.32	0.31
AFUS744	WS-1	Whin Sill dolerite	51.66	2.52	13.91	13.57	0.17	5.37	8.79	2.82	1.32	0.31
AFUS741	WS-1	Whin Sill dolerite	51.36	2.51	13.74	13.56	0.17	5.34	8.76	2.79	1.31	0.30
AFUS736	WS-1	Whin Sill dolerite	51.37	2.51	13.70	13.56	0.17	5.35	8.74	2.79	1.31	0.30
		Known reference value	**51.31**	**2.54**	**14.04**	**13.51**	**0.18**	**5.31**	**8.87**	**3.10**	**1.36**	**0.30**
		Average	*51.56*	*2.52*	*13.86*	*13.54*	*0.17*	*5.36*	*8.77*	*2.81*	*1.32*	*0.30*
		StDv	*0.2*	*0.0*	*0.1*	*0.0*	*0.0*	*0.0*	*0.0*	*0.0*	*0.0*	*0.0*
		% Rel. StDv	*0.4*	*0.2*	*0.9*	*0.3*	*0.4*	*0.3*	*0.2*	*0.8*	*0.5*	*0.8*
		Devi. from ref.	*0.3*	*0.0*	*0.2*	*0.0*	*0.0*	*0.1*	*0.1*	*0.3*	*0.0*	*0.0*
		% Dev. from ref.	*0.5*	*1.0*	*1.3*	*0.2*	*5.9*	*0.9*	*1.1*	*10.3*	*3.1*	*1.5*

Supplementary Table A.I.7. Data for restite shape and size analysis in pseudotachylyte bearing layer (collected using ImageJ).

Identifier	Area	Perimeter	Major axis	Minor axis	Circularity	Aspect ratio
	(μm²)	(μm)	(μm)	(μm)		
1	343.198	93.736	21.517	20.309	0.491	1.059
2	144.743	53.168	15.368	11.992	0.643	1.282
3	100.145	42.285	11.644	10.951	0.704	1.063
4	85.183	42.493	11.913	9.104	0.593	1.308
5	84.323	53.014	11.846	9.064	0.377	1.307
6	66.610	34.565	10.788	7.861	0.701	1.372
7	65.464	41.303	11.209	7.436	0.482	1.507
8	62.942	37.506	12.391	6.467	0.562	1.916
9	62.368	39.015	10.573	7.511	0.515	1.408
10	60.878	35.615	12.383	6.260	0.603	1.978
11	58.241	34.797	11.941	6.210	0.604	1.923
12	58.184	36.785	10.655	6.953	0.540	1.532
13	53.999	37.907	12.406	5.542	0.472	2.239
14	49.814	42.353	9.921	6.393	0.349	1.552
15	47.751	44.084	9.515	6.390	0.309	1.489
16	44.942	30.758	9.233	6.197	0.597	1.490
17	42.133	26.216	8.916	6.017	0.770	1.482
18	40.184	35.837	9.307	5.497	0.393	1.693
19	39.783	25.631	8.752	5.787	0.761	1.512
20	37.948	33.080	7.456	6.480	0.436	1.151
21	36.859	30.618	8.563	5.480	0.494	1.563
22	36.515	25.747	9.471	4.909	0.692	1.929
23	36.286	27.430	8.299	5.567	0.606	1.491
24	34.681	24.335	8.266	5.342	0.736	1.547
25	32.675	28.272	7.379	5.638	0.514	1.309
26	32.560	29.017	7.124	5.819	0.486	1.224
27	32.388	23.508	8.180	5.041	0.737	1.622
28	31.929	26.052	9.624	4.224	0.591	2.278
29	31.012	23.121	7.237	5.456	0.729	1.326
30	30.955	25.399	8.813	4.472	0.603	1.970
31	30.554	23.658	7.980	4.875	0.686	1.637
32	30.095	25.772	7.143	5.365	0.569	1.331
33	29.808	23.938	8.266	4.591	0.654	1.800
34	29.636	25.830	8.129	4.642	0.558	1.751
35	27.172	23.764	9.195	3.762	0.605	2.444
36	26.885	21.510	6.896	4.964	0.730	1.389
37	26.656	24.137	6.182	5.490	0.575	1.126
38	25.337	25.433	8.559	3.769	0.492	2.271
39	23.732	22.105	7.374	4.098	0.610	1.799
40	23.274	25.573	6.996	4.236	0.447	1.652
41	22.987	19.851	7.031	4.162	0.733	1.689
42	22.700	22.898	6.071	4.761	0.544	1.275
43	22.299	21.965	6.190	4.587	0.581	1.349
44	21.840	19.875	5.563	4.999	0.695	1.113
45	21.840	21.065	5.393	5.157	0.619	1.046
46	21.783	22.352	8.297	3.343	0.548	2.482
47	21.439	18.322	5.924	4.608	0.803	1.286
48	21.095	21.873	8.948	3.002	0.554	2.981
49	20.923	19.711	6.395	4.166	0.677	1.535
50	20.694	19.991	6.395	4.120	0.651	1.552
51	20.637	21.055	6.541	4.017	0.585	1.628
52	20.522	27.324	6.103	4.281	0.345	1.426

53	20.293	18.917	6.836	3.780	0.713	1.809
54	19.605	20.751	6.251	3.993	0.572	1.566
55	19.547	20.330	6.378	3.902	0.594	1.635
56	19.318	17.878	5.940	4.141	0.760	1.435
57	19.301	22.020	5.691	4.318	0.500	1.318
58	19.204	18.100	5.821	4.200	0.737	1.386
59	18.516	19.256	5.608	4.204	0.628	1.334
60	18.458	22.478	6.249	3.761	0.459	1.661
61	18.260	17.264	5.799	4.009	0.770	1.446
62	18.229	18.777	7.000	3.316	0.650	2.111
63	17.025	18.380	6.685	3.243	0.633	2.061
64	17.025	16.547	4.959	4.371	0.781	1.135
65	16.739	16.044	5.829	3.656	0.817	1.594
66	16.452	21.428	6.607	3.170	0.450	2.084
67	16.165	15.846	5.105	4.032	0.809	1.266
68	16.165	22.279	5.857	3.514	0.409	1.667
69	16.034	26.184	5.867	3.480	0.294	1.686
70	15.993	23.716	5.354	3.803	0.357	1.408
71	15.903	15.688	5.345	3.788	0.812	1.411
72	15.420	18.264	5.388	3.644	0.581	1.478
73	15.248	17.423	5.485	3.540	0.631	1.549
74	15.076	16.663	5.771	3.326	0.682	1.735
75	14.847	18.322	5.255	3.597	0.556	1.461
76	14.847	17.341	4.760	3.972	0.620	1.198
77	14.675	17.200	5.256	3.555	0.623	1.479
78	14.331	14.632	4.940	3.693	0.841	1.338
79	14.274	15.483	5.069	3.585	0.748	1.414
80	14.216	16.722	5.013	3.611	0.639	1.388
81	14.102	16.325	6.041	2.972	0.665	2.033
82	13.987	21.544	5.288	3.368	0.379	1.570
83	13.872	15.846	5.194	3.401	0.694	1.527
84	13.815	18.100	4.977	3.534	0.530	1.408
85	13.758	16.944	6.100	2.872	0.602	2.124
86	13.700	16.185	4.799	3.635	0.657	1.320
87	13.528	19.991	5.157	3.340	0.425	1.544
88	13.471	16.441	5.183	3.309	0.626	1.566
89	13.414	17.060	5.093	3.354	0.579	1.519
90	13.356	18.158	6.167	2.757	0.509	2.237
91	12.955	14.772	4.799	3.437	0.746	1.396
92	12.898	15.590	5.273	3.115	0.667	1.693
93	12.898	14.269	4.923	3.336	0.796	1.476
94	12.898	15.004	4.555	3.606	0.720	1.263
95	12.669	13.394	5.099	3.163	0.887	1.612
96	12.611	19.793	5.129	3.130	0.405	1.639
97	12.554	16.185	4.453	3.589	0.602	1.241
98	12.497	15.029	5.466	2.911	0.695	1.878
99	12.497	16.267	6.116	2.602	0.593	2.351
100	12.439	15.145	4.851	3.265	0.682	1.486
101	12.382	14.071	4.881	3.230	0.786	1.511
102	12.325	16.828	6.431	2.440	0.547	2.636
103	12.217	18.262	4.079	3.813	0.460	1.070
104	12.210	15.217	5.719	2.718	0.663	2.104
105	12.087	15.406	4.617	3.333	0.640	1.385
106	12.038	15.111	4.150	3.693	0.663	1.124
107	11.981	14.574	5.440	2.804	0.709	1.940
108	11.981	15.449	4.834	3.156	0.631	1.532
109	11.981	15.169	4.409	3.460	0.654	1.274
110	11.981	14.690	4.328	3.524	0.698	1.228

111	11.981	17.457	5.298	2.880	0.494	1.840
112	11.751	13.814	4.625	3.235	0.774	1.429
113	11.694	16.581	4.245	3.508	0.534	1.210
114	11.694	15.111	5.213	2.856	0.644	1.825
115	11.465	15.788	5.113	2.855	0.578	1.791
116	11.465	14.409	5.063	2.883	0.694	1.756
117	11.293	16.722	5.217	2.756	0.508	1.893
118	11.293	16.243	5.417	2.654	0.538	2.041
119	11.178	14.690	4.427	3.215	0.651	1.377
120	11.121	15.788	5.417	2.614	0.561	2.072
121	10.605	13.452	5.254	2.570	0.736	2.045
122	10.598	17.798	5.172	2.609	0.420	1.983
123	10.548	16.325	4.075	3.296	0.497	1.237
124	10.548	18.134	4.784	2.807	0.403	1.704
125	10.490	13.394	4.614	2.895	0.735	1.594
126	10.490	12.997	4.307	3.101	0.780	1.389
127	10.381	15.634	4.449	2.971	0.534	1.497
128	10.204	16.944	3.678	3.532	0.447	1.041
129	10.146	12.973	4.419	2.924	0.758	1.511
130	10.019	14.240	3.811	3.348	0.621	1.138
131	9.976	13.630	4.996	2.542	0.675	1.965
132	9.802	13.079	3.880	3.217	0.720	1.206
133	9.745	12.997	4.341	2.859	0.725	1.518
134	9.573	12.857	4.054	3.007	0.728	1.348
135	9.573	14.409	4.344	2.806	0.579	1.548
136	9.172	13.814	4.953	2.358	0.604	2.100
137	9.172	11.759	3.623	3.223	0.834	1.124
138	8.885	12.180	3.965	2.853	0.753	1.390
139	8.771	12.658	4.072	2.743	0.688	1.485
140	8.713	13.674	4.935	2.248	0.586	2.195
141	8.713	14.095	5.874	1.889	0.551	3.111
142	8.713	11.643	3.781	2.934	0.808	1.288
143	8.656	12.634	4.682	2.354	0.681	1.989
144	8.541	14.888	6.146	1.769	0.484	3.474
145	8.484	11.560	3.845	2.810	0.798	1.368
146	8.484	12.320	3.596	3.004	0.702	1.197
147	8.400	11.582	4.052	2.640	0.787	1.535
148	8.255	11.701	4.274	2.459	0.758	1.738
149	8.197	12.180	3.492	2.989	0.694	1.168
150	8.083	12.097	3.587	2.869	0.694	1.250
151	7.968	13.055	4.705	2.156	0.587	2.182
152	7.968	13.021	3.432	2.956	0.591	1.161
153	7.865	12.362	4.328	2.314	0.647	1.870
154	7.853	12.799	3.748	2.668	0.602	1.405
155	7.796	10.941	3.471	2.860	0.818	1.214
156	7.624	12.039	3.777	2.570	0.661	1.469
157	7.624	11.140	3.817	2.543	0.772	1.501
158	7.624	11.420	3.820	2.541	0.735	1.503
159	7.624	10.685	3.852	2.520	0.839	1.529
160	7.567	13.171	5.725	1.683	0.548	3.402
161	7.489	12.462	4.410	2.162	0.606	2.039
162	7.373	13.254	3.636	2.582	0.527	1.408
163	7.337	11.362	4.431	2.109	0.714	2.101
164	7.337	11.362	4.031	2.317	0.714	1.740
165	7.301	11.922	3.408	2.728	0.645	1.249
166	7.200	14.672	3.814	2.404	0.420	1.587
167	7.157	13.142	4.207	2.166	0.521	1.943
168	7.051	10.066	3.302	2.719	0.874	1.214

169	6.994	11.536	4.530	1.966	0.660	2.304
170	6.969	11.130	3.469	2.558	0.707	1.356
171	6.879	10.965	3.823	2.291	0.719	1.668
172	6.824	12.702	3.732	2.328	0.531	1.603
173	6.822	10.883	3.015	2.881	0.724	1.047
174	6.764	10.404	3.761	2.290	0.785	1.642
175	6.752	11.553	4.200	2.047	0.636	2.052
176	6.592	10.941	3.866	2.171	0.692	1.780
177	6.549	10.151	3.462	2.409	0.799	1.437
178	6.420	12.320	4.726	1.730	0.532	2.732
179	6.363	10.627	3.147	2.575	0.708	1.222
180	6.306	11.619	3.552	2.261	0.587	1.571
181	6.248	9.901	2.955	2.693	0.801	1.097
182	6.248	11.560	3.656	2.176	0.588	1.680
183	6.191	11.023	3.932	2.005	0.640	1.961
184	6.076	10.066	3.881	1.994	0.754	1.946
185	6.019	9.587	2.945	2.602	0.823	1.132
186	6.019	9.132	3.034	2.526	0.907	1.201
187	5.904	11.023	4.363	1.723	0.611	2.532
188	5.904	12.155	3.293	2.283	0.502	1.443
189	5.855	9.500	2.935	2.541	0.815	1.155
190	5.790	10.264	3.846	1.917	0.691	2.006
191	5.560	9.132	3.165	2.237	0.838	1.415
192	5.446	11.957	3.433	2.020	0.479	1.700
193	5.446	9.785	3.130	2.215	0.715	1.413
194	5.446	10.346	4.263	1.627	0.639	2.621
195	5.388	9.984	3.787	1.811	0.679	2.091
196	5.331	9.108	3.037	2.235	0.808	1.359
197	5.216	9.108	2.943	2.257	0.790	1.304
198	5.102	9.471	3.066	2.119	0.715	1.447
199	5.045	9.108	3.446	1.864	0.764	1.849
200	5.045	9.529	3.279	1.959	0.698	1.674
201	4.987	9.166	3.211	1.977	0.746	1.624
202	4.987	9.248	3.404	1.865	0.733	1.825
203	4.930	9.050	3.185	1.970	0.756	1.617
204	4.930	10.124	2.633	2.384	0.604	1.104
205	4.872	10.351	3.054	2.031	0.571	1.504
206	4.858	11.184	4.152	1.490	0.488	2.787
207	4.829	10.492	3.441	1.787	0.551	1.926
208	4.815	9.389	3.019	2.031	0.686	1.486
209	4.815	8.769	3.127	1.961	0.787	1.595
210	4.701	9.306	3.071	1.949	0.682	1.575
211	4.655	8.808	2.777	2.134	0.754	1.301
212	4.586	8.092	2.586	2.258	0.880	1.145
213	4.529	9.190	3.798	1.518	0.674	2.502
214	4.511	9.219	2.964	1.938	0.667	1.529
215	4.414	9.867	3.546	1.585	0.570	2.237
216	4.357	8.174	2.623	2.115	0.819	1.240
217	4.299	8.852	2.823	1.939	0.690	1.456
218	4.185	8.291	3.076	1.732	0.765	1.776
219	4.127	8.513	3.204	1.640	0.716	1.953
220	4.013	7.754	2.696	1.895	0.839	1.423
221	3.961	8.058	2.368	2.130	0.767	1.111
222	3.955	7.952	2.865	1.758	0.786	1.630
223	3.955	10.661	3.140	1.604	0.437	1.958
224	3.955	7.473	2.659	1.894	0.890	1.404
225	3.955	8.174	2.780	1.812	0.744	1.534
226	3.898	7.754	2.896	1.714	0.815	1.690

227	3.860	9.658	2.719	1.807	0.520	1.505
228	3.841	8.034	3.230	1.514	0.748	2.133
229	3.841	7.357	2.399	2.039	0.892	1.176
230	3.788	8.211	2.822	1.709	0.706	1.651
231	3.783	8.150	2.671	1.804	0.716	1.481
232	3.759	11.383	3.899	1.228	0.365	3.176
233	3.669	7.415	2.809	1.663	0.838	1.689
234	3.643	8.451	2.390	1.941	0.641	1.232
235	3.600	7.635	2.662	1.722	0.776	1.547
236	3.554	7.555	2.281	1.983	0.782	1.150
237	3.554	6.796	2.442	1.853	0.967	1.317
238	3.497	8.571	2.866	1.553	0.598	1.845
239	3.484	7.448	2.676	1.658	0.789	1.614
240	3.455	7.676	2.610	1.686	0.737	1.548
241	3.382	7.754	2.549	1.689	0.707	1.509
242	3.382	7.672	2.415	1.783	0.722	1.354
243	3.382	7.613	2.612	1.649	0.733	1.584
244	3.325	7.448	2.434	1.740	0.753	1.399
245	3.210	7.193	2.844	1.437	0.780	1.979
246	3.181	11.019	2.479	1.633	0.329	1.518
247	3.123	8.058	2.636	1.508	0.604	1.747
248	3.108	7.888	2.112	1.874	0.628	1.127
249	3.095	7.052	2.362	1.668	0.782	1.416
250	3.065	8.398	2.728	1.431	0.546	1.907
251	2.981	8.092	2.716	1.398	0.572	1.943
252	2.981	6.714	2.270	1.672	0.831	1.358
253	2.981	7.613	2.842	1.335	0.646	2.128
254	2.964	8.099	2.552	1.479	0.568	1.726
255	2.924	7.754	2.684	1.387	0.611	1.935
256	2.866	6.936	2.771	1.317	0.749	2.104
257	2.834	7.377	2.784	1.296	0.654	2.148
258	2.805	6.996	2.431	1.469	0.720	1.655
259	2.776	6.926	2.257	1.566	0.727	1.441
260	2.776	6.469	2.346	1.506	0.834	1.557
261	2.752	7.696	3.074	1.140	0.584	2.697
262	2.747	7.460	2.505	1.396	0.620	1.794
263	2.704	7.137	2.600	1.324	0.667	1.963
264	2.646	6.656	2.271	1.483	0.750	1.531
265	2.602	7.506	2.407	1.377	0.580	1.748
266	2.580	6.936	2.412	1.362	0.674	1.772
267	2.580	6.259	2.263	1.451	0.827	1.559
268	2.559	6.369	2.067	1.576	0.793	1.311
269	2.559	6.515	2.403	1.356	0.758	1.772
270	2.429	6.087	1.878	1.647	0.824	1.140
271	2.408	7.836	3.346	0.916	0.493	3.652
272	2.408	5.780	1.971	1.555	0.906	1.268
273	2.350	6.399	2.321	1.290	0.721	1.799
274	2.328	6.938	1.879	1.577	0.608	1.191
275	2.328	6.685	2.067	1.434	0.655	1.442
276	2.293	8.150	3.235	0.902	0.434	3.585
277	2.178	5.442	1.849	1.500	0.924	1.232
278	2.140	6.328	1.904	1.431	0.672	1.331
279	2.121	5.640	2.012	1.342	0.838	1.500
280	2.121	5.979	2.228	1.212	0.746	1.838
281	2.121	5.442	1.792	1.507	0.900	1.189
282	2.111	7.431	3.017	0.891	0.480	3.386
283	2.096	5.789	1.932	1.382	0.786	1.398
284	1.923	5.876	2.031	1.206	0.700	1.685

285	1.908	6.457	2.023	1.201	0.575	1.685
286	1.836	5.084	1.723	1.357	0.893	1.270
287	1.834	5.161	1.932	1.209	0.865	1.598
288	1.834	5.103	1.852	1.261	0.885	1.468
289	1.822	6.058	2.569	0.903	0.624	2.845
290	1.822	6.726	2.525	0.919	0.506	2.749
291	1.822	5.395	1.773	1.308	0.786	1.355
292	1.777	5.979	2.323	0.974	0.625	2.385
293	1.764	5.213	1.621	1.386	0.816	1.170
294	1.764	5.155	1.958	1.147	0.834	1.707
295	1.735	6.158	2.493	0.886	0.575	2.814
296	1.662	4.823	1.611	1.314	0.898	1.227
297	1.662	4.624	1.786	1.185	0.977	1.507
298	1.619	5.155	1.816	1.135	0.766	1.600
299	1.605	5.640	2.232	0.916	0.634	2.438
300	1.605	4.624	1.591	1.285	0.943	1.238
301	1.605	4.624	1.511	1.353	0.943	1.117
302	1.605	4.542	1.435	1.424	0.978	1.007
303	1.605	4.624	1.809	1.129	0.943	1.602
304	1.605	4.914	1.702	1.200	0.835	1.418
305	1.547	5.395	1.683	1.171	0.668	1.438
306	1.388	4.445	1.482	1.192	0.883	1.243
307	1.388	5.395	1.595	1.108	0.599	1.440
308	1.359	4.475	1.354	1.278	0.853	1.059
309	1.318	4.624	1.689	0.994	0.775	1.698
310	1.318	4.286	1.594	1.053	0.902	1.513
311	1.318	4.286	1.657	1.013	0.902	1.635
312	1.318	4.286	1.651	1.017	0.902	1.623
313	1.287	4.574	1.580	1.037	0.773	1.524
314	1.261	4.203	1.544	1.040	0.897	1.485
315	1.261	3.865	1.478	1.086	1.000	1.361
316	1.258	4.363	1.499	1.068	0.830	1.403
317	1.243	4.955	1.680	0.943	0.636	1.782
318	1.204	4.227	1.891	0.810	0.846	2.333
319	1.204	3.807	1.465	1.046	1.000	1.400
320	1.204	4.764	1.988	0.771	0.666	2.580
321	1.200	4.193	1.353	1.129	0.858	1.199
322	1.171	4.404	1.510	0.987	0.759	1.529
323	1.171	5.524	1.509	0.988	0.482	1.527
324	1.157	5.266	1.732	0.850	0.524	2.037
325	1.146	4.624	1.871	0.780	0.674	2.399
326	1.128	4.844	1.717	0.836	0.604	2.054
327	1.099	3.824	1.263	1.108	0.944	1.140
328	1.089	3.666	1.438	0.964	1.000	1.491
329	1.070	5.184	1.724	0.790	0.500	2.181
330	1.041	4.462	1.363	0.972	0.657	1.403
331	1.032	3.666	1.253	1.048	0.965	1.196
332	1.032	3.666	1.172	1.121	0.965	1.046
333	1.032	3.749	1.621	0.810	0.923	2.000
334	1.026	3.824	1.185	1.103	0.882	1.075
335	0.983	5.055	1.290	0.970	0.483	1.330
336	0.983	4.885	1.790	0.699	0.518	2.561
337	0.983	4.093	1.593	0.786	0.737	2.027
338	0.975	3.468	1.186	1.046	1.000	1.134
339	0.975	4.682	1.884	0.659	0.559	2.861
340	0.954	3.935	1.372	0.886	0.774	1.549
341	0.954	4.586	1.980	0.614	0.570	3.228
342	0.940	3.513	1.132	1.057	0.957	1.070

343	0.917	3.328	1.228	0.951	1.000	1.292
344	0.917	3.328	1.201	0.973	1.000	1.234
345	0.860	4.566	2.111	0.519	0.518	4.072
346	0.839	4.304	1.558	0.685	0.569	2.273
347	0.839	3.683	1.159	0.921	0.777	1.259
348	0.824	3.483	1.180	0.889	0.853	1.328
349	0.810	3.313	1.127	0.915	0.927	1.232
350	0.795	3.513	1.283	0.789	0.810	1.627
351	0.781	3.384	1.095	0.908	0.857	1.206
352	0.766	3.272	1.116	0.874	0.899	1.277
353	0.752	3.554	1.454	0.659	0.748	2.207
354	0.745	4.706	2.064	0.460	0.423	4.489
355	0.723	3.442	1.095	0.841	0.767	1.302
356	0.723	3.073	1.147	0.802	0.962	1.431
357	0.708	3.624	1.531	0.589	0.678	2.598
358	0.694	4.035	1.228	0.720	0.536	1.706
359	0.665	3.044	1.069	0.792	0.902	1.349
360	0.665	3.173	1.300	0.651	0.830	1.997
361	0.631	2.849	1.134	0.708	0.976	1.603
362	0.631	2.709	0.956	0.840	1.000	1.139
363	0.631	2.849	1.079	0.744	0.976	1.450
364	0.631	2.709	0.956	0.840	1.000	1.139
365	0.607	3.413	1.199	0.645	0.655	1.858
366	0.593	3.002	1.146	0.658	0.826	1.741
367	0.549	2.733	1.105	0.633	0.924	1.744
368	0.520	2.704	1.013	0.654	0.895	1.550
369	0.516	3.270	1.466	0.448	0.606	3.273
370	0.516	2.849	1.028	0.639	0.799	1.610
371	0.516	2.510	1.005	0.654	1.000	1.536
372	0.506	3.114	1.386	0.465	0.656	2.981
373	0.459	2.510	1.064	0.549	0.914	1.939
374	0.459	2.172	0.847	0.689	1.000	1.229
375	0.419	2.973	1.228	0.435	0.596	2.825
376	0.419	2.322	0.929	0.575	0.977	1.615
377	0.401	2.032	0.903	0.566	1.000	1.596
378	0.376	2.252	0.861	0.556	0.932	1.549
379	0.376	2.832	1.131	0.423	0.589	2.675
380	0.361	2.252	0.879	0.524	0.896	1.678
381	0.347	2.522	1.058	0.418	0.686	2.532
382	0.304	2.252	0.819	0.472	0.752	1.736
383	0.287	2.032	0.604	0.604	0.873	1.000
384	0.287	2.032	0.604	0.604	0.873	1.000
385	0.287	1.833	0.753	0.485	1.000	1.553
386	0.275	2.041	0.914	0.383	0.829	2.388
387	0.217	1.601	0.620	0.445	1.000	1.392
388	0.202	1.941	0.812	0.317	0.675	2.561
389	0.202	2.223	0.931	0.277	0.515	3.366
390	0.173	1.402	0.543	0.407	1.000	1.333
391	0.172	1.495	0.810	0.270	0.967	3.000
392	0.172	1.635	0.810	0.270	0.809	3.000
393	0.172	1.354	0.566	0.387	1.000	1.464
394	0.172	1.354	0.566	0.387	1.000	1.464
395	0.130	1.161	0.407	0.407	1.000	1.000
396	0.115	1.016	0.540	0.270	1.000	2.000
397	0.115	1.016	0.540	0.270	1.000	2.000
398	0.115	1.156	0.540	0.270	1.000	2.000
399	0.115	1.354	0.621	0.235	0.785	2.646
400	0.115	1.156	0.540	0.270	1.000	2.000

401	0.087	1.161	0.497	0.222	0.809	2.237
402	0.087	0.921	0.407	0.271	1.000	1.500
403	0.087	1.091	0.419	0.263	0.916	1.593
404	0.087	1.161	0.447	0.247	0.809	1.809
405	0.087	0.921	0.407	0.271	1.000	1.500
406	0.072	0.921	0.378	0.243	1.000	1.553
407	0.072	0.850	0.378	0.243	1.000	1.553
408	0.072	0.850	0.378	0.243	1.000	1.553
409	0.058	0.850	0.329	0.224	1.000	1.468
410	0.057	0.677	0.270	0.270	1.000	1.000
411	0.057	0.677	0.270	0.270	1.000	1.000
412	0.057	0.677	0.270	0.270	1.000	1.000
413	0.057	0.677	0.270	0.270	1.000	1.000
414	0.057	0.677	0.270	0.270	1.000	1.000
415	0.029	0.510	0.271	0.136	1.000	2.000
416	0.029	0.581	0.271	0.136	1.000	2.000
417	0.029	0.510	0.271	0.136	1.000	2.000

Supplementary Table A.I.8. Data for restite shape and size analysis in pseudotachylyte bearing fragment (collected using ImageJ).

Identifier	Area	Perimete	Major axis	Minor axis	Circularity	Aspect ratio
	(μm^2)	(μm)	(μm)	(μm)		
1	470.123	93.526	26.657	22.455	0.675	1.187
2	113.512	62.898	14.295	10.110	0.361	1.414
3	61.665	32.453	10.369	7.572	0.736	1.369
4	56.842	34.709	10.025	7.219	0.593	1.389
5	54.258	34.767	9.727	7.103	0.564	1.369
6	47.942	33.039	9.840	6.203	0.552	1.586
7	46.220	32.618	9.503	6.193	0.546	1.535
8	42.660	37.047	9.138	5.944	0.391	1.537
9	34.909	28.014	9.293	4.783	0.559	1.943
10	34.737	28.808	9.730	4.545	0.526	2.141
11	34.277	33.049	8.222	5.308	0.394	1.549
12	33.818	27.487	7.984	5.393	0.562	1.481
13	30.086	23.667	7.352	5.210	0.675	1.411
14	29.684	33.470	9.077	4.164	0.333	2.180
15	26.182	20.428	7.459	4.469	0.788	1.669
16	24.574	43.273	8.203	3.814	0.165	2.151
17	23.426	20.942	6.067	4.916	0.671	1.234
18	23.139	25.419	6.026	4.889	0.450	1.233
19	22.794	22.534	9.184	3.160	0.564	2.906
20	22.622	25.313	6.623	4.349	0.444	1.523
21	22.392	22.379	7.020	4.061	0.562	1.729
22	22.163	19.669	5.712	4.940	0.720	1.156
23	21.416	18.197	5.305	5.140	0.813	1.032
24	21.014	21.247	5.648	4.738	0.585	1.192
25	20.325	20.709	6.032	4.290	0.596	1.406
26	20.268	19.891	6.637	3.888	0.644	1.707
27	18.947	18.337	5.691	4.239	0.708	1.342
28	18.775	25.327	11.041	2.165	0.368	5.100
29	18.316	17.461	6.250	3.731	0.755	1.675
30	18.201	16.619	5.670	4.087	0.828	1.387
31	18.201	21.784	6.248	3.709	0.482	1.684
32	17.627	18.899	6.465	3.471	0.620	1.862
33	16.938	17.098	5.663	3.808	0.728	1.487
34	16.938	18.792	6.373	3.384	0.603	1.883
35	16.249	16.164	5.496	3.764	0.782	1.460
36	16.249	20.346	5.306	3.899	0.493	1.361
37	15.100	15.660	5.002	3.844	0.774	1.301
38	15.043	20.791	5.416	3.536	0.437	1.532
39	14.756	17.834	6.444	2.916	0.583	2.210
40	14.756	20.264	5.601	3.354	0.452	1.670
41	14.124	22.568	8.785	2.047	0.348	4.291
42	13.837	15.123	4.879	3.611	0.760	1.351
43	13.263	15.859	4.531	3.727	0.663	1.216
44	12.919	15.263	4.830	3.406	0.697	1.418
45	12.517	21.445	5.384	2.960	0.342	1.819
46	12.459	14.726	5.489	2.890	0.722	1.900
47	11.426	13.767	4.678	3.110	0.758	1.504
48	11.254	15.379	4.506	3.180	0.598	1.417
49	11.139	14.363	4.652	3.049	0.679	1.526
50	11.139	15.825	5.710	2.484	0.559	2.299
51	10.794	13.826	5.036	2.729	0.710	1.845
52	10.737	17.611	4.597	2.974	0.435	1.546

53	10.679	14.900	4.663	2.916	0.604	1.599
54	10.622	14.842	5.302	2.551	0.606	2.078
55	10.565	13.966	4.289	3.136	0.681	1.367
56	10.335	17.272	4.728	2.783	0.435	1.699
57	9.876	14.760	5.213	2.412	0.570	2.161
58	9.703	12.867	3.976	3.107	0.736	1.280
59	9.646	14.024	3.644	3.371	0.616	1.081
60	9.588	13.545	4.744	2.574	0.657	1.843
61	9.531	18.207	4.147	2.926	0.361	1.417
62	9.072	12.528	4.830	2.392	0.726	2.019
63	9.014	12.189	4.608	2.491	0.762	1.850
64	8.785	14.140	3.860	2.898	0.552	1.332
65	8.383	17.693	4.897	2.180	0.336	2.247
66	8.153	12.610	3.852	2.695	0.644	1.430
67	7.866	13.148	4.140	2.419	0.572	1.711
68	7.866	14.561	3.621	2.766	0.466	1.309
69	7.809	13.463	4.889	2.034	0.541	2.404
70	7.522	13.124	4.041	2.370	0.549	1.705
71	7.522	10.950	3.940	2.431	0.788	1.621
72	7.407	19.843	4.101	2.300	0.236	1.783
73	7.292	10.156	3.611	2.571	0.888	1.404
74	7.292	12.388	4.020	2.310	0.597	1.740
75	7.234	10.577	4.133	2.228	0.813	1.855
76	7.234	13.124	3.311	2.782	0.528	1.190
77	7.005	11.313	3.707	2.406	0.688	1.541
78	6.947	12.388	4.547	1.945	0.569	2.337
79	6.947	13.908	5.245	1.687	0.451	3.110
80	6.890	12.247	4.213	2.082	0.577	2.023
81	6.718	10.776	3.712	2.304	0.727	1.611
82	6.718	11.546	3.492	2.449	0.633	1.426
83	6.258	11.487	3.610	2.208	0.596	1.635
84	6.144	10.529	3.147	2.485	0.696	1.266
85	6.086	9.934	3.362	2.305	0.775	1.458
86	5.971	11.056	3.238	2.348	0.614	1.379
87	5.971	10.437	3.580	2.124	0.689	1.686
88	5.684	10.611	3.873	1.869	0.634	2.073
89	5.627	9.934	3.486	2.055	0.717	1.696
90	5.569	10.693	3.293	2.153	0.612	1.530
91	5.512	13.874	6.660	1.054	0.360	6.321
92	5.512	10.868	3.389	2.071	0.586	1.636
93	5.340	12.189	3.583	1.898	0.452	1.888
94	5.225	9.396	2.766	2.405	0.744	1.150
95	5.110	9.619	3.860	1.685	0.694	2.290
96	5.053	8.239	2.843	2.263	0.935	1.257
97	5.053	8.917	3.324	1.936	0.799	1.717
98	4.995	10.635	3.584	1.775	0.555	2.020
99	4.880	8.801	3.452	1.800	0.792	1.918
100	4.880	9.677	2.651	2.344	0.655	1.131
101	4.708	10.611	2.948	2.033	0.525	1.450
102	4.708	8.835	3.006	1.994	0.758	1.507
103	4.651	8.123	2.751	2.153	0.886	1.278
104	4.651	9.793	2.691	2.201	0.609	1.223
105	4.651	8.438	3.043	1.946	0.821	1.563
106	4.651	8.777	3.450	1.717	0.759	2.010
107	4.593	7.924	2.456	2.382	0.919	1.031
108	4.364	8.859	3.151	1.763	0.699	1.787
109	4.364	10.752	3.471	1.601	0.474	2.169
110	4.306	12.785	2.914	1.882	0.331	1.549

111	4.134	7.900	3.160	1.665	0.832	1.898
112	3.904	8.694	2.448	2.031	0.649	1.205
113	3.789	7.958	2.947	1.637	0.752	1.800
114	3.675	8.777	3.329	1.406	0.599	2.368
115	3.617	8.578	2.601	1.771	0.618	1.469
116	3.560	11.933	5.053	0.897	0.314	5.632
117	3.502	7.082	2.429	1.836	0.877	1.323
118	3.330	8.099	2.421	1.751	0.638	1.383
119	3.330	6.860	2.416	1.755	0.889	1.376
120	3.215	7.958	2.738	1.495	0.638	1.832
121	3.100	6.743	2.353	1.678	0.857	1.402
122	3.043	6.545	2.368	1.636	0.893	1.447
123	3.043	6.685	1.995	1.942	0.856	1.028
124	3.043	9.735	3.641	1.064	0.404	3.421
125	2.986	9.759	4.670	0.814	0.394	5.737
126	2.986	6.801	2.135	1.780	0.811	1.200
127	2.871	8.099	2.606	1.403	0.550	1.858
128	2.813	7.363	2.853	1.256	0.652	2.272
129	2.756	6.264	2.136	1.643	0.883	1.300
130	2.584	6.042	2.239	1.469	0.890	1.524
131	2.584	7.140	2.117	1.554	0.637	1.363
132	2.526	6.264	2.326	1.383	0.809	1.681
133	2.469	6.463	2.705	1.162	0.743	2.328
134	2.411	7.760	2.423	1.267	0.503	1.911
135	2.354	7.503	3.309	0.906	0.525	3.652
136	2.354	5.843	2.107	1.423	0.866	1.481
137	2.297	6.124	1.969	1.485	0.770	1.326
138	2.239	8.157	3.399	0.839	0.423	4.053
139	2.239	5.586	1.909	1.494	0.902	1.278
140	2.067	5.165	1.793	1.468	0.974	1.221
141	2.067	6.860	1.891	1.392	0.552	1.359
142	2.010	5.644	1.954	1.310	0.793	1.492
143	1.952	4.967	1.632	1.523	0.994	1.072
144	1.895	5.306	1.773	1.361	0.846	1.303
145	1.895	5.306	1.864	1.294	0.846	1.441
146	1.780	6.404	2.493	0.909	0.545	2.743
147	1.780	4.768	1.838	1.233	0.984	1.491
148	1.722	8.496	2.570	0.853	0.300	3.012
149	1.493	4.967	1.550	1.227	0.760	1.263
150	1.493	5.785	1.481	1.283	0.561	1.154
151	1.493	5.306	1.896	1.002	0.666	1.892
152	1.493	4.967	1.717	1.107	0.760	1.550
153	1.435	4.347	1.659	1.101	0.954	1.506
154	1.378	4.231	1.622	1.082	0.967	1.500
155	1.378	4.289	1.557	1.127	0.941	1.381
156	1.206	5.165	1.542	0.995	0.568	1.550
157	1.148	4.628	1.908	0.766	0.674	2.489
158	0.976	4.289	1.594	0.780	0.667	2.044
159	0.861	3.529	1.345	0.815	0.869	1.649
160	0.804	3.132	1.304	0.785	1.000	1.662
161	0.804	3.471	1.376	0.744	0.838	1.851
162	0.804	3.529	1.191	0.859	0.811	1.386
163	0.746	2.851	1.050	0.905	1.000	1.159
164	0.746	3.529	1.212	0.784	0.753	1.546
165	0.689	2.992	1.135	0.773	0.967	1.469
166	0.689	3.132	1.214	0.723	0.883	1.679
167	0.632	2.851	1.080	0.745	0.976	1.450
168	0.632	2.992	1.132	0.711	0.887	1.592

169	0.574	2.512	1.068	0.685	1.000	1.559
170	0.574	2.793	1.352	0.541	0.925	2.500
171	0.574	2.711	1.077	0.679	0.982	1.587
172	0.574	2.711	0.867	0.843	0.982	1.028
173	0.459	3.132	1.310	0.446	0.588	2.935
174	0.402	2.174	0.840	0.609	1.000	1.380
175	0.344	1.835	0.811	0.541	1.000	1.500
176	0.344	2.314	0.990	0.443	0.809	2.237
177	0.344	2.992	0.837	0.524	0.484	1.597
178	0.344	1.835	0.811	0.541	1.000	1.500
179	0.287	1.835	0.753	0.485	1.000	1.553
180	0.287	1.835	0.753	0.485	1.000	1.553
181	0.230	1.355	0.541	0.541	1.000	1.000
182	0.230	1.694	0.655	0.446	1.000	1.468
183	0.230	2.033	0.692	0.423	0.698	1.637
184	0.172	1.496	0.811	0.270	0.967	3.000
185	0.172	1.355	0.567	0.387	1.000	1.464
186	0.172	1.496	0.811	0.270	0.967	3.000
187	0.172	1.496	0.811	0.270	0.967	3.000
188	0.172	1.355	0.567	0.387	1.000	1.464
189	0.115	1.157	0.541	0.270	1.000	2.000
190	0.115	1.157	0.541	0.270	1.000	2.000
191	0.115	1.157	0.541	0.270	1.000	2.000
192	0.115	1.355	0.622	0.235	0.785	2.646
193	0.115	1.157	0.541	0.270	1.000	2.000
194	0.115	1.017	0.541	0.270	1.000	2.000
195	0.115	1.017	0.541	0.270	1.000	2.000
196	0.115	1.017	0.541	0.270	1.000	2.000
197	0.057	0.678	0.270	0.270	1.000	1.000
198	0.057	0.678	0.270	0.270	1.000	1.000
199	0.057	0.678	0.270	0.270	1.000	1.000
200	0.057	0.678	0.270	0.270	1.000	1.000
201	0.057	0.678	0.270	0.270	1.000	1.000
202	0.057	0.678	0.270	0.270	1.000	1.000
203	0.057	0.678	0.270	0.270	1.000	1.000
204	0.057	0.678	0.270	0.270	1.000	1.000
205	0.057	0.678	0.270	0.270	1.000	1.000

Appendix II – (Chapter 3)

Supplementary Table A.II.1. Mechanical and temperature data for all experiments. AAI – Arequipa Airport Ignimbrite (rhyolitic ignimbrite), PPA – Pichu Pichu Avalanche (andesitic lav.

Lithology	Sample name (upper)	Sample name (upper)	Applied normal stress	Slip rate	Rotations	Total Displacement	Wear rate	Measured normal stress	Peak shear stress	Steady state shear stress	Steady state shear stress SD	Steady state shear stress SE	Friction coeff.	Friction coeff. SD	Friction coeff. SE	Steady state conditions	Power density	Work per metre slip	T_{max}
			(MPa)	(m s^{-1})	(n)	(m)	(mm m^{-1})	(MPa)	(MPa)	(MPa)						(m)	MW m^{-2}	J m^{-2} m^{-1}	(°C)
Rhyolitic Ignimbrite	AAI1_24	AAI1_23	0.25	0.01	104	9.59	0.0337	0.2418	0.2256	0.1064	0.0399	0.0003	0.4398	0.1786	0.0012	4.00-8.00	0.0011	0.1064	41
	AAI1_20	AAI1_19	0.25	0.01	26.5	2.50	1.4055	0.2424	0.1730	0.0979	0.0288	0.0004	0.4041	0.1332	0.0018	1.00-2.00	0.0010	0.0979	42
	AAI1_24	AAI1_23	0.25	0.05	104.1	9.95	0.0365	0.2464	0.2036	0.1458	0.0338	0.0005	0.5917	0.1546	0.0024	4.00-8.00	0.0073	0.1458	81
	AAI1_13	AAI1_10	0.25	0.05	88.4	7.95	0.0305	0.2306	0.2076	0.1521	0.0184	0.0004	0.6595	0.1154	0.0025	4.00-6.00	0.0076	0.1520	72
	AAI1_24	AAI1_23	0.25	0.1	111.2	10.66	0.0257	0.2438	0.1934	0.1117	0.0318	0.0007	0.4581	0.1413	0.0032	4.00-8.00	0.0112	0.1117	112
	AAI1_24	AAI1_23	0.25	0.2	55.4	5.32	0.6367	0.2222	0.4814	0.2313	0.0493	0.0022	1.0406	0.2677	0.0119	2.00-4.00	0.0463	0.2312	235
	AAI1_21	AAI1_22	0.25	0.3	54	5.17	0.5153	0.2219	0.3799	0.1931	0.0272	0.0015	0.8698	0.1445	0.0079	2.00-4.00	0.0579	0.1934	152
	AAI1_9	AAI1_17	0.25	0.5	66.2	6.24	1.4216	0.2254	0.1887	0.1495	0.0497	0.0029	0.6631	0.2319	0.0133	2.00-5.00	0.0747	0.1494	307
	AAI1_11	AAI1_7	0.25	1	214	20.55	0.1634	0.2329	0.2227	0.1928	0.0549	0.0025	0.8277	0.2485	0.0111	15.00-20.00	0.1928	0.1925	355
	AAI1_11	AAI1_7	0.25	1.7	140.8	13.52	0.4972	0.2249	0.2052	0.1348	0.0614	0.0040	0.5994	0.2859	0.0186	4.00-8.00	0.2291	0.1345	241
	AAI1_15	AAI1_14	0.25	2.4	136.9	12.89	1.4787	0.1977	0.2102	0.0240	0.0430	0.0033	0.1216	0.2378	0.0184	4.00-8.00	0.0577	0.0235	103
	AAI1_20	AAI1_19	0.5	0.01	2.1	0.30	3.5730	0.4926	0.3897	0.2705	0.0330	0.0020	0.5492	0.0777	0.0047	0.05-0.10	0.0027	0.2700	50
	AAI1_42	AAI1_43	0.5	0.01	27.6	2.29	0.9141	0.4651	0.3411	0.2860	0.0320	0.0003	0.6148	0.0797	0.0008	0.20-1.00	0.0029	0.2860	76
	AAI1_44	AAI1_45	0.5	0.05	22	2.07	0.4836	0.4843	0.3623	0.3158	0.0330	0.0007	0.6522	0.0792	0.0017	0.30-1.30	0.0158	0.3159	118
	AAI1_47	AAI1_41	0.5	0.1	40	3.83	2.2266	0.4621	0.3931	0.2934	0.0445	0.0011	0.6348	0.1000	0.0026	0.50-2.00	0.0293	0.2933	120
	AAI1_28	AAI1_27	0.5	0.2	24.4	2.34	0.6598	0.4605	0.4965	0.2903	0.0163	0.0010	0.6303	0.0486	0.0031	0.30-0.80	0.0581	0.2903	121

	AAI1_51	AAI1_31B	0.5	0.3	15.1	1.45	1.1363	0.4524	0.5187	0.3280	0.0624	0.0054	0.7250	0.1378	0.0119	0.30-0.60	0.0984	0.4362	120
	AAI1_35	AAI1_48	0.5	0.5	15	1.44	1.4802	0.4906	0.3050	0.3106	0.0176	0.0016	0.6330	0.0412	0.0037	0.20-0.80	0.1553	0.3100	120
	AAI1_46	AAI1_39	0.5	1	14.2	1.37	1.7854	0.4957	0.3611	0.3640	0.1057	0.0190	0.7344	0.2261	0.0406	0.10-0.40	0.3640	0.3715	120
	AAI1_49	AAI1_34	0.5	1.7	60.9	5.85	1.9588	0.4913	0.2969	0.2760	0.0798	0.0056	0.5617	0.1648	0.0117	1.50-3.50	0.4691	0.4655	192
	AAI1_38	AAI1_40	0.5	2.4	36.1	3.47	2.6788	0.4879	0.3281	0.3859	0.0392	0.0060	0.7908	0.1060	0.0162	0.50-1.50	0.9261	0.3897	169
	AAI1_32	AAI1_33	1	0.01	14.1	1.13	0.4099	0.9858	0.7718	0.6030	0.0612	0.0010	0.6117	0.0654	0.0011	0.40-1.00	0.0060	0.6030	78
	AAI1_26	AAI1_25	1	0.05	1.5	0.16	3.7820	0.9817	0.9405	0.7332	0.1201	0.0132	0.7469	0.1230	0.0135	0.01-0.09	0.0367	0.7311	92
	AAI1_18b	AAI1_50	1	0.1	6.6	0.64	2.4711	1.0030	0.7692	0.6615	0.0471	0.0033	0.6595	0.0552	0.0039	0.10-0.30	0.0661	0.6603	158
Andesitic Lava	PPA_158_13	PPA_158_12	0.25	0.01	104	9.59	0.0000	0.2404	0.3712	0.2131	0.0349	0.0002	0.8862	0.1872	0.0013	4.00-8.00	0.0021	0.2131	40
	PPA_158_8	PPA_158_5	0.25	0.01	104.7	9.66	0.0004	0.2447	0.2257	0.0787	0.0211	0.0002	0.3214	0.0957	0.0010	6.50-8.00	0.0008	0.0787	37
	PPA_158_13	PPA_158_12	0.25	0.05	104.1	9.93	0.0000	0.2432	0.1960	0.0820	0.0235	0.0005	0.3371	0.1075	0.0024	6.00-8.00	0.0041	0.0820	45
	PPA_158_14	PPA_158_11	0.25	0.05	104.7	10.03	0.0000	0.2473	0.1926	0.1039	0.0407	0.0006	0.4201	0.1742	0.0027	4.00-8.00	0.0052	0.1039	66
	PPA_158_14	PPA_158_11	0.25	0.05	104.2	9.98	0.0000	0.2454	0.2175	0.1397	0.0254	0.0004	0.5692	0.1242	0.0020	4.00-8.00	0.0070	0.1397	70
	PPA_158_13	PPA_158_12	0.25	0.1	127.3	12.19	0.0000	0.2453	0.2965	0.1461	0.0430	0.0014	0.5956	0.1880	0.0059	6.00-8.00	0.0146	0.1460	106
	PPA_158_14	PPA_158_11	0.25	0.2	208.7	20.06	0.0011	0.2462	0.2670	0.2165	0.0299	0.0006	0.8795	0.1416	0.0028	5.00-15.00	0.0433	0.2165	119
	PPA_158_14	PPA_158_11	0.25	0.3	209.1	20.09	0.0000	0.2455	0.2631	0.1526	0.0127	0.0003	0.6219	0.0744	0.0018	5.00-15.00	0.0458	0.1526	67
	PPA_158_14	PPA_158_11	0.25	0.5	211.1	20.28	0.0001	0.2454	0.1597	0.0955	0.0175	0.0006	0.3894	0.0777	0.0025	5.00-15.00	0.0478	0.0955	143
	PPA_158_14	PPA_158_11	0.25	1	223.6	21.47	0.0001	0.2456	0.2954	0.2271	0.0351	0.0016	0.9247	0.1502	0.0067	5.00-15.00	0.2271	0.2270	103
	PPA_158_14	PPA_158_11	0.25	1	499.5	47.97	0.0015	0.2446	0.2407	0.1744	0.0477	0.0015	0.7132	0.2031	0.0064	20.00-40.00	0.1744	0.1744	463
	PPA_158_14	PPA_158_11	0.25	1.7	943	90.61	0.0000	0.2460	1.2673	0.1039	0.0296	0.0009	0.4222	0.1448	0.0042	20.00-40.00	0.1766	0.1038	264
	PPA_158_13	PPA_158_12	0.25	2.4	896	86.07	0.2086	0.2363	1.8576	1.7578	0.0803	0.0032	7.4374	0.9991	0.0400	65.00-80.00	4.2186	1.7571	464
	PPA_158_1	PPA_158_2	0.5	0.01	105.3	10.08	0.0004	0.4945	0.4198	0.2244	0.0247	0.0002	0.4537	0.0579	0.0004	3.50-6.00	0.0022	0.2243	52
	PPA_158_1	PPA_158_2	0.5	0.05	105.3	10.09	0.0000	0.4941	0.3724	0.2680	0.0225	0.0002	0.5424	0.0543	0.0006	2.00-6.00	0.0134	0.2680	70
	PPA_158_1	PPA_158_2	0.5	0.1	104.3	10.00	0.0000	0.4919	0.5692	0.3098	0.0692	0.0011	0.6297	0.1448	0.0023	4.00-8.00	0.0310	0.3098	127
	PPA_158_1	PPA_158_2	0.5	0.2	148.3	14.25	0.0028	0.4955	0.5221	0.3692	0.0419	0.0008	0.7451	0.0902	0.0018	2.50-7.50	0.0738	0.3692	227
	PPA_158_1	PPA_158_2	0.5	0.3	104.4	10.03	0.0025	0.4941	0.4535	0.2797	0.1187	0.0046	0.5662	0.2429	0.0094	6.00-8.00	0.0839	0.2799	185

	PPA_158_6	PPA_158_7	1	0.01	5.2	0.48	0.0528	1.0053	0.7987	0.5268	0.0793	0.0023	0.5240	0.0813	0.0023	0.13-0.35	0.0053	0.5269	69
	PPA_158_8	PPA_158_5	1	0.01	104.3	9.62	0.0019	0.9978	0.8789	0.5475	0.0306	0.0004	0.5487	0.0354	0.0005	6.00-7.00	0.0055	0.5475	73
	PPA_158_8	PPA_158_5	1	0.05	115.6	11.02	0.0000	1.0012	0.6316	0.2913	0.0575	0.0009	0.2910	0.0582	0.0009	2.00-6.00	0.0146	0.2912	121
	PPA_158_8	PPA_158_5	1	0.1	208.3	19.94	0.0056	0.9972	0.9291	0.6882	0.0470	0.0008	0.6902	0.0525	0.0009	11.00-18.00	0.0688	0.6882	459
	PPA_158_9	PPA_158_4	1	0.2	208	20.02	0.0053	1.0013	0.9133	0.6063	0.1129	0.0027	0.6055	0.1140	0.0027	7.00-14.00	0.1213	0.6061	267
	PPA_158_9	PPA_158_4	1	0.3	210	20.21	0.0112	1.0013	0.8532	0.5475	0.2024	0.0090	0.5468	0.2035	0.0091	13.00-16.00	0.1643	0.5464	267
	PPA_158_9	PPA_158_4	1	0.5	406	38.99	0.0105	1.0023	1.6082	0.5961	0.1488	0.0045	0.5947	0.1501	0.0045	13.00-24.00	0.2980	0.5960	1109
	PPA_158_8	PPA_158_5	1	1	412	78.91	0.2049	0.8483	1.8032	1.6749	0.0991	0.0026	1.9745	0.1015	0.0026	40.00-70.00	1.6749	1.6748	1239
	PPA_158_16	PPA_158_1	3	0.01	104.9	10.38	0.0000	2.9899	2.7004	2.4106	0.0796	0.0005	0.8062	0.0303	0.0002	5.00-8.00	0.0241	2.4106	169
	PPA_158_16	PPA_158_1	3	0.05	106.3	10.26	0.0103	2.9916	2.6310	2.0575	0.2070	0.0026	0.6877	0.0703	0.0009	4.95-8.00	0.1029	2.0573	399
	PPA_158_16	PPA_158_1	3	0.1	77	7.35	0.0151	2.9965	2.7536	2.1591	0.1218	0.0022	0.7205	0.0423	0.0008	2.00-5.00	0.2159	2.1596	612
	PPA_158_22	PPA_158_3	3	0.2	174.6	16.74	0.5687	2.9911	2.3297	1.8339	0.4922	0.0110	0.6131	0.1662	0.0037	11.00-15.00	0.3668	1.8334	557
Mixed	AAI1_12	PPA_158_15	0.25	0.01	104	9.84	0.0009	0.2413	0.1456	0.0707	0.0252	0.0002	0.2930	0.1123	0.0011	4.00-6.00	0.0007	0.0707	37
	AAI1_12	PPA_158_15	0.25	0.05	114.4	10.93	0.0016	0.2445	0.1565	0.1047	0.0245	0.0004	0.4280	0.1120	0.0018	4.00-8.00	0.0052	0.1047	69
	AAI1_18	PPA_158_20	0.25	0.05	104.2	9.99	0.0038	0.2462	0.2156	0.1698	0.0220	0.0003	0.6896	0.1194	0.0019	4.00-8.00	0.0085	0.1698	80
	AAI1_18	PPA_158_20	0.25	0.05	104.1	9.99	0.0032	0.2453	0.1386	0.1070	0.0186	0.0003	0.4361	0.0908	0.0014	4.00-8.00	0.0054	0.1070	69
	AAI1_12	PPA_158_15	0.25	0.1	104.3	10.00	0.0017	0.2440	0.1823	0.1641	0.0206	0.0005	0.6727	0.1099	0.0025	4.00-8.00	0.0164	0.1641	85
	AAI1_18	PPA_158_20	0.25	0.2	130.1	12.51	0.0069	0.2452	0.1351	0.1068	0.0188	0.0006	0.4356	0.0865	0.0027	4.00-8.00	0.0214	0.1069	118
	AAI1_18	PPA_158_20	0.25	0.3	209.1	20.10	0.0087	0.2436	0.1546	0.1429	0.0206	0.0005	0.5864	0.1093	0.0027	5.00-15.00	0.0429	0.1428	119
	AAI1_18	PPA_158_20	0.25	0.5	212	20.36	0.0026	0.2373	0.1900	0.1407	0.0128	0.0006	0.5928	0.0737	0.0033	10.00-15.00	0.0703	0.1407	167
	AAI1_18	PPA_158_20	0.25	1	212.2	20.38	0.0764	0.2387	0.2179	0.1829	0.0257	0.0011	0.7663	0.1168	0.0052	5.00-15.00	0.1829	0.1829	253
	AAI1_18	PPA_158_20	0.25	1.7	840.4	80.71	0.1809	0.2218	0.2450	0.0971	0.0341	0.0011	0.4379	0.1495	0.0050	35.00-50.00	0.1651	0.0971	462
	AAI1_12	PPA_158_15	0.25	2.4	1423.4	20.77	0.0103	0.2282	0.2579	0.1050	0.0263	0.0013	0.4600	0.1251	0.0061	10.00-30.00	0.2519	0.1011	461
	AAI1_30	PPA_158_18	0.5	0.01	104.1	9.86	0.0032	0.4901	0.2178	0.1604	0.0352	0.0002	0.3272	0.0756	0.0005	4.00-8.00	0.0016	0.1604	48
	AAI1_30	PPA_158_18	0.5	0.05	105.4	10.09	0.0024	0.4919	0.3146	0.3146	0.0230	0.0004	0.6397	0.0620	0.0010	4.00-8.00	0.0157	0.3146	101
	AAI1_30	PPA_158_18	0.5	0.1	105	10.07	0.0019	0.4939	0.3673	0.2876	0.0166	0.0004	0.5823	0.0484	0.0011	4.00-8.00	0.0288	0.2875	128

	AAI1_30	PPA_158_18	0.5	0.2	208.4	20.03	0.0015	0.4928	0.3352	0.2648	0.0182	0.0006	0.5374	0.0478	0.0015	1.00-5.00	0.0530	0.2647	173
	AAI1_30	PPA_158_18	0.5	0.3	209.1	20.09	0.0000	0.4966	0.3588	0.2823	0.0799	0.0028	0.5685	0.1640	0.0057	6.00-11.00	0.0847	0.2822	246
	AAI1_30	PPA_158_18	0.5	0.5	224.9	21.60	0.0000	0.4959	0.3360	0.2649	0.0784	0.0025	0.5341	0.1614	0.0051	5.00-15.00	0.1324	0.2650	254
	AAI1_30	PPA_158_18	0.5	1	420.1	40.35	0.0152	0.4922	0.3597	0.2654	0.0261	0.0008	0.5392	0.0561	0.0018	25.00-35.00	0.2654	0.2654	653
	AAI1_29	PPA_158_18	0.5	1.7	234	22.53	0.1431	0.4695	0.5045	0.1943	0.0318	0.0019	0.4138	0.0746	0.0043	5.00-10.00	0.3303	0.1947	416
	AAI1_29	PPA_158_18	0.5	2.4	173.2	16.63	0.6543	0.4642	0.2996	0.1323	0.0437	0.0030	0.2850	0.1063	0.0074	10.00-15.00	0.3175	0.1323	203
	AAI1_6	PPA_158_19	1	0.01	74.4	6.97	0.0147	1.0013	0.7114	0.6163	0.0552	0.0004	0.6155	0.0597	0.0004	2.00-6.00	0.0062	0.6163	71
	AAI1_6	PPA_158_19	1	0.05	138.1	13.19	0.0007	0.9989	0.6591	0.3653	0.0296	0.0005	0.3657	0.0316	0.0005	8.00-12.000	0.0183	0.3653	120
	AAI1_6	PPA_158_19	1	0.1	208.2	19.94	0.0097	0.9966	0.7162	0.5445	0.0818	0.0018	0.5464	0.0837	0.0019	15.00-19.00	0.0545	0.5447	242
	AAI1_6	PPA_158_19	1	0.2	276.2	26.39	0.0427	1.0037	0.5899	0.4278	0.0729	0.0015	0.4262	0.0736	0.0015	15.00-25.00	0.0856	0.4279	462
	AAI1_8	PPA_158_17	1	0.3	74.6	7.16	2.2374	0.9847	0.7905	0.4659	0.0888	0.0049	0.4731	0.0947	0.0052	3.00-5.00	0.1398	0.4664	242
	AAI1_8	PPA_158_17	1	0.5	46.8	4.49	2.3042	0.9661	0.6085	0.4270	0.0792	0.0064	0.4420	0.0854	0.0069	2.00-3.50	0.2135	0.4270	241
	AAI1_5	PPA_158_17	1	1	43.9	4.21	4.5673	0.9655	0.6742	0.5200	0.0706	0.0099	0.5386	0.0745	0.0104	1.00-2.00	0.5200	0.5172	374
	AAI1_5	PPA_158_17	1	1.7	35.9	3.45	6.3607	0.9662	0.6934	0.5301	0.1157	0.0208	0.5487	0.1259	0.0226	1.00-1.50	0.9012	1.0668	359
	AAI1_4	PPA_158_17	1	2.4	56.6	5.43	10.4742	0.9678	0.8147	0.3322	0.0820	0.0237	0.3432	0.1010	0.0292	0.90-1.43	0.7973	0.3253	209
	AAI1_3	PPA_158_18	3	0.01	0.3	0.02	0.3206	2.9537	1.7799	1.4191	0.0481	0.0089	0.4804	0.0173	0.0032	0.005-0.01	0.0142	1.3859	39
	AAI1_2	PPA_158_18	3	0.05	4.8	0.46	0.0781	2.9564	2.0497	1.8871	0.0423	0.0030	0.6383	0.0167	0.0012	0.10-0.30	0.0944	1.8879	105
	AAI1_1	PPA_158_18	3	0.1	1.2	0.11	0.3298	1.9234	1.9874	1.8351	0.0757	0.0165	0.9541	0.0250	0.0055	0.02-0.06	0.1835	1.8272	75

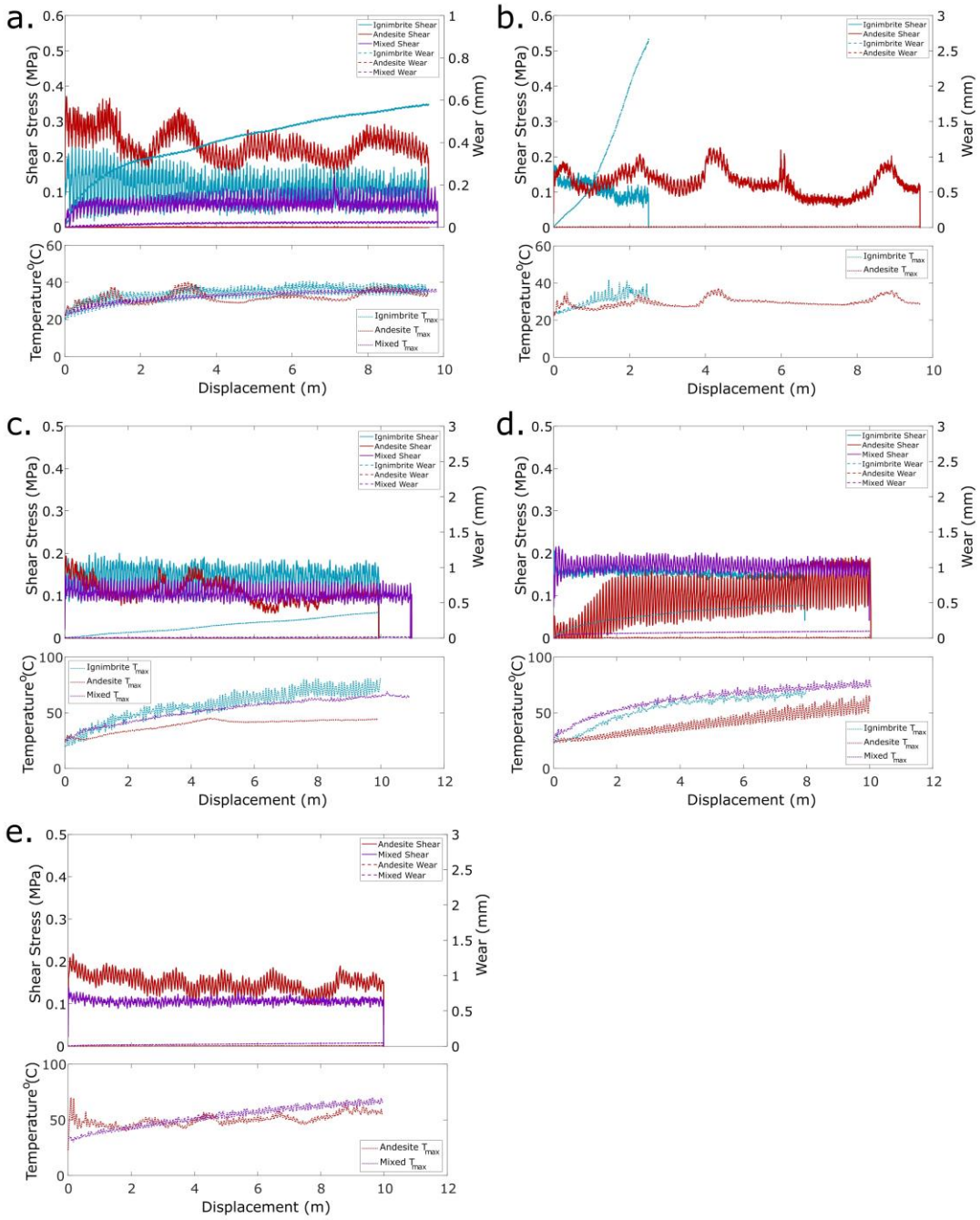

Supplementary Figure A.II.1. Evolution of friction coefficient, shortening (wear) and temperature for tests at 0.25 MPa a-b) 0.01 m s^{-1} c-e) 0.05 m s^{-1} for the three lithology combinations tested (rhyolitic ignimbrite – blue, andesitic lava – red, mixed lithology – purple). T_{max} is the peak temperature measured by the thermographic camera in any given frame.

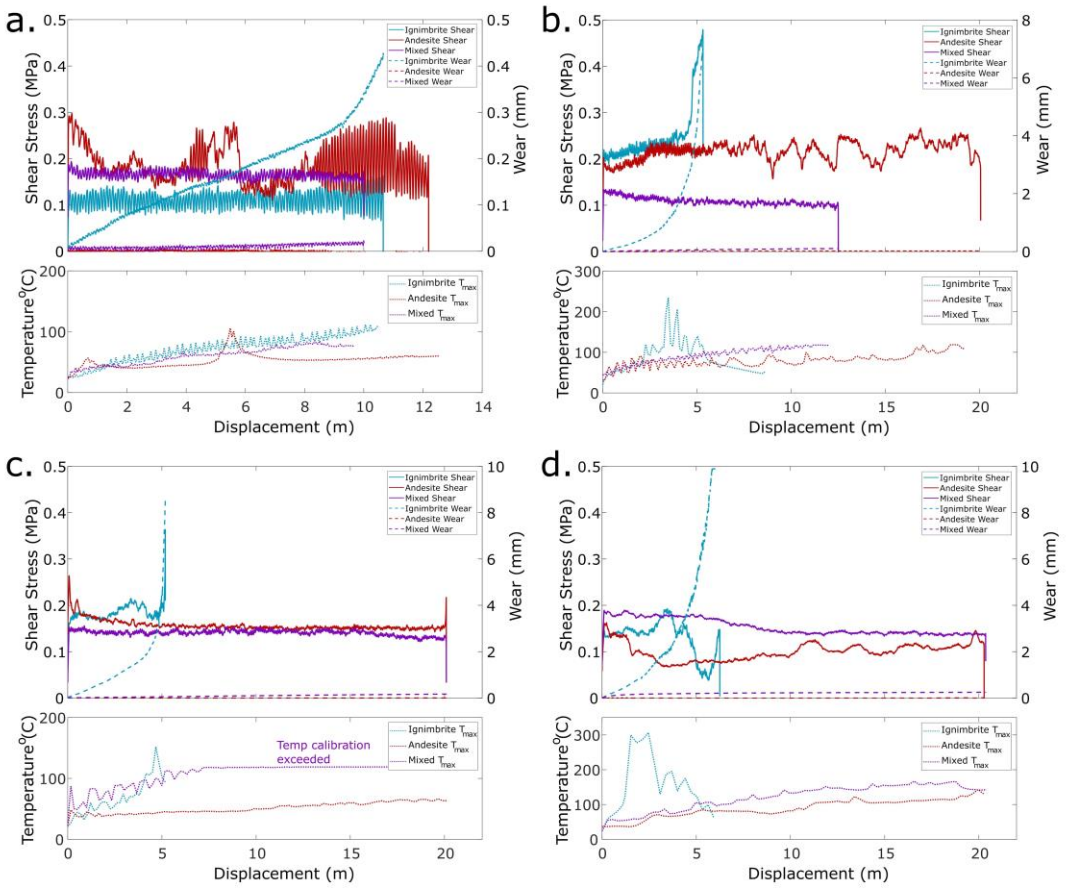

Supplementary Figure A.II.2. Evolution of friction coefficient, shortening (wear) and temperature for tests at 0.25 MPa a) 0.1 m s^{-1} b) 0.2 m s^{-1} c) 0.3 m s^{-1} d) 0.5 m s^{-1} for the three lithology combinations tested (rhyolitic ignimbrite – blue, andesitic lava – red, mixed lithology – purple). T_{max} is the peak temperature measured by the thermographic camera in any given frame.

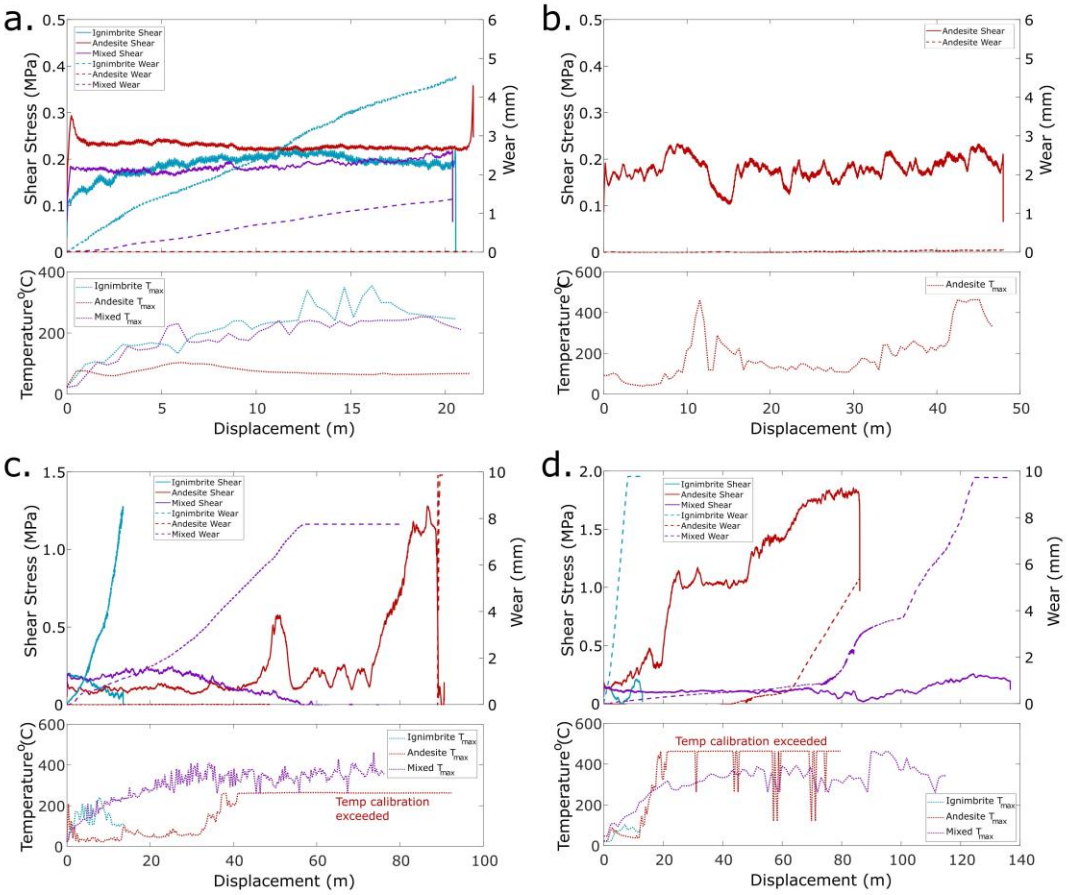

Supplementary Figure A.II.3. Evolution of friction coefficient, shortening (wear) and temperature for tests at 0.25 MPa a-b) 1 m s^{-1} c) 1.7 m s^{-1} d) 2.4 m s^{-1} for the three lithology combinations tested (rhyolitic ignimbrite – blue, andesitic lava – red, mixed lithology – purple). T_{max} is the peak temperature measured by the thermographic camera in any given frame.

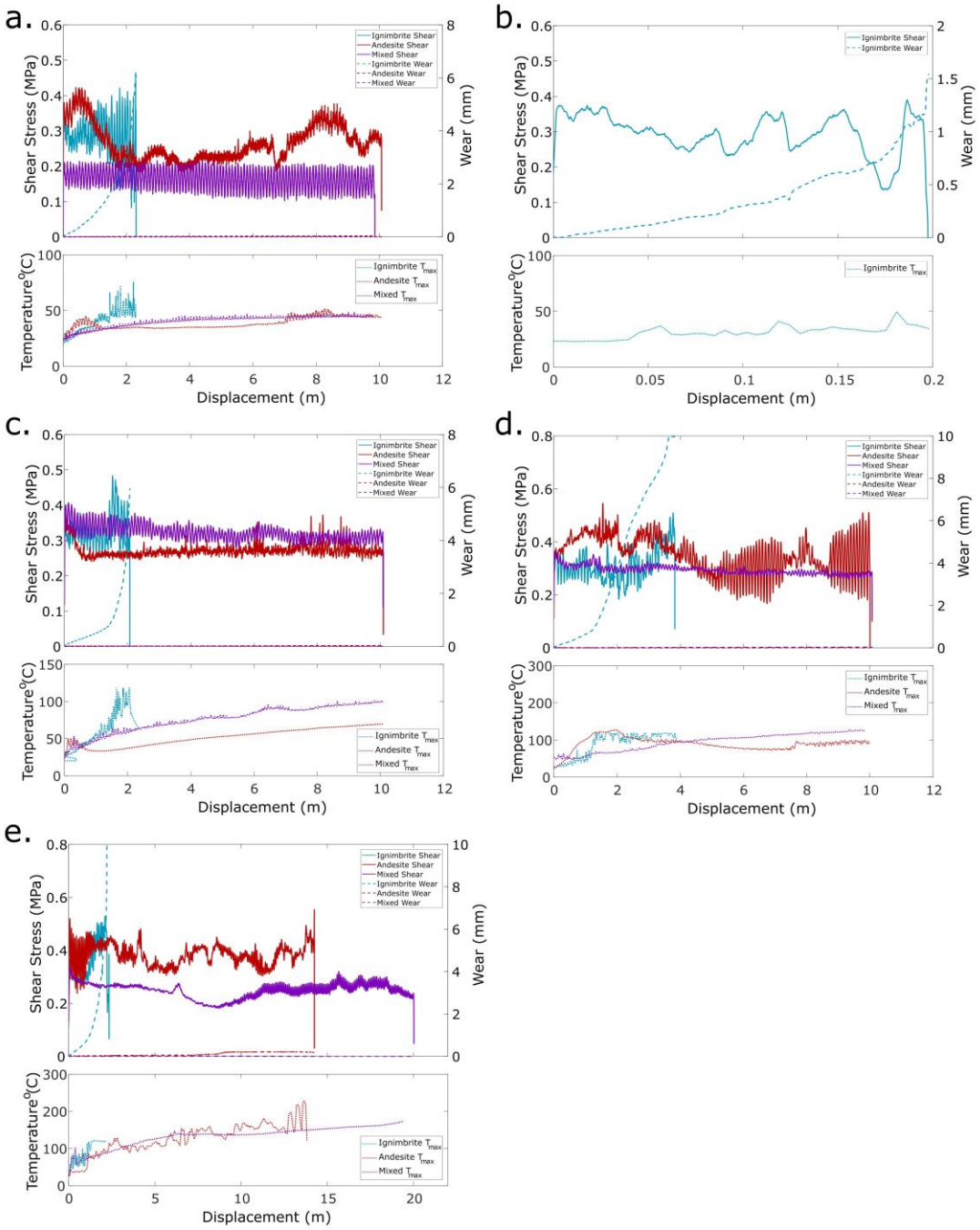

Supplementary Figure A.II.4. Evolution of friction coefficient, shortening (wear) and temperature for tests at 0.5 MPa a-b) 0.01 m s^{-1} c) 0.05 m s^{-1} d) 0.1 m s^{-1} e) 0.2 m s^{-1} for the three lithology combinations tested (rhyolitic ignimbrite – blue, andesitic lava – red, mixed lithology – purple). T_{max} is the peak temperature measured by the thermographic camera in any given frame.

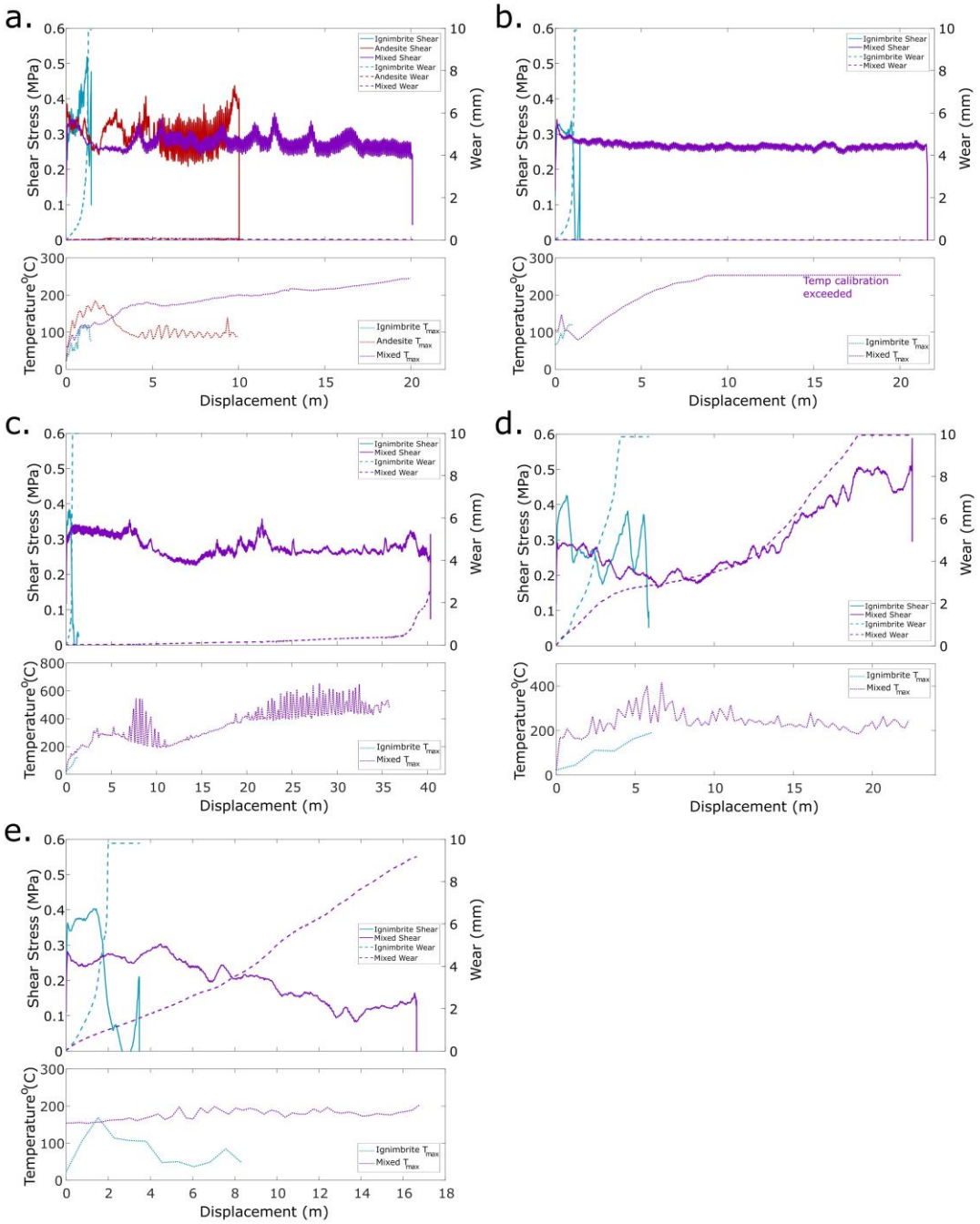

Supplementary Figure A.II.5. Evolution of friction coefficient, shortening (wear) and temperature for tests at 0.5 MPa a) 0.3 m s^{-1} b) 0.5 m s^{-1} c) 1 m s^{-1} d) 1.7 m s^{-1} e) 2.4 m s^{-1} for the three lithology combinations tested (rhyolitic ignimbrite – blue, andesitic lava – red, mixed lithology – purple). T_{max} is the peak temperature measured by the thermographic camera in any given frame.

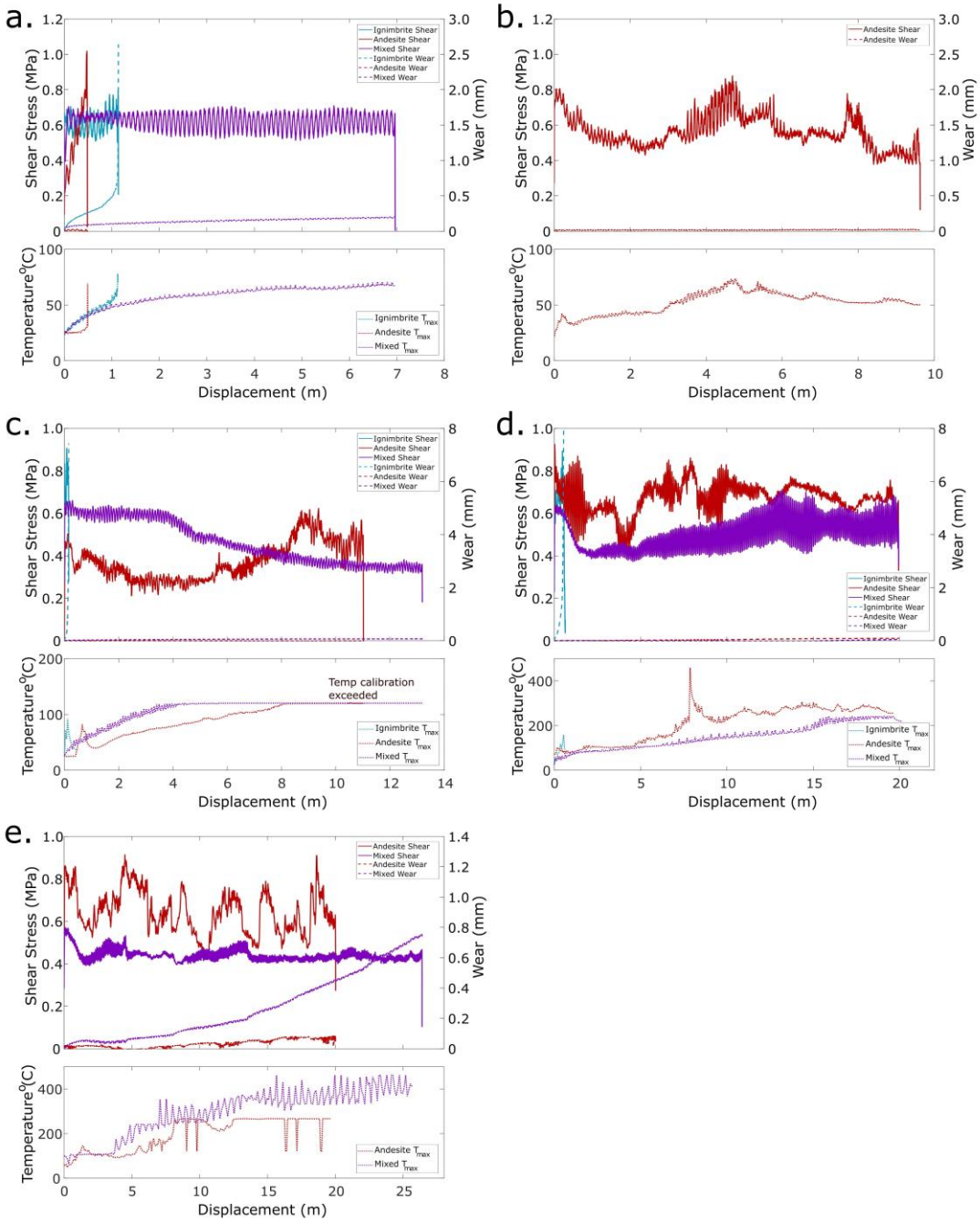

Supplementary Figure A.II.6. Evolution of friction coefficient, shortening (wear) and temperature for tests at 1 MPa a-b) 0.01 m s^{-1} c) 0.05 m s^{-1} d) 0.1 m s^{-1} e) 0.2 m s^{-1} for the three lithology combinations tested (rhyolitic ignimbrite – blue, andesitic lava – red, mixed lithology – purple). T_{max} is the peak temperature measured by the thermographic camera in any given frame.

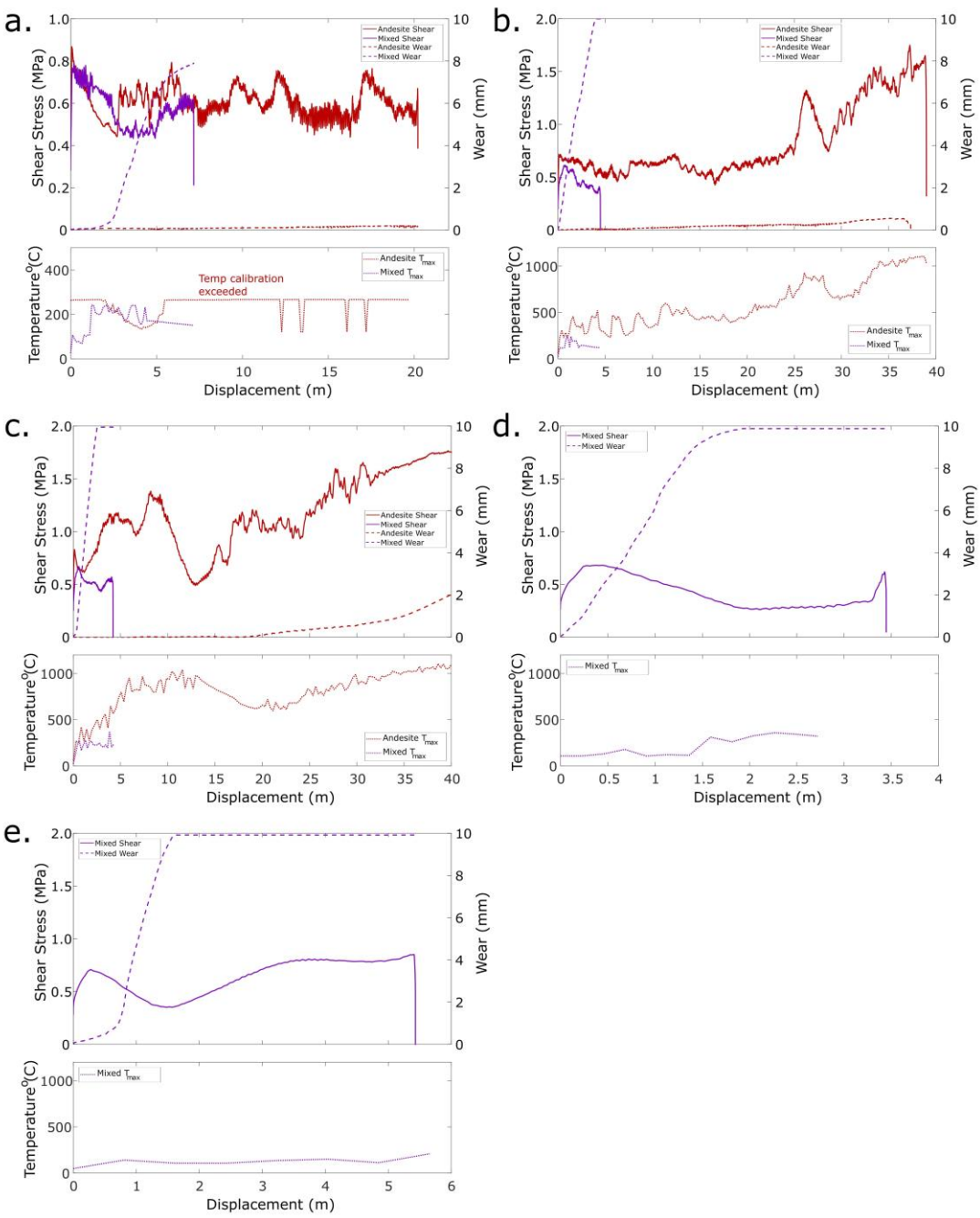

Supplementary Figure A.II.7. Evolution of friction coefficient, shortening (wear) and temperature for tests at 1 MPa a) 0.3 m s^{-1} b) 0.5 m s^{-1} c) 1 m s^{-1} d) 1.7 m s^{-1} e) 2.4 m s^{-1} for the three lithology combinations tested (rhyolitic ignimbrite – blue, andesitic lava – red, mixed lithology – purple). T_{max} is the peak temperature measured by the thermographic camera in any given frame.

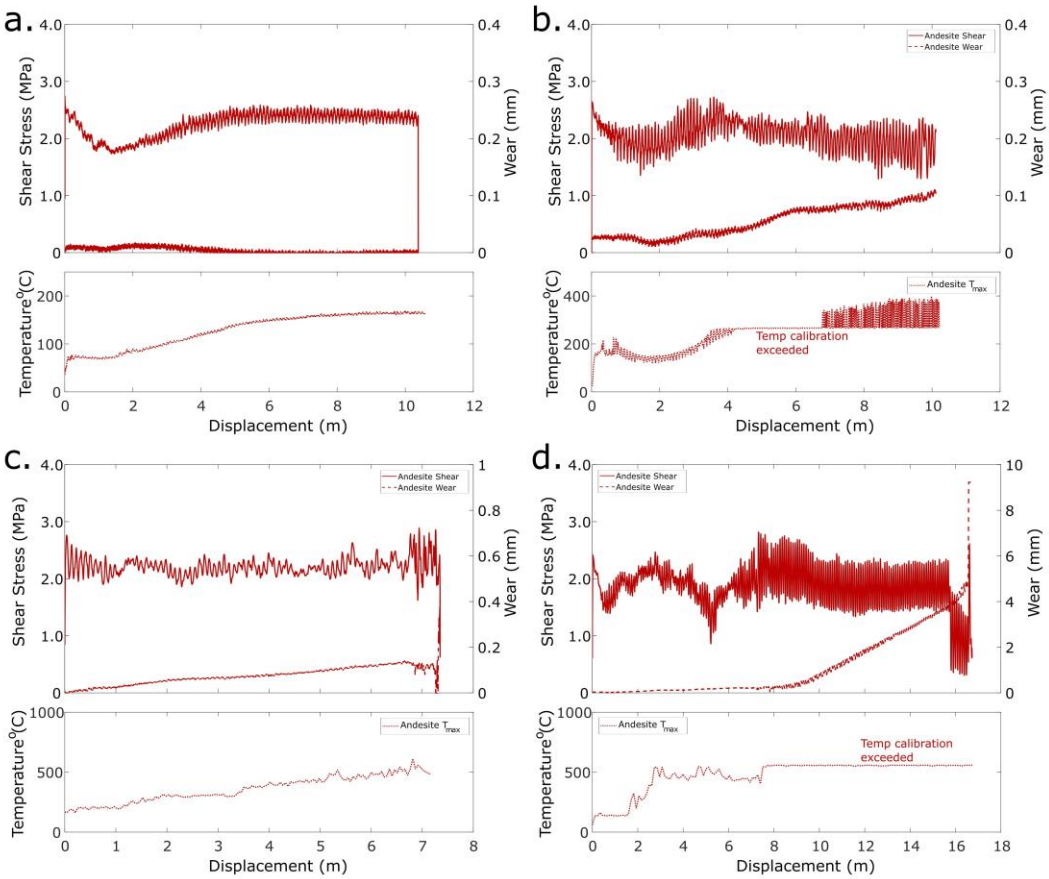

Supplementary Figure A.II.8. Evolution of friction coefficient, shortening (wear) and temperature for tests on andesitic lava (red) at 1 MPa a) 0.01 m s^{-1} b) 0.05 m s^{-1} c) 0.1 m s^{-1} d) 0.2 m s^{-1}. T_{max} is the peak temperature measured by the thermographic camera in any given frame.

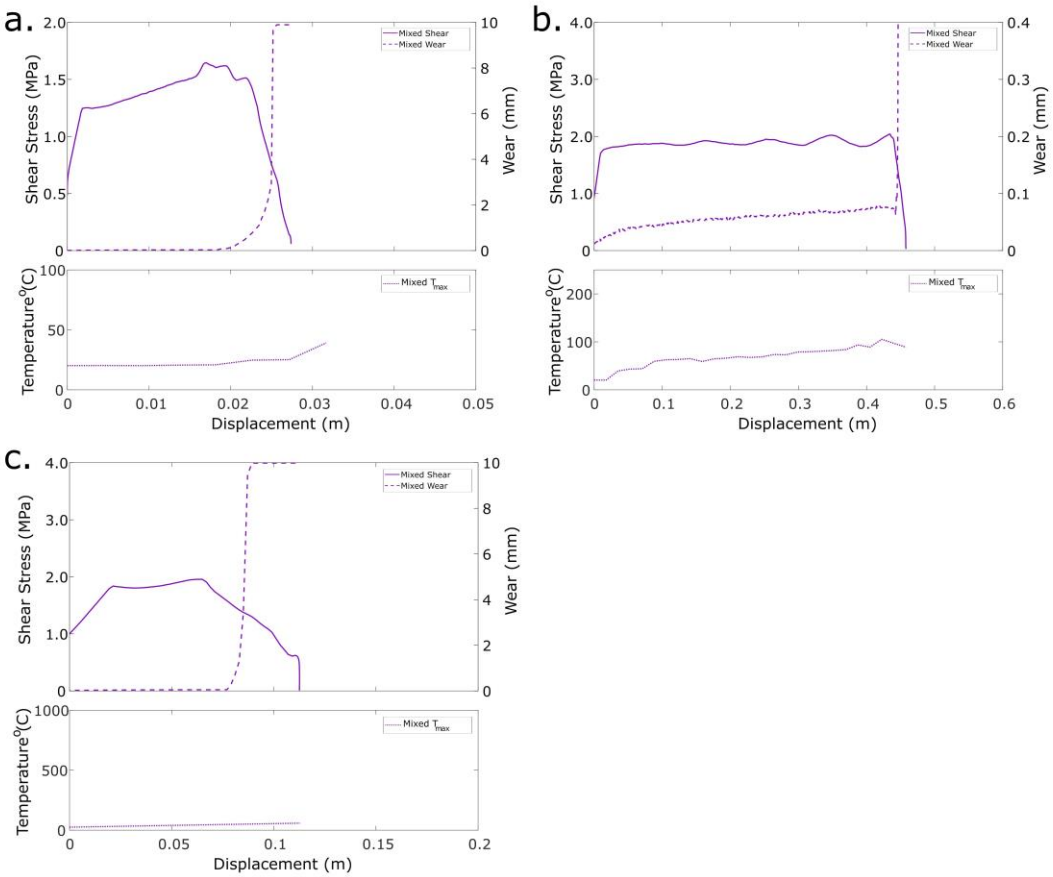

Supplementary Figure A.II.8. Evolution of friction coefficient, shortening (wear) and temperature for tests on mixed lithology (purple) at 1 MPa a) 0.01 m s^{-1} b) 0.05 m s^{-1} c) 0.1 m s^{-1}. T_{max} is the peak temperature measured by the thermographic camera in any given frame.

Appendix III – (Chapter 4)

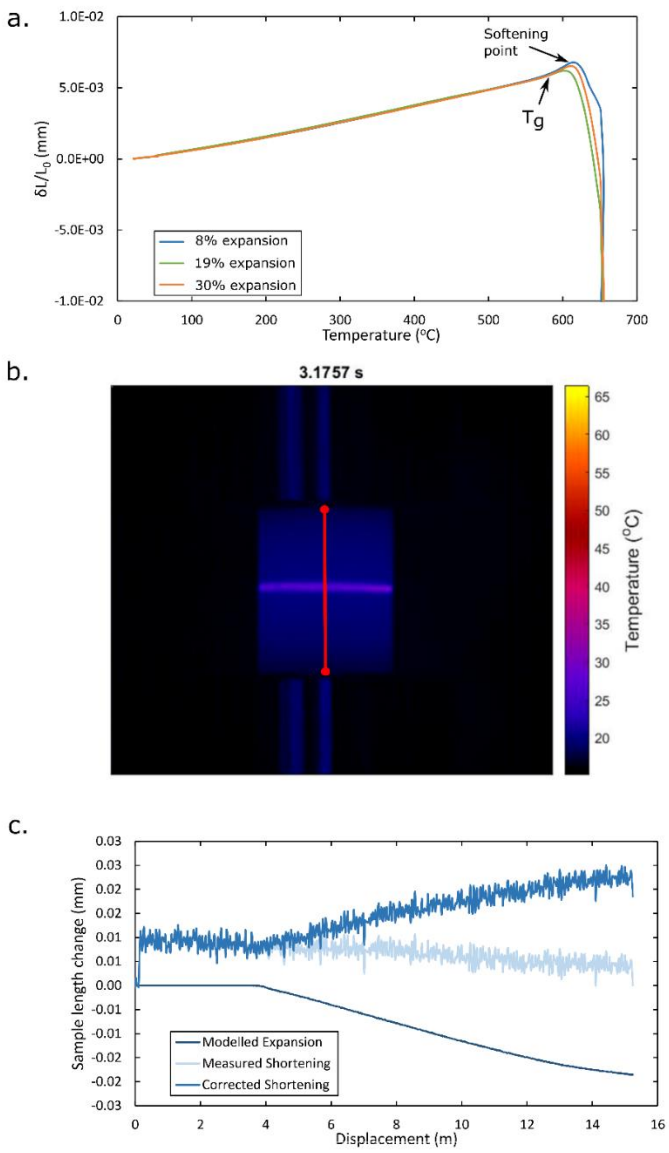

Supplementary Figure A.III.1. Process of thermal expansion correction. a) Thermal expansion profiles for 8, 19 and 30% porosity samples measured using TMA. Expansion is not influenced by porosity below T_g. b) A frame of thermographic data taken from representative test (8% porosity, 0.4 m s^{-1} at 0.5 MPa). The axial temperature profile analysed marked in red along which each pixel is given an expansion determined by the expansion profile in 1a, the sum of which is the axial thermal expansion for this frame. This is repeated for every frame of thermographic data producing a modelled expansion through time. c) Modelled expansion is correlated to displacement of the experiment and combined with the measured shortening to produce resultant corrected shortening.

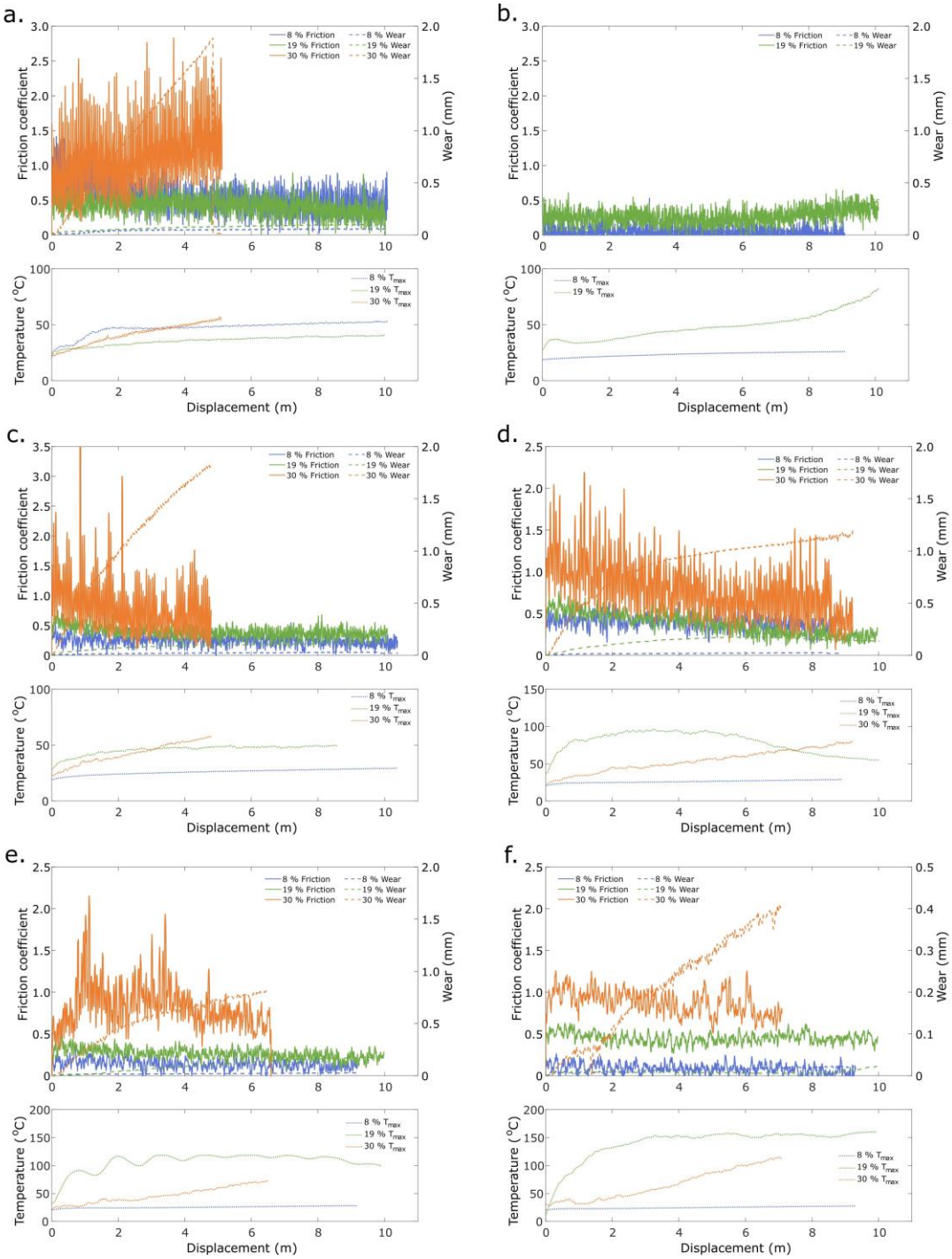

Supplementary Figure A.III.2. Evolution of friction coefficient, shortening (wear) and temperature for tests at 0.25 MPa a-b) 0.1 m s^{-1} c) 0.2 m s^{-1} d) 0.3 m s^{-1} e) 0.4 m s^{-1} f) 0.5 m s^{-1} for the suite of porosities tested (8 % blue, 19 % green and 30 % orange). T_{max} is the peak temperature measured by the thermographic camera in any given frame.

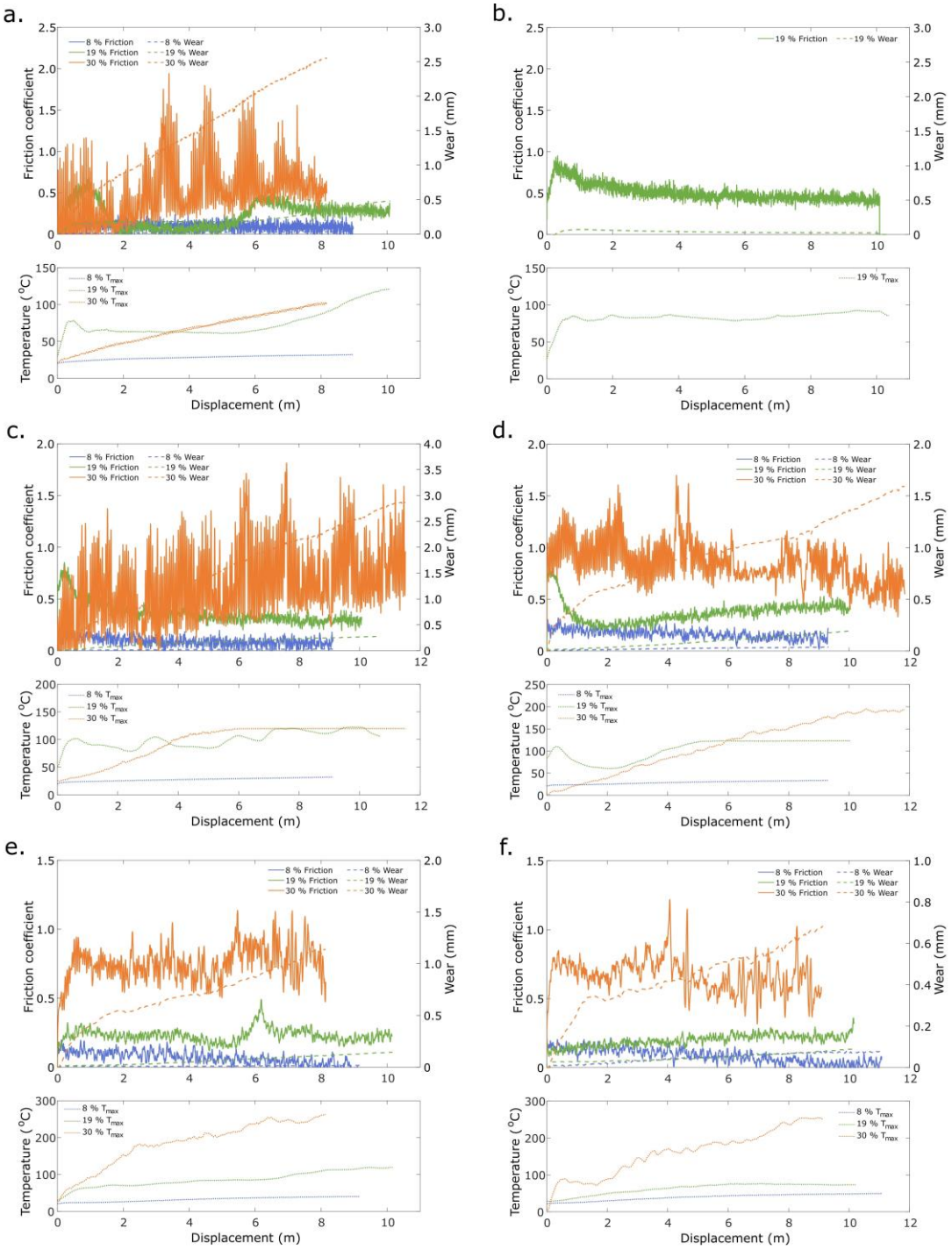

Supplementary Figure A.III.3. Evolution of friction coefficient, shortening (wear) and temperature for tests at 0.5 MPa a-b) 0.1 m s^{-1} c) 0.2 m s^{-1} d) 0.3 m s^{-1} e) 0.4 m s^{-1} f) 0.5 m s^{-1} for the suite of porosities tested (8 % blue, 19 % green and 30 % orange). T_{max} is the peak temperature measured by the thermographic camera in any given frame.

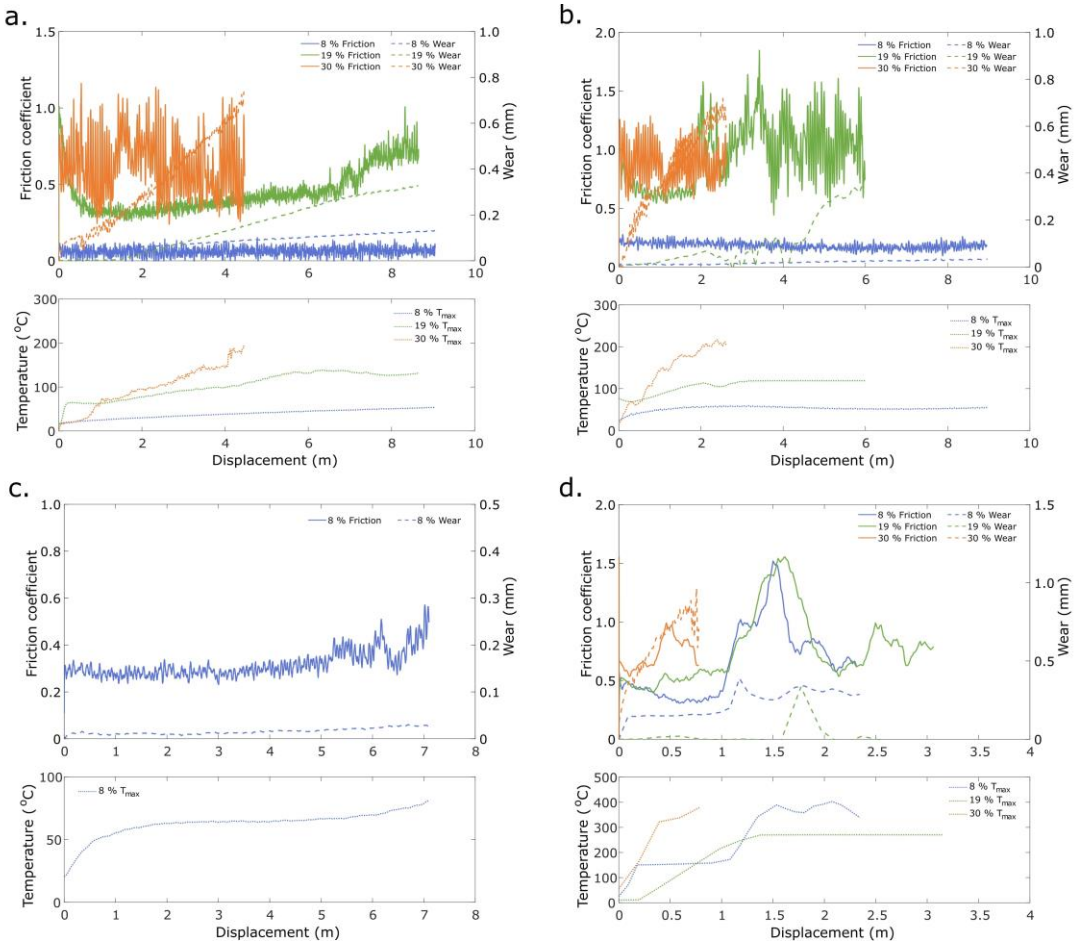

Supplementary Figure A.III.4. Evolution of friction coefficient, shortening (wear) and temperature for tests at 1 MPa a) 0.1 m s^{-1} b) 0.2 m s^{-1} c) 0.3 m s^{-1} d) 1 m s^{-1} for the suite of porosities tested (8 % blue, 19 % green and 30 % orange). T_{max} is the peak temperature measured by the thermographic camera in any given frame.

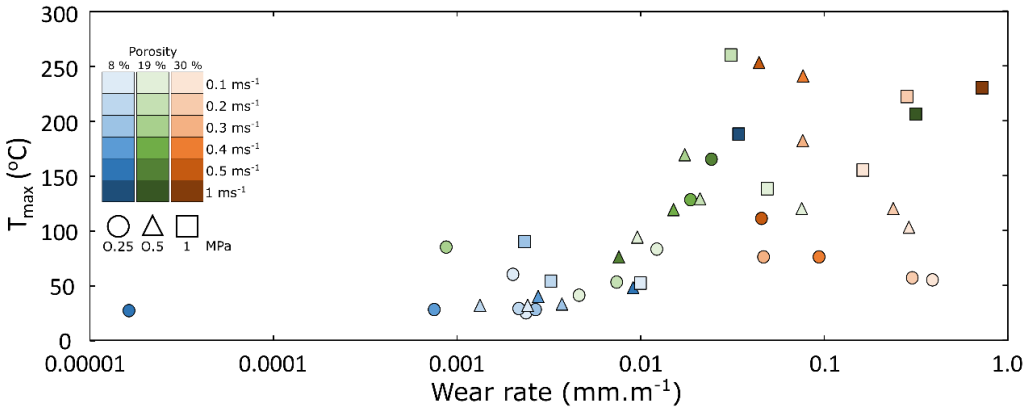

Supplementary Figure A.III.5. Peak temperature (T_{max}) versus wear rate (in log scale), showing positive correlation (as both are controlled by work), but T_{max} of the mid-porosity sample often exceeds that of the most porous sample, which has higher wear rates that may counteract temperature increase.

Supplementary Table A.III.1. Normal stress independent friction coefficient values for each porosity sample set at each slip rate constructed from the gradients in Figure 1b-d.

Porosity (%)	**Slip rate (m s^{-1})**					
	0.1	**0.2**	**0.3**	**0.4**	**0.5**	**1.0**
8	0.053	0.155	0.274	0.098	0.061	0.392
19	0.337	0.546	0.310	0.227	0.227	0.541
30	0.582	0.854	0.864	0.726	0.650	0.614